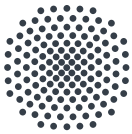

Universität Stuttgart

Imaging microspectroscopy of functional nanoplasmonic systems

Von der Fakultät Mathematik und Physik
der Universität Stuttgart zur Erlangung der Würde
eines Doktors der Naturwissenschaften (Dr. rer. nat.)
genehmigte Abhandlung

vorgelegt von

Florian Frederik Sterl

aus Pinneberg

Hauptberichter:	Prof. Dr. Harald Giessen
Mitberichterin:	Prof. Dr. Stefanie Barz
Prüfungsvorsitzender:	Prof. Dr. Siegfried Dietrich

Tag der mündlichen Prüfung: 21.07.2020

4. Physikalisches Institut der Universität Stuttgart
2020

Florian Frederik Sterl: *Imaging microspectroscopy of functional nanoplasmonic systems*, 2020

For my family
Für meine Familie
Voor mijn familie

There is a theory which states that if ever anyone discovers exactly what the Universe is for and why it is here, it will instantly disappear and be replaced by something even more bizarre and inexplicable.

There is another theory which states that this has already happened.

— Douglas Adams, *The Restaurant at the End of the Universe*

We zijn voorbij de start, maar we zijn nog niet aan het einde van het begin.

— Mark Rutte

ABSTRACT

The interaction of light with metal nanoparticles leads to a variety of interesting phenomena. The excitation of collective oscillations of the free electron cloud, the so-called *plasmon resonance*, can be used to extract information about the nanoscale environment of a particle in the optical far-field. This far-field can be accessed by measuring properties such as the transmittance or reflectance of a system consisting of plasmonic nanoparticles. This property can be used for investigating the fundamental properties of nanoplasmonic systems, but also, for example, for the development of active optical devices and optical sensors. The far-field investigation of nanoscale systems can be carried out using a variety of techniques, which often combine optical microscopy with spectroscopic methods.

This thesis covers the topic of microspectroscopy by giving the reader an extensive theoretical background, as well as an overview of possible implementations of microspectroscopy setups, which is also intended to give the reader a basic 'user manual' for microspectroscopic experiments. A theoretical foundation for the topic of plasmonics is given as well. Furthermore, several different nanoplasmonic systems are investigated in detail, with a variety of purposes and applications.

First, we look at the material magnesium (Mg), which we demonstrate to be a suitable novel candidate for nanoplasmonic applications. A highly interesting characteristic of Mg is its ability to absorb and store large amounts of hydrogen. This property can be exploited from several different perspectives. On one hand, it can be used to fabricate active plamonic nanoantennas, which can be switched between two distinct states via the absorption and desorption of hydrogen. On the other hand, the use of optical measurements enables the investigation of hydrogen diffusion in Mg nanoparticles. This is interesting for a different field of research, namely the development of metal-hydride-based hydrogen storage systems, which can play an important role in the use of hydrogen gas as an energy carrier. In this thesis, we present a novel method for observing and tracking the hydrogen diffusion within a single Mg particle. This method arises from a combination of far-field and near-field optical microscopy, with which the electric field in the direct vicinity of nanostructures can be mapped.

The second system under investigation is a nanoplasmonic design for an all-optical hydrogen sensor based on palladium (Pd) nanoparticles. The development of safe, reliable, and sensitive H_2 sensors is another important factor for the use of H_2 fuel, as well as for several industrial processes. A tailored sensor design, consisting of Pd nanodisks coupled to an optical cavity, is systematically investigated using numerical calculations and microspectroscopic measurements. The obtained insights enable us to formulate a set of design rules with regard to the structural parameters of such a sensor, which can in the future be applied to optimize the performance of plasmonic H_2 sensors, as well as other plasmonic sensor concepts..

Furthermore, we investigate a fundamental property of nanoplasmonic systems, namely the presence of order and disorder in the spatial arrangement of nanoantennas. We make use of a disorder model in which the 'disorder strength' can be gradually increased. The structural ordering of nanoparticles largely determines the far-field properties of the collective: A periodic lattice, for example, exhibits very different behavior compared to an ensemble of randomly distributed particles. In addition to determining the type and strength of disorder from far-field measurements, this can be used to engineer a desired far-field appearance via the introduction of tailored disorder.

DEUTSCHE ZUSAMMENFASSUNG

Aus der Wechselwirkung zwischen Licht und metallischen Nanoteilchen ergibt sich ein breites Spektrum an interessanten Phänomenen. So kann beispielsweise die Anregung kollektiver Schwingungen in der Wolke aus freien Elektronen, auch *Plasmonresonanz* genannt, benutzt werden, um Information aus der lokalen Umgebung eines Metallteilchens im optischen Fernfeld zu detektieren, also mittels Messungen von optischen Eigenschaften wie der Transmission oder Reflektion eines Systems bestehend aus plasmonischen Nanoteilchen. Dies ermöglicht die Erforschung fundamentaler Eigenschaften solcher Systeme, aber auch für die Entwicklung von aktiven optischen Systemen und optischen Sensoren. Es gibt verschiedene Techniken für optische Untersuchungen an Objekten auf der Nanoskala. Diese bestehen oftmals aus einer Kombination von optischer Mikroskopie mit spektroskopischen Messverfahren.

Diese Dissertation befasst sich zuerst mit dem Thema der Mikrospektroskopie, mittels einer ausführlichen Beschreibung der theoretischen Prinzipien der Mikroskopie sowie der Spektroskopie. Sie enthält eine Übersicht verschiedener möglicher Realisierungen für Mikrospektroskopie-Messaufbauten, welche dem Leser auch als eine grundlegende 'Anleitung' für mikrospektroskopische Experimente dienen soll, gefolgt von den theoretischen Grundlagen der Plasmonik. Als Nächstes werden verschiedene nanoplasmonische Systeme mit unterschiedlichen Anwendungen und Forschungszielen im Detail untersucht.

Zuerst betrachten wir das Material Magnesium (Mg), und zeigen dass dieses Material ein geeigneter Kandidat für nanoplasmonische Anwendungen ist. Eine sehr interessante Eigenschaft von Mg ist seine Fähigkeit, relativ große Mengen Wasserstoff aufzunehmen und somit zu speichern. Dies ist aus unterschiedlichen Perspektiven interessant. Einerseits kann Mg eingesetzt werden um aktive plasmonische Nanoantennen zu realisieren, die sich durch die Aufnahme und Abgabe von Wasserstoff zwischen zwei fundamental unterschiedlichen Zuständen hin- und herschalten lassen. Andererseits können optische Messungen benutzt werden um die Wasserstoffdiffusion in Mg-Nanoteilchen zu studieren. Dies ist wiederum interessant für ein ganz anderes Forschungsgebiet, nämlich die Entwicklung von Metallhydrid-basierten

Wasserstoffspeichersystemen, welche für die Nutzung von Wasserstoffgas als Energieträger eine wichtige Rolle spielen können. In dieser Dissertation stellen wir eine neuartige Methode für die Beobachtung und Nachverfolgung von Wasserstoffdiffusion innerhalb einzelner Mg-Nanoteilchen vor. Diese basiert auf einer Kombination aus klassischer optischer Fernfeldmikroskopie und Nahfeldmikroskopie, mit welcher das elektrische Feld in der direkten Umgebung von Nanostrukturen abgebildet werden kann.

Das zweite System das wir im Detail betrachten ist eine nanoplasmonische Struktur für die rein optische Detektion von Wasserstoff, basierend auf Nanoteilchen aus Palladium (Pd). Die Entwicklung sicherer, zuverlässiger und empfindlicher Wasserstoffsensoren ist ein weiterer wichtiger Faktor für die Nutzung von H_2 als Brennstoff, und ist auch für verschiedene industrielle Prozesse wichtig. Anhand von sowohl numerischen Berechnungen als auch mikrospektroskopischen Messungen untersuchen wir ein spezialisiertes Sensordesign, bestehend aus Pd-Nanoscheibchen welche an einen optischen Resonator gekoppelt sind. Eine systematische Untersuchung unterschiedlicher Strukturparameter ermöglicht uns die Formulierung einer Reihe von Entwurfsprinzipien, die in der Zukunft angewendet werden können, um die Leistung von plasmonischen H_2-Sensoren (sowie auch von anderen plasmonischen Sensorkonzepten) zu optimieren.

Darüber hinaus untersuchen wir eine fundamentale Eigenschaft von nanoplasmonischen Systemen, nämlich die Anwesenheit von Ordnung beziehungsweise Unordnung in der räumlichen Verteilung von Nanoantennen. Dafür nutzen wir ein Unordnungsmodell, in welchem der 'Grad' der Unordnung nach und nach erhöht werden kann. Die Anordnung von Nanoteilchen bestimmt zu einem Großteil die optischen Eigenschaften des gesamten Systems: Ein periodisches Gitter zeigt beispielsweise ein deutlich anderes Verhalten im Vergleich zu zufällig verteilten Nanoteilchen. Dies kann ausgenutzt werden, um die Art und die Parameter der (Un)ordnung mittels optischen Messungen zu identifizieren. Maßgeschneiderte räumliche Unordnung kann prinzipiell aber auch eingesetzt werden, um plasmonische Systeme mit bestimmten erwünschten optischen Eigenschaften zu realisieren.

NEDERLANDSE SAMENVATTING

De interactie van licht met metalen nanodeeltjes leidt tot een breed scala aan interessante fenomenen. De excitatie van collectieve oscillaties in de wolk van vrije elektronen, de zogenaamde *plasmonresonantie*, kan benut worden om informatie uit de lokale omgeving van een metalen nanodeeltje te detecteren in het optische verre veld, dus via het meten van eigenschappen zoals de transmissie of reflectie van systemen bestaande uit plasmonische nanodeeltjes. Dit kan gebruikt worden om fundamentele eigenschappen van nanoplasmonische systemen te bestuderen, maar ook voor de ontwikkeling van onder andere actieve optische systemen en optische sensoren. Voor het optisch bestuderen van objecten op nanoschaal kunnen verschillende technieken gebruikt worden. Deze bestaan vaak uit een combinatie van optische microscopie en spectroscopische meetmethodes.

Deze dissertatie behandelt allereerst het onderwerp microspectroscopie met een uitgebreide beschrijving van de theoretische principes achter zowel microscopie als ook spectroscopie, inclusief een overzicht van verschillende mogelijke realisaties van microspectroscopie-meetopstellingen. Het doel hiervan is mede om de lezer een algemene 'handleiding' voor microspectroscopische experimenten te geven. Dit wordt gevolgd door de een beschrijving van de theorie achter het onderwerp van plasmonica. Vervolgens worden verschillende nanoplasmonische systemen in detail bestudeerd, met uiteenlopende toepassingen en onderzoeksdoelen.

Allereerst bekijken we het materiaal magnesium (Mg), waarvan we demonstreren dat het een geschikte kandidaat is voor nanoplasmonische toepassingen. Een zeer interessante eigenschap van Mg is de capaciteit om relatief grote hoeveelheden waterstof te absorberen en op te slaan. Dit biedt mogelijkheden vanuit verschillende perspectieven. Aan de ene kant kan Mg gebruikt worden voor het realiseren van actieve plasmonische nanoantennes, die tussen twee fundamenteel verschillende toestanden heen en weer geschakeld kunnen worden via het opnemen en afgeven van waterstof. Aan de andere kant kunnen optische metingen gebruikt worden om de waterstofdiffusie in Mg-nanodeeltjes te bestuderen. Dit is weer interessant voor een ander onderzoeksgebied, namelijk de ontwikkeling van metaalhydridegebaseerde systemen voor waterstofopslag, die een belangrijke rol kunnen

spelen voor het gebruik van waterstofgas als energiedrager. In deze dissertatie stellen we een nieuwe methode voor om de waterstofdiffusie in een enkel Mg-nanodeeltje te observeren en te volgen. Deze methode bestaat uit een combinatie van klassieke optische microscopie en een techniek genaamd *'scanning near-field optical microscopy'*, waarmee het elektrische veld in de directe omgeving van nanostructuren in kaart gebracht kan worden.

Het tweede systeem dat we in detail bekijken is een nanoplasmonische structuur voor puur optische waterstoffdetectoren, gebaseerd op palladium (Pd) nanodeeltjes. De ontwikkeling van veilige, betrouwbare en gevoelige waterstofsensoren is eveneens een belangrijke factor voor het gebruik van waterstof als brandstof, net als voor verschillende industriële processen. Met behulp van zowel numerieke berekeningen als ook microspectroscopische metingen bestuderen we een gespecialiseerd sensorontwerp, bestaande uit palladium nanoschijfjes die gekoppeld zijn aan een optische resonator. Door de verschillende structuurparameters systematisch te onderzoeken kunnen we een aantal ontwerpregels formuleren, die gebruikt kunnen worden om de prestaties van zowel plasmonische H_2-sensoren als ook andere plasmonische sensorconcepten te optimaliseren.

Verder onderzoeken we een fundamentele eigenschap van nanoplasmonische systemen, namelijk de aanwezigheid van orde dan wel wanorde in de ruimtelijke verdeling van nanoantennes. Hiervoor maken we gebruik van een wanorde-model waarin de 'mate' van wanorde geleidelijk opgeschroefd kan worden. De rangschikking van nanodeeltjes bepaalt voor een groot deel de optische eigenschappen van het geheel. Dit kan gebruikt worden voor het bepalen van het type en de parameters van de wanorde aan de hand van optische metingen, maar specifiek ontworpen ruimtelijke wanorde kan in principe ook ingezet worden om plasmonische systemen te ontwikkelen met bepaalde gewenste optische eigenschappen.

PUBLICATIONS

Parts of this thesis and associated work have been published in scientific journals, have been submitted to a journal, are being prepared for publication, and/or have been presented at national and international conferences.

JOURNAL PUBLICATIONS

P1 F. Sterl, N. Strohfeldt, R. Walter, R. Griessen, A. Tittl, and H. Giessen, "**Magnesium as Novel Material for Active Plasmonics in the Visible Wavelength Range**", *Nano Letters* **15**(12), 7949-7955 (2015), DOI 10.1021/acs.nanolett.5b03029.

P2 F. Sterl, H. Linnenbank, T. Steinle, F. Mörz, N. Strohfeldt, and H. Giessen, "**Nanoscale hydrogenography on single magnesium nanoparticles**", *Nano Letters* **18**(7), 4293-4302 (2018), DOI 10.1021/acs.nanolett.8b01277.

P3 F. Sterl, N. Strohfeldt, S. Both, E. Herkert, T. Weiss, and H. Giessen, "**Design Principles for Sensitivity Optimization in Plasmonic Hydrogen Sensors**", *ACS Sensors* **5**(4), 917-927 (2020), DOI 10.1021/acssensors.9b02436.

P4 F. Sterl, E. Herkert, S. Both, T. Weiss and H. Giessen, "**Shaping the color and angular appearance of plasmonic metasurfaces with tailored disorder**", *Submitted.*

P5 E. Herkert, F. Sterl, S. Both, T. Weiss, and H. Giessen, "**Computing the influence of structural disorder on plasmonic metasurfaces**", *In preparation.*

P6 R. Walter, A. Tittl, A. Berrier, F. Sterl, T. Weiss, and H. Giessen,
"**Large-area low-cost tunable plasmonic perfect absorber in the near infrared by colloidal etching lithography**",
Advanced Optical Materials **3**(3), 398-403 (2014),
DOI 10.1002/adom.201400545.

P7 S. Bagheri, C. M. Zgrabik, T. Gissibl, A. Tittl, F. Sterl, R. Walter, S. De Zuani, A. Berrier, T. Stauden, G. Richter, E. L. Hu, and H. Giessen,
"**Large-area fabrication of TiN nanoantenna arrays for refractory plasmonics in the mid-infrared by femtosecond direct laser writing and interference lithography**",
Optical Materials Express **5**(11), 2625-2633 (2015),
DOI 10.1364/OME.5.002625.

P8 X. Duan, S. Kamin, F. Sterl, H. Giessen, and N. Liu,
"**Hydrogen-regulated chiral nanoplasmonics**",
Nano Letters **16**(2), 1462-1466 (2016),
DOI 10.1021/acs.nanolett.5b05105.

P9 S. Bagheri, N. Strohfeldt, F. Sterl, A. Berrier, A. Tittl, and H. Giessen,
"**Large-area low-cost plasmonic perfect absorber chemical sensor fabricated by Laser Interference Lithography**",
ACS Sensors **1**(9), 1148-1154 (2016),
DOI 10.1021/acssensors.6b00444.

P10 T. Teutsch, A. Warsewa, N. Strohfeldt, F. Sterl, E. Herkert, H. Giessen, and C. Tarín,
"**Modeling of Pressure-Composition Isotherms and Diffusion Dynamics of a Plasmonic Palladium Sensor for Hydrogen Detection**",
Conference proceedings of the 2017 IEEE International Conference on Advanced Intelligent Mechatronics (AIM), 154-159 (2017),
DOI 10.1109/AIM.2017.8014011.

P11 T. Teutsch, N. Strohfeldt, F. Sterl, A. Warsewa, E. Herkert, D. Paone, H. Giessen, and C. Tarín,
"**Mathematical Modeling of a Plasmonic Palladium-Based Hydrogen Sensor**",
IEEE Sensors Journal **18**(5), 1946-1959 (2018),
DOI 10.1109/JSEN.2017.2786939.

P12 A. Böhme, F. Sterl, E. Kath, M. Ubl, V. Manninen, and H. Giessen,
"**Electrochemistry on Inverse Copper Nanoantennas: Active Plasmonic Devices with Extraordinarily Large Resonance Shift**",
ACS Photonics **6**(8), 1863-1868 (2019),
DOI 10.1021/acsphotonics.9b00716.

P13 A. Asadollahbaik, S. Thiele, K. Weber, A. Kumar, J. Drozella, F. Sterl, A. M. Herkommer, H. Giessen, and J. Fick,
"**Highly Efficient Dual-Fiber Optical Trapping with 3D Printed Diffractive Fresnel Lenses**",
ACS Photonics, **7**(1), 88-97 (2019),
DOI 10.1021/acsphotonics.9b01024.

P14 F. Kiani, F. Sterl, T. V. Tsoulos, K. Weber, H. Giessen, and G. Tagliabue,
"**Ultra-broadband and Omni-directional Perfect Absorber based on Copper Nanowire/Carbon Nanotube Hierarchical Structure**",
ACS Photonics **7**(2), 366-374 (2020),
DOI 10.1021/acsphotonics.9b01658.

P15 E. Herkert, F. Sterl, N. Strohfeldt, R. Walter, and H. Giessen,
"**Low-cost Hydrogen Sensor in the ppm Range with Purely Optical Readout**",
ACS Sensors **5**(4), 978-983 (2020),
DOI 10.1021/acssensors.9b02314.

P16 J. Karst, F. Sterl, H. Linnenbank, M. Hentschel, and H. Giessen,
"**Watching in-situ the hydrogen diffusion dynamics in magnesium on the nanoscale**",
Science Advances **6**(19), eaaz0566 (2020),
DOI 10.1126/sciadv.aaz0566.

P17 J. Karst, M. Hentschel, F. Sterl, H. Linnenbank, M. Ubl, and H. Giessen,
"**Optimizing magnesium thin films for optical switching applications: rules and recipes**",
Optical Materials Express **10**(6), 1346-1362 (2020),
DOI 10.1364/OME.393832.

P18 T. Pohl, F. Sterl, N. Strohfeldt, and H. Giessen,
"**Optical Carbon Dioxide Detection in the Visible Down to the Single Digit ppm Range**", *ACS Sensors* (2020),
DOI 10.1021/acssensors.0c01151.

P19 N. Strohfeldt, F. Sterl, R. Griessen, and H. Giessen,
"**Direct determination of Dielectric Properties of Plasmonic Nanostructures**", *In preparation.*

P20 A. Asadollahbaik, S. Thiele, A. Kumar, F. Sterl, J. Drozella, A. Herkommer, J. Fick, and H. Giessen,
"**Structured light by 3D printed micro-optical elements enables single fibre optical tweezers**", *In preparation.*

C1 F. Sterl, A. Tittl, N. Strohfeldt, R. Walter, and H. Giessen,
"**Magnesium Plasmonics for Chemical Reaction Sensing**",
The 5th International Topical Meeting on Nanophotonics and Metamaterials (NanoMeta), Seefeld in Tirol, Austria (2015), poster presentation.
Awarded with a Poster Prize (3rd place).

C2 F. Sterl, A. Tittl, N. Strohfeldt, R. Walter, and H. Giessen,
"**Magnesium as a novel material for active plasmonics and nanochemistry**",
Spring Meeting of the German Physical Society (DPG), Berlin, Germany (2015), oral presentation.

C3 V. Manninen, N. Strohfeldt, F. Sterl, A. Tittl, and H. Giessen ,
"**Plasmonic copper nanostructures for monitoring electrochemical redox reactions**",
Spring Meeting of the German Physical Society (DPG), Berlin, Germany (2015), oral presentation.

C4 F. Sterl, N. Strohfeldt, R. Walter, A. Tittl, and H. Giessen,
"**Magnesium as a novel material for active plasmonics in the visible**",
The 7th International Conference on Surface Plasmon Photonics (SPP7), Jerusalem, Israel (2015), oral presentation.

C5 F. Sterl, N. Strohfeldt, R. Walter, R. Griessen, A. Tittl, and H. Giessen,
"**Magnesium for Active Plasmonics in the Visible Wavelength Range**",
WE-Heraeus-Seminar DNA Nanotechnology meets Plasmonics, Bad Honnef, Germany (2015), oral and poster presentation.

C6 F. Sterl, N. Strohfeldt, R. Walter, R. Griessen, A. Tittl, and H. Giessen,
"**Magnesium for Active Plasmonics in the Visible Wavelength Range**",
Spring Meeting of the German Physical Society (DPG), Regensburg, Germany (2016), oral presentation.

C7 F. Sterl, N. Strohfeldt, R. Walter, R. Griessen, A. Tittl, and H. Giessen,
"**Magnesium for Active Plasmonics in the Visible Wavelength Range**",
Gordon Research Seminar and Conference on Plasmonics and Nanophotonics (GRS/GRC), Newry, ME, USA (2016), oral and poster presentation.

C8 F. Sterl, N. Strohfeldt, R. Griessen, and H. Giessen,
"**Observing nanoscale hydrogen diffusion in plasmonic Mg particles**",
The 6th International Topical Meeting on Nanophotonics and Metamaterials (NanoMeta), Seefeld in Tirol, Austria (2015), oral presentation.

C9 F. Sterl, H. Linnenbank, N. Strohfeldt, and H. Giessen,
"**Watching hydride formation in single plasmonic magnesium nanoparticles**",

Spring Meeting of the German Physical Society (DPG), Dresden, Germany (2017), oral presentation.

C10 F. Sterl, H. Linnenbank, T. Steinle, F. Mörz, N. Strohfeldt, and H. Giessen, "**Nanoscale Hydrogenography of Individual Magnesium Nanoparticles**", *Materials Research Society (MRS) Fall Meeting*, Boston, MA, USA (2017), oral presentation (invited).

C11 F. Sterl, T. Weiss, S. Both, and H. Giessen, "**Tuning the Visual Appearance of Plasmonic Metasurfaces by Controlled Disorder**", *Spring Meeting of the German Physical Society (DPG)*, Berlin, Germany (2018), oral presentation.

C12 F. Sterl, H. Linnenbank, T. Steinle, F. Mörz, N. Strohfeldt, and H. Giessen, "**Nanoscale Hydrogenography of Individual Magnesium Nanoparticles**", *Spring Meeting of the German Physical Society (DPG)*, Berlin, Germany (2018), oral presentation.

C13 F. Sterl, T. Weiss, E. Herkert, S. Both, and H. Giessen, "**Fourier-Space Spectroscopy of Disordered Plasmonic Metasurfaces**", *Materials Research Society (MRS) Fall Meeting*, Boston, MA, USA (2018), oral presentation.

C14 F. Sterl, "**Bright-field, dark-field and Fourier space microspectroscopy of plasmonic nanoparticles**", Invited oral presentation at Brookhaven National Lab (BNL), Upton, NY, USA.

C15 F. Sterl, E. Herkert, S. Both, T. Weiss, and H. Giessen, "**Quantifying the optical properties of disordered plasmonic metasurfaces by Fourier-space microspectroscopy**", *The 7th International Topical Meeting on Nanophotonics and Metamaterials (NanoMeta)*, Seefeld in Tirol, Austria (2019), poster presentation. **Awarded with a Poster Prize (2nd place).**

C16 F. Sterl, E. Herkert, S. Both, T. Weiss, and H. Giessen, "**Fourier microspectroscopy of disordered plasmonic metasurfaces**", *AMOLF nanophotonics summer school*, Amsterdam, The Netherlands (2019), poster presentation.

C17 F. Sterl, E. Herkert, S. Both, T. Weiss, and H. Giessen, "**Fourier microspectroscopy of disordered plasmonic metasurfaces**", *Disordered Materials conference (DisoMAT)*, Potsdam, Germany (2019), oral presentation.

C18 R. Walter, A. Tittl, N. Strohfeldt, F. Sterl, and H. Giessen,
"**Large-area low-cost palladium based plasmonic perfect absorber for hydrogen sensing**",
The 5th International Topical Meeting on Nanophotonics and Metamaterials (NanoMeta), Seefeld in Tirol, Austria (2015), poster presentation.

C19 N. Strohfeldt, F. Sterl, R. Griessen, and H. Giessen,
"**Hybrid thermodynamics for hydrogen in palladium nanocubes and nanoparticles for active plasnomics**",
SPIE. Micro + Nano Materials, Devices, and Applications Conference, Sydney, Australia (2015), invited oral presentation

C20 H. Linnenbank, F. Sterl, T. Steinle, F. Mörz, and H. Giessen,
"**Near-Field optical microscopy of hydrogen absorption and desorption in magnesium-based plasmonic nanostructures**",
Focus on Microscopy (FOM), Bordeaux, France (2017), oral presentation.

C21 H. Linnenbank, F. Sterl, T. Steinle, F. Mörz, and H. Giessen,
"**Nanoscale hydrogenography of magnesium nanostructures with near-field optical microscopy**",
SPIE optoelectronics, photonic materials and devices conference (OPTO), San Francisco, CA, USA (2018), oral presentation.

C22 J. Karst, F. Sterl, H. Linnenbank, M. Hentschel, and H. Giessen,
"**Magnesium thin film nanoscale hydrogenography**",
Gordon Research Seminar and Conference on Plasmonics and Nanophotonics (GRS/GRC), Newry, ME, USA (2018), oral and poster presentation.

C23 J. Karst, F. Sterl, H. Linnenbank, M. Hentschel, and H. Giessen,
"**In-situ magnesium thin film nanoscale hydrogenography**",
The 7^{th} International Topical Meeting on Nanophotonics and Metamaterials (NanoMeta), Seefeld in Tirol, Austria (2019), oral presentation.

C24 A. Böhme, F. Sterl, E. Kath, M. Ubl, and H. Giessen,
"**Electrochemistry on copper nanostructures for active plasmonics**",
The 7^{th} International Topical Meeting on Nanophotonics and Metamaterials (NanoMeta), Seefeld in Tirol, Austria (2019), poster presentation.

C25 E. Kath, F. Sterl, M. Hentschel, and H. Giessen,
"**Magnesium nickel alloy thin films for electrochemical switching**",
Spring Meeting of the German Physical Society (DPG), Regensburg, Germany (2019), poster presentation.

C26 J. Karst, F. Sterl, H. Linnenbank, M. Hentschel, and H. Giessen,
"**Chemically specific in-situ nanoimaging of the hydrogen diffusion in magnesium**",

Spring Meeting of the German Physical Society (DPG), Regensburg, Germany (2019), oral presentation.

C27 A. Böhme, F. Sterl, E. Kath, M. Ubl, and H. Giessen,
"**Inverse copper nanostructures for active plasmonics**",
Spring Meeting of the German Physical Society (DPG), Regensburg, Germany (2019), oral presentation.

C28 E. Herkert, F. Sterl, S. Both, T. Weiss, and H. Giessen,
"**Revealing the influence of structural disorder in plasmonic systems**",
Spring Meeting of the German Physical Society (DPG), Regensburg, Germany (2019), oral presentation.

C29 T. Pohl, F. Sterl, N. Strohfeldt, and H. Giessen,
"**Optical nanoplasmonic CO_2 detection in the visible by polyethylenimine**",
Spring Meeting of the German Physical Society (DPG), Regensburg, Germany (2019), oral presentation.

C30 J. Karst, F. Sterl, H. Linnenbank, M. Hentschel, and H. Giessen,
"**Watching *in situ* the hydrogen diffusion dynamics in magnesium on the nanoscale**",
NeaSpec GmbH Nanoscale Analytics workshop, Haar (Munich), Germany (2019), oral presentation.

C31 E. Herkert, F. Sterl, S. Both, T. Weiss, and H. Giessen,
"**Computing the influence of disorder in plasmonic metasurfaces**",
London Plasmonics Forum, King's College London (2019), poster presentation.
Awarded with a Poster Prize (1st place).

C32 J. Karst, F. Sterl, H. Linnenbank, M. Hentschel, and H. Giessen,
"**Watching *in situ* the hydrogen diffusion dynamics in magnesium on the nanoscale**",
Gordon Research Seminar on Hydrogen-Metal Systems (GRS), Castelldefels (Barcelona), Spain (2019), poster presentation.

C33 J. Karst, F. Sterl, H. Linnenbank, M. Hentschel, and H. Giessen,
"**Nanoscale hydrogenography using the optical near-field**",
Gordon Research Conference on Hydrogen-Metal Systems (GRC), Castelldefels (Barcelona), Spain (2019), oral presentation.

C34 A. Asadollahbaik, S. Thiele, K. Weber, A. Kumar, J. Drozella, F. Sterl, A. Herkommer, H. Giessen, and J. Fick, ,
"**Improved optical fiber tweezers using 3D printed Fresnel lenses**",
SPIE Photonics Europe, online only conference (2020), oral presentation.

CONTENTS

LIST OF FIGURES

LIST OF ACRONYMS

A-stop	aperture stop
AFM	atomic force microscope
Ag	silver
Al	aluminum
Al_2O_3	aluminum oxide
Ar	argon
Au	gold
BFP	back focal plane
BL	Bertrand lens
BRDF	bidirectional reflectance distribution function
BS	beam splitter
CAD	computer-aided design
CCD	charge-coupled device
CIE	Commission Internationale de l'Éclairage
CMF	color matching function
CMOS	complementary metal-oxide-semiconductor
CMYK	cyan, magenta, yellow, key
CO_2	carbon dioxide
CaF_2	calcium fluoride
Cr	chromium
Cu	copper
EE	equal-energy white point
ELWD	extra long working distance
F-stop	field stop
FDTD	finite-difference time domain
FEM	finite-element method
FM	flip mirror
FP	Fourier plane
FWHM	full width at half maximum

H	hydrogen
H_2	hydrogen gas
INPS	indirect nanoplasmonic sensing
IP	image plane
IR	infrared
InGaAs	indium gallium arsenide
LED	light-emitting diode
LIL	laser-interference lithography
LSPR	localized surface plasmon resonance
MIBK	methyl isobutyl ketone
Mg	magnesium
$Mg(OH)_2$	magnesium hydroxide (brucite)
MgF_2	magnesium fluoride
MgH_2	magnesium hydride
MgO	magnesium oxide
N_2	nitrogen gas
NA	numerical aperture
NEP	ethyl pyrrolidone
NIR	near infrared
O_2	oxygen gas
PD	photodiode
PDDA	polydiallyldimethylammonium chloride
PMMA	poly(methyl methacrylate)
PS	polystyrene
PSF	point-spread function
PTFE	polytetrafluoroethylene
Pd	palladium
PdH	palladium hydride
QSA	quasi-static approximation
RGB	red, green, blue
RIBE	reactive ion beam etching
RSA	randomized sequential adsorption
SEM	scanning electron microscope
SNR	signal-to-noise ratio

SPP	surface plasmon polariton
Si	silicon
SiO_2	silicon dioxide (glass)
TE	transverse electric
TEC	thermo-electric cooler
TM	transverse magnetic
TPCF	two-point correlation function
Ti	titanium
TiO_2	titanium dioxide
UV	ultraviolet
VIS	visible
WD	working distance
nL/min	normal liter per minute
s-SNOM	scattering-type scanning near-field optical microscopy
vol.%	volume percent
wt.%	weight percent

1

INTRODUCTION

The interaction of light with metal nanoparticles leads to a variety of interesting phenomena. Collective oscillations of the free electron cloud, which is confined by the particle, can be excited by light of a wavelength matched to the particle's size, shape, and environment. This so-called *plasmonic resonance* leads to a strong enhancement of the local electric field in nanoscale volumes, which has been used to establish coupling between propagating electromagnetic radiation and nanoscale objects, such as single emitters or even single molecules. At the same time, the plasmon resonance leads to a strongly increased absorption and scattering of light. For this reason, plasmonic nanoparticles are also often called *nanoantennas*. The enhancement of scattering and absorption around the plasmonic resonance can easily be detected in the optical far-field, by analyzing the spectral properties of light interacting with plasmonic nanoparticles.

On one hand, this offers the possibility of *characterizing* the plasmonic properties of a particle, or of a whole ensemble of particles, via optical far-field measurements. On the other hand, the plasmonic resonance can also be used for detection and sensing purposes, as it is strongly influenced by parameters such as the particle's material composition, and by its direct environment. Any change in or in the direct vicinity of a nanoantenna will thus lead to a change of the far-field optical properties. A plasmonic nanoparticle, in other words, 'reports' information from nanoscale volumes into the optical far-field.

While dedicated microscopy techniques such as scanning electron microscopy (SEM) or transmission electron microscopy (TEM) are used to achieve the spatial resolution necessary to characterize the shape and morphology of nanoscale particles, different experimental methods are available

for the characterization of the optical far-field properties. Using optical microscopy, it is possible to record the far-field response of nanoscale ensembles or of single metallic nanoparticles, even if the particle size is significantly smaller than the spatial resolution limit of the microscope. To additionally obtain spectral information about the far-field response, microscopy can be combined with spectroscopic measurements. This combination is called *microspectroscopy*.

The work presented in this thesis is based on the use of a specific type of spectrometer, so-called grating spectrometers, with which measurements can be done that possess spectral as well as spatial resolution. This type of measurements is thus termed *imaging microspectroscopy*. In addition to a basic description of the principles behind this experimental method as well as the concept of plasmonics, several different types of nanoplasmonic systems are investigated. These systems are developed and studied for several different purposes and applications, ranging from a fundamental understanding of nanoscale systems to active switching of the optical far-field and the all-optical detection of trace amounts of hydrogen gas.

1.1 THESIS OUTLINE

This thesis starts by giving the reader a fundamental overview of the concept of optical microscopy, in **Chapter 2**. This includes the theory of image formation and a derivation of the spatial resolution limit. We will also look at the several technical aspects of a microscopy setup, such as the geometries of illumination and light collection, and we will see why these are very important parameters that must be well understood and considered for the implementation of microscopic measurements. In **Chapter 3**, we focus on the theoretical and technical aspects of spectroscopic devices. This chapter also gives an overview of the different types of measurements that can be performed with an imaging microspectroscopy setup. Furthermore, we will look at the data that are obtained from a microspectroscopic measurement and how different physical quantities can be extracted from a dedicated processing of these data.

Chapters 2 and 3 are not only intended as a basic theoretical overview, but also as a basic 'user guide' for implementing and performing microspectroscopic experiments.

Afterwards, we continue with a theoretical background of light-matter interaction in **Chapter 4**. Starting from a fundamental point of view, we see

how the excitation of a plasmonic resonance is influenced by the parameters of the particle and how this can be detected in the far-field. This chapter also gives a short overview of different fabrication techniques for tailored nanostructures of different shapes and size, which are used throughout the remaining chapters of this thesis.

In the field of plasmonics, a set of often used 'standard' metals exists. These are, most notably, gold (Au), silver (Ag), and aluminum (Al). The search for alternative materials is, however, ongoing. Materials with favorable chemical properties such as a high melting point have been brought forward, as have materials that promise plasmonic resonances in wavelength ranges that would otherwise be inaccessible. One of these materials is magnesium (Mg). In addition to being a suitable candidate for UV plasmonics, Mg holds another highly interesting property, namely its ability to absorb hydrogen. This absorption is accompanied by a transition from metallic Mg to dielectric MgH_2. In **Chapter 5**, we demonstrate that this property can be used to realize *active nanoplasmonic systems*. By combining Mg nanoparticles with a layer of palladium (Pd), the plasmonic resonance can be switched 'on' and 'off', which offers new possibilities for the fabrication of switchable nanoscale systems.

The use of plasmonic magnesium nanoparticles for switchable plasmonics is also interesting from another point of view: Optical measurements of the plasmonic resonance can be used to gain *understanding* about the process of hydrogen absorption and release in nanoscale metal volumes. As we will see in **Chapter 6**, this is a highly interesting area of research, since MgH_2 and other metal hydrides hold great promise for the *storage* of hydrogen as an energy carrier. This is one of the most promising technological developments for the transition from fossil fuels to sustainable energy, mainly in the sector of transportation. We gain several new insights about the mechanism of hydrogen incorporation in Mg nanoparticles by optical as well as mechanical measurements.

As a next step, we develop a novel technology for tracking the diffusion of hydrogen *inside* a single Mg nanoparticle, which we term *nanoscale hydrogenography*. As **Chapter 7** shows, this method is based on the combination of microspectroscopic far-field measurements with near-field optical microscopy. In addition to demonstrating the feasibility of this method, we obtain a clearer picture of the processes behind nanoscale H_2 diffusion, including the significance of the nanoscale crystallinity.

After having studied magnesium in detail, we next focus on the use of palladium for plasmonics in **Chapter 8**. In contrast to Mg, Pd can be used

for optical *detection* of hydrogen, since the absorption of H_2 leads to a shift in the plasmonic resonance which sensitively depends on the hydrogen concentration. The development of reliable and safe hydrogen detectors is another important factor for the use of H_2 as an energy carrier. Here, we look in detail at a specific design of plasmonic Pd-based H_2 sensors, namely the so-called *'perfect absorber'* design. We study the system in detail to understand how the optical far-field response arises, and we present an exhaustive systematic study of the design parameters. This enables us to formulate a set of *design rules* for the optimization of the sensitivity of Pd-based H_2 sensors, which can be applied to other types of plasmonic sensors as well.

In **Chapter 9**, we investigate a more fundamental property of nanoplasmonic systems, namely the effects of *order* and *disorder* in the arrangement of plasmonic particles. We introduce a model for generating *tailored* disorder, and we study its effects on the far-field properties of nanoantenna arrays. We also show how optical measurements can be used to identify the type and strength of the disorder, which also lays the foundation for *engineering* of the far-field response via tailored disorder.

Chapter 10 gives a short summary of the main findings presented in this thesis, and a short outlook of how these findings can be used in future developments of nanoplasmonic systems.

2

OPTICAL MICROSCOPY

Microspectroscopy is the combination of microscopic with spectroscopic measurement methods, in which the image generated by an optical microscope is analyzed spectroscopically. This means that one can extract the spectral properties of microscale volumes and thus investigate the behaviour of structures on this scale. In principle, the spatial resolution is limited by the optical resolution of the microscope, but as we will see, specialized illumination techniques exist to even investigate the spectral response of isolated sub-100 nm nanoparticles.

For performing microspectroscopic measurements, it is very important to fully understand the complete microspectroscopy system from light source to detector. For example, the imaging geometry can have a significant influence on which quantity is measured exactly. This chapter will thus give a theoretical background of the principles of optical microscopy, including a derivation of the optical resolution limit. The most relevant illumination and light collection options will be discussed as well.

2.1 INTRODUCTION TO MICROSCOPY

The most important part of a microscope is the microscope objective. This is a complex arrangement of different lenses, engineered to generate an image of a very small area of a sample in front of the objective, in the sample plane. A microscope objective is mainly characterized by three different factors: the magnification (M), the numerical aperture (NA), and the working distance (WD). As we will see, the numerical aperture defines the optical resolution, i.e. the smallest feature that can be resolved. This is not the same as the magnification. The magnification only defines how *large* a spatial feature occurs in the image plane, but not how *sharp* it is. The working

distance has no direct influence on the performance of the objective, as it follows from the NA and the size of the objective front lens. It is, however, an important parameter to consider in the design of an experiment, as it limits the available space between the objective and the sample.

2.1.1 *Infinity-corrected objectives*

Most modern microscopes use so-called *infinity-corrected* microscope objectives. Such an objective does in fact not generate an image of the sample at a finite distance, but generates an image at a infinite distance. This means that all light rays originating from a single point in the sample plane are parallel to each other when exiting the objective, and thus form a collimated beam. However, since the angle at which a ray exits the objective depends on the position of origin, the full beam generated by the objective can not be regarded as collimated, since the rays originating from different points are diverging with respect to each other. In microscopy, one can in fact never speak about a truly 'collimated' beam in the sense of a collimated laser beam.

To generate the required image, a second optical element is needed, namely the so-called tube lens. Figure 2.1 shows an example of such a system. All optical elements in the figure represent a real-world Nikon objective with an NA of 1.49 and a magnification of 60×. The geometry and material data are taken from the work of Kurvits *et al.* [1]. This specific objective is an oil-immersion objective, meaning that there is a thin layer of oil with a refractive index of approximately 1.5 between the sample and the objective front lens. This increases the optical resolution, as we will see later. The light rays drawn in this figure are calculated in MATLAB, using the raytracing package OPTOMETRIKA [2]. As the resulting ray diagram shows, all rays originating from the same point in the sample plane are recombined into the same point in the image plane. Because of the collimated nature of the individual ray bundles exiting the objective, this in principle works for any distance between the objective and the tube lens. The only limitation is that the full beam must not diverge to larger diameters than the tube lens diameter, so that no information is lost. This presents a major advantage of infinity-corrected microscope objectives, since the space between objective and tube lens can be extended at will to include additional components, such as filters or beam splitters connecting to other optical illumination or collection paths. At the same time, the objective can always be moved to bring a sample into focus.

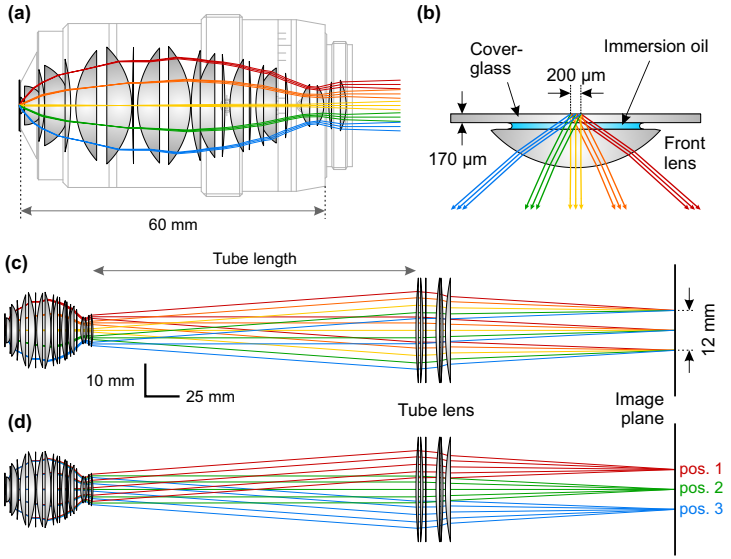

Figure 2.1. Optical elements and calculated rays in a Nikon 60×, NA 1.49 microscope objective, overlaid on the actual objective dimensions (a). The optical element data are taken from Ref. [1], and the objective dimensions from Nikon documentation. The raytracing calculations are performed using the Optometrika package for Matlab [2]. Rays originating from three separated points in the sample plane under five different angles are considered (b). The ray color indicates the angle. The objective generates an image at infinite distance (c). A tube lens, placed at a variable distance called the tube length, 'bends' the rays into an image. Note that the vertical dimension is stretched for clarity. This diagram is replicated in (d), but with the ray color representing the *position* of origin instead of the angle.

The image generated in the image plane can directly be projected onto an optical detector, such as a CCD camera. In this case the pixel resolution of the detector is an additional factor in the optical resolution of the recorded image. Alternatively, a lens system called the *eyepiece* can be used to project the image into the human eye.

2.1.2 *Numerical Aperture and resolution*

To understand the factors that determine the spatial resolution of a microscope objective, in other words, the smallest spatial feature that can be

resolved, it is useful to look at *Abbe's theory of image formation*. A detailed description of this theory, which was brought forward by Professor Ernst Abbe (1840-1905), can be found in Ref. [3].

Consider the optical system depicted in Figure 2.2(a). A plane, monochromatic wave of wavelength λ hits a grating with periodicity d at normal incidence. A 'transform lens' with focal length f, located at an object distance s_o behind this grating, creates an image at a screen a certain distance s_i away. This distance follows from the Gaussian Lens Formula ($s_o^{-1} + s_i^{-1} = f^{-1}$). The incoming wave is diffracted by the lattice, which results in a new set of plane waves, corresponding to different diffraction orders m, where $m = 0$ can be seen as the portion of the light that is transmitted without being disturbed. The diffraction angle θ for a certain m depends on the wavelength, the grating periodicity, and the refractive index of the surrounding medium n:

$$\sin\theta_m = \frac{m\lambda}{nd} \tag{2.1}$$

This relation implies that diffraction orders hold spatial information, as smaller spatial features (d) lead to a larger angle of diffraction. In a medium with a higher refractive index, this angle decreases.

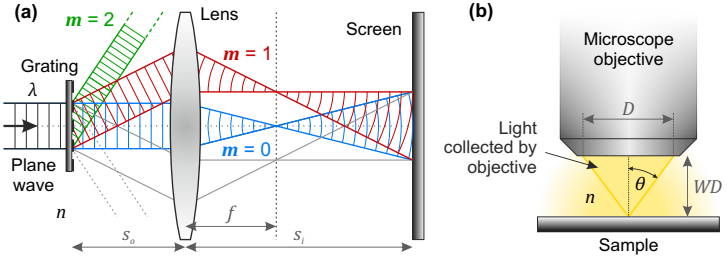

Figure 2.2. (a) Illustration of image formation of a diffraction grating according to Abbe's theory of image formation. (b) The resolving power of a microscope objective is defined via its numerical aperture (NA), which follows from the maximum collection angle θ and the refractive index n. The working distance WD defines the required distance between the objective and the sample plane, which is the same as the front focal plane.

In a ray optics picture, each diffraction order can be regarded as a collimated beam hitting the lens and is thus focused in a single point at a distance

f behind the lens. This is called the *back focal plane* (BFP) of the lens, a concept we will see more about later. The distance of a point in the BFP from the optical axis thus carries information about spatial features of a certain size. Objects of smaller periodicities form a point further away from the optical axis. The diffraction pattern generated in the BFP consequently forms a *spatial Fourier transform* of the grating. The same holds true for any type of object at the position of the grating, since any object can be constructed from a superposition of an infinite amount of periodic patterns, each with its own weight. For this reason, the BFP is also referred to as the *Fourier plane*, and the diffraction pattern formed in this plane as the *Fourier image*.

Behind the Fourier plane, the diffracted waves in the example of Figure 2.2(a) interfere to form an image of the grating in the *image plane*. This plane is said to be *conjugated* to the object plane, in which the grating is situated. The image can thus be seen as an inverse Fourier transform of the Fourier image, which retrieves the original. However, the image is not complete: Only a *finite* amount of diffraction angles can be captured by the lens. Radiation coming from the sample at angles too large to be captured do *not* contribute to the Fourier image. The aperture thus acts as a low-pass filter. Rays carrying information about high spatial frequencies, and thus about small spatial features, are removed. If only the 0^{th} diffraction order would be transmitted, the grating could not be resolved anymore in the image plane, since the 0^{th} order carries no more spatial information than the plane wave would if the grating were removed.

This means that some spatial information is always lost. The smallest spatial features that can be resolved by a microscope objective, termed the resolution Δl, are thus defined by the maximum collection angle of the objective, in combination with the refractive index of the medium between the sample and the objective. Microscope objectives are therefore characterized by the *numerical aperture* (NA):

$$\mathrm{NA} = n \cdot \sin\theta, \tag{2.2}$$

with θ the largest possible collection angle and n the refractive index of the medium between the objective and the sample, as illustrated in Figure 2.2(b). The factor n in the NA explains why many high-NA objectives use oil immersion (see Figure 2.1). This definition is closely related to the *f-number* used in photography, $f/\#$, which is defined as the ratio of the focal distance

f over the aperture diameter D.[1] Several different definitions based on this NA exist for the spatial resolution, or minimum resolvable distance Δl, of a microscopy system, such as Abbe's estimation:

$$\Delta l = \frac{\lambda}{2\mathrm{NA}}. \tag{2.3}$$

However, other, more sophisticated definitions of the resolution exist as well.

2.1.3 *Rayleigh diffraction limit*

One such definition is the *Rayleigh criterion*, which was named after Lord Rayleigh (1842-1919). It considers the minimum distance that two point sources in the object plane must have to still be distinguishable in the image plane. To understand this, we can look at the situation depicted in Figure 2.3. Here, light from two point sources at an arbitrary distance is transmitted through a circular aperture with radius a. The refractive index is 1 everywhere. One can imagine the light sources to be at a distance s_0 from the aperture, and a screen at a distance s_i behind the aperture, onto which the transmitted light is projected. These distances are then equivalent to the object and image distance in Figure 2.2(a). However, in a first step it is not necessary to bring these distances into play, as it is sufficient to look at the *angular* position and light distribution. The distances are effectively no more than a scaling factor to convert the angular position ϕ into a spatial coordinate q, and the angular distance between the two points $\Delta\phi$ into a spatial distance Δl. The argument thus holds for points at different distances, such as faraway stars observed through a telescope.

A point source imaged by a finite, circular aperture generates a so-called *Airy pattern* or *Airy disk*, named after Sir George Biddell Airy (1801-1892), in the image plane [3]. This is the fringe pattern given by the squared modulus of the Fourier transform of the circular aperture itself. An intuitive way to

1 In the case of a microscope objective, the distance between sample and aperture is technically speaking not the same as the *focal distance*, since the objective consists of a complex lens system and the focal distance is defined with respect to this system's principle planes. If one would use this plane, however, the 'aperture' would have to be scaled as well, so that the outcome would not change. To define an f-number, one could be tempted to use the working distance WD. However, this is not necessarily the same either, as the objective body can extend beyond the front lens (especially for dark-field objectives, as we will see later).

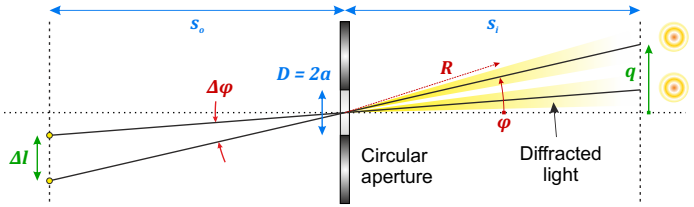

Figure 2.3. Circular aperture geometry: two point sources at an arbitrary distance are imaged onto a screen via a circular aperture. Using only the angular coordinates, the *angular resolution* $\Delta\phi$ can be calculated via the Rayleigh criterion.

understand this is as follows: The spatial distribution of a point source in the image plane corresponds to a Dirac delta peak, the Fourier transform of which is 1 for all spatial frequencies and thus for all emission angles. The transform lens only transmits a rectangular (or, in a 2D picture, disk-shaped) function. The inverse Fourier transform of this gives a blurred version of the delta peak. Since the transmitted intensity distribution is simply the shape of the aperture, this is the same as the inverse Fourier transform of the aperture. The shape of the Airy disk is also known as the *point-spread function* (PSF) of a circular aperture, as it literally indicates how far a point is being spread out in the far field.

The diffraction pattern of a circular aperture is given by:[2]

$$I(\phi) = I(0)\left[\frac{2J_1\,(ka\sin\phi)}{ka\sin\phi}\right]^2, \tag{2.4}$$

where ϕ is the diffraction angle relative to the angle of the center beam, $I(0)$ is the intensity in the center of the spot, and k is the wavevector $\frac{2\pi}{\lambda}$. If we consider a point source on the optical axis, ϕ is thus simply the angular coordinate as indicated in Figure 2.4(a). J_1 indicates the first-order Bessel function:

$$J_m(u) = \frac{i^{-m}}{2\pi}\int_0^{2\pi} e^{i(mv+u\cos v)}\,dv, \tag{2.5}$$

which is tabulated in many textbooks. The shape of the resulting curve is plotted vs. $ka\sin\phi$ in Figure 2.4(a), and the corresponding two-dimensional Airy disk in Figure 2.4(b).

2 This function is similar, but not identical, to the function giving the diffraction pattern of a single slit on a screen. The discrepancy results from the fact that a flat screen at a finite distance is considered in the latter case, while the Airy pattern gives the *angular* distribution.

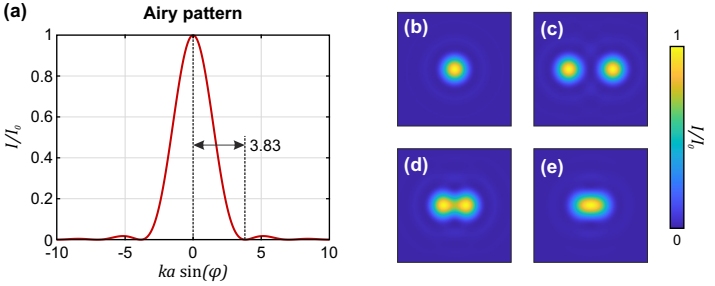

Figure 2.4. (a) Diffraction pattern of the circular aperture, also called the Airy pattern or Airy disk, as shown in (b). If the diffraction patterns of both point sources are sufficiently separated, they can be resolved (c). If the maximum of one pattern overlaps with the first dark ring of the other, the patterns can *just* be resolved (d). This occurs when $ka\sin\Delta\phi = 3.83$. At smaller angular distances, the patterns are indistinguishable (e).

The Rayleigh diffraction limit gives *the minimum angular separation between two points, so that the center of the Airy disk generated by one point overlaps exactly with the first dark fringe of the Airy disk generated by the other point.* The first minimum of $J(x)$ occurs when $x = 3.83$, which means that:

$$ka(\Delta\sin\phi)_{\min} = 3.83. \tag{2.6}$$

If this condition is met, the two points can *just* be resolved in the angular diffraction pattern. This is examplified in Figures 2.4(c-e), in which the center distance between the two Airy disks is 7.66, 3.83, and 1.92, respectively. In this last case, the two disks form one broadened peak and can thus not be distinguished anymore.

Since the angles ϕ in question are very small, we can assume that $\sin\Delta\phi \approx \Delta\phi$. Using this assumption, Equation 2.6 can be rewritten as follows:

$$\Delta\phi = 1.22\frac{\lambda}{D}, \tag{2.7}$$

which is the *angular limit of resolution* according to the Rayleigh criterion.

At this point, we can bring back the object and image distances, and assume that the diffraction patterns are imaged onto a screen. In this case we are not interested in the angular resolution, but in the spatial resolution Δl. We thus need to know how far apart the centers of the Airy pattern are located on the screen. Again using the small angle approximation, which

implies that $\phi \approx \frac{q}{s_i}$, and that $R \approx s_i$ in the image plane (see Figure 2.4(a)), we find that:

$$\Delta l = 1.22 \frac{\lambda s_o}{D}. \tag{2.8}$$

The entire reasoning leading to Eq. 2.8 is only based on diffraction by a circular aperture, without any lens effects. However, the result basically tells us that only the distance to the aperture and the aperture size are important. Taking into account that the aperture size works as a low-pass filter for spatial frequencies, as outlined in Section 2.1.2, the argument holds for any type of imaging system in place of the aperture. Even if the exit angle of a ray is changed with regard to the entrance angle, this simply introduces a scaling factor to the size of the Airy disk in the image plane, which does not contribute to the result of Equation 2.8. If we apply this limit to a microscope objective, the object distance s_o is the same as the focal distance f (see Figure 2.2(b)). This leads to the *spatial limit of resolution* according to the Rayleigh criterion:

$$\Delta l = 1.22 \frac{\lambda f}{D}, \tag{2.9}$$

which again shows that a large aperture in combination with a small focal distance, and thus a large range of collection angles, makes smaller spatial features resolvable. It should be noted that this whole argument is based on the assumption that aberrations of the imaging system do not play a significant role. An optical instrument that is not limited by such aberrations, but operates at the maximum spatial resolution given by the theoretical limits described above, is thus said to be *diffraction-limited*.

Interestingly, Equation 2.9 is not the only definition of the Rayleigh criterion. The definition most commonly found in literature, and used by, e.g., microscope manufacturers [4, 5], is based on the numerical aperture (Equation 2.2):

$$\Delta l = 0.61 \frac{\lambda}{\mathrm{NA}}, \tag{2.10}$$

which holds true when the small angle approximation is applied to the maximum collection angle θ. This angle is directly connected to f and D via $\tan\theta = \frac{D}{2f}$. The definition of the NA, however, uses $\sin\theta$ instead of $\tan\theta$. The approximation $\sin\theta \approx \tan\theta$ can be used as long as θ is small. However,

for a typical high-resolution microscope objective, this is *not* the case. The correct way of writing Equation 2.9 in terms of the NA would be as follows:[3]

$$\Delta l = 0.61 \frac{\lambda}{\tan\left(\sin^{-1} \mathrm{NA}\right)}, \tag{2.11}$$

which deviates more and more from the common definition (Equation 2.10) as the NA increases, as shown in Figure 2.5. The interesting aspect here is that the *higher* the NA of an objective gets, and thus the *better* the spatial resolution Δl should be, the stronger the common definition *underestimates* the actual performance of a diffraction-limited microscope objective according to the Rayleigh criterion. A possible explanation for this discrepancy is that the higher the NA of an objective, the more difficult it becomes to eliminate all aberrations, so that the instrument is in fact not operating at its diffraction limit. The approximation in Equation 2.10 thus provides a certain factor of safety, so that the definition is sufficient for all practical applications.

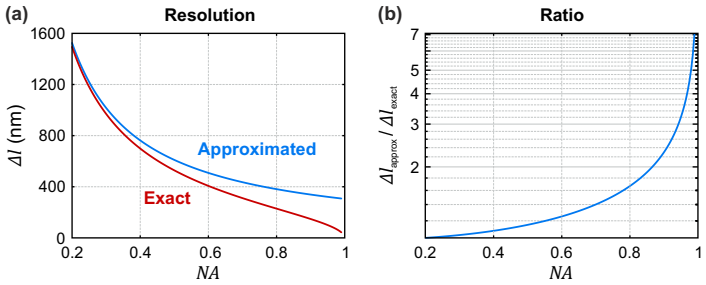

Figure 2.5. (a) Spatial resolution Δl according to the Rayleigh criterion vs. numerical aperture NA, calculated for a wavelength of 500 nm in air, via the approximate definition (Eq. 2.10) and the exact calculation (Eq. 2.11). (b) Ratio of the two resulting Δl curves.

Apart from this, a slightly more elaborate version of Equation 2.10 does not only take into account the NA of the *objective*, but also that of the light

3 The NA also brings back the refractive index. Equations 2.4-2.9 could also be rewritten for a system in a medium with a refractive index larger than 1, in which case λ would have to be corrected by $\frac{1}{n}$, as seen from Equation 2.1.

incident on the sample. The device that focuses the incoming light onto the sample is called the *condenser*. The condenser can either be a separate optical system with numerical aperture $\mathrm{NA}_{\mathrm{cond}}$, or the objective itself, as we will see later. If the objective acts as the condenser, $\mathrm{NA}_{\mathrm{obj}}$ and $\mathrm{NA}_{\mathrm{cond}}$ are not necessarily the same, since it is possible to use only a fraction of the full NA for illumination. The Rayleigh criterion then reads:

$$\Delta l = 1.22 \frac{\lambda}{\mathrm{NA}_{\mathrm{obj}} + \mathrm{NA}_{\mathrm{cond}}}. \tag{2.12}$$

These different definitions of Δl are each somewhat arbitrary, but nevertheless show that the NA must be maximized in order to obtain the highest possible spatial resolution.

Another interesting aspect of the resolution limits above is that these only apply for *on-axis* illumination and light collection. In principle, it is possible to extract extra spatial information by tilting the condenser with respect to the objective, even when $\mathrm{NA}_{\mathrm{obj}}$ and $\mathrm{NA}_{\mathrm{cond}}$ remain the same, since higher diffraction orders scattered in the direction of the tilt can reach the objective. This would correspond to tilting the angle of incidence of the plane wave in Figure 2.2(a). However, this only brings additional spatial resolution along one spatial axis. We will see more about this in Chapter 9.

2.2 MICROSCOPE CONFIGURATIONS

So far, we have looked at the collection of light by a microscope objective, but not yet at the illumination of the sample. Depending on what exactly one wants to observe, different configurations for this illumination exist. The most basic distinction is between reflected and transmitted light. In so-called *episcopic* microscopy, the sample is illuminated via the objective itself with the aid of a beam splitter, so that reflected light is collected. In *diascopic* microscopy, the sample is illuminated from the other side using a *condenser*. The purpose of the condenser is to illuminate a defined area of the sample under a defined range of angles (and is thus characterized by its numerical aperture $\mathrm{NA}_{\mathrm{cond}}$).

A second important distinction is the geometry of the microscope itself, as schematically shown in Figure 2.6. In an upright microscope, the objective is situated above the sample. Typically, the objective is fixed. The sample plane can be moved to bring the sample into focus and the condenser can be aligned to the sample plane. In an inverted microscope, the objective is below

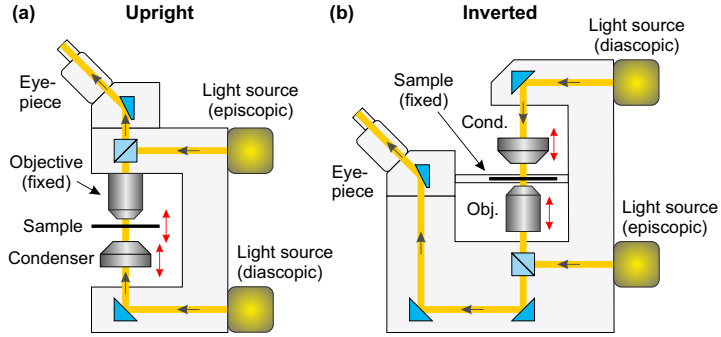

Figure 2.6. Schematic illustration of diascopic and episcopic illumination in an upright (a) and inverted microscope (b).

the sample. The sample plane is typically fixed, while the microscope and the condenser can be moved independently. In both configurations, episcopic as well as diascopic illumination is possible. An advantage of having the sample above the objective is that the sample can be reached from above (if held on a transparent substrate). This is beneficial, for example, for measurements in a liquid environment, as the liquid can be on top of the sample. Only the substrate itself is then in between the sample and the objective. The optical dispersion of the substrate induces a defocusing of the image, but many microscope objectives intended for such measurements feature a so-called *coverslip correction collar*, which moves a lens group inside the objective to compensate for this dispersion. An advantage of upright microscopes is the fixed objective, and that the sample can be reached from below, for example for heating. All in all, the best choice between an upright and an inverted microscope strongly depends on the intended measurements.

Furthermore, there are several fundamentally different illumination modes that are relevant for microspectroscopy. In this work, we consider *bright-field* and *dark-field* illumination, as illustrated in Figures 2.7 and 2.8 for diascopic and episcopic illumination, respectively. In bright-field illumination, all the light transmitted/reflected by the sample is collected by the objective. The resulting image thus features a uniform background, on which absorbing/reflecting objects appear dark (as in Figure 2.7(b)) or, in episcopic illumination, dark and bright depending on the reflectance. In dark-field illumination, only *scattered* light is collected. This is accomplished via either a specialized dark-field condenser (Figure 2.7(c)) or via a dark-field objective, which has

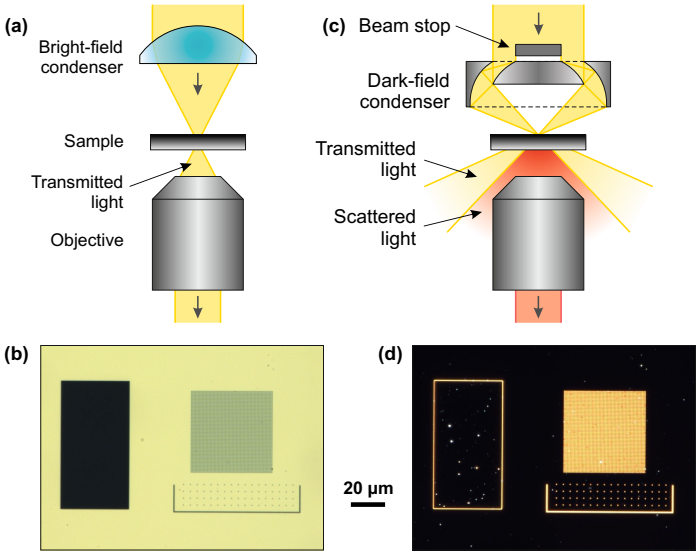

Figure 2.7. Sketch of diascopic (transmission) bright-field and dark-field microscopy. In bright-field microscopy (a), all light transmitted through the sample is collected by the microscope objective, as long as the condenser NA does not exceed the objective NA. Any structures on the sample that scatter and/or absorb light appear dark against a bright background (b). In dark-field microscopy (c), a specialized condenser illuminates the sample from a range of large angles, so that only scattered radiation is collected. Scattering structures on the sample thus appear bright against a dark background (d). For large structures, only the edges are visible.

the same function (Figure 2.8(b)). Light is only focused onto the substrate in an annular ring of large incident angles. A dark-field condenser is thus specified by an NA *range*. As long as the minimum incident NA exceeds the collection NA of the objective, all transmitted/reflected light thus passes by the objective. Only light scattered into the objective is collected. Scattering features thus appear bright on a dark background (Figure 2.7(d)). For large, flat structures, this means that only the edges are visible.

Bright-field microscopy is the logical choice if one wants to characterize the reflactance and/or transmittance of a microscopic sample. Dark-field microscopy is highly useful to characterize the far-field response of individual, isolated nanoparticles. These can even be much smaller than the diffraction limit. The particle size can in this case not be determined from the image,

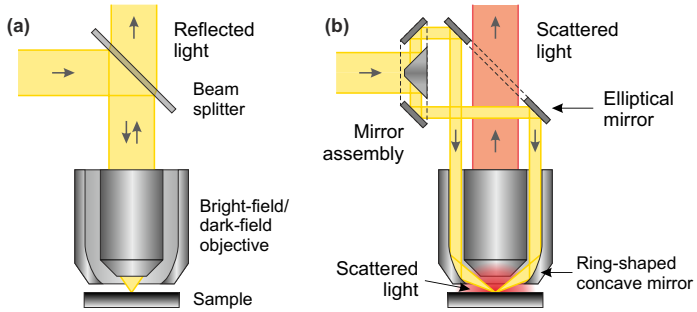

Figure 2.8. Sketch of episcopic (reflection) bright-field and dark-field microscopy. In bright-field microscopy (a), the objective, which serves as the condenser at the same time, is illuminated via a beam splitter. All light reflected by the sample is collected by the objective. In dark-field microscopy (b), a specialized mirror assembly illuminates only the outside ring of the dark-field objective. The sample is illuminated from a range of large angles via a concave mirror.

but since the scattering cross-section of especially metallic nanoparticles is often much larger than their geometric size, the bright spot generated by a single particle contains all the *spectral* information about the particle. This will be discussed in Chapter 4.

The main advantage of dark-field microscopy is the dark background: the exposure time of any detector, be it a camera or a spectrometer, can be increased to maximize the intensity of the scattered spot, without significantly increasing the background signal (assuming that the substrate scatters no light). This leads to a high signal-to-noise ratio, even for weakly scattering particles. In bright-field microscopy, an increased exposure time also increases the background signal, so that the optical contrast between a scattering particle and the background can not be enhanced.

An often used method for the characterization of nanoparticles is to fabricate a large ensemble of particles, which all contribute to the optical signal, so that bright-field microspectroscopy can be employed. If this is not possible, or if one is specifically interested in the response of a *single* particle rather than a many-particle average, dark-field illumination is the method of choice. In this case, one should be aware that an accurate modeling of scattering is less straightforward than that of 'simple' transmittance or reflectance, as the objective NA and the incident angle determine which scattering angles are collected, and since the ring-shaped illumination cannot be modeled as a plane wave anymore [6, 7].

2.2.1 *Illumination*

In bright-field microscopy, it is furthermore important to look at how the light source illuminates the sample plane. The most straightforward configuration is *critical illumination*. As illustrated in Figure 2.9(a),b, the light is collimated by a collector lens and refocused on the sample by the condenser. The illuminated spot on the sample is thus an image of the light source itself. If the light source features a uniform intensity distribution, such as the end of a fiber, this is not necessarily a problem, except for the disadvantage that the illuminated area can not be changed. However, a non-uniform source, such as a lamp filament, would produce an image of this filament in the sample plane.

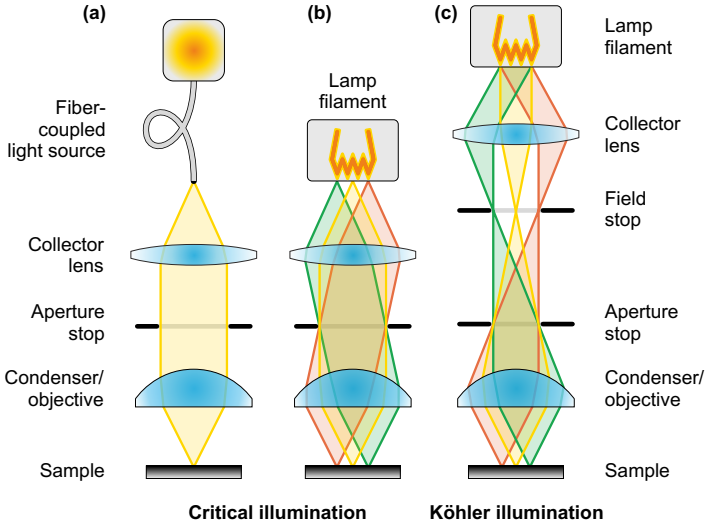

Figure 2.9. Sketch of critical illumination and Köhler illumination. In critical illumination, the light source is imaged onto the sample plane. When a light source with a uniform intensity distribution is used, such as the end of an optical fiber, the intensity distribution on the sample is also uniform (a). When a non-uniform light source is used, such as a lamp filament, an image of the filament appears in the sample plane (b). In Köhler illumination, this is circumvented by imaging the back focal plane (BFP) of the collector lens onto the sample plane (c).

To circumvent this problem, the so-called *Köhler illumination* geometry was invented by August Köhler (1866-1948). In this case, the image of the light source is not projected onto the sample plane, but onto the back focal plane of the condenser lens (see Section 2.1.2). The BFP of the collector lens is thus imaged onto the sample plane, as illustrated in Figure 2.9(c). This means that the illuminated spot in the sample plane is the *Fourier image* of the light source. As one can see in the color-coded beams, all rays that leave the light source under the same *angle* reach the sample in the same *position*, and vice versa. As long as the emission by the lamp filament is uniform, this leads to a nicely uniformly illuminated spot. An additional

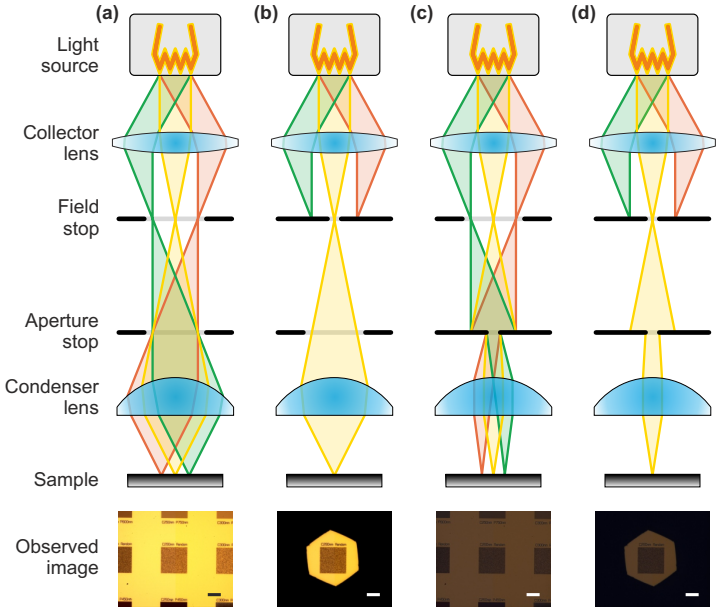

Figure 2.10. Sketch of different illumination modes in a Köhler illumination path. The field stop (F-stop) is located at a position conjugated to the sample plane, which is the back focal plane as seen from the light source. The aperture stop (A-stop) is conjugated to the light source. When both stops are open, the sample is illuminated at the full available field size and NA (a). Closing only the field stop reduces the illuminated area on the sample (b). Closing only the aperture stop reduces the illumination NA (c). Closing both stops means that only a small spot in the sample plane is illuminated at near-normal incidence (d). The photos show 100×100 µm^2 arrays of palladium nanodisks (scale bars: 50 µm).

advantage in this configuration is that two different stops can be added in the optical path, with which one can control the illuminated area as well as the incident range of angles. The so-called *field stop*, or *F-stop*, is situated in the back focal plane of the collector lens, which is conjugated to the sample plane.[4] The F-stop is thus directly imaged on the sample. The *aperture stop*, or *A-stop*, is located in the back focal plane of the condenser (conjugated to the light source). It thus limits the maximum incident angle (NA_{cond}; see Eq. 2.12). In contrast to the F-stop, an A-stop can also be added in a critical illumination path.

Understanding the effects of the F-stop and the A-stop is very important in bright-field microscopy, especially when combined with spectroscopy. Figure 2.10 presents an overview of the four different combinations of open and closed F- and A-stop. When both stops are open, a large area is illuminated under a large range of angles. Closing the F-stop limits the illuminated area. This can be used to block stray light from positions outside the range of interest. Closing the A-stop limits the incident NA. This influences the optical resolution as well as the image contrast, and it has the additional effect of limiting the amount of light that reaches the sample, so that the image becomes darker. This is all assuming that both stops are correctly aligned with respect to the lenses. An incorrect positioning of either stop can again lead to an inhomogeneous and/or asymmetric sample illumination [8].

Which of these configurations must be used is again strongly dependent on the experimental conditions. For example, if the goal is to compare measured reflectance/transmittance data to numerical simulations in which a defined angle of incidence was used, the A-stop should be adjusted to these conditions. If the goal is to perform time-resolved measurements which limit the maximum exposure time of the detector, a higher illumination intensity might be needed and it is beneficial to open the A-stop. Nevertheless, it is always important to be aware of the different effects of all the elements in a Köhler illumination scheme.

2.3 FOURIER MICROSCOPY

A specialized case of optical microscopy is *Fourier plane imaging microscopy*, Fourier microscopy for short. In this case, one observes not the image plane of the microscope, but the Fourier plane (see Section 2.1.2). To accomplish

4 To add some confusion, the terms F-stop and A-stop are often used interchangeably in photography.

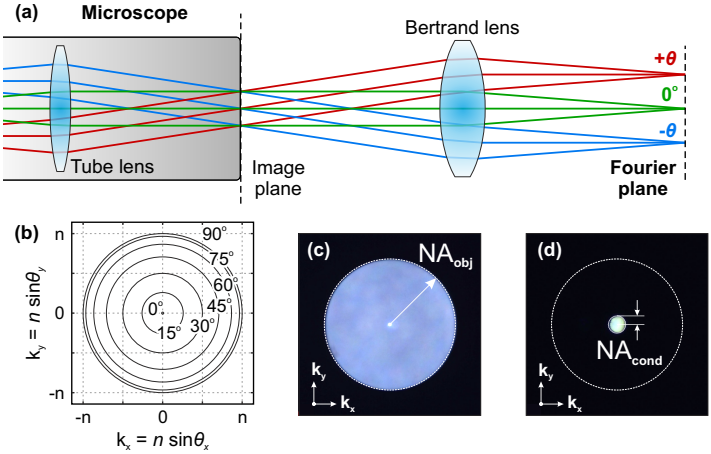

Figure 2.11. Example of a Fourier microscopy setup, in which a Bertrand lens behind the microscope generates an image of the Fourier plane (a). The ray color represents the angle at which the ray exits the sample. The position in this plane corresponds to the angle in the image plane (b). Typical Fourier images of a scattering sample and a reflecting sample, illuminated with a small A-stop, are shown in (c) and (d), respectively.

this, one needs one extra lens, commonly termed the *Bertrand lens*, which generates a new Fourier image outside the microscope, as exemplified in Figure 2.11(a). A Fourier microscopy optical path can thus be imagined as an inverted Köhler illumination setup - in the example of Figure 2.9, the lamp filament and/or the A-stop would be seen in the Fourier image.

As outlined before, the radial position of the image in the Fourier plane corresponds to the angle in the image plane (and thus in the sample plane) via $k = n \sin\theta$, with k the radial coordinate. One can thus construct the so-called *k-space*, as illustrated in Figure 2.11(b). Since the Fourier plane is also the back focal plane (BFP) of the microscope objective, the three terms 'Fourier microscopy', 'k-space microscopy' and 'back focal plane microscopy' are often used interchangeably.[5]

5 The observant reader may have noticed that there does not appear to be a BFP in the microscope objective diagram in Figure 2.1. In fact, the BFP is in this example a highly curved plane inside the objective.

For a uniform distribution of light transmitted or reflected by the sample, such as a uniformly scattering surface, the k-space image corresponds to a circle of uniform intensity (Fig. 2.11(c)). The radius of this circle corresponds to the NA of the objective (and can thus be used for calibration of the obtained k-space image). If the condenser NA is lower than the objective NA, and the surface does not scatter, a smaller spot is seen (Fig. 2.11(d)). When using Fourier microscopy, one thus effectively removes all *spatial* information from the microscope image and replaces it by *angular* information. This can be very useful for characterizing the angle-dependent behaviour of a microscopic sample. For samples with a periodic structure, the diffraction orders appear in the k-space image. We will see some applications of this in Chapters 8 and 9. Using dedicated illumination techniques, Fourier microscopy can even be used to reconstruct the real-space image at a higher spatial resolution than if one would directly record the image, as outlined by Dominguez *et al.* [9].

It should be noted that the example in Figure 2.11 is by far not the only possible Fourier microscopy configuration. An overview of different configurations can be found in Ref. [1]. Furthermore, a comprehensive guide to Fourier microscopy is offered by Bryche *et al.* in Ref. [10].

3

MICROSPECTROSCOPY

So far, we have only considered the functionality of optical microscopes, understanding how an image is formed and how its magnification and spatial resolution are determined. However, we have not yet looked at the components required to add *spectral* resolution to the system (except for the 'three-channel spectrometer' that is the human eye). To spectrally analyze a microscopic system, a spectrometer must be connected to the microscope. In the *imaging microspectroscopy* setups used in this thesis, a grating spectrometer is used to extract spectral information from the microscope image. This chapter will first give a theoretical background of grating spectroscopy, followed by an overview of how different types of measurements can be performed with a microspectroscopy setup, and how the desired quantity can be extracted from the measurement results.

In combination with Chapter 2, this chapter is not only intended to give a theoretical background of microspectroscopy, but also as a basic 'user guide' for microspectroscopic experiments.

3.1 GRATING SPECTROMETERS

Figure 3.1(a) displays a schematic overview of a grating spectrometer connected to a microscope. The spectrometer consists of a grating monochromator and a 2D detector, typically a cooled CCD, CMOS or (for infrared applications) InGaAs camera. The monochromator features an entrance slit through which the light enters. The light from the slit is projected onto a rotating diffraction grating (see Section 2.1.2) via a curved mirror. Most grating monochromators use blazed gratings, as depicted in Figure 3.1(b). The entrance slit is positioned in the focus of the first mirror, so that the light impinging the grating is collimated. The light diffracted into the first

order is collected by a second curved mirror, which focuses it onto the exit port. This means that the entrance and exit port are conjugated to each other - if the 0^{th} order of the grating is used, the camera detector simply receives an image of the entrance port.[1] As long as the focal lengths of both mirrors are the same, the magnification of this image is $1:1$. The exit port can feature a second slit, so that only the wavelengths that hit this slit can exit the monochromator again (hence the name). This can, for example, be used to select a narrow range of wavelengths from a broad-band light source, to achieve tunable, monochromatic illumination of a sample. In the case of a 2D detector, each wavelength is projected onto a different position, so that a large range of wavelengths can be recorded at the same time. The rotation angle of the grating and the grating parameters determine the center wavelength and the wavelength range of the resulting detector image.

In a typical microspectroscopy setup, the monochromator is connected to the microscope such that the image plane of the microscope intersects with the entrance port of the monochromator. The image before entering the spectrometer thus contains two dimensions of *spatial* (or, in the case of Fourier microscopy, angular) information (Figure 3.1(c)). The entrance slit 'cuts' a one-dimensional strip from this image (Figure 3.1(d)), which is broadened into a *spectral* dimension before reaching the detector (Figure 3.1(e)). The functionality of the grating spectrometer can thus be imagined as removing one spatial dimension and replacing it with a spectral one. The 'lost' spatial dimension can be retrieved by moving the image across the slit (via moving optics or by simply moving the sample, as we will see later). This approach is called *hyperspectral imaging*.

3.1.1 *Spectral resolution*

The performance and spectral resolution of a grating spectrometer are influenced by a number of parameters. Apart from the focal length and the mirror size, these are mainly the width of the entrance slit and the grating parameters. As shown in Figure 3.1(b), a blazed grating features a sawtooth pattern that is defined via the groove distance d and the blaze angle γ. While the blaze angle mainly determines the efficiency with which

1 In fact, using the 0^{th} order and removing or opening the slit is a useful tactic to align the sample position to the slit.

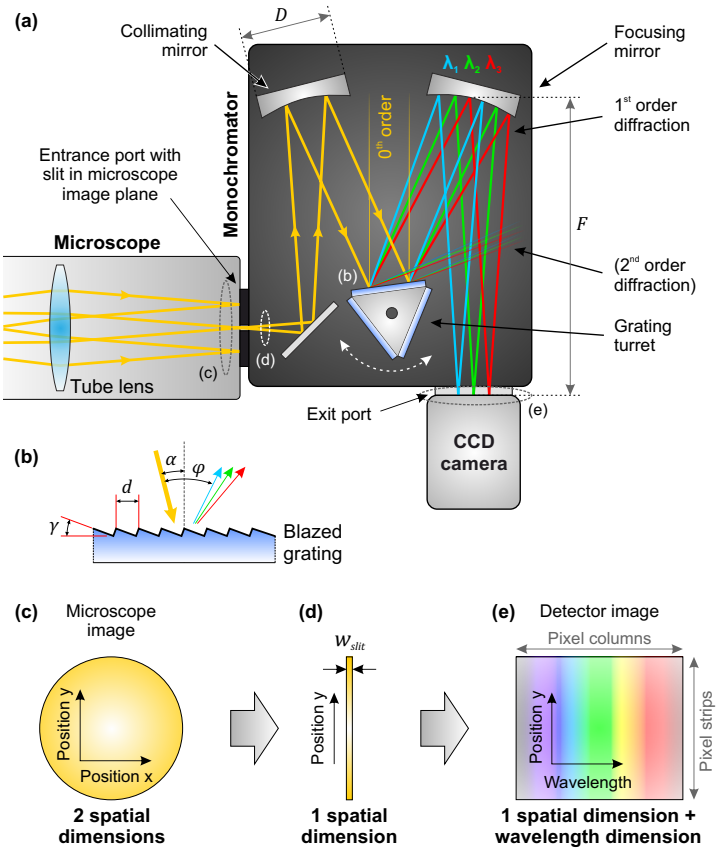

Figure 3.1. Schematic overview of a grating spectrometer connected to a microscope. (a) The image generated by the microscope is projected onto the entrance slit of a grating monochromator, which is projected onto a blazed grating (b) via a curved mirror. A second curved mirror focuses the first diffraction order onto a 2D detector. The functionality of the grating spectrometer can thus be imagined as follows: from the microscope image with two spatial dimensions (c), one dimension is removed (d) and replaced with a spectral dimension (e). The resulting image still has spatial resolution along one dimension.

each wavelength is diffracted (and thus the optimum spectral range for the grating), the wavelength resolution is determined by d.

As follows from the diffraction theory presented in Section 2.1.2, the incident angle α and the diffraction order ϕ for a certain wavelength λ are related via the following equation [11]:

$$\sin\alpha + \sin(\phi + \alpha) = \frac{m\lambda}{d} = m\lambda g, \tag{3.1}$$

with m the diffraction order (usually 1) and defining the groove number g as the inverse of the groove distance d.

Assuming that the light hits the grating at close to normal incidence ($\alpha \approx 0$), this can be simplified to the monochromator dispersion equation:

$$\lambda = \frac{\alpha(1 + \cos\phi) + \sin\phi}{mg}. \tag{3.2}$$

If the slit would be perfectly one-dimensional, the wavefront hitting the grating would be perfectly flat. Each wavelength would then be projected into a perfect monochromatic line at the exit port (apart from aberrations induced by the mirrors themselves). However, the slit has a finite width w, which can usually be varied to increase or decrease the amount of light entering the monochromator. In combination with the focal length of the curved mirrors F, this induces a divergence of the incident angle:

$$\Delta\alpha = \frac{w}{F}, \tag{3.3}$$

which leads to a broadening of the diffraction orders and thus to a small overlap of different wavelengths at the output. Following Equation 3.2, the spectral resolution of the monochromator can be quantified as:

$$\Delta\lambda = \frac{w(1 + \cos\phi)}{Fmg}. \tag{3.4}$$

In other words, the use of a monochromator with a higher focal length provides a better wavelength resolution. However, this is not the only influence of the focal length. In combination with the size of the curved mirrors D, it defines the *angular aperture* of the system $\frac{D}{F}$, which determines the maximum deviation of the incoming beams from the optical axes; in other words, the largest collectable incident angle. As we have seen in Section 2.1.2, the loss of larger-angle rays leads to a loss of spatial resolution. A high $\frac{D}{F}$ ratio prevents this, but also leads to bigger aberrations and might thus

decrease resolution. This means that, depending on the system parameters, some spatial resolution might be lost inside the monochromator compared to the image generated by the microscope.

In the case of a grating *spectrometer* with a 2D detector, the spectral resolution of the full system is furthermore influenced by the detector size and the number of pixel columns. Since the full 'image' formed at the exit port is taken into account instead of only the central stripe, distortion due to optical aberrations can also be of influence. For example, a high field curvature may lead to reduced spatial resolution at the sensor edges. This can generally be compensated via a high F value.

In practice, the parameters F and D and the detectore size and number of pixels of a grating spectrometer can be considered to be fixed parameters. This leaves three tuning parameters that can be used to increase the spectral resolution of the system:

- Decreasing the slit width w,
- Choosing a grating with a higher groove number g,
- Using a higher diffraction order m.

The optimal settings of these parameters strongly depend on the type and goal of the measurements performed. A maximization of the spectral resolution might not always be the primary goal. For example, if a time-resolved series of measurements is performed, one might want to *increase* the slit width to allow more light into the spectrometer and thus decrease the required detector exposure time. A higher g increases the distance between individual wavelengths on the detector, but thus also decreases the *wavelength range* that can be captured for a fixed angle α. If measurements over a large wavelength range are required, one might thus want to decrease the groove number.[2] This is in fact the case for most measurements presented in this thesis.

2 Care must be taken when the groove number gets very low: The lower-wavelength end of the second diffraction order can start to overlap with the higher-wavelength end of the first order on the detector, which distorts the resulting spectrum.

3.2 MICROSPECTROSCOPY SETUPS

In the work presented in this thesis, two different microspectroscopy setups were used. The first setup is based on an inverted microscope (Nikon ECLIPSE TE2000-U) and a Princeton Instruments SP2500 monochromator, equipped with a Princeton Instruments PIXIS-256E Peltier-cooled CCD camera. A photograph of this setup is shown in Figure 3.2. The monochromator is connected to a side output port of the microscope. A second grating spectrometer equipped with an InGaAs camera for near-infrared measurements can also be connected to the microscope, but is not used in the work presented here. The microscope is equipped with a Märzhäuser motorized XY stage with micrometer accuracy. A customized Köhler illumination path was constructed for episcopic illumination (not shown in the photo). Critical illumination is used for diascopic illumination, for which only fiber-coupled light sources are used. Typically, a halogen lamp (Oriel) or a high-intensity laser-driven light source (Energetiq EQ-99XFC) is used for sample illumination. An advantage of the laser-driven light source is its high intensity combined with its high temporal stability, while an advantage of the halogen lamp is its smooth emission spectrum.

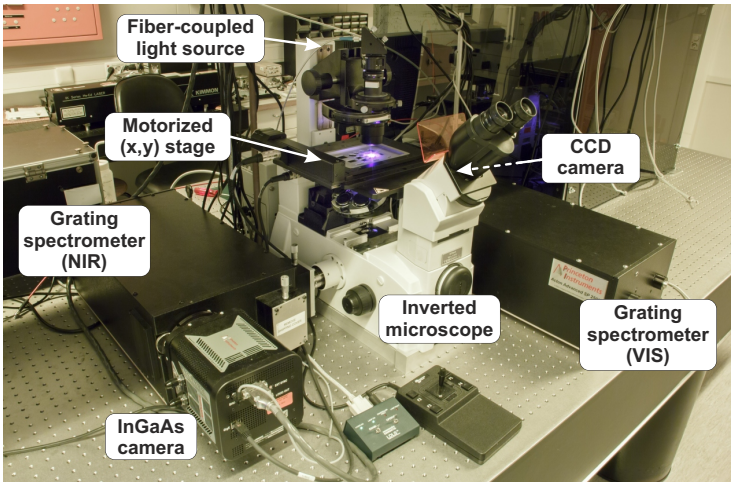

FIGURE 3.2. Photograph of the microspectroscopy setup based on a Nikon ECLIPSE TE2000-U inverted microscope and a Princeton Instruments SP2500 monochromator used in this thesis. The CCD camera attached to the VIS grating spectrometer is invisible behind the microscope. (Photograph by Dominik Flöß)

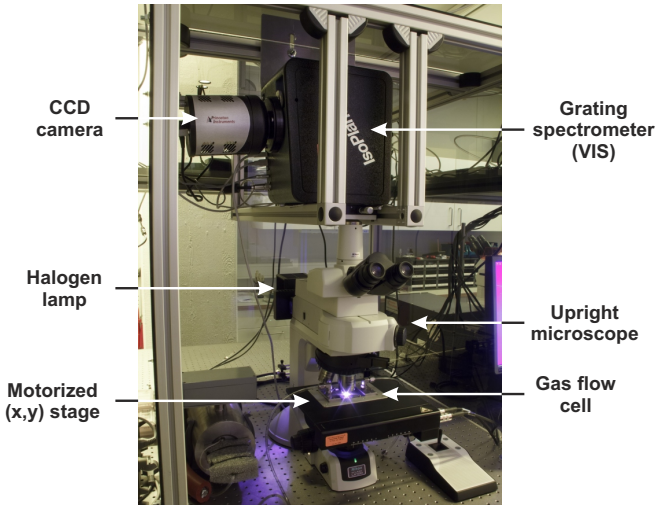

Figure 3.3. Photograph of the microspectroscopy setup based on a Nikon Eclipse LV100 upright microscope and a Princeton Instruments IsoPlane-160 monochromator used here. (Photograph by Dominik Flöß)

The second setup is based on an upright microscope (Nikon LV100) combined with a Princeton Instruments IsoPlane-160 monochromater and a PIXIS-256E camera, as shown in Figure 3.3. In this setup, Köhler illumination is used for both episcopic and diascopic illumination. The microscope is also fitted with a Märzhäuser XY stage. The spectrometer, the XY stage and an additional RGB imaging camera in both setups are connected to a PC and controlled via a custom-built LabView control software, which enables fully automated measurement cycles for different center wavelengths and sample positions.

For bright-field measurements, there is no essential difference between these two setups, at least regarding the optical design. For dark-field measurements, however, there is a difference. The upright microscope setup is optimized for episcopic (reflection) dark-field measurements via specialized dark-field objectives (see Figure 2.8), while the inverted microscope setup is optimized for diascopic (transmission) dark-field measurements. This is mainly because in these two cases, the position of the light source is fixed with respect to the dark-field condenser. In the inverted microscope setup, this is because the entire custom-built critical illumination path is connected to a vertical stage and thus moves as a whole.

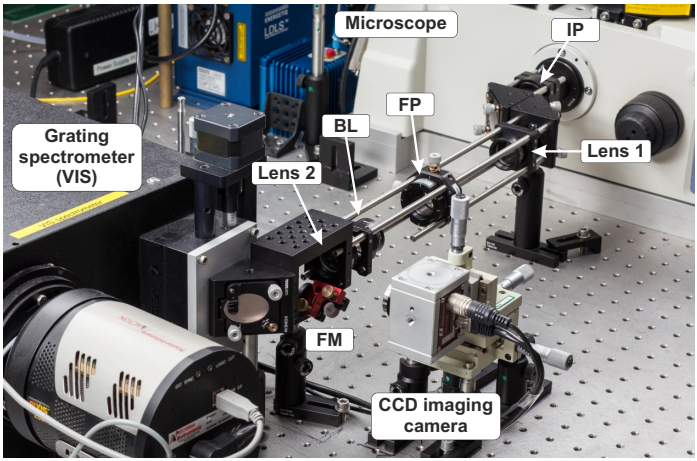

Figure 3.4. Photograph of the Fourier microspectroscopy optical path used in this thesis. Kinematic mirror cubes are used for alignment. A CCD imaging camera (Allied Vision Prosilica gc2450c) in combination with a flip mirror (FM) is used to observe the image projected onto the spectrometer slit, for focusing and alignment purposes. IP: Image plane, FP: Fourier Plane, BL: Bertrand lens. (Photograph by Moritz Flöß)

In addition to these two basic setups, a Fourier imaging optical path was constructed for the inverted microscope setup, as shown in Figure 3.4. It consists of a 4-f setup installed between the microscope and the spectrometer using the Thorlabs cage system. A 4-f setup consist of two lenses of focal length f (150 mm in this case), which are placed at a distance $2f$ from each other. Lens L1 is placed at a distance f from the image plane of the microscope output port, and the spectrometer entrance slit is placed at a distance f from lens L2. An intermediate Fourier plane (FP) is generated in between the two lenses, similar to the setup illustrated in Fig. 2.11. The advantage of this intermediate FP is that it can be used to insert e.g. a stop to block the 0^{th} order of transmitted/reflected light. In front of L2, a third lens can be inserted, which acts as the Bertrand lens (BL). The lens system formed by the BL and L2 acts as an imaging lens, which images the intermediate Fourier plane onto the spectrometer entrance slit. The system then represents a 'modified 4-f setup' as described in Ref. [1]. The focal length and position of the BL depend on the desired size of the Fourier image on the entrance slit and the actual size of the image in the FP, which strongly varies for different objectives.

A dedicated addition to these microspectroscopy setups are two specialized gas flow cells, which are used to perform microspectroscopic measurements on metal nanoparticles in a defined gas flow and characterize their response upon exposure to different gases. This is used in the work shown in Chapters 5 through 8 of this thesis. As shown in Figure 3.5(a), a gas flow cell suitable for transmittance as well as reflectance measurements was constructed, consisting of a titanium top and bottom and featuring thin optical windows (170 µm thick coverslips) for illumination and observation. This cell can also be seen in Figure 3.3. The material Ti was chosen for its low thermal expansion coefficient, in order to reduce the risk of sample drift during a measurement. A second gas flow cell was constructed for measurements at elevated temperatures, in which the sample is heated from below by a stack of Peltier elements (Fig. 3.5(b)). The Peltier elements are controlled via a Meerstetter Engineering TEC controller in combination with a resistive temperature sensor on the sample surface, which can keep the temperature stable to within 0.1 °C. Only episcopic measurements are possible with this cell.

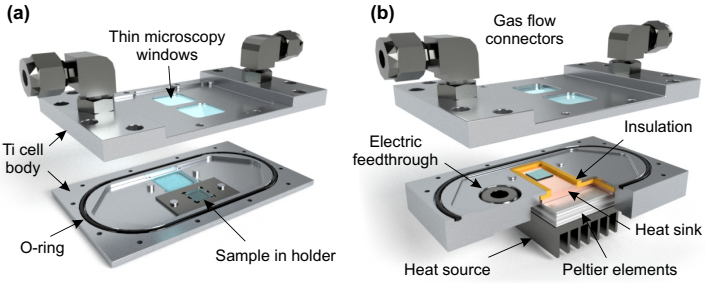

Figure 3.5. 3D renderings based on CAD models of the standard transmission/reflection microscopy gas flow cell (a) and the temperature-controlled gas flow cell (b).

3.3 MEASUREMENTS AND DATA PROCESSING

For any of the previously described configurations, the image generated by the setup can be analyzed spectroscopically. However, it strongly depends on the configuration which quantity can be extracted from the acquired data and how these data must be processed. This section aims to give an overview of typical data processing for bright-field, dark-field, and k-space microspectroscopy.

3.3.1 *Bright-field spectroscopy*

Figure 3.6 shows a typical example of a bright-field microspectroscopic measurement, in which the reflectance of an array of nanoparticles is to be characterized. The spectrometer entrance slit 'cuts' a vertical stripe from the image of one array. The resulting CCD image does not directly show the sample reflectance, but rather the light source emission spectrum modulated by the sample (and all the optics in the setup). To extract the sample reflectance, one thus needs to record a reference measurement.

The simplest quantity to measure using bright-field microspectroscopy is the *transmittance* (T) of a sample, as illustrated in Figure 2.7(a). The transmittance is measured by recording the spectrally resolved intensity transmitted through the sample, removing the sample from the optical path, recording a reference intensity measurement, and normalizing the intensity spectrum measured at the sample to this reference spectrum. In most cases, the sample of interest is located on a transmissive substrate, which means that the reference measurement should preferably be performed at an empty spot on the same substrate:

$$T = \frac{I_{\text{sample}}}{I_{\text{substrate}}} \tag{3.5}$$

It becomes slightly more complicated when one is not interested in the transmittance of a sample, but in the *reflectance* (R), as in the example of Figure 3.6. This could be the case if the sample is designed to provide a certain reflectance spectrum, but also if the sample is situated on a non-transmittive substrate for any operational reason. In a reflectance measurement, the microscope objective serves as condenser at the same time (Figure 2.8(a)). For the reference measurement, it is in this case required that *all* the light projected into the sample plane is reflected back into the objective. A mirror must thus be placed in the sample plane. If the mirror reflectance is

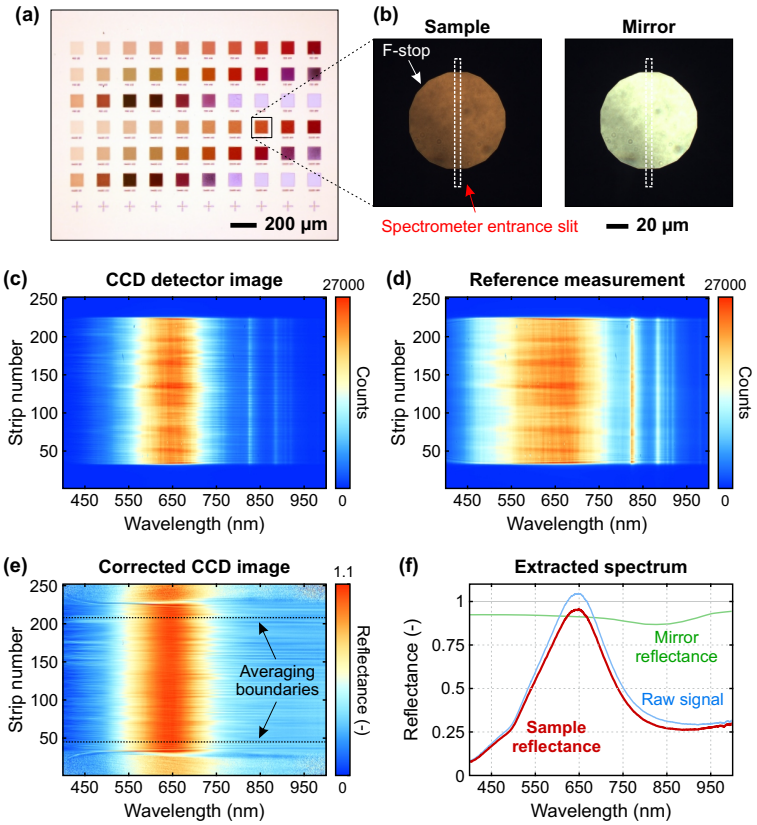

Figure 3.6. Example of a bright-field (episcopic) microspectroscopic measurement. A reflective sample with several arrays of nanoparticles (a) is observed via a Nikon TU Plan Fluor ELWD 60×, NA 0.70 objective (b). The closed F-stop blocks stray light from areas outside of the array. An Al mirror is used to record a reference spectrum. The detector image of the sample shows the emission spectrum of the light source (in this case an Energetiq EQ-99XFC laser driven light source) modulated by the sample reflectance (c) and must thus be corrected by the reference spectrum (d). Averaging over a large range of pixel strips inside the F-stop gives the normalized reflectance spectrum (e). Finally, this spectrum must be corrected by the known mirror reflectance (f).

sufficiently close to unity, this reference spectrum can directly be used for normalization. If this is not the case, the normalized intensity must be corrected by the known mirror reflectance:[3]

$$R = \frac{I_{\text{sample}}}{I_{\text{mirror}}} \cdot R_{\text{mirror}} \tag{3.6}$$

This is demonstrated in Figure 3.6(f), for the case of an aluminum mirror. In the visible range, the reflectance of Al is around 90%, with a pronounced dip in the 700-900 nm region [12]. If the sample reflectance is higher than this, a direct normalization to the mirror thus leads to reflectance values higher than 100% (blue line). The mirror correction eliminates this (red line).

In some cases, another correction must be applied. Light reflected towards the beam splitter by the microscope objective itself can contribute to the measured signal. In most cases, this is negligibly small compared to the sample reflectance, but if the sample reflectance is very low, it can play a significant role. Furthermore, only light reflected by the objective under very small angles overlaps with the light reflected by the sample and is thus projected onto the detector. This means that under a small illumination NA (closed A-stop; see Section 2.2.1) the relative contribution of this back reflection is much larger than under a large illumination NA.

The contribution of the objective back reflection can be measured by imaging an empty sample plane, so that the objective collects no light. Since the back reflection contributes to I_{sample} as well as I_{mirror}, the correction looks as follows:

$$R = \frac{I_{\text{sample}} - I_{\text{empty}}}{I_{\text{mirror}} - I_{\text{empty}}} \cdot R_{\text{mirror}} \tag{3.7}$$

This was, for example, applied in the work published in P14, where very small reflectances had to be characterized under a very small incident NA.

Furthermore, it is important to note that in reflectance measurements, it is not always possible to entirely disentangle the contribution of the substrate from the measured signal. This critically depends on the *definition* of the 'sample reflectance'. For instance, if the 'sample' is a structure consisting of the reflecting substrate plus an array of nanoantennas placed above it, the sample signal is simply all the light collected at the sample position

3 One could of course also use any other reflective sample for normalization, as long as its reflectance spectrum is known. However, a metal mirror is usually most convenient. For example, one can easily coat a part of the substrate with a layer of metal, so that the reference measurement can be done on the same substrate. The mirror layer must be thick enough to not allow transmission.

(Chapter 8 will present an example of such structures). However, if one is interested only in the reflectance of an array of nanoantennas, but the antennas are placed on a reflective substrate, one inevitably records light reflected by the antennas *plus* light reflected by the substrate. Measuring the substrate reflectance separately and subtracting it from the sample reflectance can give incorrect results as well, since the nanostructures decrease the amount of light reaching the substrate and thus the amount reflected by it. If the substrate reflectance is very low compared to the nanostructure reflectance, it can often be ignored. In the opposite case, the substrate could be directly used for referencing according to Eq. 3.6. If both reflectances are in the same order of magnitude, however, this is not possible.

All of this does not necessarily pose a problem - it strongly depends on the type and goal of the measurements. If the goal is to compare the reflectance of nanostructures to numerical calculations, the substrate could be taken into account in the calculations as well. If the goal is to track a spectral change upon some stimulus, this is still possible, as long as the substrate itself shows no response. It should nonetheless be stated that the method of data analysis and spectral normalization deserves special attention in the case of reflectance measurements.

3.3.2 *Dark-field spectroscopy*

As discussed before, dark-field microspectroscopic measurements can be employed to characterize the far-field scattering behaviour of isolated nanoparticles. Figure 3.7 shows an example of such a measurement, in which a single gold nanosphere with a diameter of approximately 30 nm is investigated. A sample with such particles was prepared by dropcoating a solution containing colloidal Au particles onto a glass substrate. As the dark-field image in Figure 3.7(a) shows, it is very difficult to distinguish an isolated particle from other scattering sources, which can mainly be attributed to residue from the solution. As the close-up shows, a good way of identifying metal nanoparticles is by their color: as the particles can be expected to show a very narrow far-field scattering peak, in contrast to all other structures, a colored spot in the microscope image indicates such a particle.

Similar to the case of bright-field measurements, the light scattered by the particle into the objective NA still includes the emission spectrum of the light source. Removing the sample would provide no signal at all and can thus not be used for a reference measurement. Rather, a certified reflectance standard must be used for referencing, as shown in Figure 3.7(b). A reflectance

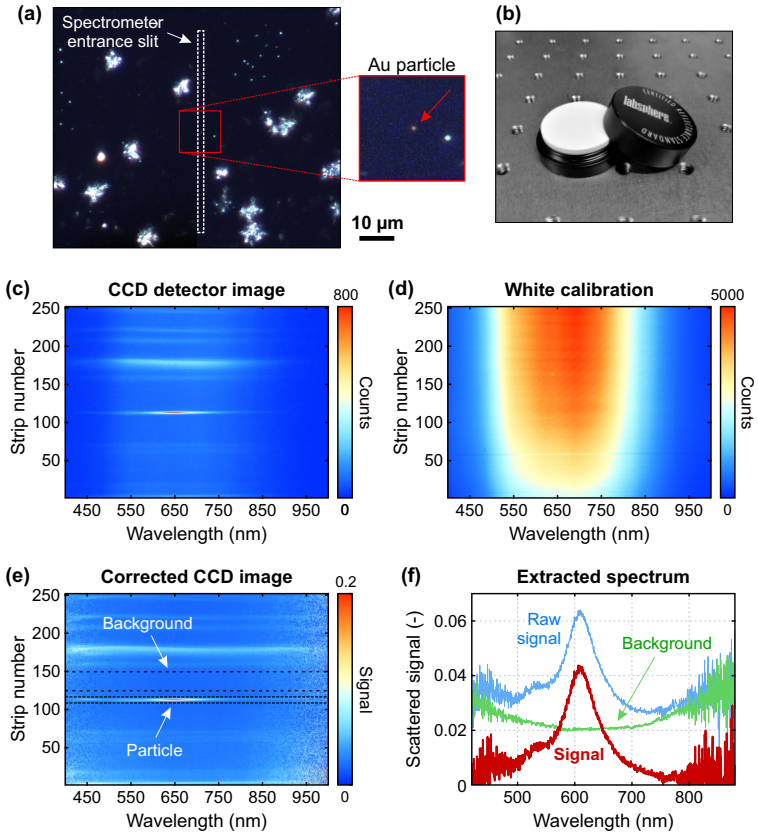

Figure 3.7. Example of a dark-field microspectroscopic measurement. A sample with very weakly scattering colloidal Au nanoparticles (diameter 20 nm) from a dropcoated solution is observed via a Nikon LU PLAN ELWD 100×, NA 0.80, dark-field objective (a). A certified reflectance standard (Labsphere) is used to record a white calibration measurement of the (halogen) light source (b). The sample detector image shows light scattered from the particle as well as from pollution on the substrate (c). This image is normalized by the white calibration measurement (d) to give the corrected CCD image (e). The raw particle signal extracted from this image is background-corrected to give the particle scattering signal (f).

standard is a piece of material which has been engineered to scatter all wavelengths isotropically. A measurement performed on this standard is then called the *white calibration*, and can be used for normalization of the detector image of the sample:

$$S_{\text{scatt}} = \frac{I_{\text{sample}}}{I_{\text{whitecal}}} \tag{3.8}$$

The resulting signal S_{scatt}, shown in Fig. 3.7(e), is expressed in arbitrary units.

The scattering signal of the single particle can be extracted from the normalized CCD image by averaging or integrating the signal over a small number of pixel strips around the particle (Fig. 3.7(d)).[4] The spatially resolved CCD image furthermore offers the possibility of recording the scattering spectra of several particles in one shot, if these can be placed 'inside' the spectrometer slit simultaneously.

Similar to the background correction described for bright-field measurements (Eq. 3.7), an additional background correction may be necessary for dark-field measurements, especially for very weakly scattering particles. This is also the case in Figure 3.7, where the background scattering of the substrate itself leads to a nonzero signal away from the particle. In this case, the background measurement does not have to be taken separately, but is already contained in the data: the signal averaged over several 'empty' pixel strips can be subtracted from the extracted spectrum to give the particle signal (Fig. 3.7(f)). The corrected expression for the scattered signal thus reads:

$$S_{\text{scatt}} = \frac{I_{\text{particle}} - I_{\text{background}}}{I_{\text{whitecal}}} \tag{3.9}$$

In contrast to bright-field measurements, it is in this case *not* important that the measurement parameters are exactly the same for the sample and white calibration, as the resulting signal is expressed in arbitrary units anyway. Typically, the white calibration signal is orders of magnitude stronger than the sample signal, so that the exposure time of the spectrometer must be chosen differently. In the example of Figure 3.7, the exposure times were 1 s for the white calibration and 10 s for the nanoparticle. The slit width does not need to be the same either. For the white calibration measurement, it should be *small* to increase the spectral resolution (see Eq. 3.4). In the particle measurement, however, the slit can be opened further - particles of

4 When no background correction is applied, it makes no difference if the signal is integrated or averaged - only when the scattered intensity of different particles is compared, the number of used pixel strips must be taken into account.

sub-diffraction sizes act as point sources, so that w_{slit} does not significantly affect the spectral resolution. A wider slit can in this case prevent the particle from drifting 'out of the slit' due to mechanical disturbances during the measurement.

3.3.3 *Fourier-plane spectroscopy*

As explained before, Fourier-space microscopy can give information about the angle-dependent behaviour of a sample. Figure 3.8 shows an example of a measurement of the angle-dependent transmittance of a nanodisk array on a glass substrate. The setup shown in Figure 3.4 was used for this measurement, so that the image on the spectrometer slit can be switched between real-space and k-space image by inserting the Bertrand lens. First, the real-space image is monitored to bring the nanodisk array into focus and position (Fig. 3.8(a)). Then the Bertrand lens is inserted and aligned to show the Fourier plane (panel (b)), which is aligned so that the entrance slit cuts the central stripe from this image. In this way, all angles θ_y for $\theta_x = 0^\circ$ (see Figure 2.11(b)) are accessed. This corresponds to all polar angles for an azimuthal angle of 0°. The maximum accessible angle is given by $\min\left(\text{NA}_{\text{obj}}, \text{NA}_{\text{cond}}\right)$. In this example, NA_{obj} defines the limit. Since all spatial information is removed from the image, and one thus effectively averages over all positions within the illuminated area, it is very important to close the F-stop. Otherwise, light transmitted by the sample outside of the array would contribute to the signal and distort the resulting transmittance.

Since transmittance is measured, a simple normalization can be done according to Equation 3.5. Panels (c-d) show the corresponding sample and reference CCD images. The angular illumination of the sample is non-uniform, which has to do with the angular emission of the optical fiber that was used in critical illumination. This inhomogeneity is removed in the corrected CCD image (panel (e)), just as in a real-space bright-field measurement. Diffraction modes arising from the rectangular lattice of the nanodisks, as will be addressed in Chapter 8, are clearly visible in this image. In the CCD image, pixel strip numbers can be converted to angles, since the borders of the illuminated area correspond to the known NA. Averaging over all strips thus gives the angle-averaged sample transmittance, while the spectrum in a single pixel strip corresponds to a certain angle (panel (f)). The angular resolution is determined by the size of the Fourier image on the spectrometer slit and the number of pixels of the CCD detector.

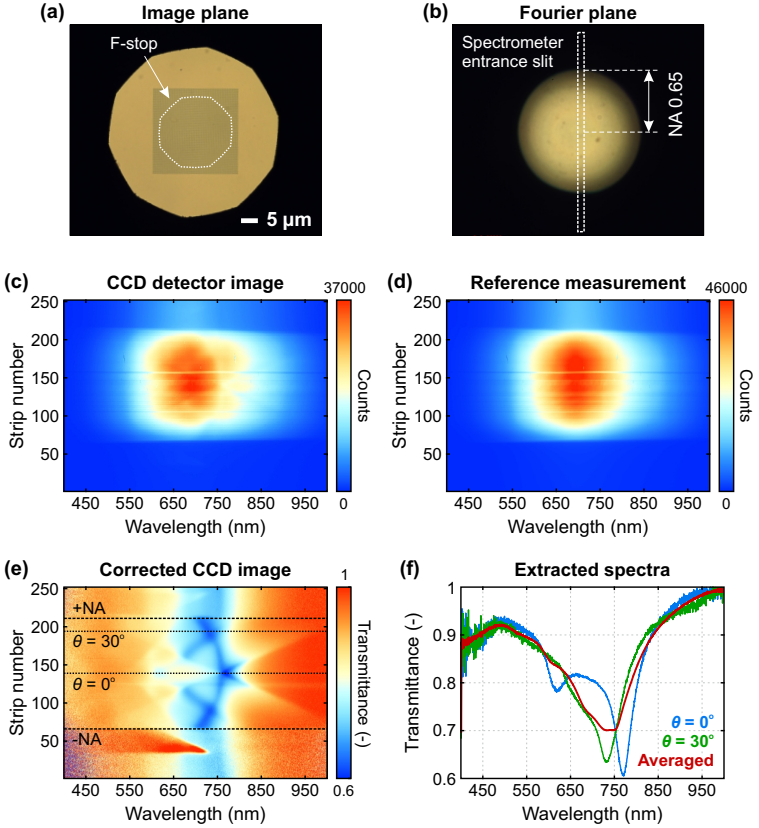

Figure 3.8. Example of a Fourier-space microspectroscopic measurement. A 25×25 µm^2 array of Au nanodisks on a glass sample is illuminated by a halogen lamp via a condenser with NA 0.65, and observed with a Nikon TU PLAN FLUOR ELWD 100×, NA 0.90 objective (a). The F-stop is closed, so that only light which passes through the array enters the objective, and the Bertrand lens is inserted to produce the Fourier image (b). The extent of the Fourier image is determined by the condenser NA. From the sample and reference detector images (c,d), the normalized image is extracted (e). The strip number in this image can be converted to the angle, so that transmittance spectra for all collected angles are recorded in one shot.

Fourier-space microspectroscopy can thus be used for angular, instead of spatial, characterization of far-field spectra. In this case, the influence of the condenser/objective NA on the spatial resolution is not important. Rather, the NA defines the maximum accessible range of angles. An additional advantage of Fourier-space measurements can be that the signal is automatically averaged over all illuminated positions, instead of only a 1D stripe. This can, for example, be exploited if a large-area average measurement of transmittance or reflectance is desired.

3.3.4 *Hyperspectral imaging*

As discussed in Section 3.1, a microspectroscopic measurement effectively trades one spatial (or, in Fourier-space imaging, angular) dimension for the spectral dimension. However, the 'lost' dimension can easily be brought back by moving the position of the spectrometer entrance slit with respect to the sample. In real-space imaging, this can easily be done by moving the

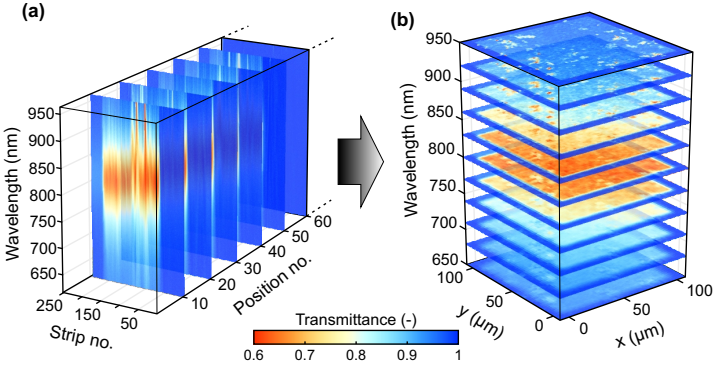

Figure 3.9. Example of a hyperspectral, real-space, bright-field, microspectroscopic transmittance measurement of an Au nanoantenna array, observed with a Nikon TU Plan Fluor ELWD 60×, NA 0.70 objective. The recorded CCD images for different sample positions (a) are combined into a wavelength-resolved image of the full array (b). In the higher-wavelength range, pollution of the array, in this case caused by iodinium salt, can be recognized.

sample using a motorized stage.[5] In Fourier-space imaging, the full Fourier plane can be moved accross the entrance slit via movable optics, such as a rotating mirror in front of the spectrometer [13]. Figure 3.9 shows an example of a real-space bright-field measurement, performed on an array of Au nanoantennas polluted with iodinium salt flakes. By converting the pixel strips into positions and using the measurement positions of the XY stage, all recorded transmittance spectra can be combined into a three-dimensional datacube, which is called the *hyperspectral image*. This can, for example, be used to extract the spatially resolved center wavelength of a transmittance feature. An application of this hyperspectral imaging microscopy technique will be shown in Chapter 9.

5 Another option is to omit the monochromator altogether and use a wavelength-tunable light source. It is then, however, difficult to reach the same spectral resolution as with a grating monochromator.

4

PLASMONICS

After the description of microscopy and microspectroscopy in the previous chapter, we will now focus on the concept of plasmonics to lay a foundation for the further work in this thesis. We will first examine a generalized description of the interaction of light and matter, specifically metals, and then focus on the consequences of this interaction on the optical response of metal nanoparticles. We will show how a *localized surface plasmon resonance* can be excited in such particles, and how its effects in the optical far-field are connected to the optical near-field. We will furthermore see how this facilitates the use of plasmonic nanoparticles - also termed *nanoantennas* - for different applications, such as switchable optical devices and the optical detection of chemical changes in nanoscale volumes.

4.1 LIGHT-MATTER INTERACTION

This section mostly follows the argumentations found in the work of Griffiths [14] and Novotny and Hecht [15].

As a starting point for understanding the interaction between light and matter, we consider the fundamental Maxwell equations, which couple the electric field $\boldsymbol{E}$, the dielectric displacement $\boldsymbol{D}$, the magnetic field $\boldsymbol{H}$, and the magnetic induction flux density $\boldsymbol{B}$.

Expressed in differential form, the Maxwell equations in matter read as follows:

$$\nabla \times \boldsymbol{E} = -\frac{\partial \boldsymbol{B}}{\partial t}, \tag{4.1}$$

$$\nabla \times \boldsymbol{H} = \frac{\partial \boldsymbol{D}}{\partial t} + \boldsymbol{j}_{\text{ext}}, \tag{4.2}$$

$$\nabla \cdot \boldsymbol{D} = \rho_{\text{ext}}, \tag{4.3}$$

$$\nabla \cdot \boldsymbol{B} = 0. \tag{4.4}$$

Here, $\boldsymbol{j}_{\text{ext}}$ is the external current density, and ρ_{ext} is the external charge density.

These four macroscopic fields are furthermore linked to each other via the polarization $\boldsymbol{P}$ and the magnetization $\boldsymbol{M}$:

$$\boldsymbol{D} = \epsilon_0 \boldsymbol{E} + \boldsymbol{P}, \tag{4.5}$$

$$\boldsymbol{H} = \frac{1}{\mu_0}\boldsymbol{B} - \boldsymbol{M}. \tag{4.6}$$

The proportionality constant $\epsilon_0 = 8.85418782 \times 10^{-12}$ C^2/Nm^2 is known as the *dielectric permittivity* of free space, and $\mu_0 = 1.25663706 \times 10^{-6}$ N/A^2 as the *dielectric permeability* of free space. In linear, isotropic media, these equations reduce to the following linear relations:

$$\boldsymbol{D} = \epsilon_0 \epsilon \boldsymbol{E}, \tag{4.7}$$

$$\boldsymbol{B} = \mu_0 \mu \boldsymbol{H}. \tag{4.8}$$

Here, $\epsilon(\omega)$ is the *relative dielectric permittivity* of the material. This wavelength-dependent quantity, also called the *dielectric function*,[1] fully characterizes the electric response of a material to an external electric field. Analogously, the relative dielectric permeability $\mu(\omega)$ describes the material's magnetic response to a magnetic field.

Since ϵ is complex-valued, it is often expressed in terms of its real part ϵ_1 and its imaginary part ϵ_2:

$$\epsilon(\omega) = \epsilon_1(\omega) + i\epsilon_2(\omega). \tag{4.9}$$

Another way to express the dielectric function is in terms of the *complex refractive index*, which is defined as the square root of the dielectric function times the dielectric permeability:

$$n(\omega) = \sqrt{\epsilon(\omega)\mu(\omega)}. \tag{4.10}$$

Most naturally occurring materials, and all materials considered in this thesis, are non-magnetic at optical frequencies. This means that $\mu(\omega)$ equals one, and Eq. 4.10 reduces to $n(\omega) = \sqrt{\epsilon(\omega)}$.

1 Or, sometimes, the *dielectric constant*, as it can be regarded a material constant, albeit one that varies with wavelength.

Throughout Chapter 2, we have only considered the real-valued refractive index, which is sufficient for non-absorbing materials. For metals, however, an imaginary part must be introduced. The complex refractive index $\tilde{n}$ is then expressed as:

$$\tilde{n}(\omega) = n(\omega) + i\kappa(\omega), \tag{4.11}$$

in which the real part can be identified with the normal refractive index of a material, which defines its dispersion. The imaginary part κ determines the attenuation of electromagnetic waves (and is thus related to the so-called *skin depth*, which indicates how deep electromagnetic radiation can penetrate into the material). In other words, a purely real-valued refractive index indicates a fully transparent material.

Expressing a material's dielectric properties in terms of ϵ or in terms of $\tilde{n}$ is thus equivalent. It is easy to convert between the two quantities using the following relations:

$$\epsilon_1 = n^2 - \kappa^2, \qquad \epsilon_2 = 2n\kappa, \tag{4.12}$$

and

$$n = \sqrt{\frac{\sqrt{\epsilon_1^2 + \epsilon_2^2} + \epsilon_1}{2}}, \qquad \kappa = \sqrt{\frac{\sqrt{\epsilon_1^2 + \epsilon_2^2} - \epsilon_1}{2}}. \tag{4.13}$$

For most dielectric (non-metallic) materials, the refractive index and thus the dielectric function does not vary strongly with wavelength. Next, we will look at metals, for which this is an entirely different story.

4.1.1 *Drude-Sommerfeld theory*

The response of a metal to electromagnetic radiation is characterized by the behavior of its free electrons. This means that the Drude-Sommerfeld model for the free-electron gas can be applied to the displacement $\boldsymbol{r}$ of the electrons, and the following equation of motion can be established:

$$m_e \frac{\partial^2 \boldsymbol{r}}{\partial t^2} + m_e \Gamma \frac{\partial \boldsymbol{r}}{\partial t} = -e\boldsymbol{E_0}\exp(-i\omega t), \tag{4.14}$$

where m_e and e are the effective mass and the charge of the free electrons, respectively. $\boldsymbol{E_0}\exp(-i\omega t)$ represents a plane wave as the external oscillating field, as described in Section 4.1. This equation of motion does not contain a restoring force, since it considers free electrons. Furthermore, the damping

term Γ is proportional to v_F/l, where v_f is the Fermi velocity and l is the mean free path of the electrons between scattering events.

Using the ansatz $\boldsymbol{r}(t) = \boldsymbol{r_0}\exp(-i\omega t)$ for this second-order linear differential equation yields:

$$\boldsymbol{r}(t) = \frac{e}{m_e\omega^2 + im_e\Gamma\omega}\boldsymbol{E_0}\exp(-i\omega t). \tag{4.15}$$

If we now use the fact that the displaced electrons give the macroscopic polarization $\boldsymbol{P}$, according to the relation $\boldsymbol{P} = -n_e e\boldsymbol{r}$, with n_e the density of free electrons, we obtain:

$$\boldsymbol{P} = -\frac{n_e e^2}{m_e\omega^2 + im_e\Gamma\omega}\boldsymbol{E}, \tag{4.16}$$

and this can be combined with Equation 4.7:

$$\boldsymbol{D} = \epsilon_0\left(1 - \frac{\omega_p^2}{\omega^2 + i\Gamma\omega}\right)\boldsymbol{E}, \tag{4.17}$$

in which ω_p denotes the *volume plasma frequency* of the material:

$$\omega_p = \sqrt{\frac{n_e e^2}{m_e\epsilon_0}}. \tag{4.18}$$

This implies that the dielectric function $\epsilon(\omega)$ according to the free-electron model can be written as:

$$\epsilon_{\text{Drude}}(\omega) = 1 - \frac{\omega_p^2}{\omega^2 + i\Gamma\omega}. \tag{4.19}$$

The resulting dielectric function can be separated into its real and imaginary parts ϵ_1 and ϵ_2 as:

$$\epsilon_{\text{Drude}}(\omega) = 1 - \frac{\omega_p^2}{\omega^2 + \Gamma^2} + i\frac{\Gamma\omega_p^2}{\omega(\omega^2 + \Gamma^2)}. \tag{4.20}$$

This result means that, as long as only the effects of *free* electrons are considered, a metal can be fully described by its volume plasma frequency ω_p and damping coefficient Γ.

In Figure 4.1, the real and imaginary parts of the dielectric function of gold are plotted versus wavelength, according to Equation 4.20 and using

the literature values $\omega_p = 8.95$ eV and $\Gamma = 65.8$ meV.[2] In addition to this analytic result, the experimentally measured dielectric function of gold is displayed, as reported in the work of Johnson and Christy [17].

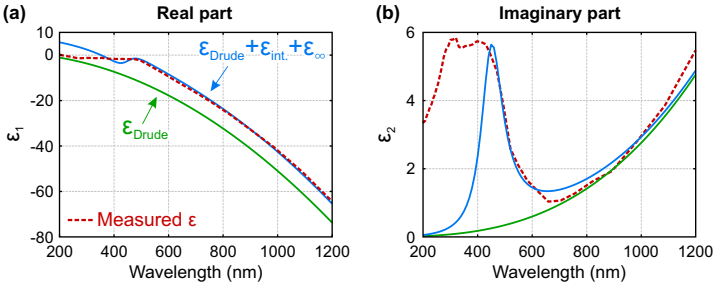

Figure 4.1. Real (a) and imaginary part (b) of the dielectric function of gold, calculated using only the free-electron model, the free-electron model including the correction for one interband transition, and as measured by Johnson and Christy.

As the comparison between the analytic and experimental data clearly shows, the Drude-Sommerfeld model is able to reproduce the shape of the real dielectric function of gold rather accurately in the higher-wavelength range. At wavelengths below approximately 600 nm, however, a strong discrepancy occurs, mainly in the imaginary part ϵ_2. This is because at these lower wavelengths, which correspond to higher photon energies, electrons can be promoted from lower-lying bands into the conduction band. This can be described as exciting the oscillation of bound electrons. Similar to the case of free electrons, as in Equation 4.14, an equation of motion can be written for these bound electrons:

$$m\frac{\partial^2 \boldsymbol{r}}{\partial t^2} + m\gamma\frac{\partial \boldsymbol{r}}{\partial t} + \alpha \boldsymbol{r} = -e\boldsymbol{E}_0 \exp(-i\omega t), \tag{4.21}$$

in which m is the effective mass of the bound electrons, which is not necessarily the same as the effective mass of *free* electrons in a periodic potential m_e. Furthermore, γ is the damping constant for these bound electrons, mainly

2 Several different parameter sets for ω_p and Γ exist in the literature. These are usually claimed to result from the best fit to experimental data. See, for example, Ref. [16] for an overview. Here, I used the values from Ref. [15].

describing radiative damping, and α is the spring constant that describes the potential keeping the electrons in place. Analogous to the derivation of Eq. 4.19, the contribution of bound electrons to the dielectric function can be written as:

$$\epsilon_{\text{interband}}(\omega) = 1 + \frac{\tilde{\omega}_p^2}{(\omega_0^2 - \omega^2) - i\gamma\omega}, \tag{4.22}$$

where, analogous to Eq. 4.18, $\omega_p = \sqrt{n_b e^2/m\epsilon_0}$, with n_b being the bound electron density, and $\omega_0 = \sqrt{\alpha/m}$. The result can again be separated into real and imaginary parts:

$$\epsilon_{\text{int.}}(\omega) = 1 + \frac{\tilde{\omega}_p^2(\omega_0^2 - \omega^2)}{(\omega_0^2 - \omega^2)^2 + \gamma^2\omega^2} + i\frac{\gamma\tilde{\omega}_p^2\omega}{(\omega_0^2 - \omega^2)^2 + \gamma^2\omega^2}. \tag{4.23}$$

As Figure 4.1 shows, a correction of ϵ_{Drude} by the addition of $\epsilon_{\text{interband}}$ is able to reproduce the experimentally measured data much more accurately. The parameters used here are $\tilde{\omega}_p = 2.96$ eV, $\gamma = 0.59$ eV, and $\omega_0 = 2.76$ eV (which corresponds to 450 nm). However, to achieve this, one also has to add a constant offset $\epsilon_\infty = 6$ to Eq. 4.23. This offset accounts for the integrated effect of all higher-energy interband transitions. Also, Eq. 4.23 only considers *one* interband transition. This explains why even this extended model fails to accurately reproduce the measured data of gold for wavelengths below 450 nm. In fact, the high values of ϵ_2 for gold in this region and the associated absorption of light are what gives gold its characteristic color.

The expressions for the dielectric function above provide some further insight into the physical meaning of the plasma frequency ω_p. As Eq. 4.20 shows (thus, for the moment, ignoring interband transitions), the imaginary part ϵ_2 vanishes when ω approaches ω_p (assuming that $\omega \gg \Gamma$) and the real part simplifies to:

$$\epsilon_1(\omega) = 1 - \frac{\omega_p^2}{\omega^2}, \tag{4.24}$$

indicating that the metallic character is only maintained for frequencies below the plasma frequency. For most (noble) metals, ω_p lies in the ultraviolet wavelength range, so that this condition is fulfilled in the visible wavelength range and above.

To summarize, the Drude-Sommerfeld free electron model, in combination with the correction for interband transitions, provides a good tool to approximate the dielectric function of a material and to understand its underlying physical principles. Nevertheless, for accurate numerical modeling of the response of metallic systems to excitation with light, it is much more useful

to use tabulated experimental data, which can be found in the literature. For example, the work of Palik [18] provides an extensive overview of dielectric functions for different metals. Throughout this thesis, besides gold, dielectric function datasets for magnesium (Mg), titanium (Ti), palladium (Pd), and aluminum (Al) will be used. The corresponding literature sources are cited where applicable.

4.2 PLASMON RESONANCES

So far, we have looked at the optical properties of bulk materials. The next step is to look at the implications that these properties have for nanoscale volumes of metal; in other words, for plasmonic metal nanoparticles. The term 'plasmon' in this case refers to a collective excitation of the free electrons in a nanoscale confined volume. A plasmon excited in a single particle is also termed a *localized surface plasmon resonance*, abbreviated as LSPR. This stands in contrast to plasmon waves excited at a metal surface, so-called *surface plasmon polaritons*, or SPPs. The work in this thesis mainly considers plasmonic nanoparticles, although SPPs will make a brief appearance at the end of Chapter 8. This section will thus focus on the physical principles behind plasmons in metal nanoparticles, mostly following the arguments in Refs. [15] and [19].

4.2.1 *Near-field response*

Here, we consider a metal nanoparticle with radius a and dielectric function ϵ_m, embedded in an environment with constant dielectric function ϵ_e, excited by a plane wave $\boldsymbol{E}_0$. We will consider this system in a spherical coordinate system, as shown in Figure 4.2. If the particle is much smaller than the wavelength ($a \ll \lambda$), we can assume that the $\boldsymbol{E}_0$ is homogeneous for any moment in time. We will thus search for an expression for the electric field at any point $P(r, \theta)$ in and around the particle at these conditions, also called the *quasi-static approximation* (QSA). Because of the rotational symmetry of the problem the azimuthal angle ϕ can safely be ignored. For larger particle sizes, this approximation breaks down, as retardation effects of the traveling electromagnetic wave come into play and the electric field cannot be regarded constant anymore. Nevertheless, the QSA offers a good basic understanding of LSPR resonances.

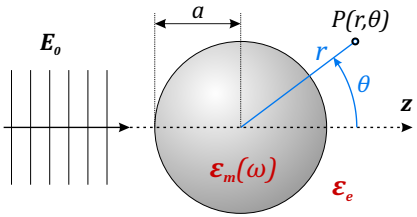

Figure 4.2. Coordinate system used to evaluate the electric field in and around a metallic nanoparticle.

Using the coordinate system in Figure 4.2, the electric field on the sphere surface is given by:

$$\boldsymbol{E}_0 = E_0 \boldsymbol{n}_z = E_0 \cos\theta \boldsymbol{n}_r, \tag{4.25}$$

with $\boldsymbol{n}_z$ the unit vector along the direction of propagation, and $\boldsymbol{n}_r$ in the radial direction. In the quasi-static limit, the electric field of the particle can be represented as a potential $\boldsymbol{\Phi}$:

$$\boldsymbol{E} = -\nabla \cdot \Phi, \tag{4.26}$$

which must satisfy the Laplace equation:

$$\nabla^2 \Phi = 0. \tag{4.27}$$

If the Laplace equation is expressed in spherical coordinates, its solutions are of the form:

$$\Phi(r,\theta) = \sum_{l=0}^{\infty} \left[A_l r^l + \frac{B_l}{r^{l+1}} \right] P_l(\cos\theta), \tag{4.28}$$

where A_l and B_l are parameters to be determined by the boundary conditions of the problem, and P_l indicates the l^{th} order Legendre polynomial.

There are two boundary conditions that apply to this problem. First, the *tangential* electric fields at the particle surface must be continuous:

$$\left[\frac{\partial \Phi_1}{\partial \theta} \right]_{r=a} = \left[\frac{\partial \Phi_2}{\partial \theta} \right]_{r=a}, \tag{4.29}$$

where Φ_1 and Φ_2 indicate the potential *inside* and *outside* the sphere, respectively.

Furthermore, the *normal* component of the electric displacement must be continuous as well:

$$\epsilon_m \left[\frac{\partial \Phi_1}{\partial r} \right]_{r=a} = \epsilon_e \left[\frac{\partial \Phi_2}{\partial r} \right]_{r=a}. \tag{4.30}$$

Evaluation of these boundary conditions, in combination with the assumption that the incoming electric field is static (Eq. 4.25), leads to:

$$\Phi_1 = -E_0 \frac{3\epsilon_e}{\epsilon_m + 2\epsilon_e} r \cos\theta, \tag{4.31}$$

$$\Phi_2 = -E_0 r \cos\theta + E_0 \frac{\epsilon_m - \epsilon_e}{\epsilon_d + 2\epsilon_e} a^3 \frac{\cos\theta}{r^2}. \tag{4.32}$$

The potential outside the sphere is composed of the potentials of the incoming field and the field scattered by the particle, so that $\Phi_2 = \Phi_0 + \Phi_{\text{scatt}}$. The second part of Equation 4.32 is thus Φ_{scatt}. This can also be expressed as a dipole, located in the center of the particle:

$$\Phi_{\text{scatt}} = \frac{\boldsymbol{p} \cdot \boldsymbol{r}}{4\pi\epsilon_0\epsilon_e r^3}, \tag{4.33}$$

where $\boldsymbol{p}$ is the dipole moment:

$$\boldsymbol{p} = 4\pi\epsilon_0\epsilon_e a^3 \frac{\epsilon_m - \epsilon_e}{\epsilon_m + 2\epsilon_e} \boldsymbol{E}_0. \tag{4.34}$$

In other words, the external electric field $\boldsymbol{E}_0$ induces a dipole moment in the nanoparticle, with a magnitude proportional to $|\boldsymbol{E}_0|$.

The next step is to introduce the *polarizability*, which links the dipole moment to the applied field. This polarizability $\alpha(\omega)$ is defined via:

$$\boldsymbol{p} = \epsilon_0\epsilon_e\alpha(\omega)\boldsymbol{E}_0, \tag{4.35}$$

which means that it can be expressed as:

$$\alpha(\omega) = 4\pi a^3 \frac{\epsilon_m(\omega) - \epsilon_e}{\epsilon_m(\omega) + 2\epsilon_e}. \tag{4.36}$$

Here, we have reintroduced the energy (wavelength) dependence to show that the dielectric function of the metal particle, ϵ_m, governs the wavelength-dependent behavior of the polarizability.

From the potentials (Eqs. 4.31 and 4.32), the electric fields inside and outside the particle can be evaluated using Equation 4.26. This yields:

$$\boldsymbol{E}_1 = E_0 \frac{3\epsilon_e}{\epsilon_m + 2\epsilon_e} r \cos\theta \boldsymbol{n}_r \tag{4.37}$$

and

$$\boldsymbol{E}_2 = \boldsymbol{E}_0 + \frac{\epsilon_m(\omega) - \epsilon_e}{\epsilon_m(\omega) + 2\epsilon_e} \frac{a^3}{r^3} E_0 (2\cos\theta \boldsymbol{n}_r + \sin\theta \boldsymbol{n}_\theta), \tag{4.38}$$

with $\boldsymbol{n}_r$ and $\boldsymbol{n}_\theta$ the unit vectors along the radial and polar direction, respectively.

Interestingly, Eq. 4.37 implies that the electric field inside the nanosphere is homogeneous. This is an unexpected result, as the electric field is expected to decay exponentially into a metal. This identifies the limits of the QSA model, which is only valid for particles smaller than the skin depth of the metal. In the visible wavelength range, the QSA is usually a valid approximation for $a < 100$ nm.

For convenience, the electric field can also be written in terms of the polarizability (Eq. 4.36). The absolute value of the electric field, $|\boldsymbol{E}|$, then reads:

$$|\boldsymbol{E}(\omega, r, \theta)| = \begin{cases} E_0 \frac{3\epsilon_e}{\epsilon_m + 2\epsilon_e} & r \leq a \\ E_0 \left(1 + \frac{\alpha(\omega)}{4\pi r^3} \sqrt{3\cos^2\theta + 1}\right) & r > a \end{cases} \tag{4.39}$$

Figure 4.3 shows the enhancement of the electric field, $|\boldsymbol{E}|/|\boldsymbol{E}_0|$, in and around a gold sphere, according to Eq. 4.39 and using the experimentally determined dielectric function displayed in Fig. 4.1. The particle diameter is arbitrary, since the shape of the field distribution scales with a, as Eq. 4.38 shows. In particles small enough for the quasi-static approximation to be valid, the maximum enhancement of the electric field is thus size-independent. The distribution of the electric field around the particle highlights its dipolar character. The zones of strongly enhanced electric field, which is highest around the particle 'poles', are also known as *hotspots*. These can be understood via the accumulation of charges on either side of the particle, caused by the collective oscillation of the free electron cloud.

The field distribution plots furthermore indicate a resonant behavior of this enhancement: at 550 nm, a much stronger field enhancement is obtained than at higher as well as lower wavelengths. Indeed, from the shape of the polarizability α (Eq. 4.36), it is clear that a resonance must occur if the absolute value of $\epsilon_m(\omega) + 2\epsilon_e$ reaches a minimum. Assuming that

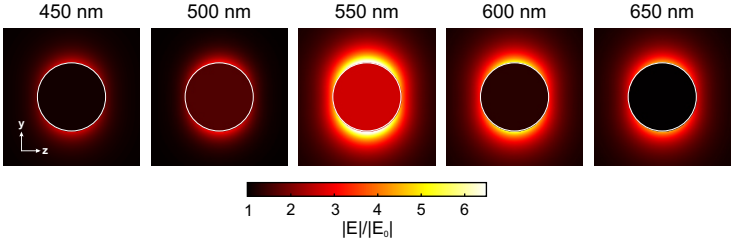

FIGURE 4.3. Calculated electric field enhancement $|\boldsymbol{E}|/|\boldsymbol{E}_0|$ in the quasi-static limit in and around a gold nanoparticle of arbitrary size, embedded in an environment with refractive index 1.5, for different wavelengths. The field is evaluated at $y = 0$. The exciting electromagnetic field propagates in the z-direction. Note that the color scale is clipped at 1; the field enhancement inside the sphere is lower than 1 for wavelengths away from the resonance.

the imaginary part of ϵ_m is small or only slowly varying in the wavelength range around the resonance, the resonant condition can thus be expressed as:

$$\mathrm{Re}\left[\epsilon_m(\omega)\right] = -2\epsilon_e, \tag{4.40}$$

which is known as the *Fröhlich condition*.

If we now consider the typical shape of ϵ for a metal according to the Drude-Sommerfeld model (Section 4.1.1), we obtain a fundamental understanding of the localized surface plasmon resonance and its dependence on both the dielectric field of the metal and of the environment. The exact shape of $|\mathrm{Re}(\epsilon_m)|$ (also termed ϵ_1) determines the resonance wavelength for a given ϵ_e. Since ϵ_1 is increasing for higher wavelengths, an increase of ϵ_e leads to a redshift of the resonance condition and thus of the wavelength at which the strongest electric field enhancement occurs. The imaginary part of ϵ_m can furthermore be understood as a damping term, since it prevents the denominator of $\alpha(\omega)$ from fully vanishing. A method of quantifying the efficiency of a material for plasmonic near-field enhancement, based on the reasoning of the quasi-static approximation model, can be found in Ref. [20].

The local electric field enhancement of a plasmonic nanoparticle is one of the main factors that drive the scientific interest in plasmonics, especially because of its nanoscale confinement and sensitive dependency on the environment. This has, for example, been applied to efficiently couple individual quantum emitters to plasmonic antennas [21–23] and to detect

changes in the direct environment of a nanoantenna [24, 25]. A wealth of different nanostructures have been brought forward to optimize the maximum obtainable field enhancement, including gap antennas and more complex geometries [26]. In these cases, more advanced numerical calculation methods, such as finite element (FEM) simulations, can be used to model the electric field distribution, as we will see in later chapters.

The work in this thesis, however, is not directly concerned with the *near-field* response of plasmonic nanostructures, but rather with the *far-field* response, the two of which are of course intertwined.

4.2.2 *Far-field response*

The far-field response of a plasmonic nanoantenna is dominated by two effects, namely light absorption and light scattering. These are the two processes that 'remove' power from a beam of light passing through the antenna. If one measures the transmittance of a sample containing plasmonic antennas, one thus sees the effect of both processes as a decreased intensity. By measuring the scattered intensity of a single particle, as described in Section 3.3.2, one only sees the effect of light scattering.

Both processes can be quantified via the *scattering cross-section* and the *absorption cross-section* of an individual particle. The scattering cross-section σ_{scatt} is defined as the ratio of power scattered by the particle over the intensity of the exciting light, and is thus expressed in units of area (hence the name). In the quasi-static approximation, this follows from the total power radiated by the sphere's point dipole, a theoretical description of which can be found in, e.g., Ref. [14]. This results in:

$$\sigma_{\text{scatt}} = \frac{k^4}{6\pi\epsilon_0^2}|\alpha(\omega)|^2, \tag{4.41}$$

with k the wavevector in the surrounding medium ($k = 2\pi/\lambda$). Similarly, the absorption cross-section can be determined from the power dissipated by the dipole:

$$\sigma_{\text{abs}} = \frac{k}{\epsilon_0^2}\text{Im}[\alpha(\omega)]. \tag{4.42}$$

The sum of these two cross-sections, which gives the total amount of power removed, is termed the *extinction cross-section*:

$$\sigma_{\text{ext}} = \sigma_{\text{scatt}} + \sigma_{\text{abs}}. \tag{4.43}$$

An interesting aspect is that σ_{ext} can easily be orders of magnitude *larger* than the geometrical cross-section of a particle. The polarizability α scales with the the third power of the particle radius (see Eq. 4.36), which means that σ_{abs} scales with a^3 and σ_{scatt} with a^6. This shows that a metal nanoparticle, especially around the resonant enhancement of α, can interact much more strongly with light in the far-field than a dielectric particle of similar size. Furthermore, the different dependencies on a show that as the particle size increases, σ_{scatt} quickly becomes much larger than σ_{abs}, and a single particle's optical response is thus governed by scattering.

Instead of the transmittance spectrum T of a sample of plasmonic antennas, as described in Section 3.3.1, it is customary to express the far-field response in terms of *extinction*:

$$\text{ext}(\lambda) = -\log_{10} T(\lambda). \tag{4.44}$$

This is often considered a more convenient representation, as it scales linearly with the extinction cross-section of a single particle, via the amount of particles through which the light passes.[3]

The dependence of σ_{ext} on α is resonantly enhanced along with the electric near-field. This shows that far-field optical measurements can in fact be used to determine the resonance wavelength(s). This is illustrated in Figure 4.4 for the case of silica-coated silver nanospheres dispersed in water. The extinction cross-section, which was determined from transmittance measurements in combination with the known optical path length and nanoparticle concentration, shows a clear extinction peak at around 470 nm, which is where the plasmon resonance occurs. In the far-field, this means that light in the lower-wavelength range is scattered, so that the transmitted light appears red.

In this section, we have thus seen how measurement of the optical far-field can give information about the plasmon resonance. As we have seen in Section 4.2.1, this resonance depends sensitively on the dielectric properties of a plasmonic nanoantenna as well as its surroundings. This means that far-field measurements can be used to investigate effects occuring in nanoscale volumes, much smaller than the diffraction limit (see Section 2.1.2). This can

3 The optical extinction is also termed the *optical density* or OD. This term is mostly used for measurements in which the path length of the medium through which the light travels is known, such as the solution-filled cuvette in Figure 4.4. For a single layer of nanoantennas on a substrate, it is a bit more problematic to determine this length. Another frequently used term is the *absorbance*. This term is somewhat misleading, since it appears to ignore the effects of scattering.

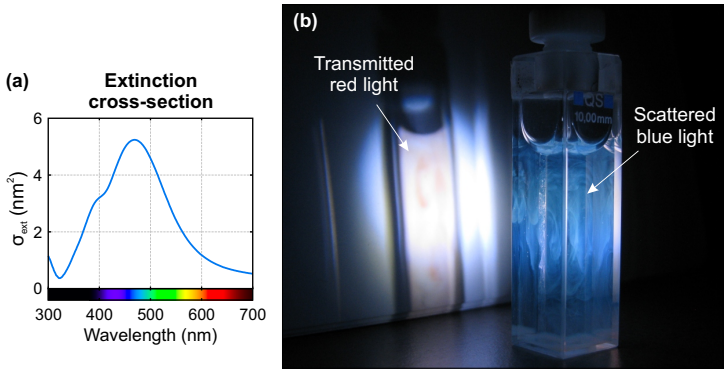

Figure 4.4. (a) Experimentally determined extinction cross-section of Ag nanospheres with a silica shell (Ag diameter 90 nm, shell thickness 22 nm) in water. (b) Photograph of a 10 mm quartz cuvette filled with water, just after dispersing a drop of concentrated solution with these particles. The cuvette is illuminated from the right by a white flashlight. Since the peak of the scattering cross-section lies in the blue part of the spectrum, the solution appears blue, and the transmitted light red. (Data and photograph were recorded as part of my Master's thesis; Ref. [27].)

be used in different ways for sensing purposes, as we will see in Chapter 8, but also for active tuning of the far-field response in *active plasmonics*, as Chapter 5 will show. Furthermore, we have only considered isolated particles so far. The arrangement of nanoparticles on a substrate can, however, have a significant influence on the far-field behavior of the full ensemble. Chapter 9 will study this in detail.

As a final remark on the subject, it is important to take into account exactly which quantity one is measuring in optical far-field measurements. For example, in bright-field measurements with a high NA (Section 2.2.1), the collected transmitted light automatically includes some scattered light as well. Similarly, the intensity measured using dark-field microscopy excludes all light scattered into angles outside the objective NA. It is consequently very difficult to determine the absorption cross-section of a nanostructure, for which both the transmittance and the scattering must be known exactly. These considerations are only important for the *exact* determination of quantities like the absorption and scattering cross-sections, and not for plasmonic sensing purposes or active plasmonics, but should nevertheless be mentioned.

4.3 NANOFABRICATION

As mentioned before, plasmonic nanoantennas come in a wide variety of shapes and sizes. Technological developments of recent decades have brought forward a wide variety of methods to fabricate metallic nanostructures. These include chemical synthesis of nanoparticles in solution (such as the example in Figure 4.4), but also different methods to fabricate a pattern of metallic nanostructures directly on a substrate. Some of these techniques are tailored for the fast and cost-effective patterning of large areas, such as nano-imprint lithography (NIL) and laser-interference lithography (LIL) (see, e.g., publications P7 and P9). Others are designed to fabricate individual nanostructures of any desired shape and size with nanometer accuracy, such as focused ion beam milling (FIB). This section describes the techniques used in this thesis, namely the large-area fabrication method of colloidal hole-mask lithography (and its derivative colloidal etching lithography) and the high-accuracy electron-beam lithography.

4.3.1 *Colloidal methods*

Colloidal nanopatterning methods exploit the pattern that is generated by polymer nanospheres, typically polystyrene (PS) beads, attached to a surface. Dropcoating a solution containing such spheres, which are chemically treated to have an electrostatic charge and thus repel each other, leads to a relatively uniform distribution of individual beads on the sample surface, which can be transferred into a pattern of metallic nanodisks.

Figure 4.5 illustrates the procedure of *colloidal hole-mask lithography*, which was first described by Fredriksson *et al.* [28]. This method was, for example, used in the work published in P1 (Chapter 5). The procedure consist of the following steps:

1. The substrate is cleaned, typically using acetone in an ultrasonic bath, and spincoated with a layer of PMMA (poly(methyl methacrylate)) solution.

2. The sample is baked on a hotplate to evaporate the solvent, which yields a uniform layer of hardened PMMA, with a typical thickness of around 200 nm.

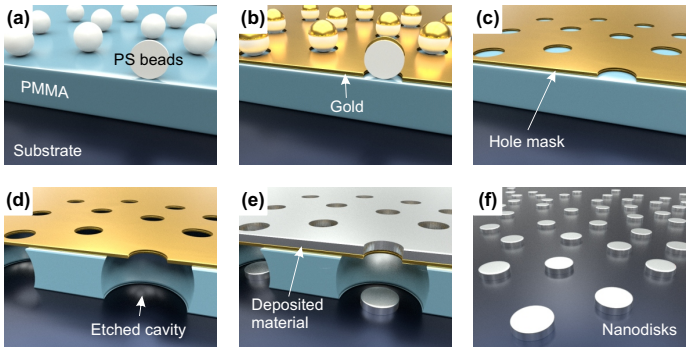

Figure 4.5. Illustration of colloidal hole-mask lithography. The substrate is covered with PMMA and a layer of PS beads (a). The sample is covered with a thin gold layer (b), after which the beads are removed to produce a hole mask (c). The PMMA below the mask is etched away (d), after which the desired material is deposited onto the sample (e). PMMA lift-off removes the mask and leaves only the nanostructures (f).

3. The PMMA surface is hydrophilized by a short O_2 plasma exposure, followed by dropcoating with a layer of PDDA (polydiallyldimethylammonium chloride). The hydrophilization ensures good wetting and thus a good surface coverage.

4. The sample is dropcoated with a layer of PS (polystyrene) nanobeads of the desired diameter (Fig. 4.5(a)). The cathodic character of the PDDA binds the anionic PS beads. The repelling electrostatic charge of the beads, in combination with the concentration of the beads solution, determines the density of the beads on the sample.

5. The sample with the beads is covered with a thin (typically 20 nm) layer of gold (Fig. 4.5). This can happen either via thermal evaporation or via e-beam evaporation. It is important that the evaporated material hits the sample from one direction, so that no gold is deposited in the 'shadow' of the PS beads. Deposition by sputtering is thus not suitable.

6. The PS beads are removed from the sample by ultrasonicating. This can be aided by a solvent that attacks only the PS, and not the PMMA, such as cyclohexane. The pattern of the PS beads is thus transferred into a 'hole mask' pattern in the Au film (Fig. 4.5(c)).

7. The PMMA beneath the holes in the Au film is etched away via O_2 plasma ashing. This is an isotropic etching technique, meaning that the material is etched away in all directions, thus forming cavities (Fig. 4.5(d)). This underetching is important, since the material deposited through the holes should not cover the inner cavity walls. This step is critical: if the exposure to O_2 plasma is too short, the cavity does not reach the substrate. If it is too long, the cavities beneath different holes might expand too much and interconnect, leading to the film collapsing onto the substrate and the sample becoming unusable.
8. The desired material is deposited onto the sample (Fig. 4.5(e)). Again, a directional thin-film deposition technique must be used. Several materials can be deposited in sequence to produce a stacked structure. For taller structures, the holes tend to become smaller with more evaporated material, so that the nanostructures become cone-shaped [29].
9. If desired, the sample can be tilted in between different evaporation steps, to produce connected nanodisks of different materials. Another option is to rotate the sample during evaporation to produce more complex shapes [30].
10. In a last step, lift-off is performed by dissolving the PMMA layer and thus removing the hole mask. The dissolution can be done in, e.g., acetone or NEP (ethyl pyrrolidone). After this, only the nanostructures deposited through the hole mask are left (Fig. 4.5(f)).

Since in this method the nanostructures are deposited through a mask followed by lift-off, it is a *bottom-up* nanofabrication method. An equivalent *top-down* nanofabrication method exists as well, which is termed *colloidal etching lithography*. This method was demonstrated in publication P6 and used in, e.g., publications P11 and P15. In this method, the pattern of the PS beads is directly transferred into the metallic film:

1. A cleaned substrate is covered with a thin film of the desired material (or, again, a stack of materials).
2. This film is covered by PS beads as described above (steps 3,4).
3. The PS beads are used as an etching mask in a reactive ion beam etching (RIBE) step, in which the sample is bombarded with argon ions. This removes all material around the PS beads, leaving nanodisks. The etching time is critical in this step: A too short etching time is not sufficient to reach the bottom of the film, while a too long etching time can attack the substrate beneath and lead to the formation of nanopillars. This might, of course, also be a desired effect.

4. Lift-off of the PS beads is performed by O_2 plasma ashing. Lift-off in cyclohexane does not work well, since the PS surface is contaminated with redeposited material during the Ar etching step.

These two methods produce nanostructure patterns of very similar character. Which method is most suitable strongly depends on the materials involved. For example, while colloidal etching lithography follows a simpler procedure, it is only possible if the nanostructure material is not affected by the PS bead liftoff process and/or the Ar ion beam etching step.

4.3.2 *Electron-beam lithography*

Colloidal fabrication methods as described in the previous section are a proven way of fabricating uniformly distributed nanostructures over large areas at relatively low cost. However, these methods do not allow much freedom in the arrangement, size, and shape of the individual structures. In many cases, however, nanostructures of tailored shapes and sizes and in specific arrangement are desired. Moreover, it is very often useful to fabricate different types of structures on the same substrate to perform parameter studies. In this work, the dedicated technique of electron-beam (e-beam) lithography was used, in which a focused electron beam generates a predefined pattern in a layer of photoresist. This was employed in the work published in P3 (Chapter 8) and shown in Chapters 6 and 9. The method consists of the following steps, as illustrated in Figure 4.6:

1. A cleaned sample is spincoated with PMMA, which acts as the photoresist. In contrast to colloidal hole-mask lithography, two PMMA layers are used (Fig. 4.6(a)). The bottom layer consists of PMMA with a shorter chain length than the upper layer, leading to a higher electron sensitivity. The first layer is baked before dropcoating the second layer, to prevent intermixing of both layers.

2. If the substrate is non-conducting, the photoresist is spincoated with a layer of so-called 'e-spacer' solution, which leads to a thin conductive layer on top.

3. The sample is mounted in the electron beam lithography device (for this work, a Raith Nanofabrication eLINE Plus was used). The sample is aligned to the focus of the electron beam, similar to the operation of a scanning electron microscope (SEM).

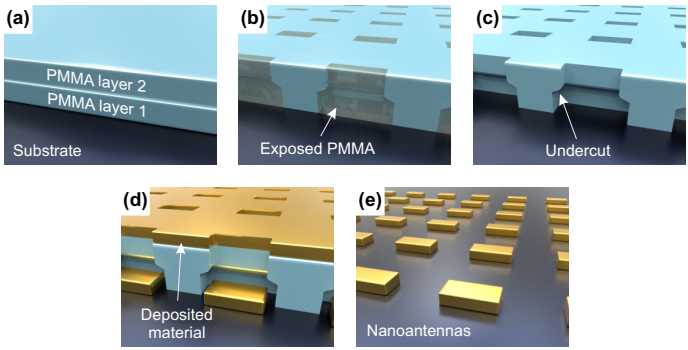

Figure 4.6. Illustration of electron-beam lithography nanofabrication. A substrate is spincoated with two layers of PMMA with different electron sensitivities (a). The photoresist is exposed to a focused electron beam in a predefined pattern (b). After developing, this pattern remains in the PMMA, including an undercut caused by the difference in sensitivity (c). After directional deposition (d) and resist lift-off, the nanostructures remain (e). This procedure can be repeated to fabricate structures of different materials on the same substrate.

4. The predefined nanostructure pattern is transferred into the resist by the electron beam, which is raster scanned across the sample. The PMMA exposed to the beam degrades, changing its solubility (Fig. 4.5(b)). The exact electron dose and the dwell time per pixel are critical parameters, which depend on the used substrate.

5. The area on the sample that can be patterned without moving the sample is called a *writefield*, and is typically in the order of 100×100 μm^2. For patterning another writefield, the sample is moved. This can lead to small alignment errors for structures spanning several writefields.

6. The exposed photoresist is developed by immersion in MIBK (methyl isobutyl ketone) diluted in isopropanol, which removes the exposed resist. The higher electron sensitivity of the bottom layer leads to a pronounced undercut (Fig. 4.6(c)).

7. The desired material (or stack of materials) is deposited using a directional deposition technique (Fig. 4.6(d)).

8. Similar to colloidal hole-mask lithography, the photoresist is removed in a last lift-off step.

This whole procedure can be repeated any number of times on the same substrate, in case nanostructures of different materials and/or thicknesses are desired on the same sample. In this case, the first patterning step must include a set of alignment markers, which can be used in the subsequent steps to correctly align the coordinate system for patterning. This was used, for example, in the work published in P2 (Chapter 7) and P8.

The procedure described above uses a *positive* photoresist, meaning that the exposed areas are removed. It thus also constitutes a bottom-up nanofabrication technique. E-beam lithography can, however, also be employed for top-down fabrication, similar to colloidal etching lithography. In this case, a *negative* photoresist is used. In publication P12, a dedicated electron-beam-based technique for the fabrication of copper nanoslits was demonstrated.

5

MAGNESIUM PLASMONICS

Investigating new materials plays an important role for advancing the field of nanoplasmonics. This chapter shows the tuning of the plasmon resonance of magnesium (Mg) nanodisks throughout the whole visible wavelength range. Furthermore, a catalytic palladium (Pd) cap layer is employed to transform the metallic Mg particles into dielectric MgH_2 particles when exposed to hydrogen gas (H_2). This transition can be reversed in the presence of oxygen. This yields plasmonic nanostructures with an extinction spectrum that can be repeatedly switched on or off, or kept at any intermediate state, offering new perspectives for active plasmonic metamaterials. This chapter is mostly based on publication P1:

F. Sterl, N. Strohfeldt, R. Walter, R. Griessen, A. Tittl, and H. Giessen, "**Magnesium as Novel Material for Active Plasmonics in the Visible Wavelength Range**", *Nano Letters* **15**(12), 7949-7955 (2015), DOI 10.1021/acs.nanolett.5b03029.

5.1 INTRODUCTION

In recent years, the field of plasmonics has become an important driving force for progress in the area of nanophotonics. Building on initial applications in chemical and biological sensing devices [24, 31], there has been an increased focus on active plasmonics [32]. Here, metamaterial structures can be actively reconfigured via temperature change [33], mechanical stress [34], optically [35], electrically [36], or electrochemically [37] (see also publication P12). This promises interesting applications in, for example, all-optical

data network switches [38] and smart solar [39]. A previously demonstrated approach for realizing reconfigurable metamaterials is via the absorption of hydrogen, which was realized for yttrium (Y) [40] and palladium (Pd) [41, 42] nanoparticles.

One particularly interesting metal for plasmonic applications is magnesium (Mg). Mg has several very promising properties for applications in plasmonics in general and switchable plasmonic metamaterials in particular. As mentioned by Sanz *et al.* [43], Mg nanoparticles support localized surface plasmon resonances at wavelengths down to the ultraviolet. Thus, Mg constitutes an ideal alternative to established materials for UV plasmonics such as aluminum [44], providing higher extinction efficiencies in the same wavelength range. This indicates that via adequate tuning of the particle size, resonances throughout the visible spectrum can be obtained.

Figures 5.1(a,b) display the dielectric function of magnesium, obtained from the works of Palik [18], Appusamy *et al.* [45], and (more recently) Palm *et al.* [46]. These data indicate that the dielectric function of Mg is

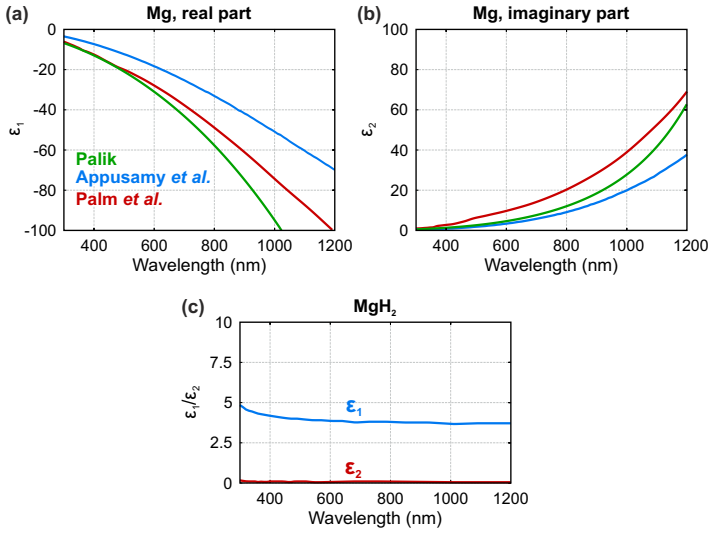

Figure 5.1. Real (a) and imaginary part (b) of the dielectric function of magnesium, obtained from the works of Palik [18], Appusamy *et al.* [45], and Palm *et al.* [46]. (c) Real and imaginary part of the dielectric function of magnesium hydride (MgH_2), obtained from Isidorsson *et al.* [47].

similar to that of other plasmonic materials such as Al. The difference between the data from different sources can be attributed to differences in the measured systems, most notably the substrate supporting the Mg films and the use of additional wetting/sticking layers and resulting differences in film morphology. This will be addressed in more detail in Chapter 6. Apart from its optical properties, magnesium has been widely investigated for applications in a different context, namely the field of solid-state hydrogen storage. Mg is known to be able to absorb up to 7.6 wt.% of hydrogen gas [48], making it one of the most promising candidates for hydrogen storage in the advent of a hydrogen economy [49, 50]. Upon absorption of hydrogen gas, the metallic magnesium changes into dielectric magnesium hydride (MgH_2). The dielectric function of MgH_2, as measured by Isidorsson *et al.* [47], is shown in Figure 5.1(c). One issue associated with magnesium, however, is the high thermodynamic stability of MgH_2 and the relatively slow hydrogen diffusion at room temperature. In order to address these challenges, several solutions have been proposed, including the fabrication of various Mg-based alloys [51, 52] the addition of different catalysts [53–55], and the use of nanocrystalline magnesium [48, 56].

In this chapter, we demonstrate that magnesium nanoparticles exhibit a pronounced plasmonic response that is tunable throughout the whole visible wavelength range. The plasmon resonance vanishes upon exposure to hydrogen gas at room temperature if a catalytic layer of palladium (Pd) is added on top of the Mg layer. This happens because the dielectric MgH_2, into which the Mg is transformed, does not support plasmonic resonances. This Pd caplayer technique has previously been applied to magnesium films [57–60] as well as small Mg nanoparticles, allowing for the observation of hydride formation via indirect nanoplasmonic sensing [25]. In publication P1, we showed for the first time that the hydriding process of Mg nanoparticles can be reversed by exposure to oxygen, upon which the MgH_2 dehydrogenates and returns to its metallic Mg state. This process can be repeated over multiple cycles without significant degradation and with hydrogen loading/unloading times in the order of minutes at room temperature.

5.2 EXPERIMENTAL SECTION

5.2.1 *Fabrication of Mg nanoparticles*

To investigate the plasmonic properties of magnesium nanostructures, we fabricated Mg nanodisks of different sizes using colloidal hole-mask lithography (see Section 4.3.1) and subsequent electron-beam evaporation. This low-cost method provides large-area samples of randomly distributed and

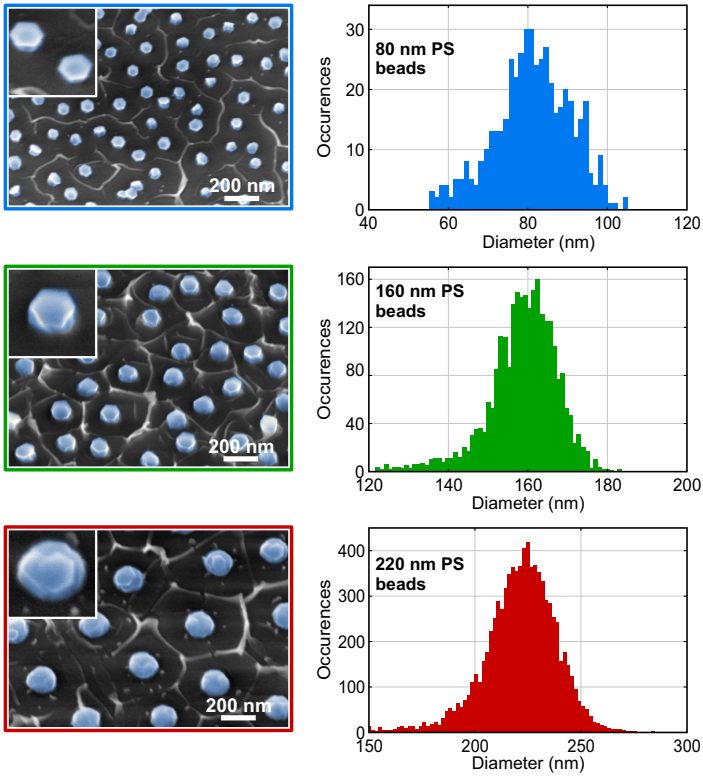

FIGURE 5.2. Size distribution histograms for typical large-area nanodisk samples fabricated by colloidal hole-mask lithography using polystyrene (PS) beads of 80, 160, and 220 nm, respectively. The histograms are obtained by using large overview SEM micrographs and a custom script, which uses the MATLAB circle finder algorithm.

well-separated nanodisks with a relatively narrow size distribution, avoiding any lattice effects in the extinction spectra. The method can easily be extended to obtain more complex nanostructure geometries such as plasmonic perfect absorbers (see, for example, Ref. [61] and publication P6). Nanodisk samples with average diameters of approximately 80, 160, and 220 nm were obtained, with a typical Mg thickness of 80 nm. Figure 5.2 shows exemplary SEM images of the nanostructures obtained in this way, alongside size histograms showing the distribution of diameters of the particles. The size distribution histograms were obtained from high-resolution, large-area SEM micrographs of each sample.

5.2.2 *Extinction measurements*

Figure 5.3 shows the measured extinction spectra of Mg nanodisks on a glass substrate. The optical extinction was calculated from ensemble transmittance measurements (see Section 4.2.2). The measurements were performed using a fiber-coupled halogen light source and a Nikon Eclipse te2000-u inverse microscope in bright-field illumination mode with a fiber-coupled halogen light source, combined with a Princeton Instruments sp2500 grating spectrometer and a pixis-256e 2D CCD detector (see Section 3.3.1). Unpolarized illumination was used, since the structures are rotationally symmetric and randomly arranged.

It should be noted that the number of nanodisks contributing to each measured spectrum, and thus the absolute measured extinction value, differs from sample to sample, as the density of particles varies strongly with the used PS beads (as well as between individual fabrication runs). The obtained extinction spectra are thus labeled in arbitrary units.

The measurement results displayed in Figure 5.3 demonstrate that the plasmonic response of Mg nanodisks can be tuned throughout the visible wavelength range by adequate choice of the disk diameter, from resonance wavelengths below 500 nm up to 800 nm and further into the near-infrared. Furthermore, the SEM micrographs in Figure 5.2 indicate that the magnesium nanoparticles take on a hexagonal mono-crystalline shape at relatively small sizes (Figures 5.3(a,b)) and tend to form polycrystalline particles when the particle size increases (Figure 5.3(c)). This is consistent with findings in earlier studies on sputtered magnesium films, which show that these films consist of crystalline grains with sizes in the order of 100-200 nm, with a dominating (0002) orientation perpendicular to the substrate [45].

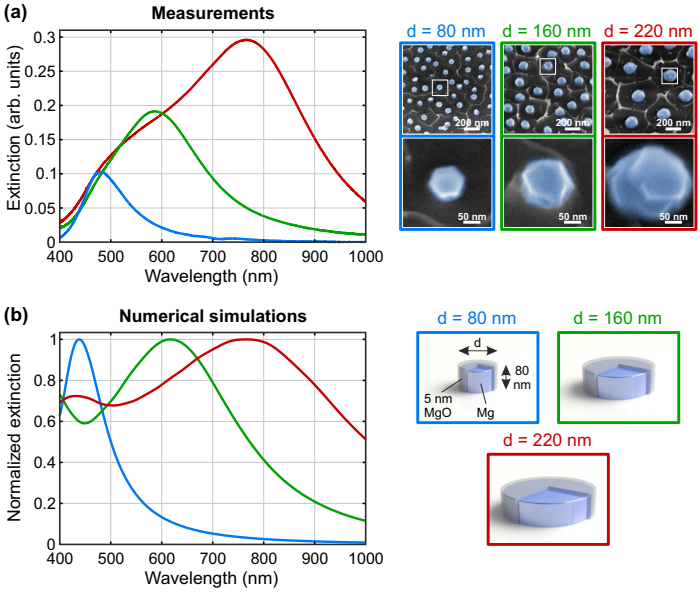

Figure 5.3. Magnesium nanodisks as a model system for magnesium plasmonics. (a) The resonance wavelength of such nanodisks can be tuned throughout the visible wavelength range by varying the diameter. The smaller particles (average diameter 80 and 160 nm) appear to be monocrystalline, while the particles with an average diameter of 220 nm appear to take on a polycrystalline shape. (b) Extinction spectra obtained from numerical (FDTD) simulations on cylindrical Mg particles with different diameters, encapsulated in a 5 nm thick layer of magnesium oxide (MgO), and placed on a SiO_2 substrate.

To validate the measured spectra of Mg disks, we use numerical FDTD (finite difference time domain) based calculations on a system consisting of a single cylindrical Mg particle on a glass substrate. The calculations were performed in Lumerical FDTD solutions. To accommodate for the degradation of magnesium after removal of the sample from the evaporation chamber [62], a 5 nm thick layer of magnesium oxide (MgO) is assumed on the surface of the nanoparticle. The dielectric data of magnesium are taken from the work of Palik [18]. The extinction spectra resulting from these simulations, for disks of the same diameters as the fabricated particles, are displayed in Figure 5.3(e). Surprisingly, the measured resonances turn out to be narrower than the simulations predict, especially for the 160 and 220 nm

particles. The resonance wavelengths, however, are in good agreement with the simulations. This outperformance of the measured particles compared to the simulations can possibly be attributed to the very high crystallinity of our nanodisks, whereas the dielectric data used in the simulations were obtained from measurements on extended, polycrystalline films.

5.2.3 *Chemical stability*

Magnesium is a comparatively reactive element, which can undergo several chemical reactions when exposed to ambient concentrations of different gaseous environments. Most of these reactions produce relatively stable compounds and cannot be easily reversed to obtain pure magnesium again. Consequently, Mg nanoparticles are subject to degradation when exposed to air after they are removed from the vacuum of the evaporation chamber. As it turns out, the plasmon resonance of Mg disks, when exposed to air at room temperature, slowly shifts into the red by approximately 10-20 nm while slightly increasing in extinction. This behavior can be attributed to the high refractive index of a slowly growing outer layer of corrosion products. This shift takes place over the course of days, after which it saturates and the particles can remain stable over several months. This is shown in the extinction spectra in Figure 5.4, which were obtained from the same sample, directly after sample fabrication and after four months. If the sample is exposed to an atmosphere of pure oxygen, however, no resonance shift is measured at all. This is consistent with previous studies on the oxidation of Mg films, which show that a layer of MgO with a thickness of several nm is formed on the Mg surface, which then self-terminates by preventing the underlying material from further oxidation [63–65]. This is similar to the oxidation of aluminum [66]. However, in a humid environment, this oxide surface can become hydroxilated and form ($Mg(OH)_2$), also called brucite [67]. Ambient concentrations of CO_2 also contribute to the degradation of the Mg particles, forming a magnesium hydroxy carbonate on the surface [68]. In principle, such reactions could form the basis for magnesium-based nanoplasmonic sensors for different gases. Applications like this would, however, suffer from the chemical stability of magnesium-based compounds and the irreversibility of the associated chemical reactions, and thus only constitute a 'single-use' sensor.

As mentioned above, the chemical reaction of magnesium which is subject to most extensive investigation is the absorption of hydrogen, which yields magnesium hydride (MgH_2). The high hydrogen content of MgH_2 is the

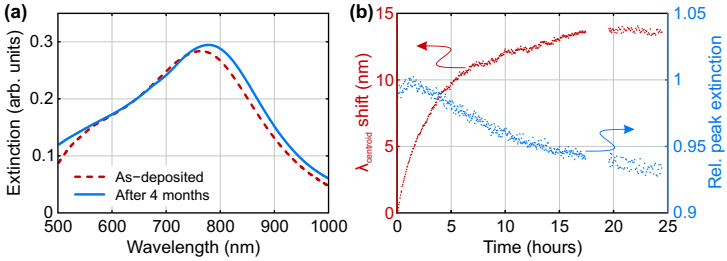

Figure 5.4. Pure Mg particles are very stable when stored in an environment with a relatively low humidity. (a) Extinction spectrum of a Mg nanodisk sample with an average diameter of 220 nm directly after evaporation and after a period of four months. (b) Shift of centroid wavelength [69] and relative peak extinction for a Mg nanoparticle sample exposed to laboratory air. Over the course of several hours, the resonance shifts into the red spectral range and the peak extinction slightly decreases, after which the shift saturates and the particles remain stable. To prevent this, a capping layer (consisting of, e.g., MgF_2, SiO_2, or Al_2O_3) could encapsulate the Mg nanoparticles.

major reason for the long-lasting interest in Mg as a hydrogen storage medium. Simply exposing the particles to an ambient concentration of H_2 gas is, however, not sufficient to induce this reaction: the hydride formation in bulk Mg only takes place at temperatures of several hundred degrees Celsius and pressures of tens of atmospheres [48, 49, 56], and even then it takes several hours. The dehydrogenation of magnesium hydride requires even higher temperatures [70]. Due to the relatively low melting point of bulk Mg (923 K) [71], such temperatures would threaten the stability of nanostructured magnesium.

The main limiting factor in these reactions is the impossibility of absorption of molecular hydrogen, which requires a means of splitting the hydrogen molecules at the surface of the nanodisk. To circumvent this problem, the use of several catalysts (which aid the dissociation of molecular hydrogen into single hydrogen atoms) has been investigated. Most importantly, many studies have been performed on the hydrogenation of extended Mg films with the aid of a thin catalytic layer of palladium (Pd) [47, 58, 59, 72, 73].

5.3 ACTIVE PLASMONICS

Palladium nanoparticles, which are also able to sustain plasmonic resonances themselves, have previously been employed as plasmonic hydrogen sensors [41, 74], utilizing the transformation of palladium into palladium hydride (with a relative hydrogen content depending on the external hydrogen concentration), and the associated shift of the plasmonic resonance. We will see more about this subject in Chapter 8. The atomic hydrogen present in the palladium can be used to hydrogenate other materials, such as Mg. For this reason, we fabricated magnesium nanodisks with a 10 nm thick Pd layer on top. As shown by Baldi *et al.* [58], simply capping the Mg with a Pd layer has the disadvantage that a Mg-Pd alloy is formed in the interfacial region, which significantly hinders the diffusion of hydrogen through the Mg/Pd interface into the Mg. This can be avoided by separating the Mg and Pd layers from each other by a layer of titanium (Ti) acting as a buffer layer. This buffer layer has two functions: not only does it prevent the Mg and Pd layers from alloying, but it also elastically decouples the two layers, releasing the mechanical stress induced when Mg and Pd expand laterally at different rates. Here, we used a Ti layer thickness of 5 nm. A slight drawback of the titanium layer is that it causes some damping of the plasmonic resonance of the Mg particle [75].

The switching dynamics of the palladium-capped magnesium nanodisks are investigated by placing the samples in a custom-built gas cell (see Section 3.2) in the microspectroscopy setup and continuously recording transmission spectra. The gas cell is continuously purged with N_2, to which H_2 and O_2 are added at predefined intervals, while keeping the total gas flow rate constant at a value of 1 nL/min (liter normal per minute). All measurements shown here were carried out at room temperature. Figure 5.5 provides a schematic overview of the different stages that are observed during such a cycle, along with the corresponding extinction spectra.

When the initial Mg/Ti/Pd particles (red curve in Figure 5.5(b)) are exposed to hydrogen gas (4 vol.% H_2 in N_2), the Pd layer catalyzes the splitting of the hydrogen molecules into atomic hydrogen, which easily diffuses into the titanium layer and further into the magnesium. This forms dielectric magnesium hydride MgH_2 (see Fig. 5.1). During hydrogenation Mg, Ti and Pd lattices expand by different factors (approximately 30%, 25% and 11%, respectively). The dielectric MgH_2 particles do not exhibit any plasmonic resonances (green curve). When the H_2 flow is switched off and the particles are exposed to pure N_2, the Pd dehydrogenates, inducing a small increase

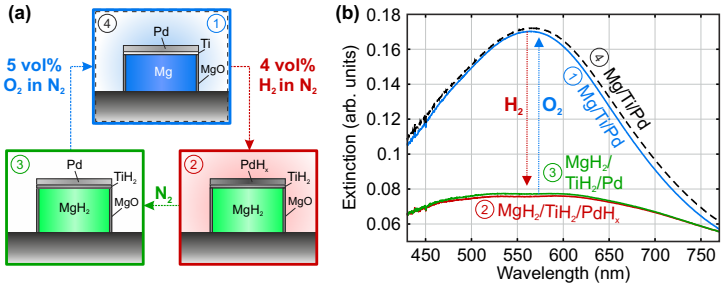

Figure 5.5. (a) Switching of magnesium particles to magnesium hydride and vice versa with the aid of a 10 nm catalytic Pd layer and a 5 nm Ti buffer. (b) Extinction spectra of 160 nm Mg/Ti/Pd particles (Mg thickness 80 nm) in the different stages of a typical hydrogenation/dehydrogenation cycle.

in extinction (blue curve). The pronounced resonance peak of magnesium does, however, not come back, indicating that the Mg layer remains in its hydrogenated state.

As it turns out, dehydrogenation of the MgH_2/Ti/Pd particles takes place in the presence of oxygen: when the gas flow cell is flooded with O_2 diluted in N_2, or even simply with dry air, the resonance is fully restored in tens of minutes, after which the cycle can start over. This oxidative dehydrogenation has been observed before in magnesium-based films [39, 73]. The peak optical extinction of the dehydrogenated system is slightly enhanced and redshifted after one gas cycle (see Figure 5.5(b)). This is likely due to cracking of the oxide shell around the Mg layer during hydrogenation, induced by the volume expansion of the Mg. Crack formation can cause some additional oxidation when the particles are exposed to O_2 for dehydrogenation. Our experiments indicate that the plasmon resonance can be reliably switched off and back on over 10 or more gas cycles without significant degradation.

5.3.1 *Time-resolved measurements*

To investigate the dynamics of the forth-and-back switching of Mg nanoparticles, we first focus on the changing extinction spectrum of disks of 220 nm in diameter with a Pd cap during a typical gas cycle measurement. We do this both for the case where the Ti buffer layer is present (Mg/Ti/Pd disks), and the case where the Pd is in direct contact with the Mg (Mg/Pd disks). Figure 5.6 presents color-coded plots in which the extinction spectrum on the

vertical wavelength axis is plotted as a function of time on the horizontal axis for both of these geometries. The measurements displayed here illustrate that the plasmon resonance of Mg/Ti/Pd disks can be switched off within a few minutes, while the dehydrogenation is completed in approximately 15 minutes.

The comparison of the measurements on Mg/Ti/Pd disks with the measurements on Mg/Pd disks elucidates the necessity of the Ti buffer layer.

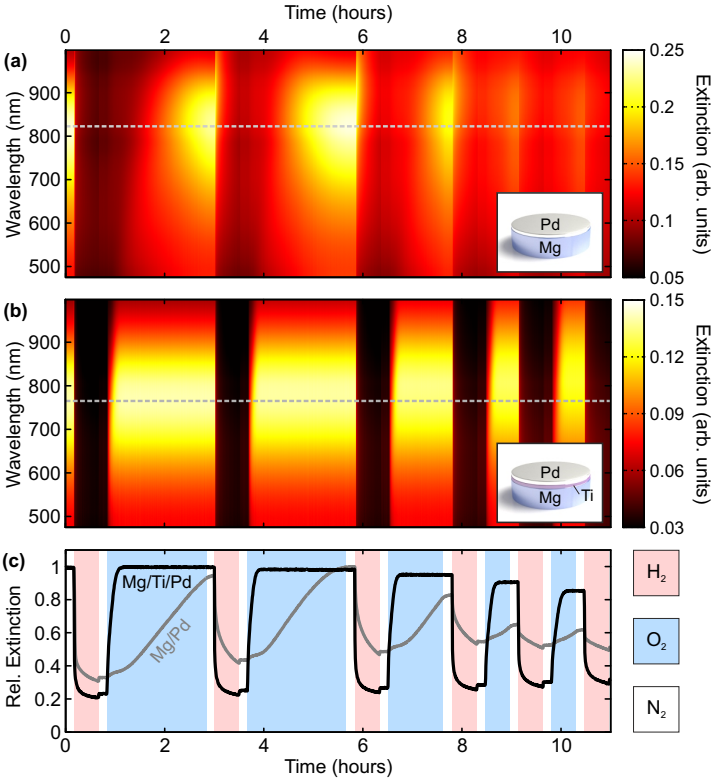

Figure 5.6. (a,b) Color-coded plots of extinction spectrum vs. time upon repeated hydrogen and oxygen exposure for magnesium-palladium disks (diameter 220 nm, thicknesses 80 and 10 nm) without and with an additional 5 nm titanium buffer layer. (c) Relative extinction at the spectral location of the initial peak (indicated by the dashed gray lines in (a) and (b)). Gray and black curves indicate the disks without and with the 5 nm Ti buffer, respectively.

In the absence of this layer, the dehydrogenation of the hydrogenated particles takes over two hours instead of only 15 minutes, while the rate of hydrogenation (as represented by the relative change in extinction at the original peak wavelength in Figure 5.6(c)) decreases from cycle to cycle. This indicates a severe degradation of the particles during one hydrogenation/dehydrogenation sequence, which can most likely be attributed to the alloying of magnesium and palladium and to mechanical stress caused by the lateral expansion of the two materials [25]. The influence of an Mg-Pd alloy layer on the hydrogen diffusion into and out of the Mg disk is supported

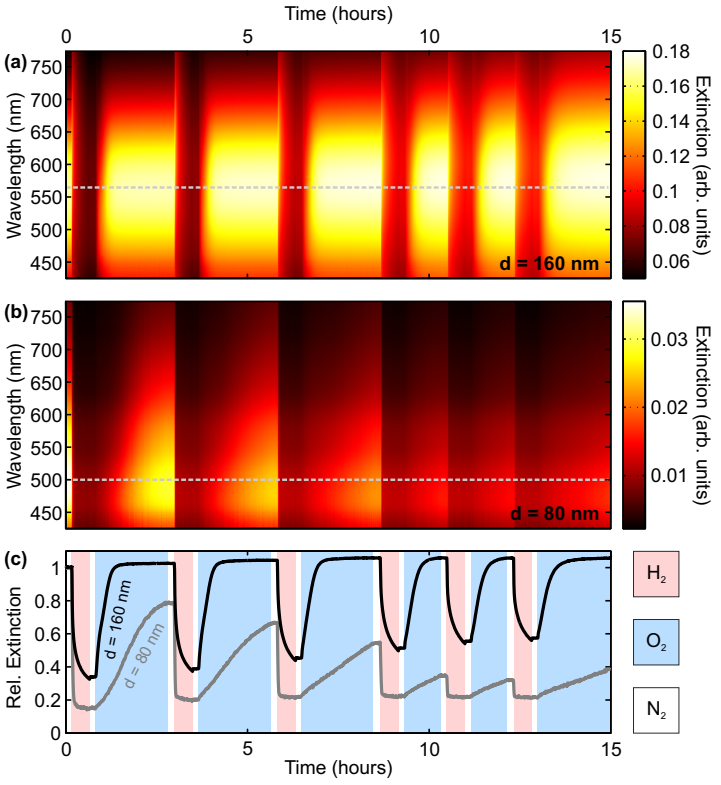

Figure 5.7. Color-coded plots, analogous to Figure 5.6, of extinction versus wavelength and time during repeated hydrogen and oxygen exposure for Mg/Ti/Pd disks with diameters of 160 nm (a) and 80 nm (b). The relative extinction at the initial peak wavelengths (560 and 500 nm, respectively) is plotted versus time in (c).

by one-dimensional numerical calculations of the diffusion dynamics of a multilayer system, as we will see in Section 5.4.

Furthermore, the data displayed in Figure 5.7 show that this behavior is reproducible for nanodisks of different diameters. Gas exposure measurements on an Mg/Ti/Pd nanodisk sample with a disk diameter of 160 nm (panel (a)) indicate that the switching times are in the same order as for the larger nanodisks. For a disk diameter of 80 nm, however, a significantly faster degradation can be observed, as the peak extinction reached after each subsequent cycle rapidly decreases. This is in part due to the increasing unloading time, which means that unloading is not complete at the end of the O_2 exposure.

Nevertheless, one very intriguing aspect of these switchable Mg nanodisks is the fact that both the hydrogenation and the dehydrogenation of magnesium are active processes: the plasmonic resonance can only be switched off by introducing ambient concentrations of hydrogen, and can only be switched back on by adding oxygen to the system. In an atmosphere of pure nitrogen, the state of the particles remains fixed. This behavior stands in stark contrast to the hydrogenation of other commonly used materials, such as yttrium [40] and palladium [42], which automatically release the stored hydrogen as soon as the hydrogen pressure in the environment drops. This makes it possible to keep Mg nanoparticles not only in their fully metallic or fully non-metallic state, but also at any state in between, where the Mg disk is only partially hydrogenated, simply by means of regulating the duration and concentration of H_2 and/or O_2 exposure.

5.3.2 *Switching characteristics*

A closer investigation of the spectral shift during hydrogenation and dehydrogenation of the magnesium nanodisks reveals a large hysteresis between the two switching directions. Figure 5.8 illustrates this for the example of nanodisks with an average diameter of 160 nm. As shown in Figure 5.8(a), the plasmon resonance undergoes a rapid decrease while redshifting over more than 50 nm, after which the peak position slowly blueshifts while decreasing further in intensity. During dehydrogenation (Figure 5.8(b)), the plasmonic resonance follows a completely different pathway: it re-emerges at a wavelength which is blueshifted with respect to the original peak, and returns to its initial position and intensity via a gradual redshift. This behavior occurs for all measured particle sizes and is not limited to the first hydrogenation/dehydrogenation cycle, but appears reproducibly over

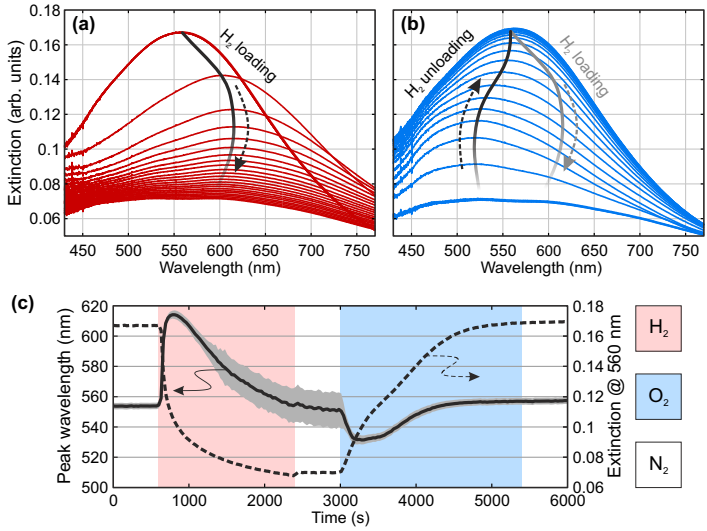

Figure 5.8. Hysteresis between hydrogen loading and unloading of Mg/Ti/Pd nanodisks (diameter 160 nm) at room temperature. (a) During hydrogenation, the plasmonic resonance shifts into the red while decreasing in intensity, followed by a slight blueshift before completely vanishing. The black curve indicates the trajectory of the extinction peak over time. (b) During dehydrogenation, the peak re-emerges at a lower wavelength, followed by a constant redshift until the original spectrum is restored, thereby following another trajectory than during hydrogenation. (c) Plot of the resonance wavelength over time (solid curve) along with the extinction measured at the original peak wavelength (560 nm; dashed curve). As the plasmon resonance is disappearing, the accuracy of the peak detection decreases (grey area).

several gas cycles (see Figures 5.6 and 5.7). The hysteresis, which is more pronounced in the resonance position than in the peak extinction value, becomes evident if one tracks the resonance wavelength of the plasmon peak over time alongside the extinction value at the original peak position (see Figure 5.8(c)). The resonance wavelength (solid curve) is obtained by fitting a Lorentzian function to the measured spectrum, with an estimated error (gray area) of 0.2% of the linewidth of the Lorentzian. The measured extinction at 560 nm is displayed as a dashed line.

A possible explanation for this pronounced hysteresis behavior can be found in differences of the Mg/Ti/Pd particle geometry and hydrogen concentration between hydrogenation and dehydrogenation. Specifically, the

position, shape, and propagation direction of the Mg/MgH_2 interface will play a significant role for the optical response of the full particle. In a simple model, a layer of MgH_2 can be assumed to form directly beneath the hydrogenated Ti layer [59] during hydrogenation, after which it expands towards the substrate while 'consuming' the Mg particle. This is supported by the observation of an initial resonance redshift, which can be explained by an effective decrease of the thickness of the metallic Mg disk. During dehydrogenation, the lower wavelength at which the plasmon resonance emerges suggests that the magnesium layer that forms inside the MgH_2 particle grows faster in the vertical direction, after which it expands from the inside outwards before returning to its original shape. However, in a realistic system, the phase change behavior will be influenced by additional effects, such as localized strain due to different hydrogen-induced lattice expansions for Mg, Ti, and Pd. The resulting elastic constraints between the constituent materials and the forces exerted on the entire particle by the surrounding passivating MgO layer also influence its geometrical shape and thus its extinction spectrum.

In conclusion, a more thorough investigation of this complex nanoscale system will be necessary to provide more conclusive insights into the detailed hydrogenation dynamics of Mg nanostructures. In Chapters 6 and 7, we will look at the H_2 diffusion mechanism in more detail.

5.4 MODELING OF THE H_2 DIFFUSION

To investigate the hydrogen loading and unloading dynamics of the Mg/Pd system, and to understand the influence of the Ti buffer layer, we perform numerical calculations based on the diffusion model proposed by Pasturel *et al.* [76]. In this model, a trilayer film of metal hydrides without any H-H interaction is considered. Particularly, the diffusion coefficients of hydrogen in the different materials, in combination with the enthalpies of hydride formation ΔH, are used to calculate the hydrogen concentration profile throughout this multilayer system as a function of time. The maximum hydrogen/metal ratio is set equal to 1. Since the model only considers a one-dimensional system, it does not take into account the influence of the nanostructuring of the materials. Therefore, factors such as the elastic constraints of the particles, the influence of the MgO layer, and the lateral concentration profile are not accounted for. Nevertheless, this model provides a good approximation of the Mg/Pd nanoparticle system and can thus be employed to gain a basic understanding of the (de)hydrogenation dynamics.

Two different situations are considered, as illustrated in Figure 5.9(a). In the first situation, an 80 nm thick Mg layer is separated from a 10 nm thick Pd layer by a 5 nm Ti buffer layer. As a first-order approximation, the diffusion coefficient of hydrogen in the buffer layer and in Mg is assumed to be 10% of the diffusion coefficient in Pd [77–79]. For the input enthalpies of hydride formation of Mg and Pd, $\Delta H_{Mg} = -26.1$ kJ/mol H and $\Delta H_{Pd} = -19.0$ kJ/mol H are used [80, 81]. Furthermore, it is assumed that the buffer layer does not consist of pure titanium ($\Delta H_{Ti} = -54.3$ kJ/mol H), but rather of a Ti-Pd alloy, with an enthalpy of hydride formation in between the values for Pd and Ti ($\Delta H_{TiPd} \approx -22.0$ kJ/mol H) [82]. In the second situation, the Ti layer is omitted from the simulations, while a 5 nm thick layer of Mg-Pd alloy is assumed to form below the Mg/Pd interface. As shown by Wang and Flanagan [82], the alloying of Mg with Pd drastically decreases its hydrogen absorption capacity, and the enthalpy of hydride formation

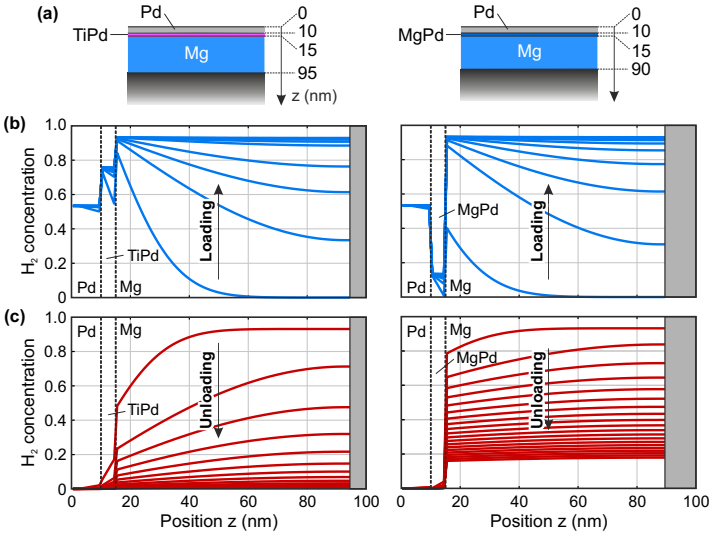

Figure 5.9. Results of 1D simulations on the diffusion of hydrogen into and out of a Mg film covered by Pd, with and without the Ti buffer layer (a). In case of direct contact between Mg and Pd, a 5 nm thick layer of Mg-Pd alloy is assumed. (b) Hydrogen concentration profiles throughout the Mg/(Ti-Pd)/Pd film during hydrogen loading for both cases. (c) Hydrogen concentration profiles throughout the film during unloading.

of this alloy layer is less negative than that of Pd. In this model, a value of $\Delta H_{MgPd} \approx -15.0$ kJ/mol H is used.

The results of these calculations are displayed in Figure 5.9(b,c). The hydrogen concentration profiles throughout the simulated one-dimensional systems are plotted for both geometries during the hydrogen loading process in panel (b). The individual profiles correspond to the simulation results at equidistant time intervals. The high H affinity of the Ti-Pd alloy layer, and the comparatively low H affinity of the Mg-Pd alloy, is easily visible, while the concentration profiles in the Mg layer do not greatly differ. Concentration profiles during hydrogen unloading are displayed in panel (c). Here, the system with an Mg-Pd alloy layer shows a significantly slower unloading than the system with the buffer layer.

The average hydrogen concentration inside the Mg layer as a function of time is displayed for both geometries in Figure 5.10. Qualitatively, these results show a reasonable agreement with the extinction measured on Mg/(Ti)/Pd nanodisks (see Figure 5.6), as the optical extinction is approximately inversely proportional to the hydrogen content in the Mg disks. An interesting feature of the simulation results is that the hydrogen concentrations appear to saturate at a maximum value of approximately 90-95%, as this behavior can also be identified in the measured extinction values (Figure 5.6(c)). This provides an explanation for the fact that after hydrogen loading, the measured extinction peaks do not completely disappear, but a rather broad and flat feature is still visible in the spectrum (Figures 5.8(a,b)). The fact that the H_2 unloading takes significantly longer for the Mg/Pd

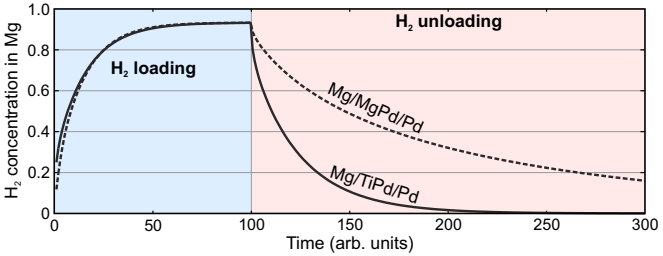

FIGURE 5.10. Averaged hydrogen concentrations in the Mg layer for both cases as a function of time. Note that the model does not consider dihydrides, so that the maximum concentration is always equal to 1. The Mg/Mg-Pd/Pd film clearly exhibits a lower unloading rate than the Mg/Ti-Pd/Pd film due to the presence of the Mg-Pd alloy layer, while the loading rates are hardly affected.

system compared to the Mg/Ti/Pd system, while the difference in loading time is much less pronounced, is also reproduced by the simulations. This indicates that the improved switching dynamics of the buffered system can indeed be explained by the absence of an interfacial Mg-Pd alloy, which hinders the hydrogen diffusion into the Mg particle.

5.5 PLASMONIC COLOR PRINTING WITH MAGNESIUM

One prime example of a plasmonic technique that can benefit from switchable plasmonic structures is *plasmonic printing*. In this technique, arrangements of plasmonic nanoparticles are used to realize different reflection, transmission or scattering spectra in the visible wavelength range and thus different visible colors [83, 84]. The nanostructures can be arranged into very small color pixels; pixels consisting of only 2×2 nanoantennas have been demonstrated in the literature [83]. In this way, sub-diffraction resolution can be achieved in color printing. A wide variety of nanostructure designs has been brought forward for different applications, often consisting of nanoparticles suspended above a metallic reflector to generate reflected colors [84–86], but other designs for generating transmitted or scattered colors have been implemented as well [87–89]. Most implementations of plasmonic color printing to date show only static colors. However, several different methods for switchable colors have also been implemented, using, e.g., polarized light [88], electrochemical switching [90], temperature-responsive films [91], or mechanical stretching [89].

The switching of plasmonic Mg structures via H_2 exposure offers a new method for fabricating switchable plasmonic color pixels. To demonstrate this, we fabricated plasmonic pixels of Mg nanostructures which were subsequently exposed to hydrogen, as shown in Figure 5.11. The structures we used are square nanopatches of Pd-capped Mg with a Ti separation layer, which were fabricated using E-beam lithography (see Section 4.3.2). The structures were fabricated on a silicon substrate, of which the top 100 nm were oxidized to produce an atomically flat SiO_2 layer. A Ti adhesion layer was used below the Mg. The thicknesses of the fabricated Ti/Mg/Ti/Pd nanostructures are 3/50/5/10 nm. The nanopatches are arranged in a rectangular grid. The patch size L and the interparticle spacing s are used as tuning parameters to achieve different reflectance spectra and thus different colors.

As Figure 5.11(b) shows, the nanostructurs are arranged in 20×20 μm^2 pixels. The demonstration sample contains a matrix of such pixels, with the spacing s being varied from 120 to 240 nm, and the size L from 60 to 200 nm.

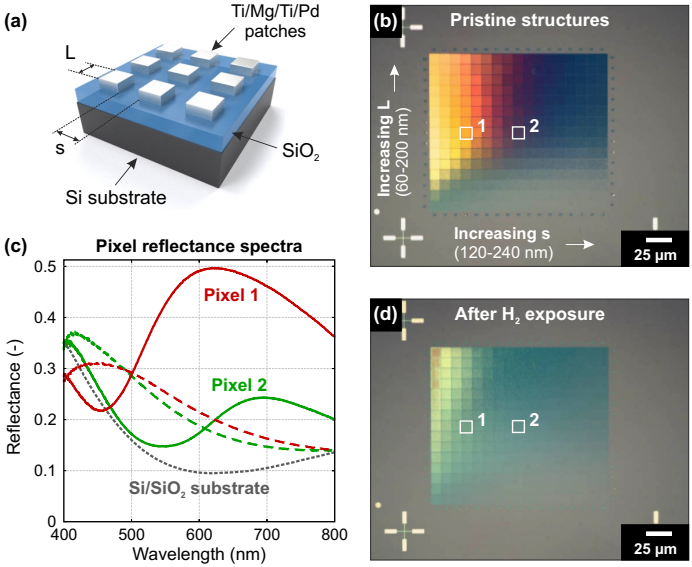

FIGURE 5.11. Example of plasmonic color printing with Mg nanostructures. (a) The sample consists of Ti/Mg/Ti/Pd square nanopatches (thicknesses 3/50/5/10 nm) on top of a Si substrate, of which the top 100 nm have been oxidized to form SiO_2. The patch size L and the spacing s between the patches are varied to achieve different colors. (b) Bright-field microscope photograph of a matrix of 'color pixels' of 20×20 µm^2 in size, before exposure to H_2. By varying L and s, a wide range of reflected colors can be achieved. (c) Measured bright-field reflectance spectra of the two marked pixels before H_2 exposure (solid lines). A silver mirror was used for spectral normalization. The reflectance of the Si/SiO_2 substrate is shown in grey. (d) After exposure to H_2 gas (4% in N_2), the colors have faded to mostly greenish tones. The corresponding reflectance spectra are plotted in (c) (dashed lines). Note that the photographs in (b) and (d) are contrast-enhanced.

Colors varying from yellow through red to blue are obtained in this way. Figure 5.11(c) shows the measured bright-field reflectance spectra of two selected pixels, measured using a Nikon ECLIPSE LV100 upright microscope-based microspectroscopy setup (see Section 3.3.1). A silver mirror was used for normalization. The reflectance spectrum of the bare Si/SiO_2 substrate is shown as well. A comparison between these spectra reveals that the plasmonic pixels in fact have a *higher* reflectance than the substrate, so that they appear bright against a darker background. Figure 5.11(d) shows

a photograph of the sample after hydrogen absorption in 4% H_2 gas. The colors have faded to mainly greenish shades, which can also be recognized in the corresponding reflectance spectra.

5.6 CONCLUSION AND OUTLOOK

In this chapter, we have shown that magnesium is a suitable material for nanoplasmonic applications, providing strong resonances that are tunable throughout the visible wavelength range. Magnesium nanoparticles suffer slightly from corrosion through reactions with different gaseous compounds, but the self-limiting native oxide layer of only a few nanometers prevents rapid degradation, keeping Mg nanoparticles stable over time periods of several months. We have extended the use of Mg nanoparticles to the field of active plasmonics, showing that Pd-capped Mg nanodisks can be transformed into the non-metallic magnesium hydride by simple exposure to hydrogen gas. This reaction can be reversed by exposure to oxygen. Via this reversible transformation, the plasmonic resonance of the particles can be repeatedly switched off and back on, with hydrogen loading and unloading times in the order of minutes. In combination with the abundance and low cost of Mg, these characteristics make the material a highly promising candidate for novel applications in active plasmonic metamaterials, which can not only be held in a fully metallic 'on' state or a fully dielectric 'off' state, but can also be stable at any state in between for extended periods of time. The findings on the loading and unloading dynamics of Mg/Pd disks also pave the way for future investigations into the chemical processes behind the hydrogenation of magnesium, as we will see in Chapters 6 and 7.

At the time of writing of this thesis, new insights about Mg as a plasmonic material, including the ones presented in this chapter and in publication P1, have already brought forward several interesting applications. In addition to UV plasmonic applications [92, 93], dynamic plasmonic color printing, as described in Section 5.5, has undergone rapid improvements [94–96], as has the development of switchable plasmonic holograms [97, 98].

6

HYDROGEN DIFFUSION IN MAGNESIUM NANOPARTICLES

In the previous chapter, we have demonstrated the application of palladium-capped magnesium nanoparticles for active plasmonics via the absorption of hydrogen. There is, however, another highly interesting field for which this process is relevant, namely the field of hydrogen storage in metal hydrides. The absorption of H_2 in metal nanoparticles, such as Mg, offers a model system to investigate the process of hydrogen absorption and desorption in metals on the nanoscale. Here, we will thus use the insights from the previous chapter in combination with mechanical measurements on Pd-covered Mg particles to gain some insight into this process.

6.1 INTRODUCTION

Currently, much of the worlds energy need is satisfied by fossil fuels. Besides the fact that these natural resources are slowly being exhausted, the release of greenhouse gases into the atmosphere causes a change in global climate. This is putting a severe strain on many of the Earth's ecosystems (in addition to the strain these ecosystems are already experiencing from, e.g., pollution [99]). Furthermore, many studies in the previous decades have shown that even a relatively small increase in the long-term average of global temperatures can significantly influence weather patterns. The exact interplay between a heating atmosphere and, e.g., global ocean temperatures is a highly complex process, which is why sophisticated computer models in combination with real-time as well as historic data are employed to gain a better understanding and provide predictions for the future [100, 101].

6.1.1 *Hydrogen storage in metals*

In order to prevent this global warming, it is thus very important to find alternative energy sources to fossil fuels. This is particularly problematic for transportation applications, such as automotive, railways and aviation, since most technological developments so far have aimed at the optimization of combustion engines, and the infrastructure is centered around this. Another important factor is the high energy density of fossil fuels, such as gasoline and kerosene, which is very difficult to surpass. However, vehicle fuels are in fact not to be regarded as a *source* of energy, but rather as a *storage* for it: It does, in principle, not matter whether the energy consumed by a car engine comes from fossil fuels or was generated by sustainable, environmentally friendly processes beforehand. This is why hydrogen is of great interest for future mobility applications [102, 103]. Hydrogen gas (H_2) can be generated using electric power, and the chemical energy thus stored in this gas can be converted back to electric energy in a fuel cell. The energy needed for H_2 production can be generated from renewable sources, such as solar and wind power, which are abundant in many parts of the world [104, 105]. Hydrogen can thus not be regarded a sustainable fuel by definition, but in stark contrast to fossil fuels, the possibility *exists* (and has shown to be feasible) to generate it exclusively from sustainable energy sources.

However, one of the main problems that need to be tackled for a widespread usage of hydrogen fuel is the storage. A significant drawback of hydrogen gas is its much lower energy density compared to fossil fuels. One potential solution to overcome this is the storage of H_2 in metal hydrides [106, 107].

In Figure 6.1, the volumetric H_2 density is plotted versus the gravimetric H_2 density for different types of hydrogen storage. These quantities can be directly interpreted as the amount of energy contained per unit volume and per unit mass, respectively. In general, for mobility applications, one wants to maximize both, to minimize the size of the required hydrogen storage as well as the necessary mass, which must be carried and thus increases the total amount of required energy.

As shown in the plot, the most straightforward hydrogen storage method, namely pressurizing it in a thick-walled container, does not reach very high values on either axis. As the H_2 pressure increases, the amount of material required for the tank itself also increases, adding to the total weight that must be carried. In Ref. [107], the authors also consider a container made of a hypothetical composite material. In this way, the gravimetric H_2 density

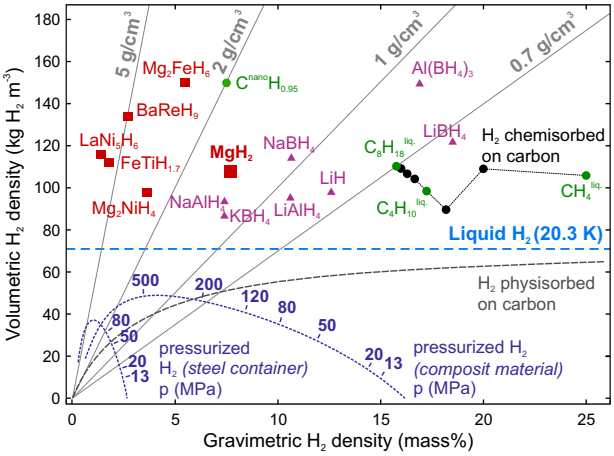

FIGURE 6.1. Volumetric and gravimetric hydrogen (energy) density of selected hydrides and other methods of hydrogen storage. By pressurizing hydrogen in a tank, only relatively low densities are reached, even with a hypothetical composite material (tensile strength $\sigma_V = 1500$ MPa, density 3000 kg/m^3). Liquefied hydrogen provides a higher density, but requires a very low temperature. Metal hydrides can offer significantly higher densities. The data in this figure are taken from Ref. [107].

can be increased significantly, but not the volumetric one. The next logical step might be to use liquefied H_2. In principle, this is feasible, although the liquefaction process itself consumes energy (aside from the obvious disadvantages of having to carry a liquid at just above 20 K in a vehicle). Nevertheless, this method would provide higher volumetric H_2 densities than pressurized gas.

Furthermore, the plot shows several different types of metal hydrides. These all provide significantly higher volumetric H_2 densities than pressurized or even liquefied H_2. The somewhat counterintuitive consequence of this is that the individual H atoms can be packed closer together when embedded in a metal lattice, than when floating around in gaseous form even at very high pressures. The storage of H_2 in metals is thus a promising step towards hydrogen-based mobility. Requirements for such a storage are easy loading and unloading processes and a good stability over many cycles. While many different Mg-based alloys have been brought forward for this [51, 52, 80, 108, 109], the relatively simple magnesium-hydrogen system can serve as a good model system for understanding the diffusion dynamics.

6.1.2 *Magnesium crystallinity*

Extensive research has been performed on the absorption/desorption dynamics in nanostructured Mg, such as films and powders [48, 110, 111]. One interesting finding in many thin-film-based investigations is the observation of a nucleation-and-growth process for the hydrogen absorption, in which MgH_2 starts to form at a certain number of nucleation sites before expanding throughout the film [112, 113]. Another aspect in the transformation from Mg to MgH_2 is the large difference in crystalline structure between the two materials, and the associated volume expansion, which has to be somehow accommodated. Figure 6.2 shows an artistic rendering of both crystal unit cells. The lattice parameters are from ref. [114]. As the figures show, magnesium posesses a hexagonal close packed (hcp) structure, while MgH_2 possesses a rutile (TiO_2-like) structure. Other polymorphs of MgH_2 with modified crystal structures can exist as well, but only at much higher pressures [115].

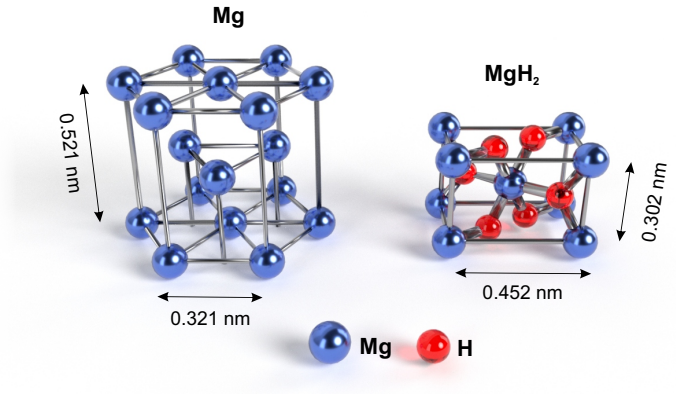

Figure 6.2. Artistic impression of the crystal structures of Mg (hexagonal close packed) and MgH_2 (rutile; TiO_2-like).

The large difference in crystal structure between Mg and MgH_2 leads to an increase in volume of over 30% upon H_2 absorption. Nevertheless, the MgH_2 unit cell is smaller than the Mg unit cell, as it contains fewer atoms. A second consequence is a strong lattice mismatch. To explain how MgH_2

can grow on Mg, it was proposed that MgH_2 grows mostly along the [110] direction, in which the compound forms quasi-hexagonal planes [116].

Furthermore, the hexagonal crystal structure of Mg leads to the formation of hexagonal crystallites in Mg films, with typical sizes of up to a few hundred nm. We have already seen this in Mg nanodisks in Chapter 5. Figure 6.3 shows some additional examples of Mg crystallites occurring in different types of structures. In extended films, individual potruding crystallites are sometimes found on the surface. If the substrate is not sufficiently cleaned before Mg deposition, the film formation can be obstructed, leading to the formation of many individual crystallites. A vertical structure on the sample can also lead to the seemingly random formation of large crystallites. This is, for example, observed in the grid-like structure formed atop a photoresist mask for densely packed Mg patches after a failed lift-off process (see Section 4.3.2), as shown in panel (c). A comparison between panels (d) and (e) furthermore highlights the influence that the substrate on which the Mg grows can have. In the case of a relatively rough substrate (in this case MgF_2), individual crystallites appear to grow in different directions, leading

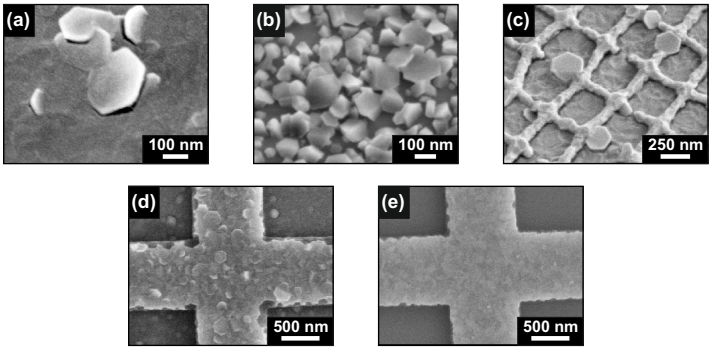

FIGURE 6.3. SEM images showing examples of hexagonal Mg crystallite formation in different situations. (a) large Mg crystallites potruding from an Mg film on a flat Si substrate. (b) Individual Mg crystallites on a Si substrate without prior substrate cleaning and without the use of an adhesion layer, which prevents the Mg from forming a closed film. (c) Mg crystallites occurring in the pattern left by a failed lift-off procedure of densely packed Mg nanopatches on flat SiO_2. (d) Individual Mg crystallites visible in an E-beam lithography alignment marker on a relatively rough surface (evaporated MgF_2). (e) A comparison to a similar structure on a flat (SiO_2) substrate shows that the film morphology is strongly influenced by the substrate.

to a film which appears to consist of many crystallites on top of each other. On a flat substrate (in this case atomically flat SiO_2), on the other hand, a much smoother film is formed.

6.2 OPTICAL MEASUREMENTS

In the bright-field transmittance measurements presented in Figures 5.6 and 5.6, we have seen that the structures show some degradation over many switching cycles. However, these measurements were done on a large number of particles at once, and thus constitute an ensemble average. From such measurements, one can thus not draw any conclusions about the exact nature of the degradation. It could be that all particles simultaneously show some form of degradation (such as the aforementioned cracking and subsequent oxidation), but it could also be the case that after each cycle, several particles show a 'breakdown', so that with time, fewer and fewer particles contribute to the switching.

To investigate the behavior of individual particles, we perform single-particle dark-field measurements, as described in Section 3.3.2. To enable the simultaneous observation of several particles, samples containing such particles are fabricated by means of electron-beam lithography (see Section 4.3.2). The particles are arranged in a grid with a spacing of 10 µm. This means that the sample can be positioned such that several particles are aligned to the spectrometer entrance slit at the same time, while the interparticle spacing is large enough to extract the scattering spectrum of each particle separately. These measurements are performed using the microspectroscopy setup based on a Nikon ECLIPSE LV100 upright microscope (Section 3.2). The sample is again positioned in the microscopy gas flow cell and illuminated by a halogen lamp via an episcopic dark-field objective (Nikon TU PLAN ELWD 50×, NA 0.60.). The illumination is unpolarized.

Figure 6.4 shows the resulting spectrally resolved single-particle scattering time traces of such a measurement, in which nine Mg/Ti/Pd particles with a diameter of 160 nm were observed simultaneously. The layer thicknesses are 80, 5 and 10 nm, respectively, similar to the structures investigated in Chapter 5. The substrate consists of silicon (Si), of which the top 100 nm was oxidized to form an atomically flat SiO_2 layer. The nanoparticles were fabricated with a target diameter of 160 nm, leading to a scattering peak centered around 700 nm. The sample was subjected to two subsequent H_2 and O_2 exposures to drive the hydrogenation and dehydrogenation (see Section 5.3.2). The scattered intensity is normalized to the maximum

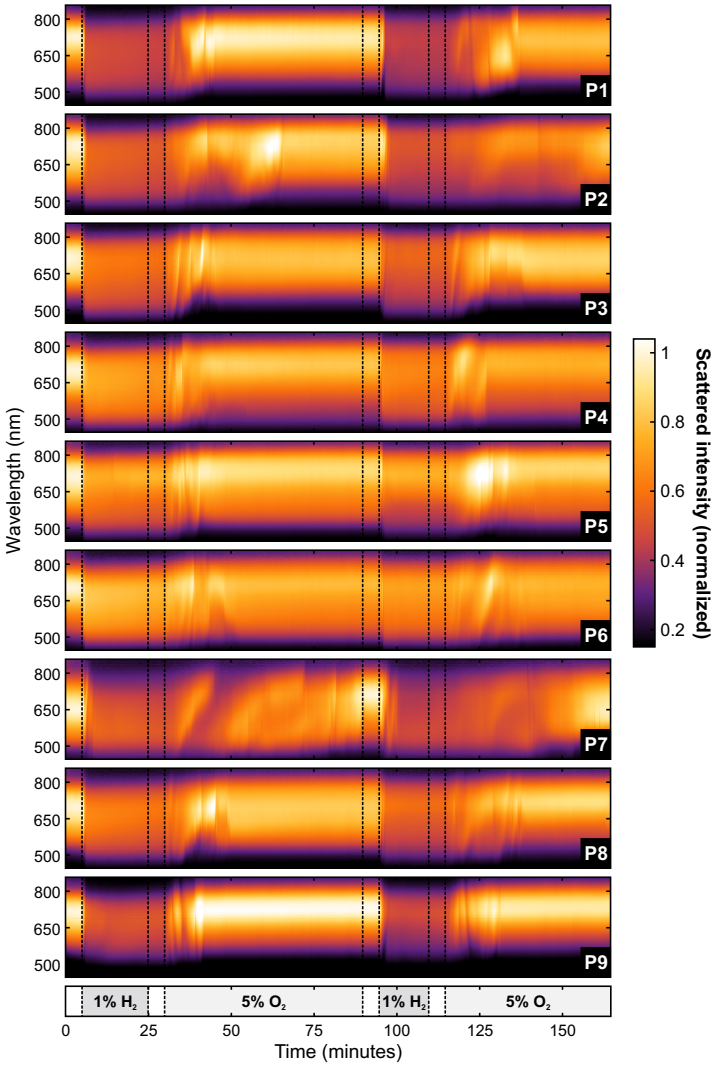

Figure 6.4. Spectrally resolved dark-field scattering time traces of nine individual Mg/Ti/Pd particles (thicknesses 80/5/10 nm; diameter 160 nm) on an Si/SiO_2 substrate, during two subsequent H_2 and O_2 exposures (indicated on the bottom and by the dashed vertical lines).

value of the spectrum initially measured for each particle. A lower H_2 concentration than before was used (1% instead of 4%), in order to minimize the influence of the Pd layer (we will see more about this in Chapter 8). Furthermore, Figure 6.5 shows the time traces of the integrated scattered intensity extracted from these spectrally resolved measurements.

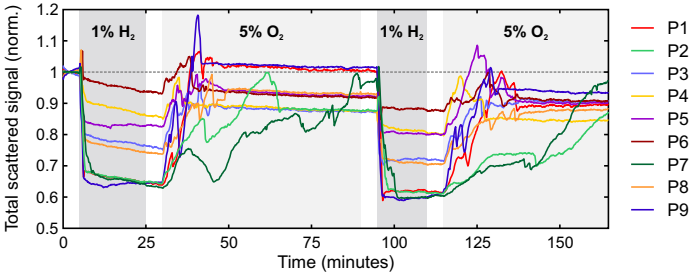

Figure 6.5. Time traces of the total scattered intensity, extracted from the data presented in Figure 6.4. The total scattered intensity is obtained from the area under the spectrum curve for each time step. Each time trace is normalized to the averaged value before the first H_2 exposure.

These time traces clearly show that each particle exhibits a pronounced individual behavior, regarding the loading and unloading time and the peak scattering value after the completed first cycle, and regarding the 'trajectory' of the scattering peak during both transitions. While some particles (e.g. P4, P5) return to the original scattering spectrum in less than 5 minutes, other particles need much more time to recover and, moreover, show seemingly random 'jumps' during both transitions. These jumps can best be recognized during unloading, as this process takes longer, but can occur in the loading process just as well (particle P7). Measurement noise as a cause for the jumps can be ruled out, because of the simultaneous observation of the particles. Signal changes caused by, e.g., mechanical or thermal drift would appear in each measured time trace. The spectrally resolved time traces in Fig. 6.4 furthermore show that the jumps occur in scattering intensity as well as peak position. This is a strong indication that the jumps occur due to a changing arrangement of the material inside the particle - as individual parts of a nanodisk transform from Mg to MgH_2 and back, along with the corresponding volume change and reorientation, the effective shape

of the volume of metal constantly changes. Since this shape determines the plasmon resonance position(s) in the particle, the recorded scattering spectra show such strong jumps.

These data thus show that the degradation of Mg nanoparticle ensembles in fact occurs due to the breakdown of individual Mg particles, rather than a gradual degradation of all particles simultaneously. Furthermore, the jumps in combination with the aforementioned crystallite formation leads to the suspicion that individual crystallites are (de)hydrogenating one-by-one, each time causing a deformation of the particle along with dislocations in the crystal lattice [117], which can be observed in the optical far-field.

6.3 MECHANICAL MEASUREMENTS

To investigate the deformation occurring during H_2 absorption and desorption in Mg nanoparticles, we compare the shapes of particles before and after several H_2/O_2 cycles.

6.3.1 *SEM imaging*

As a first step, we use scanning electron microscope (SEM) imaging of Mg nanostructure samples to compare the shape before and after hydrogen cycling. Again, electron-beam lithography is used for fabrication, to facilitate an easy localization of specific particles for a one-to-one comparison. Figure 6.6 shows exemplary SEM images of Ti/Mg/Ti/Pd nanopatches of two different sizes arranged in a rectangular grid (Mg thickness 70 nm). The bottom Ti adhesion layer was added to minimize the influence of the substrate roughness. The SEM micrographs were recorded before and after three subsequent H_2/O_2 cycles. These were carried out at an elevated temperature of 90 °C, in order to speed up the loading and unloading. In previous bright-field reflectance measurements, we confirmed that different temperatures show significant influence on the reflectance spectra of these nanopatch arrays.

In the close-up images, one specific particle is shown before and after the three repeated gas exposures. The shapes of the Mg and Pd layers can be identified in these images and have been highlighted by coloration for clarity. It is clear that the Mg 'body' of the particles has undergone a lateral expansion and has thus not fully returned to the original size, supporting the

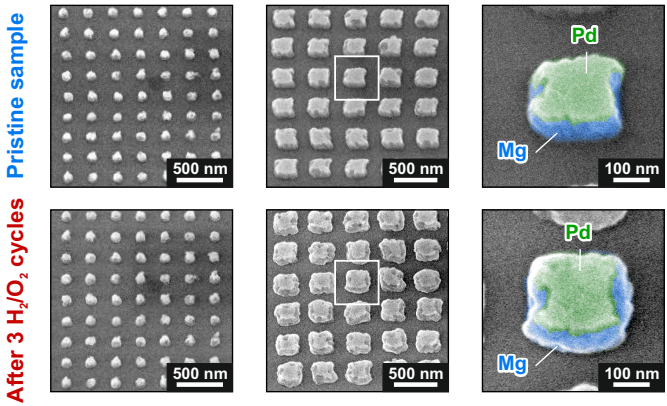

Figure 6.6. SEM micrographs of Ti/Mg/Ti/Pd nanopatches of two different sizes (thickness 3/70/5/10 nm) directly after evaporation and after three H_2-O_2 absorption-desorption cycles at 90 °C. The images were taken at the exact same position on the sample, so the particles are one-to-one the same. In the magnified images on the right, one specific particle has been colorized to highlight the Mg and Ti/Pd layers. After three cycles, the Ti/Pd cap layer is still recognizable, whereas the Mg layer has significantly expanded laterally. All images were recorded under an angle of 30°.

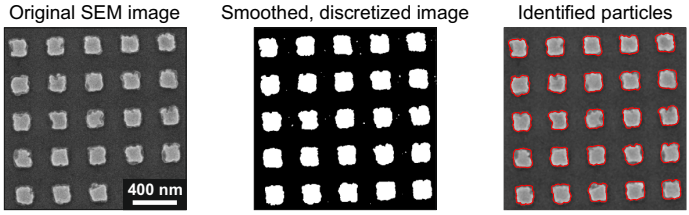

Figure 6.7. Example of 'blob detection' in SEM images of Mg nanopatches. The SEM image is discretized into a black-and-white image by a certain pixel value threshold, after which the white areas are identified as particle. The edge length of each particle follows from the square root of its area in pixels.

suspected material rearrangement inside the particle, along with a potential increase of the oxide shell thickness. This shows that the volume expansion is not exclusively accommodated by an expansion in the vertical direction, as in thin films. Another interesting observation is that this expansion appears much more pronounced for the larger particles.

Since electron-beam lithography enables the fabrication of many different particle sizes, we can use these samples to investigate the influence of particle size on the expansion. To this end, we record high-resolution images containing hundreds of nanopatches each before and after cycling, for target sizes between 80 and 300 nm. We extract the individual particle sizes from these images using a 'blob detection' algorithm, which is illustrated in Figure 6.7. Here, all pixels in the SEM image with an intensity higher than a certain threshold value are identified as part of a nanopatch, after which all connected 'nanopatch' areas are found and their surface area in pixels is extracted. The square root of each surface area can then be taken as the edge length and converted to nm, so that a histogram of edge lengths can be created for each nanopatch array. The extracted edge lengths can then

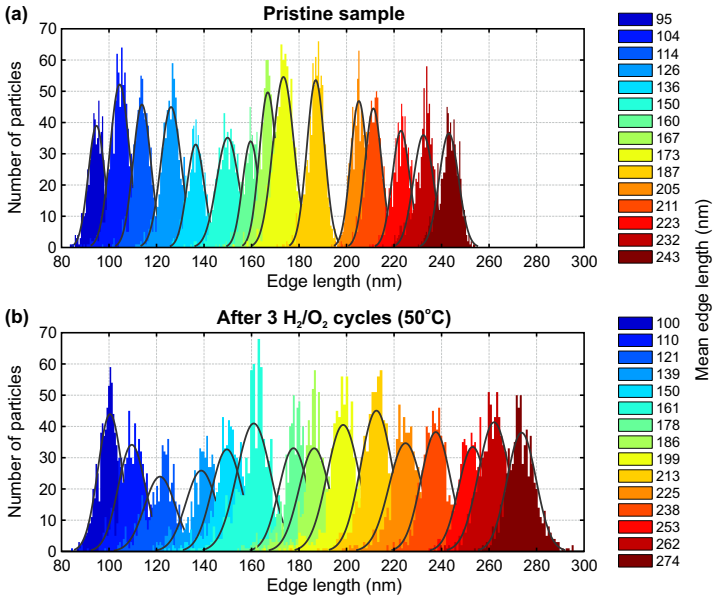

Figure 6.8. Edge length histograms of a sample containing Ti/Mg/Ti/Pd nanopatches (thickness 3/58/5/10 nm) directly after evaporation (a) and after 3 absorption-desorption cycles (b), extracted from high-resolution SEM images as shown in Figure 6.7. Each SEM image contains several hundreds of nanopatches of the same target size. The mean edge lengths resulting from the histograms are shown in the legends (nm).

be plotted as histograms. An example of this data processing is shown in Figure 6.8.

By assuming a normal distribution of nanopatch sizes and fitting a Gaussian curve to each histogram, the edge length before and after H_2/O_2 cycling can be extracted as a many-particle average, so that an average lateral expansion can be determined. As Figure 6.8 shows, this expansion can reach rather high values of up to 10%. Taking into account the expected volume expansion of Mg of around 30%, this appears to indicate that the expansion in these particles happens isotropically, and that the outer particle shell does not shrink back to its original shape upon dehydrogenation but rather retains the shape of the expanded particle. However, to get a full picture of what is happening, additional information on the vertical expansion is needed.

6.3.2 *AFM measurements*

To additionally gather information about the vertical shape change of Ti/Mg/Ti/Pd nanopatches, we employ atomic force microscope (AFM) measurements. Besides high-resolution SEM images, we record AFM measurements before and after several H_2/O_2 exposure cycles for each particle size on the sample. The measurements are carried out using a Veeco Dimension Icon AFM. Exemplary height maps are shown for four different particle sizes in Figure 6.9, before and after the gas exposures.

Figure 6.10 furthermore shows cross-sectional height profiles of several nanopatches, extracted from these AFM images. Each image covers an area of $3 \times 3\ \mu m^2$ at a resolution of 512×512 pixels. The area was restricted compared to the SEM images since AFM measurements take significantly longer. Nevertheless, enough nanopatches are contained in each image to extract a reliable average value. The Mg layer thickness was 50 nm. (De)hydrogenation was performed at 60 °C with H_2 and O_2 concentrations of 1% and 5%, respectively. During the AFM measurements, the sample was exposed to air. However, as mentioned in Section 5.2.3, no significant degradation is expected in air at room temperature.

The AFM measurements show a clear change in the particle shapes. While the top surface of the nanopatches appears flat after fabrication, the nanopatches appear to have 'swollen' after several cycles. The particles have expanded laterally, although this effect is more pronounced for larger particles. Furthermore, the larger particles have developed thick 'bulges' at the

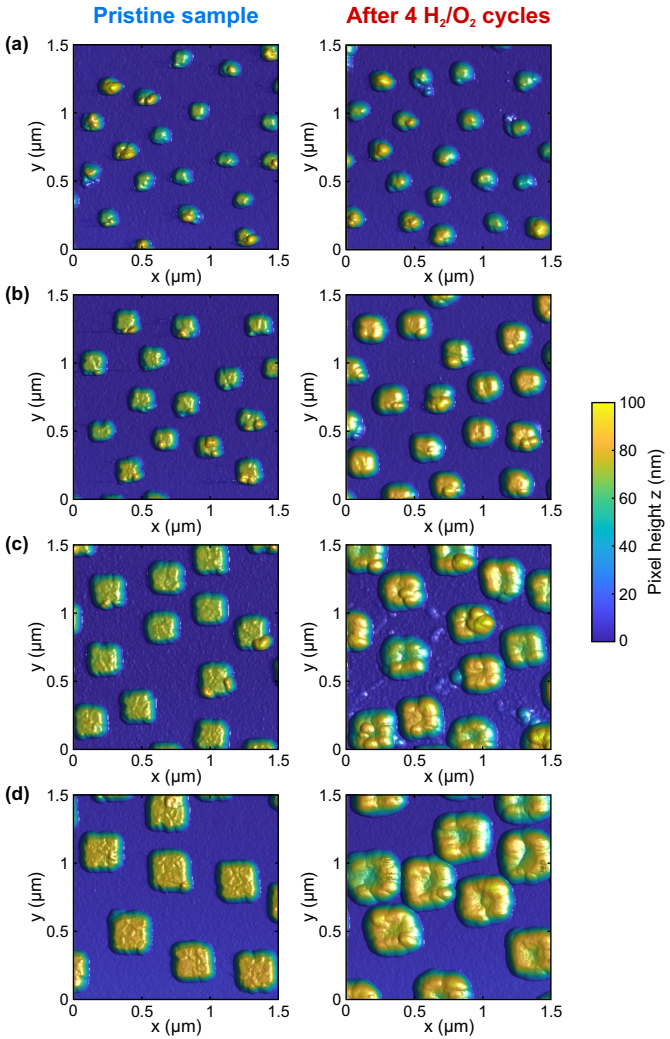

Figure 6.9. AFM images of Ti/Mg/Ti/Pd nanopatches of four different nominal sizes, before and after four subsequent H_2/O_2 cycles at 60 °C. The 3D surfaces are illuminated from the side to highlight the shapes.

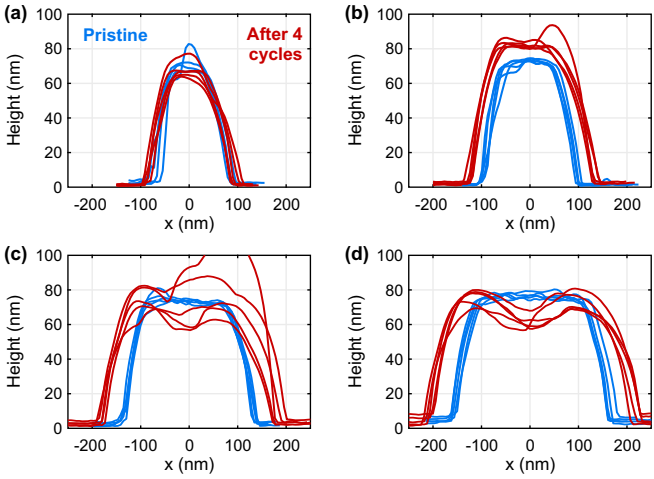

FIGURE 6.10. Cross-sectional height profiles of several Ti/Mg/Ti/Pd nanopatches before (blue) and after (red) four H_2/O_2 cycles. The profiles are extracted from the AFM data in Figure 6.9.

edge, while the thickness in the center has not changed or, in some cases, even decreased. The data in Fig. 6.9 also suggest that the particle surface on the bulges is less rough than the flat surface of the pristine particles. These effects could not be distinguished in the SEM images, since SEM imaging gives no height information. In addition to the apparent change in shape, the cross-sectional profiles clearly show an influence of the particle size. Whereas the smallest particles (panel (a), side length approx. 100 nm) show almost no shape change, somewhat larger particles (panel (b), side length approx. 160 nm) appear to expand more or less isotropically. The largest particles (panels (c,d), side lengths up to 300 nm), the aforementioned bulging, in combination with a mainly lateral expansion, can be observed.

In principle, it would be possible to calculate a volume expansion from the AFM images shown in Figure 6.9. However, while the AFM measurements provide a good *vertical* spatial resolution, the *lateral* resolution is limited, due to the finite size of the AFM tip. This effect manifests itself in the relatively large angle measured at the particle edges, which is unexpected in the pristine particles. To circumvent this problem, we combine the vertical expansion data extracted from AFM measurements with the lateral expansion data obtained from SEM image analysis as described in Section 6.3.1.

6.3.3 *Particle expansion*

Figure 6.11 shows the lateral (in-plane) expansion vs. particle size calculated from SEM measurements alongside the vertical expansion calculated from AFM images, as well as the volume expansion calculated from the combination of these data. All data were collected on the same sample before and after gas exposure. The initial particle sizes are always extracted from the SEM images. The lateral and vertical expansion are both defined as:

$$\text{Expansion} = \frac{L_{\text{final}} - L_{\text{initial}}}{L_{\text{initial}}}, \tag{6.1}$$

with L the mean particle side length or the mean particle height, respectively. The volume expansion, which is plotted in Fig. 6.11(c), is defined analogously. Here, the particle volume was calculated by multiplying the mean particle height from the AFM data by the mean particle surface area from SEM data.

Several interesting features can be observed in these expansion data. First, the in-plane expansion increases with particle size. Second, a local maximum appears to occur in the vertical expansion, at sizes of around 150 nm, as was observed before in the AFM profiles (Fig. 6.10). The combination of these data yields a volume expansion which appears to saturate at around 30% with increasing particle size, which is in agreement with the expected volume expansion of 30% upon hydrogenation of Mg (see Section 6.1.2).

An interesting consequence is that the shape of larger particles shows a 'memory effect' after hydrogenation and dehydrogenation. This effect is size-dependent. The shape of small particles does not appear to change much, while the edges of larger particles are pushed outward due to the volume expansion of the particle core. In combination with the observations that larger particles appear more stable over many cycles than smaller ones (see Section 5.3.1), this gives an interesting picture of the processes involved. A likely interpretation is a mechanical influence of the particle shell. As explained before, an MgO shell of several nm in thickness is expected to form around the Mg layer, possibly including some hydroxide formation. As the Mg expands, it is thus laterally bound by this shell. The smaller the particle, the stronger the effective compression force of the shell, so that the particle expands mainly in the *vertical* direction. At the same time, smaller particles are more likely to consist of a single crystallite (Section 6.1.2). In combination with the clamping by the shell, this is likely to result in the formation of crystal dislocations and cracking, leading to a rapid 'breakdown' of the particle.

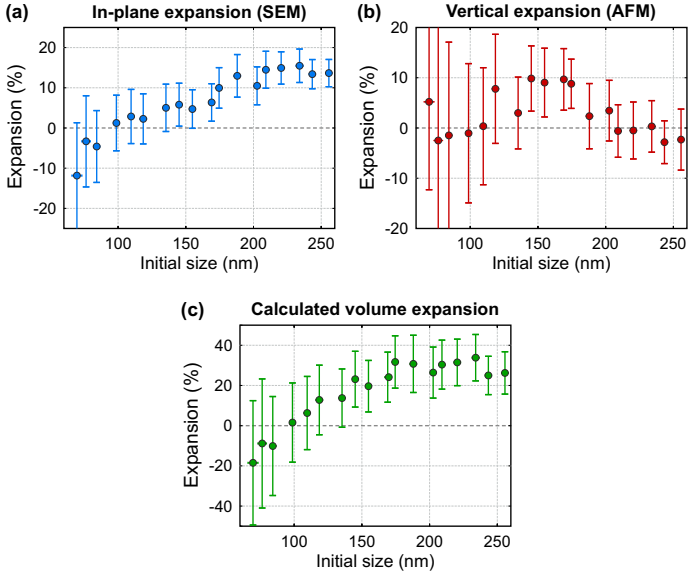

Figure 6.11. (a) In-plane (lateral) expansion of Ti/Mg/Ti/Pd patches after four hydrogenation-dehydrogenation cycles plotted versus initial particle size, extracted from SEM images. (b) Out-of-plane expansion of the same patches, extracted from the AFM data in Figure 6.9 vs. initial size. (c) Volume expansion calculated from the data in (a) and (b). The error bars follow from the standard deviations of the edge length distributions (from SEM images) and the particle height distributions (from AFM images).

In larger particles, in contrast, the compressing force by the oxide shell can more easily be overcome by the expanding Mg, which pushes the shell outward so that the volume expansion can be accommodated.[1] During dehydrogenation, the shell does not contract again, but stays in place. This in fact means that the first H_2 loading step is the slowest one, an effect that can indeed be observed in repeated gas cycles. The contraction of the Mg within the expanded shell additionally leads to the formation of cavities within the particle. Through the cracked shell, oxidation can occur within these cavities, leading to an increasing dielectric function in the direct

1 Another possible explanation for the apparent shape change of the Mg layer is that the particle melts during H_2 absorption and solidifies in this molten shape. However, this theory could be ruled out, since the heat generated in an Mg nanoparticle due to hydrogen absorption is not large enough to melt the material [118].

surroundings of the Mg and thus to a redshift of the plasmon resonance (see Section 4.2.1), as was indeed observed.

6.4 CONCLUSION AND OUTLOOK

The measurement results presented in this chapter provide an interesting picture regarding the process of hydrogen absorption and desorption in Mg nanoparticles. We have seen that the expansion of the Mg is accommodated by a particle expansion in all three directions, and that this mechanism works differently for smaller particles. We have also found a partial explanation for the better stability and faster loading times that were previously observed in Mg nanodisk ensembles. These considerations must be taken into account for the design of active plasmonic devices, such as switchable nanoscale displays.

Nevertheless, we still do not have a complete picture of the hydrogen absorption and desorption process itself, as we have only compared the before-and-after situations. We have, for example, not yet been able to identify the 'pathway' of hydrogenation inside a particle, and how it is influenced by the exact particle morphology, although the single-particle optical measurements provide a strong indication that a crystallite-by-crystallite hydrogenation and dehydrogenation occurs.

To investigate this process in more detail, one thus needs an in-situ method to observe the morphology as well as the local material composition of an Mg particle *during* hydrogen loading and unloading. In the next chapter, we will present such a method, which is based on combined optical far-field and near-field measurements.

7

NANOSCALE HYDROGENOGRAPHY

Magnesium with its particle plasmon resonances in the visible spectral range is a suitable material for active plasmonics via hydrogen exposure. However, the exact process of hydrogen absorption at the nanoscale has not yet been sufficiently understood. This chapter introduces a new method, namely nanoscale hydrogenography, which combines near-field scattering microscopy, atomic force microscopy, and single-particle far-field spectroscopy, to visualize the H_2 absorption process in single Mg nanodisks. These measurements highlight the influence of the individual nanocrystallites. We are able to monitor the spatially resolved forward and backward phase transitions of several individual nanoparticles, demonstrating differences and similarities of that process. This method lays the foundations for gaining a better understanding of hydrogen diffusion in metal nanoparticles and for improving active nano-optical switching devices of the future.

This chapter is based on the work presented in publication P2:

F. Sterl, H. Linnenbank, T. Steinle, F. Mörz, N. Strohfeldt, and H. Giessen, "**Nanoscale hydrogenography on single magnesium nanoparticles**", *Nano Letters* **18**(7), 4293-4302 (2018), DOI 10.1021/acs.nanolett.8b01277.

7.1 INTRODUCTION

Recently, it was shown that hydrogen-absorbing metals can be employed to realize active plasmonic systems, in which the plasmon resonance of metal nanoantennas can be switched off in the presence of hydrogen gas. This was, for example, demonstrated for yttrium [40] and magnesium nanostructures,

as described in Chapter 5. Magnesium, which offers the significant advantage of plasmon resonances in the visible wavelength range, was also employed in switchable chiral structures (publication P8) as well as dynamic color displays [94, 95]. In order to engineer switchable nanostructures with a short response time and a reproducibility over many absorption-desorption cycles, it is very important to understand the mechanism of hydrogen absorption and diffusion in the metal.

Furthermore, tailoring of the hydrogen absorption/desorption kinetics of metal-hydride systems by nanostructuring has gained significant interest in recent years [48, 119–121], as the hydrogen absorption and desorption kinetics at the nanoscale may differ significantly from the corresponding bulk materials, especially on the size scale of individual metal crystallites. This scientific interest is in part fueled by the potential application of metal hydrides as solid-state hydrogen storage systems, which can significantly outperform pressurized or even liquefied H_2 in terms of volumetric energy density [106, 122, 123].

7.1.1 *Hydrogenography*

Extensive studies have been performed on hydrogen kinetics in the model system of palladium nanoparticles [122, 124, 125], and even a direct visualization of hydrogen absorption in Pd by means of in-situ transmission electron microscopy (TEM) was demonstrated [126–129]. However, studies on nanostructured systems of other metal hydrides such as MgH_2 mainly rely on a one-dimensional nanostructuring, i.e., the use of thin films. In addition to analysis techniques such as X-ray diffraction and other ion beam techniques [60, 130–133], a plethora of studies on thin film systems have been carried out using the high-throughput optical characterization method termed hydrogenography [134]. This method exploits the contrast between the dielectric functions of a metal and its hydride by recording the optical transmittance through a film, which is directly related to the local ratio of metallic and hydrogenated domains. This concept is schematically illustrated in Figure 7.1.

Hydrogenographic measurements make use of the Lambert-Beer law, which relates the attenuation of light propagating through a certain medium to its properties [135]. In the case of a metallic film with thickness t and attenuation coefficient α_M, the measured transmitted intensity I_M (i.e. the

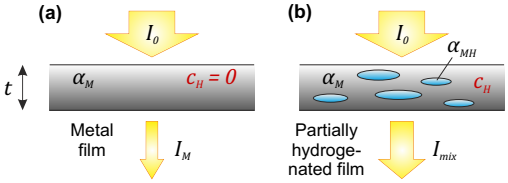

Figure 7.1. Schematic illustration of the principle of hydrogenography: the optical transmittance through a metal thin film is related to the film thickness and the optical absorption coefficient via the Lambert-Beer law (a). In a partially hydrogenated film, the hydrogenated fraction c_H can be obtained from the logarithm of the ratio of the film's transmittance to that of the unhydrogenated film (b).

ratio of transmitted over incident power at a certain wavelength, or in a certain wavelength range) is equal to:

$$I_M = I_0 \exp(-\alpha_M t). \tag{7.1}$$

A partially hydrogenated film can be approximated as a mixture of the metal with optical absorption coefficient α_M and the corresponding metal hydride with absorption coefficient α_{MH}, with the normalized hydrogen concentration ($0 \leq c_H \leq 1$) defining the fraction occupied by metal hydride. The transmitted intensity then becomes:

$$I_{mix} = I_{in} \exp\left(\left[-(1-c_H)\alpha_M - c_H\alpha_{MH}\right] t\right). \tag{7.2}$$

By taking the logarithm of the ratio between the intensity transmitted through the partially hydrogenated film I_{mix} and the intensity transmitted through the pristine, unhydrogenated film, one obtains the following expression:

$$\ln\left(\frac{I_{mix}}{I_M}\right) = c_H\,(\alpha_M - \alpha_{MH})\,t, \tag{7.3}$$

which means that, if the film thickness and the attenuation coefficients of the metal and its metal hydride at the used wavelength(s) are known, the fraction of hydrogenated metal c_H can be directly determined from a measurement of the optical transmittance during hydrogenation. Even when the attenuation coefficients are not known, the proportionality relation $\ln(T) \propto c_H$ still holds, with $T = I_{mix}/I_0$ the optical transmittance. For this reason, the transmittance through thin films is often used to investigate the spatially and temporally resolved absorption of hydrogen, even for materials that show only a small change in dielectric function upon hydrogenation (such as Pd). The full

metal-insulator transition of the Mg-H system leads to a very strong optical contrast (see Section 5.2.2). This was, for example, applied for investigating the role of nucleation and growth in the (de)hydrogenation of Pd-capped Mg films [112, 113, 136] and Mg-based alloys [137], as well as the influence of elastic constraints of Mg films [58, 138]. Investigating the dynamics of such films is possible on a scale down to several nanometers in the direction perpendicular to the substrate, while the resolution in the horizontal plane remains limited by the optical diffraction limit (see Section 2.1.2). This prevents a direct investigation of the hydrogen diffusion on the size scale of individual Mg crystallites, which is typically in the order of 100 nm [45, 60] (see also Chapter 5).

7.1.2 *Nanoscale hydrogenography*

As plasmonic resonances sensitively rely on the dielectric properties of the host material, plasmonic spectroscopy is ideally suited to study the ab- and desorption dynamics of metal nanoparticles [25, 74, 139]. Plasmonic dark-field spectroscopy enables the investigation of individual nanoparticles, which has been used to address single Pd nanocrystals [24, 25, 140]. This method can be used to probe the amount of hydride in Mg particles smaller than the diffraction limit, thus outperforming thin-film hydrogenography. Furthermore, as previous studies have highlighted the importance of the crystallinity of Mg films [60, 130, 131], a visualization of the hydrogen diffusion inside a single Mg nanoparticle or crystallite is an important step in understanding the nanoscale H_2 diffusion dynamics.

This chapter presents an approach to perform hydrogenographic measurements on submicron-sized particles of Mg, with a spatial resolution in the order of a few tens of nanometers, which relies not on transmission measurements but rather on the change of the local optical properties at the material surface. Overcoming the optical diffraction limit is possible via the use of scattering-type scanning near-field optical microscopy (s-SNOM), which in parallel allows us to monitor topographical changes [141].

The strong contrast between metallic and dielectric materials has been extensively exploited for imaging by means of s-SNOM. By excitation with mid-infrared or terahertz radiation, free-carrier concentrations and distributions can be visualized, which can be used to analyze the doping of semiconductors or the carrier injection mechanism [142]. Alternatively, a strong contrast can be obtained by the resonant excitation of vibrational modes. This has, for example, been used to visualize the phase transition associated

with the (de)lithiation of $LiFePO_4$ taking place during charging/discharging of Li-ion batteries [143] and reversible switching in optical phase change materials [144]. In other approaches, s-SNOM measurements have been combined with scanning and/or transmission electron microscopy [145, 146]. This combination of methods has, for example, been employed to observe metal-dielectric phase transitions in phase change materials [147]. However, to the best of our knowledge, the experiments described in this chapter constitute the first near-field based investigation of the phase transition from a metal to a dielectric associated with the absorption of hydrogen.

7.2 EXPERIMENTAL SECTION

7.2.1 *Measurement principle*

The system used to demonstrate the usability of s-SNOM measurements for tracking the nanoscale hydrogen diffusion consists of disk-shaped Mg particles. In principle, these follow the same design as the nanoparticles used in Chapters 5 and 6. The main difference is the layer structure, which is in this case inverted, as shown in Figure 7.2(a). The catalytic palladium layer is now on the bottom and the Mg layer on top. The reasons for this altered structure are twofold. Firstly, in order to image the formation of MgH_2 in the Mg layer by means of s-SNOM, the metallic tip must be in contact with this layer and not with the Pd layer (Figure 7.2(b)). Secondly, the Mg nanodisks must be kept in a stable state during the s-SNOM measurements. However, air exposure before and/or during these measurements is inevitable. With the Pd layer on top, this would lead to a dehydrogenation of the Mg, as shown in Chapter 5. This can be circumvented by placing the Pd layer on the bottom and thus leaving only a very small surface area of the Pd exposed, which strongly slows the hydrogenation as well as the dehydrogenation. This means that the sample must be heated to drive the hydrogen absorption at acceptable time scales, but also that practically no dehydrogenation occurs when the sample is exposed to air.

For all combined far-field/near-field monitoring measurements, two different setups are necessary. The measurement routine employed for all experiments shown in this chapter is as follows:

1. One s-SNOM image or set of images is recorded of several of the pristine particles.

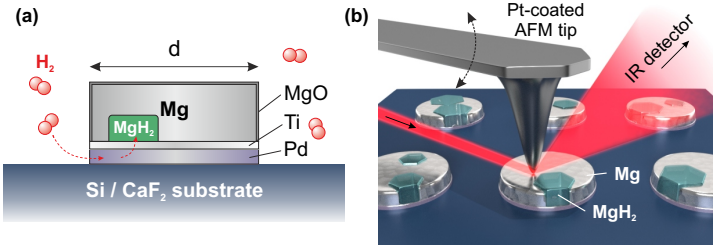

Figure 7.2. Measurement principle. (a) The nanodisks consist of a Mg layer (typically 40 nm) on top of a Pd layer, separated by a 5 nm thick Ti buffer layer. The Pd layer acts as a catalyst for the splitting of H_2, and thus as a gate for the hydrogen diffusion into the Mg layer. A thin shell of MgO can be assumed to coat the Mg disk. (b) In the s-SNOM setup, a laser beam with a wavelength of 4 µm is focused onto a Pt-coated AFM tip, which is raster scanned over the sample surface. The light scattered back from the sample surface is recorded with a liquid nitrogen-cooled IR detector, producing a map of the local scattering amplitude. In order to monitor the hydrogenation of the Pd/Ti/Mg nanodisks, dark-field spectroscopy is employed to record the far-field scattering spectra of individual particles during hydrogen exposure.

2. The sample is placed in the microspectroscopy setup in the heated gas-flow cell (see Figure 3.5) and heated, typically to 60 °C, under a constant N_2 flow (total flow rate 1 nL/min).

3. Hydrogen is added to the gas flow, typically at a concentration of 2% (partial pressure 20 mbar). The optical far-field response of the particles is monitored during hydrogenation.

4. After a chosen time, based on the visible response, the H_2 flow is turned off again. The sample is cooled down to room temperature under constant N_2 flow.

5. The (partially) hydrogenated sample is taken out of the gas flow cell and mounted in the s-SNOM setup (air-exposed).

6. Using visual aids such as alignment markers, an s-SNOM scan of the exact same set of particles is performed. The very small exposed Pd surface prevents dehydrogenation.

7. These steps are repeated several times until the Mg particles are fully dehydrogenated. The routine can be repeated for dehydrogenation in the gas flow cell, either by exposure to O_2 at 60 °C, or by heating to higher temperatures.

7.2.2 *Scattering scanning near-field microscopy*

In the s-SNOM measurement setup (NeaSNOM, NeaSpec), a platinum-iridium coated silicon AFM tip with a nominal radius below 30 nm is raster scanned across the sample surface, thus producing a topographic map of the sample. The AFM is operated in tapping mode with a tapping frequency of 250 kHz. At the same time, a laser beam with a wavelength of 4 µm is focused onto the AFM tip, as illustrated in Figure 7.2(b). A parametric frequency converter system (Alpha-HP, Stuttgart Instruments [148]) is used to generate this excitation beam with a 1/e bandwidth of approximately 130 nm. A liquid nitrogen-cooled IR detector records the intensity of the light scattered between the sample surface and the tip [141, 149, 150]. This signal is then demodulated at the 4$^{\text{th}}$ harmonic of the tip oscillation frequency, which allows for discriminating the optical near-field scattering from the total amount of scattered light [151]. In order to enhance the generally weak scattered light, interferometric enhancement is employed [152, 153]. To this end, the AFM tip is positioned at the end of one arm of an asymmetric Michelson interferometer. Thus, the backscattered light is superimposed on the detector with the reflected light from the reference arm. The position of the reference mirror is kept fixed in such a way that all spectral components simultaneously interfere constructively (white-light position), thus maximizing the detector signal [152, 153].

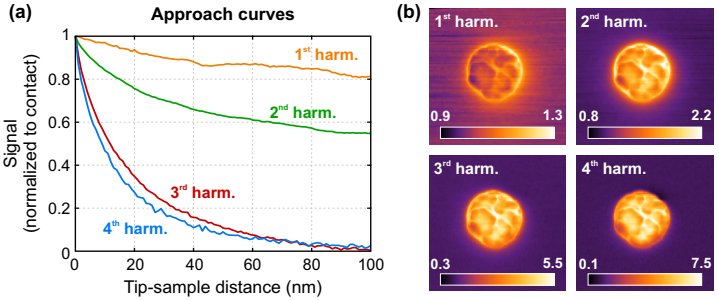

Figure 7.3. (a) Approach curves for the s-SNOM signal demodulated at the first, second, third and fourth harmonic of the tip oscillation frequency, recorded on the surface of a pristine Pd/Ti/Mg nanodisk. (b) Exemplary s-SNOM images of a pristine Pd/Ti/Mg particle on CaF_2, using the optical signal from each of the four demodulation channels, normalized to the background (substrate) signal. The s-SNOM images cover 800×800 nm^2.

An approach curve confirming the background-free measurement of the optical near-field [154] is shown in Figure 7.3(a). The corresponding approach curves for the signal demodulated at the 1st, 2nd, and 3rd harmonic are shown as well, demonstrating that the optical contrast improves with each harmonic order. In this way, the local optical properties of the sample surface in the nanometer vicinity of the tip can be resolved, which in turn depend on the local dielectric properties of the material [155]. An s-SNOM image therefore provides a map of the local dielectric properties alongside the topography, which is ideally suited for visualizing the distribution of Mg and MgH_2 because of the strong dielectric contrast between the two materials. Figure 7.3(b) shows such exemplary images of a pristine Pd/Ti/Mg nanodisk, using the signal demodulated at the first four tip oscillation frequency harmonics.

7.2.3 *Dark-field spectroscopy*

In order to monitor in-situ the total amount of hydrogen absorbed by each Mg particle, we make use of the plasmon resonance of the particles, which is designed to lie in the visible to near-infrared wavelength range via the nominal particle diameter of 240 nm. The sample is situated in a temperature-controlled gas flow cell in a dark-field imaging/spectroscopy setup, where the optical signal scattered into the far-field can be recorded for multiple particles in parallel during gas exposure (see Chapter 2). The setup consists of a Nikon Nikon Eclipse lv100 upright microscope combined with a Princeton Instruments IsoPlane-160 spectrograph and a pixis-256e Peltier-cooled front-illuminated CCD camera. A high-intensity laser driven light source (Energetiq eq-99xfc) is used to illuminate the sample via a 50× dark-field condenser/objective (Nikon tu Plan elwd, NA 0.60). An exposure time of 10 s is used to record dark-field scattering spectra. The sample temperature is regulated by Peltier elements with an accuracy of less than 0.1 °C. The large interparticle distance of 10 µm makes it possible to record the scattered signal of each particle individually. Since the plasmon resonance can only be sustained in a volume of metallic Mg, and not in the dielectric MgH_2, the strength of the plasmon resonance and thus the total far-field signal decreases with an increasing relative amount of MgH_2.

The particle geometry with the thin Pd bottom layer leads to a relatively small exposed Pd surface area, which acts as a ‘gate’ for the hydrogen absorption/desorption. This small exposed surface leads to a relatively slow absorption and desorption, with hydrogenated particles showing virtually

no desorption when exposed to air at room temperature. This geometry was deliberately chosen, since it enables us to remove a sample from the gas cell in the dark-field spectroscopy setup and transfer it to the s-SNOM setup in order to record a 'snapshot' of the optical near-field. In this way, we can monitor the changing distribution of Mg and MgH_2 as well as the particle morphology during both hydrogen absorption and desorption.

7.2.4 *Sample design and fabrication*

For dark-field imaging measurements experiments, arrays of Pd/Ti/Mg nanodisks are used. As long as the particles are spaced far enough apart to distinguish them from one another, based on the diffraction limit of the used objective (see Section 2.1.2), the hydrogenation of each particle can in principle be observed. For dark-field spectroscopic measurements, a more complicated sample geometry is necessary, as individual particles must be spaced further apart (see Section 3.3.2) and must be aligned to the spectrometer entrance slit. To achieve this, the structures are situated in a grid with a spacing of 10 µm, next to Au structures. These Au structures are used for sample alignment and for signal normalization in far-field as well as near-field measurements. The samples are fabricated using two-step electron beam lithography and electron-beam assisted evaporation (see Section 4.3). First, plasma-cleaned substrates (CaF_2 or Si) are covered with resist (PMMA) through spin coating. The pattern of the Au structures, along with alignment markers, is then transferred into a resist mask. Afterwards, a 2 nm thick adhesion layer of Cr is deposited, followed by 20 nm of Au. A Pfeiffer Vacuum PLS 500 system is used for this. After lift-off, the substrate is again covered with resist, and the Au alignment markers are used to re-align the sample. After writing the mask for the second layer, the same evaporation system is used to deposit the appropriate thicknesses of Pd, Ti, and Mg, at a chamber pressure in the range of 10^{-7} mbar. The different material layers are deposited subsequently without breaking the vacuum in between, to prevent the formation of intermediate oxide layers. CaF_2 substrates are used to ensure optical transparency at both the visible wavelength used for dark-field spectroscopy and the infrared wavelengths used for s-SNOM measurements. Si substrates do not provide optical transparency in the visible range and are only used for dark-field imaging, but not for dark-field microspectroscopy.

Figure 7.4 shows an overview of the sample layout used for the combined s-SNOM/AFM measurements. The sample contains a grid of Pd/Ti/Mg particles of varying sizes (blue) and different Au alignment markers (red). The overview shows one e-beam writefield with a size of $100 \times 100\ \mu m^2$. The area of the sample which is projected onto the monochromator of the dark-field spectroscopy setup is indicated by the black rectangle. From the eight particles observed in total, four particles were picked for s-SNOM imaging based on their responses during the first H_2 exposure period. The selection was performed to include particles with fast as well as with slow responses to H_2.

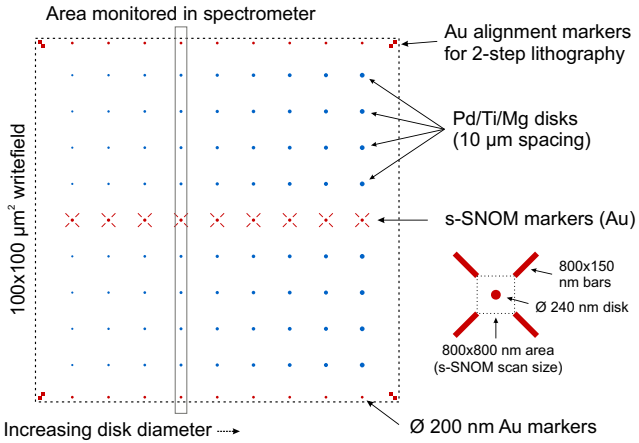

Figure 7.4. Schematic overview of the sample geometry used for combined single-particle far-field scattering spectroscopy and near-field scattering (s-SNOM) optical measurements on Pd/Ti/Mg nanodisks. Nanodisks of varying diameter are fabricated on one CaF_2 substrate within one e-beam writefield, so that the most suitable diameter for dark-field spectroscopic measurements can be selected during a measurement run. The 200 nm Au disks are used for signal normalization and to align the sample in the microspectroscopy setup when the far-field signal of the Mg disks has decreased too much. The ×-shaped Au markers are used for alignment as well as height normalization in the s-SNOM setup.

The rectangular Au markers in the corners of the e-beam writefield serve as alignment markers for the two-step lithography process. The disk-shaped markers at the upper and lower ends of each column serve as alignment

markers in the dark-field spectroscopy setup, which is especially important for measurements on (almost) fully hydrogenated particles with a very low scattering signal. The cross-shaped Au markers in the center of each column serve both as normalization reference for the far-field scattering and for s-SNOM alignment and height normalization. For each set of s-SNOM measurements, the Au markers act as a visual aid to find the same writefield on the sample. Next, a low-resolution scan is used to find the correct s-SNOM alignment marker, and s-SNOM images of the central disk are recorded until the sample position relative to the s-SNOM tip has stabilized. After this, it is easy to move to the selected particles without retracting the tip from the sample. This measurement routine ensures that the exact same particles are recorded every time. Furthermore, since the tip is not retracted in between scans, the Au disk can be used as a reference to normalize the measured AFM height of the Pd/Ti/Mg particles.

7.3 RESULTS AND DISCUSSION

7.3.1 *s-SNOM and dark-field imaging measurements*

In early experiments, we made use of dark-field imaging to monitor the Pd/Ti/Mg nanodisks during hydrogenation. Figure 7.5(a) shows typical dark-field microscopic images of an array of disks in the pristine state and after total hydrogen exposure times of 20 seconds and 10 minutes. A zoom-in view of the nine disks that were observed in the s-SNOM scans in between the H_2 exposure periods is shown in the insets. The layer thicknesses of the Pd/Ti/Mg structures are 20 nm, 5 nm, and 40 nm, respectively, and the nominal disk diameter d is 400 nm. The structures are fabricated on a Si substrate. A comparison between the dark-field image of the pristine sample and after H_2 exposure for 20 s reveals that the individual particles exhibit very different hydrogen absorption times, as some particles have already gone completely dark, while others maintain the original brightness. This suggests the same behavior as observed in dark-field spectroscopic measurements on Mg/Ti/Pd nanodisks, as presented in Section 6.2. After 10 minutes of H_2 exposure, all particles appear to have settled in a stable hydrogenated state, showing a very low and uniform overall scattering brightness.

The corresponding s-SNOM images of the nine highlighted particles are shown in Figure 7.5(b). The s-SNOM scans of the partially and fully hydrogenated particles were recorded after the corresponding dark-field

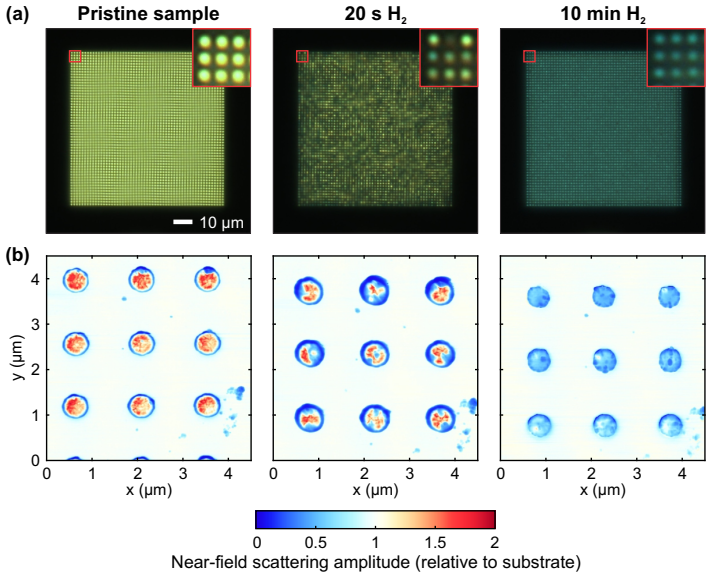

FIGURE 7.5. (a) Dark-field images of an array of Pd/Ti/Mg nanodisks (thicknesses 20/10/40 nm; $d = 400$ nm) in the pristine state, after 20 seconds of H_2 exposure at 60 °C, and after 10 minutes of H_2 exposure. In the last frame, the camera exposure time was increased to make the 'dark' particles visible. (b) s-SNOM scans of the nine nanodisks shown in the insets in (a) in the pristine state and after the two H_2 exposure periods. The substrate is Si in this case. The dark edges around the nanodisks in the second frame can be attributed to s-SNOM tip abrasion.

images in panel (a). Owing to the relatively close particle spacing of 1 µm, all nine particles could be recorded in one s-SNOM scan, covering 4.5×4.5 µm^2 at a resolution of 500×500 pixels (taking approximately 40 minutes in total). The s-SNOM images clearly show how the scattering intensity at the particle surfaces strongly decreases, from approximately twice the scattering intensity of the Si substrate to approximately half of it. Especially in the second frames, a dark ring of very low scattering intensity can be seen around the particles. This can be attributed to abrasion of the s-SNOM tip after repeated particle scanning, making the tip more blunt and thus unable to resolve features near the sharp particle edge. In the last frame, a new tip was used to solve this.

Furthermore, in the second frame (after 20 s H_2 exposure), it is interesting to compare the near-field signal of the individual particles to their far-field signal. In the particles that are brightest in the far-field image, the fraction of the surface that still exhibits a high scattering (and can thus be regarded as metallic) appears to be still relatively high. In the particles that show a weak far-field signal, only a small fraction of metal is detected at the particle surface. Apart from this correlation, it is very interesting to note that the near-field scattering intensity does not undergo a uniform decrease over the particle surface, but rather small areas of metallic Mg appear switch to dielectric MgH_2 one-by-one. This demonstrates that the s-SNOM measurements indeed enable the locally resolved observation of H_2 absorption in metallic nanoparticles. Furthermore, this observation supports the claims made in Section 6.2, namely that the hydrogenation of a Mg nanoparticle progresses from crystallite to crystallite and is thus governed by its crystalline composition.

These measurements thus demonstrate the concept of our 'nanoscale hydrogenography' measurement method and present first interesting results regarding the hydrogenation of Mg nanodisks. In the next section, we will look at s-SNOM measurements combined with true single-particle far-field spectroscopy. We will also use the topographic (AFM) data of the s-SNOM measurements to gain a further understanding of the H_2 absorption mechanism.

7.3.2 *s-SNOM and spectroscopic dark-field measurements*

The measurements presented in this section provide a more in-depth investigation of several single Pd/Ti/Mg nanodisks, using true single-particle dark-field spectroscopic measurements (see Section 3.3.2) instead of pure imaging. Pd/Ti/Mg nanodisks with layer thicknesses of 10 nm, 5 nm, and 40 nm, respectively, were used. The particles are placed on a CaF_2 substrate, following the sample design displayed in Figure 7.4. Four nanoparticles with a nominal disk diameter of 240 nm are selected for s-SNOM imaging. For each of these nanoparticles, an s-SNOM image is recorded with a scan size of 800×800 nm^2 at a resolution of 200×100 pixels. In order to image the exact same particles before and after each H_2 exposure or heating period, the lithographically defined Au reference structures are detected by AFM imaging before imaging the Mg nanoparticles. The Au structures are simultaneously used as height reference for the separate measurement sequences. A full set of images from all four particles takes around one hour to complete.

During H_2 exposure in the microspectroscopy setup, the far-field scattering spectra of eight particles, including the four selected ones, are continuously monitored in parallel, so that the H_2 exposure can be stopped at chosen times to record an intermediate s-SNOM image of the very same particles.

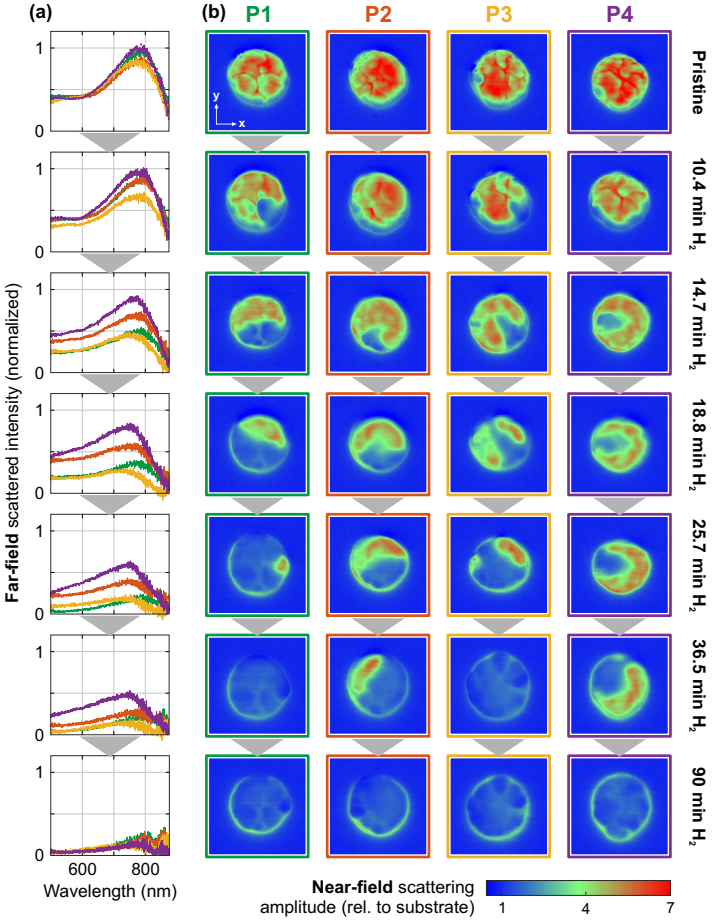

Figure 7.6. (a) Far-field scattering spectra of four individual Mg nanoparticles (P1-P4) before and after discrete hydrogen exposures at 60 °C. (b) Near-field scattering maps of the same particles, showing an area of 600×600 nm^2. The s-SNOM images are recorded in between the H_2 exposures.

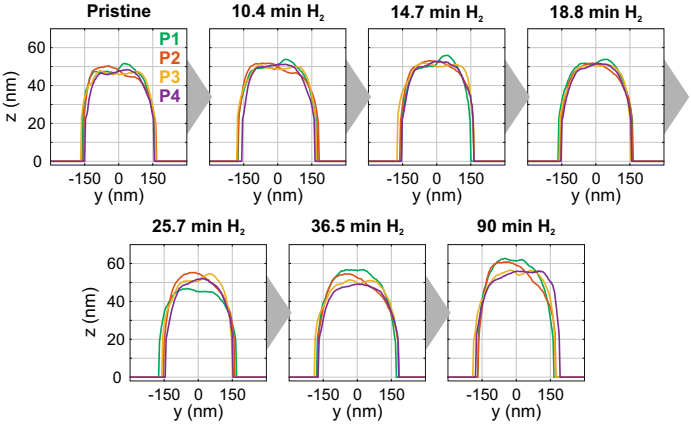

Figure 7.7. Cross-sections of the topography of the same particles as in Figure 7.6. The cross-section curves are obtained by averaging along the x direction over all 200 scan lines, omitting pixels with a height below 5 nm. The underlying topography is recorded in parallel to the near-field scattering maps presented in Figure 7.6.

Figure 7.6(a) shows the recorded far-field scattering spectra of four selected particles at different stages of hydrogenation. The first depicts the spectra of the particles in their pristine state, and the subsequent frames show the spectra recorded just before H_2 exposure was terminated and the sample was taken out of the gas flow cell. The corresponding s-SNOM images are shown in Figure 7.6(b). The near-field scattering amplitude has been normalized to the signal from the dielectric CaF_2 substrate for each frame. Since CaF_2 has a much lower reflectance than Si, this leads to higher relative values than in Figure 7.5. Furthermore, Figure 7.7 show height profiles of all particles, obtained by averaging along the x direction over the AFM data recorded simultaneously with the s-SNOM images.

Although the four particles are fabricated in the same way, the recorded far-field scattering spectra reveal a difference in the dynamics of the hydrogen absorption of the four individual particles. After 25.7 minutes of H_2 exposure, the far-field spectra of particles P1 and P3 do not show any changes anymore, indicating that they are fully hydrogenated. In contrast, particle P2, which exhibits a comparable change of its spectrum in the beginning, still does not appear completely hydrogenated after 36.5 min, as indicated by the region with a high near-field scattering amplitude and the difference in far-field scattering between the last two frames. The same

holds true for particle P4, which additionally shows a much slower response in the beginning, as a significant change with respect to the pristine particle only starts occurring after 14.7 minutes.

The s-SNOM images of the pristine particles (Figure 7.6(b)) show that the scattering amplitude recorded on the metallic Mg surface is approximately five to seven times as high as the signal recorded on the bare substrate. To verify this signal, one can compare the signal of the Pd/Ti/Mg disks to that of gold structures of similar size, as displayed in Figure 7.8. The scattering amplitudes arising from both materials are virtually the same, as one would expect from the very similar dielectric functions of Mg and Au at a wavelength of 4 µm. The s-SNOM images in Figure 7.6 exhibit structural features as well: especially on particles P1 and P4, one can recognize edges with a lower scattering amplitude indicating roughly hexagonal shapes. These features are not only visible in the near-field signal, but also in the raw AFM data (phase as well as amplitude), as Figure 7.9 shows. As Mg has a hexagonal crystal lattice [45], these features most likely arise from individual Mg crystallites protruding from the particle surface (see also Chapter 5).

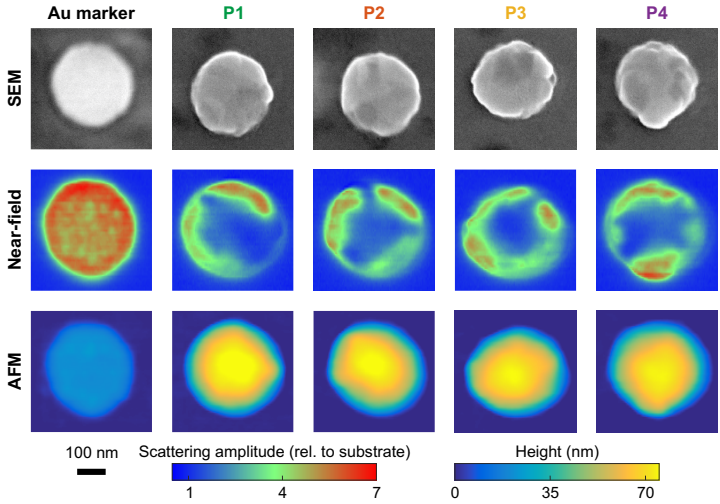

Figure 7.8. SEM micrographs and corresponding s-SNOM and AFM images of the Au marker and Pd/Ti/Mg particles P1-P4, *after* the finished H_2 loading/unloading cycle.

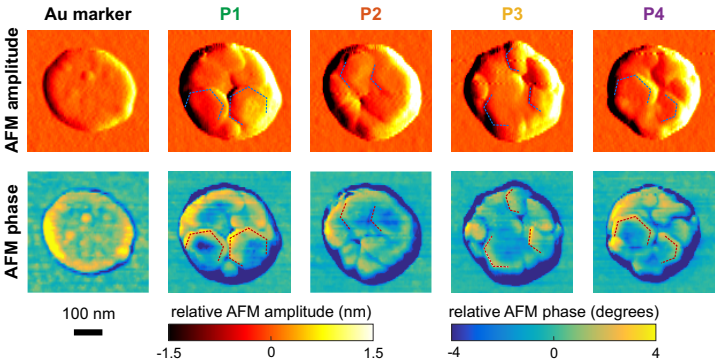

Figure 7.9. AFM amplitude and phase maps for the Au marker and particles P1-P4 in the pristine state. The blue and red dashed lines indicate features with an angle of approximately 120° visible in either data set.

The s-SNOM images recorded after different H_2 exposure periods exhibit in great detail how the strongly scattering metallic Mg particles are transformed into dielectric particles, whose near-field scattering amplitude is almost uniform and similar to that of the dielectric substrate. However, the near-field scattering amplitude is not decreasing in a spatially uniform way. Instead, nucleation sites with a near-field scattering amplitude similar to that of the dielectric substrate become visible at early stages of the H_2 exposure. These nucleation sites expand throughout the entire particle during hydrogen absorption. This growth appears not to progress continuously through the particle, but instead it appears as if individual regions of a particle change one after another. Of course, one has to keep in mind that our ex-situ measurements cannot resolve the entire temporal evolution of the hydrogen absorption. Furthermore, the images indicate a correlation between the material transition and the particle topography. This effect is most pronounced in particles P1 and P4.

A comparison between the s-SNOM images and the far-field scattering spectra reveals a correlation between the total intensity scattered into the far-field and the portion of the particle with high near-field scattering amplitude, which corroborates the validity of our measurement method. For example, as the near-field scattering amplitude of particle P1 has become almost uniformly similar to that of the substrate after 36.5 minutes, its far-field scattering has diminished as well. The same comparison can be carried out for the other particles. Furthermore, the AFM measurements represented

by cross-sections in Figure 7.7 reveal an increasing particle thickness. This can be attributed to the strong lattice expansion in Mg of around 30% upon hydrogenation. The expansion appears to be anisotropic, taking place mostly

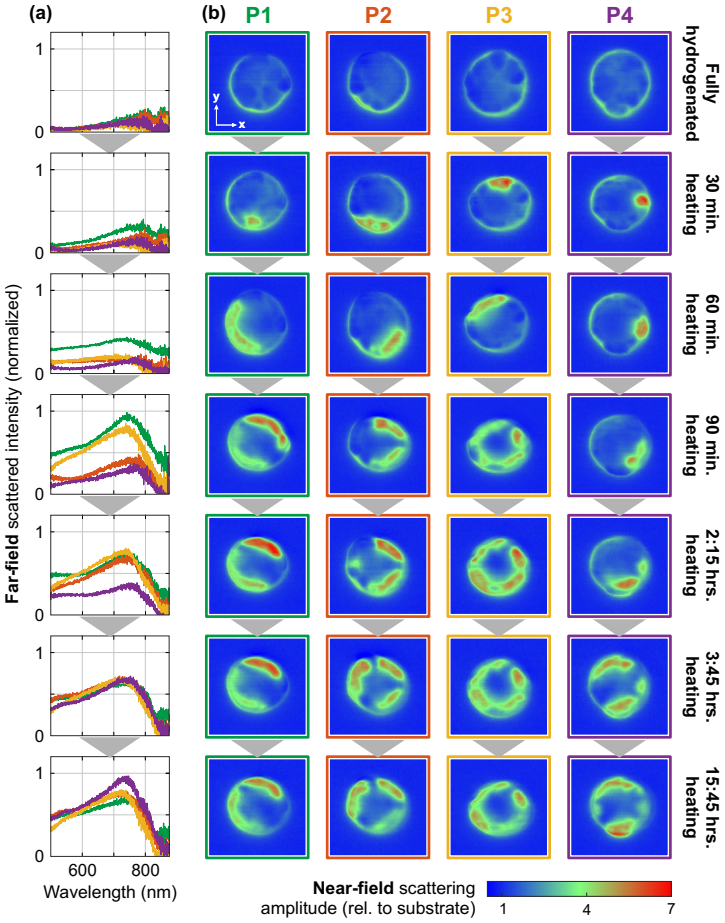

FIGURE 7.10. (a) Far-field scattering spectra of the same nanoparticles as presented in Figure 7.6 (P1-P4; green, red, yellow, and purple, respectively) before and after discrete annealing periods at 95 °C in Ar. (b) Near-field scattering maps of the same particles, showing an area of 600×600 nm^2. The s-SNOM images are recorded in between the annealing periods. The total H_2 exposure time is indicated to the right of each row.

in the vertical direction, which could be caused by the presence of an oxide shell which prevents a strong lateral expansion (see also Section 6.3). The measured expansion further validates the full hydrogenation indicated by the vanishing far-field as well as near-field scattering of the metallic Mg.

A similar measurement routine was applied to visualize the morphology and material composition during hydrogen desorption. The sample was placed in the gas cell and heated to a temperature of 95 °C in an argon atmosphere, at which the Pd/Ti/Mg nanoparticles dehydrogenate over the course of several hours. Dehydrogenation by heating was favored over oxygen exposure to avoid potential corrosion, which could form $Mg(OH)_2$. At chosen times, the dehydrogenation process was stopped by cooling down the sample to room temperature in order to record an s-SNOM image. The far-field scattering spectra and corresponding s-SNOM images and AFM profiles are shown in Figures 7.10 and 7.11 for the exact same particles as in Figure 7.6.

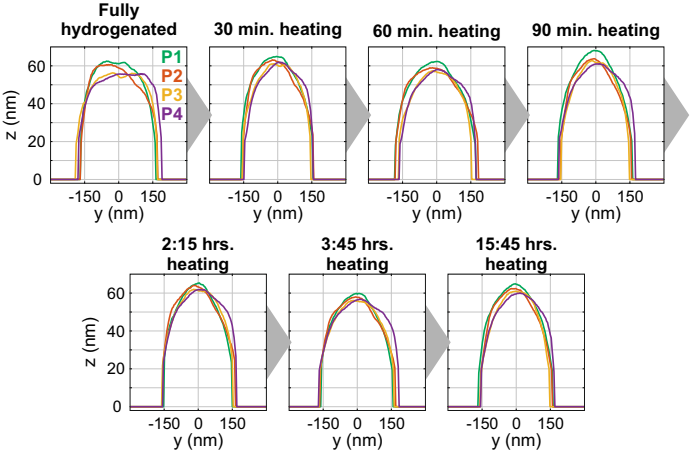

Figure 7.11. Cross-sections of the topography of the same particles as in Figure 7.10. The cross-section curves are obtained by averaging along the x direction over all 200 scan lines, omitting pixels with a height lower than 5 nm.

Similar to the data recorded during hydrogenation, the far-field scattering spectra (Figure 7.10(a)) display a similar trend as the corresponding s-SNOM images (Figure 7.10(b)). The far-field scattering spectra furthermore do not

fully return to their original shape after more than 15 hours heating. The decreased overall scattering intensity of the dehydrogenated particles (Figure 7.10(b)) compared to the pristine particles (Figure 7.6(a)) indicates that only partial dehydrogenation has taken place before the particles settle in a stable state. This behavior can be recognized in the s-SNOM images as well. While regions with a higher near-field scattering amplitude, indicating the presence of metallic Mg, start to emerge along the particle rim after dehydrogenation for 30 minutes, the central part of the particle surface maintains its low scattering amplitude. A comparison to Figure 7.6 furthermore shows that the particles that have become fully dielectric within the shortest time span are also the first ones to reach a stable state after dehydrogenation (P1, P3), while the slower particles (P2, P4) also dehydrogenate last. This indicates that the time needed for the absorption as well as desorption process is largely determined by the structure and morphology of the particle. Depending on the number, size, and arrangement of the crystallites which compose a particle, different pathways for hydrogen diffusion might form, which determine the speed of both processes alike.

7.3.3 *Correlation of near-field and far-field response*

A quantitative comparison of the spectrally integrated far-field scattering and the spatially integrated near-field scattering is exemplarily shown for particles P1-P4 in Figure 7.12, for hydrogen absorption as well as desorption. Since the particles undergo a full metal-dielectric transition upon hydrogenation, the total far-field scattered intensity decreases dramatically and thus constitutes a very clear measure of the progress of the hydrogenation.

Alongside the far-field and near-field optical responses, the particle shape undergoes a strong change as well, as evidenced by the AFM profiles. While the fully hydrogenated particles (Figure 7.7) feature an increased thickness with respect to the pristine particles, the particle caps remain relatively flat. As the dehydrogenation progresses, however, the particles adopt a more rounded shape. Overall, this demonstrates that our nanoscale hydrogenography method based on s-SNOM imaging also provides valuable information on topographical changes alongside the optical properties, which will be correlated in the following.

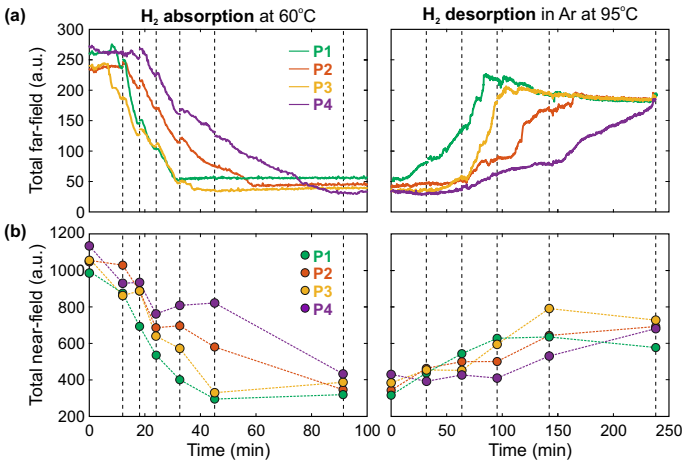

Figure 7.12. Total optical far-field and near-field versus time for particles P1-P4 (Figures 7.6 and 7.10) during H_2 absorption and desorption. (a) Total far-field scattered signal during H_2 exposure/heating, obtained by integrating the recorded far-field spectra from 620 nm to 870 nm. (b) Total near-field scattering amplitude recorded at each of these instances, obtained by integrating over all pixels of the corresponding s-SNOM image after subtraction of the substrate signal. The vertical dashed lines indicate the times at which the absorption/desorption process was interrupted to record s-SNOM images. The hydrogen exposure/heating periods between the dashed lines include 50 s of N_2 purging at the start and at the end.

7.3.4 *Correlation between topography and optical properties*

In Figures 7.13 and 7.14, the color-coded relative optical near-field scattering amplitude has been overlaid onto a three-dimensional representation of the measured AFM thickness at selected stages of hydrogen absorption and desorption of particle P1. Projections of the particle geometry onto the xz and yz plane are displayed in grey, while contour lines are shown in white at 10 nm intervals. Several interesting observations can be made from these images.

Most importantly, one can clearly see how individual crystallites switch from Mg to MgH_2 independently one after another. This effect is most pronounced in the first three frames of Figure 7.13. In the first frame, the two roughly hexagonal protrusions (which were already visible in Figure 7.6(b)) both feature a strong near-field scattering amplitude in the middle, with a slightly lower scattering amplitude along the edges. In the second frame,

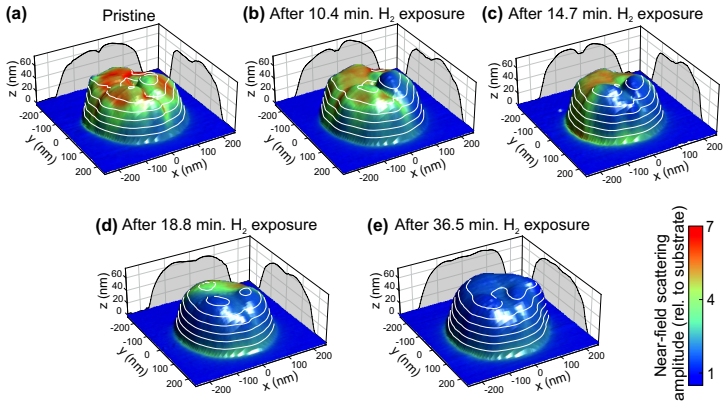

Figure 7.13. Overlay of the color-coded near-field scattering amplitude on the topography of particle P1 at different stages of hydrogenation. The white contour lines have a vertical distance of 10 nm. The grey areas show the projections of the particle onto the xz and yz plane.

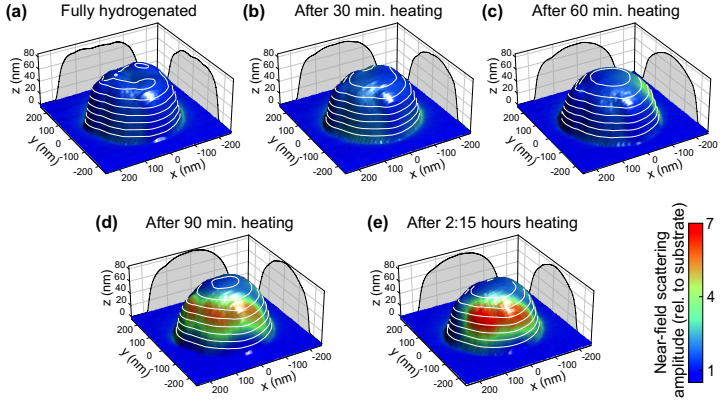

Figure 7.14. Overlay of the color-coded near-field scattering amplitude on the topography of particle P1 at different stages of dehydrogenation. Note that the view has been rotated by 180° with respect to Figure 7.13.

the rightmost of these protrusions has turned dark, and at the same time has increased in thickness. The left protrusion shows the same change in the third frame. In the fourth frame, the protrusion on the back of

the particle has slightly increased in height and the near-field scattering amplitude has partly decreased, whereas in the fifth frame it has grown to the same height as the rest of the particle and its near-field scattering amplitude is likewise indistinguishable from the rest of the particle and the substrate. This apparently subsequent hydrogen loading of individual crystallites is comparable to the observations of Narayan *et al.* in mono- and polycrystalline palladium nanoparticles [127].

7.3.5 *Analysis of AFM data*

Apart from the optical measurements, it is also very interesting to look in detail at the AFM data of the Pd/Ti/Mg nanodisks, similar to the analysis presented in Section 6.3). The data analysis in the following is mainly based on pixel height histograms of AFM data, as depicted in Figure 7.15. The particle size, thickness, and volume can be extracted from the shape of the resulting curves. From the AFM histogram curves of particle P1 in different stadiums (Figure 7.15(a)), one can already recognize the significant shape change which the particle undergoes. In its pristine state (blue curve), the histogram curve shows a clear peak, corresponding to a particle with a more or less flat cap. The particle thickness can in this case be extracted from the position of the histogram peak. After hydrogenation (green curve), this histogram peak has slightly broadened and shifted to a larger height value, indicating that the particle has expanded with a slightly bigger thickness variation on its cap. In the dehydrogenated state, the histogram curve shows

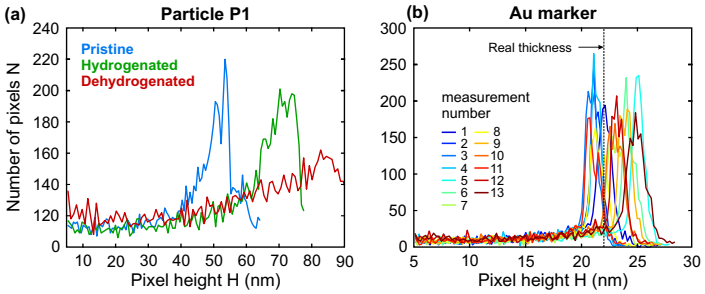

Figure 7.15. Examples of AFM histogram curves for particle in the pristine, fully hydrogenated and fully dehydrogenated state (a) and for the Au s-SNOM marker for each recorded image (b).

a significantly broader peak at much higher values, corresponding to a particle with a rounded shape.

Since the Au marker is not affected by H_2 exposure or heating, it can be used as a reference for the particle thickness. As shown in Figure 7.15(b), the shape of the marker histogram is always roughly the same, but the measured thickness is not. This is due to the fact that the AFM tip of the s-SNOM has to be retracted, brought back into position, and re-calibrated prior to each set of measurements. By comparing the measured marker thickness to its actual thickness of 22 nm (2 nm Cr adhesion layer and 20 nm Au), the AFM data recorded on all other particles can be normalized.

From the normalized AFM data, the base area of the particle is extracted by taking the total number of pixels with a height value larger than a threshold of 5 nm, which follows from:

$$A = \sum_{H=5nm}^{\infty} N(H). \tag{7.4}$$

Again, the extracted base area of the Au marker is compared with the value extracted from SEM images (see Figure 7.8) in order to find a correction factor for each set of measurements. Furthermore, the measured particle volume can be extracted by taking the area under the histogram curve multiplied by the pixel heights:

$$V = \sum_{H=5nm}^{\infty} N(H)H. \tag{7.5}$$

After the base area correction is applied to the measured volume, a relative volume expansion can be obtained for each particle (see Figure 7.16(a)). The surface area of each particle can be extracted from the three-dimensional shape of the thickness-corrected AFM data to obtain the surface area to volume ratio (see Figure 7.16(b)).

Figure 7.16 presents the results of this analysis. In panel (a), the relative volume expansion is plotted vs. time. These curves show how the volume, as a general trend, increases and decreases along with the far- and near-field signals (see Figure 7.12) and thus with the amount of MgH_2. This is exactly what one would expect from the lattice expansion of Mg upon hydrogenation of approximately 30%. Figure 7.16(b) shows the surface-to-volume ratios extracted from the AFM data. Interestingly, this ratio decreases during H_2 absorption, but remains roughly constant during H_2 desorption. Based on this observation, we believe that the rearrangement of material due to H

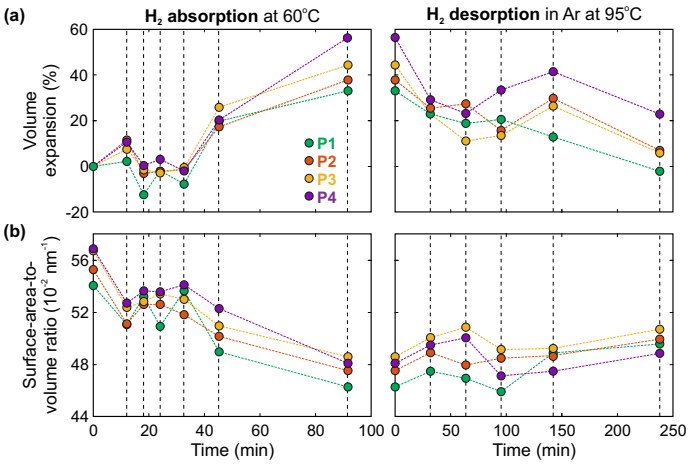

Figure 7.16. (a) Relative volume expansion of particles P1-P4, extracted from the AFM height data obtained simultaneously to the near-field data. (b) Surface-to-volume ratio of the particles, extracted from the AFM data.

diffusion facilitates a minimization of the surface energy, which leads to the rounded shape of the particles after dehydrogenation.

It should be noted that Figure 7.16(a) shows an increasing particle volume after the 5th measurement, but a roughly constant or even decreasing volume in the measurements preceding this. We believe that this behavior can mainly be attributed to the AFM measurements and the numerical analysis method. As mentioned before, we make use of the measured thickness as well as the measured diameter of the Au reference structures and correct the measured volume of the Pd/Ti/Mg disks for these values, which we believe to be the most accurate calculation method. There are, however, still several effects which this method cannot compensate for. For instance, while the AFM measurements can rather accurately measure the particle thickness and the morphology of the top surface, the shape of the side walls cannot be accurately detected due to the conical tip shape. This effect is even stronger due to some tip abrasion after many scans with the same tip. Furthermore, dents in the particle surface smaller than the tip radius are not accurately detected. Since such features occur most strongly in the first frames and less in the following frames when the particle surface becomes smoother, our measurements might somewhat overestimate the particle volume in the first few frames.

All in all, this means that the determination of the particle volume from AFM measurements is not sufficiently accurate to draw conclusions about the behavior of individual particles. The overall trend nevertheless shows a particle expansion, matching the expectations.

In contrast, the time traces of the optical near-field measurements shown in Figure 7.12 *do* appear to match the behavior expected from the total far-field time traces. The 'fast' particles P1 and P3 clearly show a different behavior than the 'slower' particles P2 and P4. We believe that this difference highlights how the optical near-field does give an accurate representation of the metal/metal hydride distribution in a single particle, even though the AFM data obtained in the same measurement are not sufficiently accurate.

7.3.6 *s-SNOM control experiments*

In order to check the influence of air exposure in the s-SNOM setup on the samples, several extra samples are fabricated with the purpose of testing

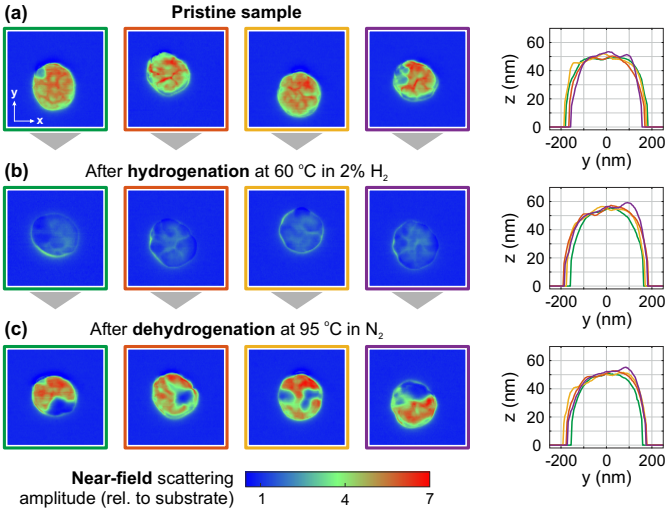

Figure 7.17. s-SNOM images and AFM profiles of four particles in the pristine state (a), after hydrogenation at 60 °C without interruptions (b), and after dehydrogenation at 95 °C in N_2 without interruptions (c). The area of the near-field maps is 800×800 nm^2.

different ways of hydrogenation/dehydrogenation. We record only s-SNOM scans before and after completed hydrogenation/dehydrogenation, to compare the particle shapes and near-field intensities. Far-field spectra are not recorded, but the particles are observed in the dark-field microscope to follow when hydrogenation/dehydrogenation is completed.

In the first control measurement (Figure 7.17), the sample is never in contact with air during hydrogenation as well as dehydrogenation. The particles appear to return to their original thickness after dehydrogenation. However, the near-field distribution does not fully return to its original state. This indicates that particles are only partially dehydrogenated, similar to the observations presented in Section 7.2.3.

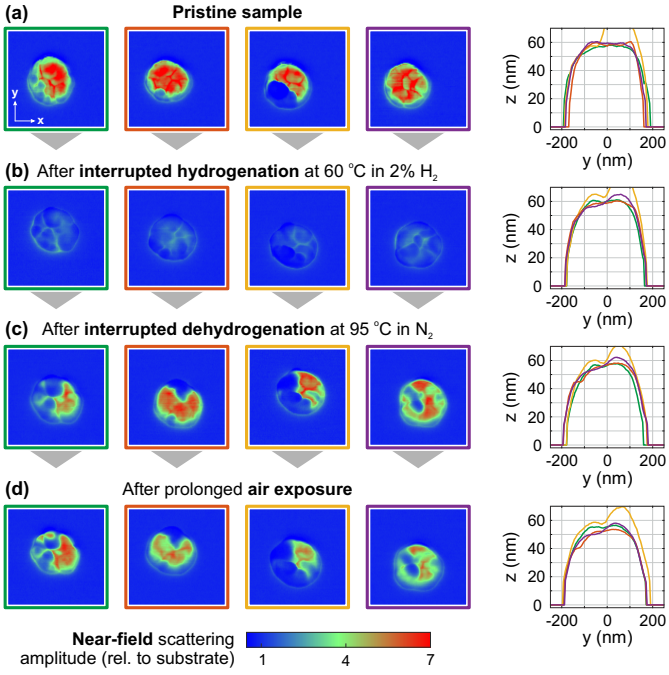

Figure 7.18. s-SNOM images and AFM profiles of four particles in pristine state (a), after hydrogenation at 60 °C with interruptions (opening the gas cell several times for a few minutes) (b), after dehydrogenation at 95 °C with interruptions (c), and after a long (overnight) exposure to ambient air at room temperature (d). After the long air exposure, the optical near-field appears weaker. The area of the near-field maps is 800×800 nm^2.

In the second control measurement (Figure 7.18), the hydrogenation as well as the dehydrogenation process are interrupted several times, by opening the gas cell for several minutes and thus bringing the particles in contact with air. This does not appear to have a large effect compared to the uninterrupted hydrogenation/dehydrogenation. The particles are expanded after hydrogenation but appear to return to their original thickness after dehydrogenation. The optical near-field does not return to its original value everywhere (indicating that the dehydrogenation is only partial), but it does return to its original value in the dehydrogenated areas. After the full hydrogenation-dehydrogenation cycle, the sample is left in contact with air overnight. After this long air exposure, the near-field scattering amplitude appears to have decreased, indicating that some degradation does take place at the particle surface. It is thus likely that this degradation has also contributed to the appearance of the particles after dehydrogenation as presented in Section 7.2.3.

7.4 CONCLUSION AND OUTLOOK

At this point, we can pool together our measurement results in order to explain the dynamic switching behavior of the Mg plasmonic structures. The switching off of the plasmonic resonances due to hydrogen absorption is not a strictly continuous process, and they do not react linearly to hydrogen exposure, as visible in Figures 7.6(a) and 7.12(a). Instead, each particle exhibits an individual hold-back time in the beginning. We attribute this to the fact that the grain boundaries of the individual crystallites in a single nanostructure act as a barrier for the hydrogen diffusion, as visible in the s-SNOM images in Fig. 7.6(b), as well as Fig. 7.14(a). In the end, however, the plasmonic resonances can be completely switched off, relying on the fact that the nanoparticles are completely turned into a dielectric material. However, this process is not entirely reversible, as the plasmonic resonances cannot be brought back to their original oscillator strength. This can be deducted from a qualitative comparison of the spectral shapes in Figs. 7.6(a) and 7.10(a), as well as the absolute far-field scattering intensity displayed in Fig. 7.12. As the resonances of plasmonic nanostructures are artificially tailored by the particle geometry, it is quite clear that even minor changes of the geometry will alter their spectra. Such geometrical changes are clearly visible in the AFM data (Figs. 7.7 and 7.11), and even more in the time series displayed in Figs. 7.13 and 7.14. Furthermore, the s-SNOM images in Figure 7.10 indicate that the particles do not become completely metallic again in the end. This

comprises that the local conductivity, which microscopically governs the plasmonic response of a structure, has been altered after one switching cycle.

In summary, we have recorded s-SNOM image time series of four individual magnesium nanoparticles during hydrogen absorption and desorption. This allows us to observe the phase change from metallic to dielectric of individual domains. The topographical maps recorded in parallel to the s-SNOM images show that these domains very likely correspond to separate nanocrystallites. This indicates that the phase change from Mg to MgH_2 occurs rapidly within a single crystalline domain, before progressing towards adjacent nanocrystallites. We have additionally compared the overall near-field scattering to the plasmonic far-field scattering of the particles. From the combination of both methods, it becomes clear how the properties of the individual nanoparticle change during the full forward and backward switching cycle: While the s-SNOM images show a change of the particle morphology, the plasmonic resonances do not regain their original strength. The insights gained from our s-SNOM measurements, namely the formation of hydride domains during hydrogenation and the morphological change during dehydrogenation, reveal the underlying processes of the optical switching behavior. Our nanoscale hydrogenography by means of s-SNOM imaging is thus a highly promising research tool for investigating the dynamics of hydrogen diffusion in single metal nanoparticles, allowing for a lateral resolution in the order of a few tens of nm. The technique allows for studying a wide variety of structures and material combinations for active nanoplasmonic devices at different time and length scales. For instance, the influence of the average crystallite size on the switching behavior of different metal-hydride systems can be addressed in the future. Furthermore, our results show that the crystalline structure of individual Mg nanoparticles appears to be crucial for the speed of the hydrogen absorption and desorption processes. Our findings thus also highlight the importance of the exact fabrication conditions for the quality, reproducibility, and switching speed of future active plasmonic devices as well as magnesium-based hydrogen storage systems.

7.4.1 *In-Situ nanoscale hydrogenography*

At the time of writing of this thesis, we have used the insights presented in this chapter (publication P2) to implement an improved s-SNOM nanoscale

hydrogenography measurement technique for in-situ measurements on Mg thin films. This technique is detailed by Karst *et al.* in publication P16.

To overcome the geometric constraints given by the fact that the Mg layer must be on top, a specialized sample geometry is implemented, in which free-standing Pd films are used as substrate. After evaporation of Pd, Ti and Mg layers, this yields entirely free-standing Pd/Ti/Mg films, which can be hydrogenated through the Pd layer. These samples are mounted on a custom-built gas flow cell, which is mounted in the s-SNOM setup. The films can thus be exposed to H_2 and O_2 without being removed from the setup, which omits the need for careful realignment after each gas exposure step. A second, major improvement as compared to the s-SNOM measurements described here is that not only the near-field scattering *intensity* is recorded, but also its *phase*. A phonon resonance mode of MgH_2 occurring around a wavenumber of 1320 cm^{-1} (approx. 7.75 µm) [156] leads to a strongly increased local absorption of the incident radiation. This feature causes a scattering phase difference of approx. 130°. By using a wavelength in this range, the contrast between Mg and MgH_2 can thus be clearly recognized in the optical phase. This offers a significant advantage over using the scattering intensity, as the phase is barely influenced by the topography, and thus provides a much clearer image of the local distribution of Mg and MgH_2. Furthermore, the mechanical phase of the recorded data is used to extract the boundaries between individual crystalline grains on the film surfaces.

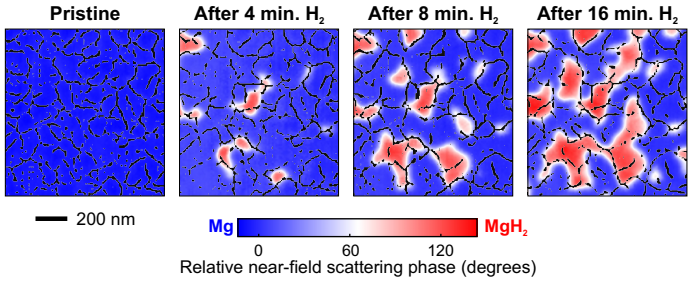

Figure 7.19. Near-field scattering phase maps of a free-standing Pd/Ti/Mg film (Mg thickness 50 nm), recorded on the pristine film and after 4, 8, and 16 minutes H_2 exposure. The regions with a large scattering phase diferrence (indicated in red) can be identified as MgH_2. The crystallite grain boundaries extracted from the mechanical phase are overlaid on the phase maps in black. The data are shown in P16.

Figure 7.19 displays four frames of a near-field scattering phase map time series, recorded on a 1×1 μm^2 area of a 50 nm thick Mg film. The grain boundaries are overlaid on the scattering phase in black. Using such measurements, the formation of MgH_2 can not only be tracked, but can also be *correlated* with the positions of these boundaries. The results presented in P16 confirm the strong influence of local morphology on the MgH_2 formation. Furthermore, an analysis of the loading time of individual Mg crystallites clearly shows that the hydrogenation of a single crystallite happens very fast compared to the hydrogenation of the entire film. These observations thus confirm the picture of 'crystallite-by-crystallite' hydrogen absorption, offering new possibilities for optimization of the loading and unloading dynamics.

8

HYDROGEN SENSOR OPTIMIZATION

So far, we have looked at the diffusion of hydrogen in magnesium on the nanoscale, with the aid of a catalytic palladium layer. However, we have not yet looked in detail at the palladium layer itself, even though Pd nanostructures hold some very interesting applications as well. The most prominent of these applications is the optical detection of hydrogen gas, owing to the dielectric function of Pd that changes with the H_2 concentration. The development of a reliable, low-cost, and widely applicable H_2 detector requires a simple optical readout mechanism and an optimization of the lowest detectable hydrogen concentration. So-called 'perfect absorber'-type structures, consisting of plasmonic Pd nanoantennas coupled to a cavity, can provide such sensors. The spectral change of the far-field reflectance can be analyzed using spectroscopic measurements. However, tracking the reflectance at a specific wavelength offers a cheaper alternative. This chapter presents a systematic investigation of the geometry of such structures as well as the optical readout system. Through this, we formulate a set of design rules for optimizing the sensitivity. These are not limited to H_2 sensing, and can be applied to any type of plasmonic sensor. This work has been published in P3:

F. Sterl, N. Strohfeldt, S. Both, E. Herkert, T. Weiss, and H. Giessen, "**Design principles for sensitivity optimization in plasmonic hydrogen sensors**", *ACS Sensors* **5**(4), 917-927 (2020), DOI 10.1021/acssensors.9b02436.

8.1 INTRODUCTION

The development of safe, reliable, and low-cost hydrogen detectors is key for a widespread usage of hydrogen as an energy carrier, which holds great promise as an alternative to fossil fuels and for energy storage. First, hydrogen detection is needed to address safety issues, considering the explosive nature of H_2 gas at concentrations between 4.2% and 74% in air [157]. Reliable H_2 detection is, for example, important to ensure safe working conditions in hydrogen fuel filling stations, and is also necessary in nuclear waste repositories [158, 159]. Second, the detection of trace amounts of H_2 at concentrations down to the 100 ppm range is crucial in process monitoring in, e.g., hydrolysis plants and power transformers [160, 161].

While hydrogen sensors with an electrical readout make use of the change in electrical conductivity upon hydrogen absorption in metals [161, 162], recent developments have brought forward optical sensing schemes, in which the change in reflectance and/or transmittance of hydrogen-absorbing materials is detected [163–166]. In such sensors, no electrical contact has to be introduced in the sensing area. A fiber-based readout enables the spatial separation of the sensing substrate and any sensor electronics [158, 167–169]. This separation is especially beneficial for sensing applications in hazardous areas, where fiber-based sensors can be installed without the need for costly and large shielding.

8.1.1 *The palladium-hydrogen system*

One particularly suitable material for optical hydrogen detection is palladium (Pd). This is due to the formation of palladium hydride (PdH_x) upon hydrogen exposure, with a composition that reversibly depends on the ambient hydrogen concentration. Due to the catalytic activity of the Pd, hydrogen molecules (H_2) split up into H atoms at the surface and diffuse into the Pd lattice, which has a face-centered cubic (fcc) structure. The fraction of hydrogen atoms per Pd atom x is strongly dependent on the ambient hydrogen partial pressure p_{H_2} as well as the temperature. This is shown in the phase diagram in Figure 8.1.

The phase diagram contains pressure-composition isotherms of bulk Pd exposed to different partial pressures of H_2, measured at different temperatures. The data are extracted from Ref. [170]. Looking at the shape of these isotherms, one sees that at low p_{H_2} values, only a very small H fraction x

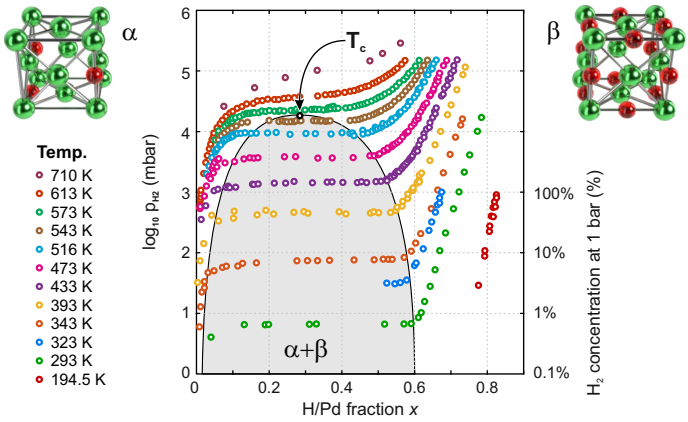

FIGURE 8.1. Pressure-composition isotherms (p_{H_2} vs. atomic ratio x = H/Pd) of bulk Pd exposed to different hydrogen partial pressures, for different temperatures. The data are extracted from Ref. [170]. The grey shaded area indicates the coexistence region of α and β phase PdH. At higher temperatures, the transition from α to β phase occurs at higher partial pressures, until the critical temperature T_c = 556 K is reached. At even higher temperatures, the phase transition becomes more gradual. For reference, the hydrogen concentration at a total pressure of 1 bar is indicated on the axis to the right, as these are the conditions at which the measurements presented in this chapter are performed.

exists in the PdH lattice. In this regime x follows Sieverts Law, as in most other metals [171]:

$$x = \frac{\sqrt{p_{H_2}}}{K_s}, \tag{8.1}$$

in which K_s is the Sieverts constant. In this regime, the H atoms occupy interstitial lattice sites. This state is known as the α phase (see inset). However, when a certain pressure is reached, x rapidly increases. After this, the hydrogen content again slowly increases with p_{H_2}. In this region of high hydrogen pressures, the H atoms do not only occupy interstitial lattice sites anymore, but saturate the Pd lattice. This state is known as the β phase. The maximum H fraction in this phase is approximately 0.82. Furthermore, at temperatures below the critical temperature T_c, which is 556 K for Pd [171], a region of α and β phase *coexistence* exists during the rapid phase transition. The pressure at which this happens is strongly temperature-dependent; at

room temperature it is typically around 10-20 mbar, or a hydrogen concentration of 1-2% at atmospheric pressure (indicated on the vertical axis to the right). An increase in the temperature leads to a higher plateau pressure and to a narrower coexistence region. If the temperature exceeds T_c, the coexistence region vanishes and the phase transition becomes smooth. Furthermore, it has been shown that for sufficiently small particles (typically smaller than 50 nm), the coexistence region can disappear [124]. One should thus keep in mind that the data presented in Figure 8.1 apply to *bulk* Pd.

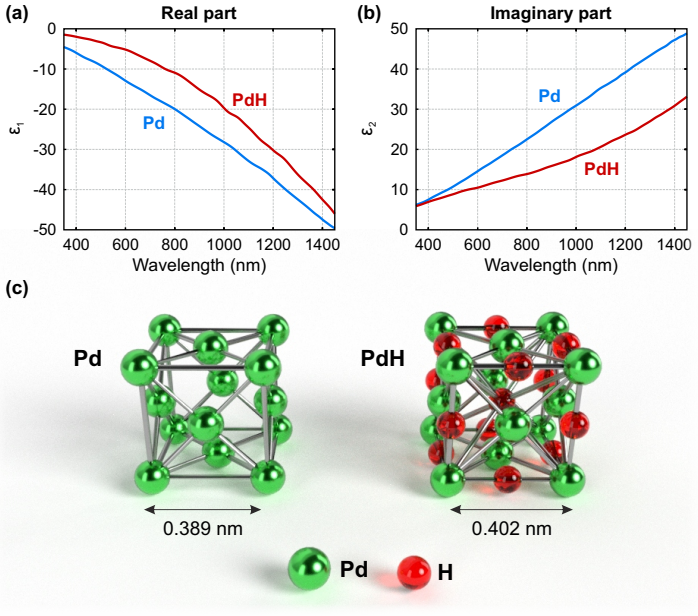

FIGURE 8.2. Real part (a) and imaginary part (b) of the dielectric functions of α phase palladium (Pd) and β phase palladium hydride (PdH), calculated from the (n, κ) measured by Von Rottkay *et al.* on a 10 nm thin Pd film [172]. (c) Artistic impression of the crystal structures of Pd and PdH.

The change from Pd to PdH_x manifests itself in a change in the dielectric function, as shown in Figure 8.2 for pure Pd and for fully saturated β phase PdH. In the β phase, this is accompanied by an increase of the lattice constant

of over 10% (from 0.3889 nm to 0.4023 nm) [173, 174]. This adds to the shift of the plasmon resonance in PdH_x nanoparticles, which follows the rapid increase of the H uptake around the transition pressure. In the rest of this chapter we will simply use 'PdH' to indicate β phase PdH_x.

8.1.2 *Plasmonic hydrogen sensing*

In recent years, different sensor geometries have been investigated, which can mainly be divided into thin films and plasmonic nanoparticles. In the case of Pd thin films, the optical transmittance and/or reflectance can be analyzed as a measure of the hydrogen concentration [175–177]. In Pd nanoparticles, the localized plasmon resonance (LSPR) undergoes a shift upon hydrogen absorption, so that tracking the centroid wavelength via spectroscopic measurements offers another detection method [69, 74, 139, 178], that has also been employed to study the behavior of individual Pd nanoparticles [24, 25, 125, 140]. On the other hand, the relative simplicity of reflectance measurements makes this method more suitable for large-scale, low-cost sensor applications. While both optical readout mechanisms can be used to reliably extract the hydrogen concentration, there are significant differences between films and particles from a thermodynamical viewpoint [124, 140, 179–181].

The freedom of volumetric expansion and the sensitivity of the plasmonic resonance makes nanoantennas preferable over thin films, even though Pd nanoparticles suffer more strongly from undesirable effects such as a hysteresis in the loading and unloading of hydrogen, a non-linear behavior of the sensor response (due to the transition from α to β phase as mentioned in Section 8.1.1), and a deactivation through poisoning by other gases [74, 176]. These challenges can be tackled by, for example, protecting the particles with hydrogen-permeable cover layers (e.g. PTFE [163, 182], PMMA [183], or platinum [176]) and by using lattice-matched substrates (e.g. CaF_2, MgF_2 [176]). Another widely used approach, mainly for overcoming the nonlinearity and the loading/unloading hysteresis, is using Pd-based alloys instead of pure Pd. This has, for example, been demonstrated for Pd-Au alloys [168, 181, 184–186], but recently also for ternary Pd-Au-Cu alloys [109].

Additionally, one can employ advanced prediction algorithms based on mathematical modeling of the sensor, as was shown in publication P11. Furthermore, different nanostructure geometries including stacked structures have been investigated to enhance the hydrogen sensitivity, both in thin films [187] and in nanoparticles [139, 188]. Recently, H_2 detection with a

combination of nanoantennas and hydrogen-reactive thin films was demonstrated as well [189]. Another recent development is the use of alternative materials such as hafnium (Hf) [190] and tantalum (Ta) [191] for hydrogen sensing, which can overcome the challenge of hysteresis. However, these materials still require a catalytic Pd layer and generally higher operation temperatures, whereas Pd and its derivatives are usable at room temperature.

Here, we will focus on pure Pd nanodisks, which serve as a model system for a plasmonic hydrogen detector. It should be noted that all qualitative claims made in this chapter are just as applicable for H_2 sensing structures made of other materials or equipped with a coating layer.

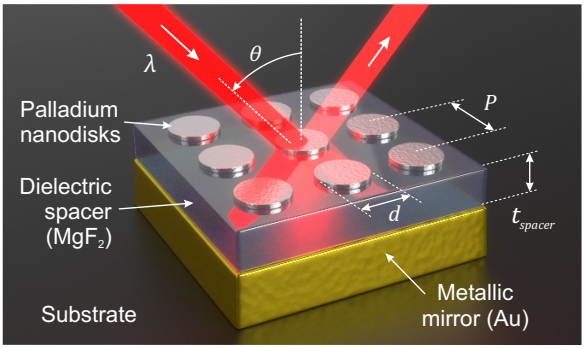

Figure 8.3. Schematic of the plasmonic hydrogen sensor structures considered in this chapter. Palladium (Pd) nanodisks are separated from a metallic mirror (gold) by a dielectric spacer layer (magnesium fluoride, MgF_2). Upon hydrogen absorption, the dielectric function and the size of the Pd nanodisks change, leading to a change in the reflectance spectrum of the structure.

One highly promising type of sensor geometry is the so-called *perfect absorber* layout, as shown in, for example, Ref. [41] and in publication P9. In this design, an array of Pd nanostructures is separated by a dielectric spacer layer from a metallic film, which acts as a mirror (see Figure 8.3). Using this nanostructure layout, it is possible to achieve near-unity absorption through careful tuning of the design parameters (hence the name), as shown in, e.g., Refs. [61, 192] and publication P6. In the literature, one often finds the argument for using 'perfect absorber' nanostructures for gas sensing that a very high *relative* change in the optical reflectance upon H_2 exposure

can be obtained [41]. This reasoning, however, does not take into account the *noise* in the sensor response, i.e., in the reflectance $R(\lambda, p_{H_2})$ of the sensor substrate. The noise is an important factor in the case of a simple, single-wavelength readout scheme based on, e.g., an LED light source and a photodiode (PD), rather than centroid wavelength tracking in spectroscopic measurements. Such a single-wavelength, fiber-based sensor design was demonstrated and extensively tested in the work published in P15. In order to minimize the lowest detectable amount of hydrogen, the signal-to-noise ratio (SNR) of the detected signal must be maximized, since it defines the lowest distinguishable signal. In the following section, we will investigate in detail how this goal can be reached.

8.2 DERIVATION OF THE SIGNAL-TO-NOISE RATIO (SNR)

In the optical signal of a single-wavelength optical hydrogen sensor, as described above, the plasmonic sensor substrate exhibits a certain reflectance $R(\lambda, p_{H_2})$ as a function of the hydrogen partial pressure p_{H_2} in the environment. At nonzero p_{H_2}, absorption of hydrogen by the palladium nanoparticles leads to a change in R. From this, one can define the *absolute* as well as the *relative* difference in reflectance as

$$\Delta R_{abs} = R(p_{H_2}) - R_0, \tag{8.2}$$

and

$$\Delta R_{rel} = \frac{R(p_{H_2}) - R_0}{R_0}, \tag{8.3}$$

respectively. Here, $R_0 = R(p_{H_2} = 0)$ is the reflectance in the absence of hydrogen gas.

The central question that this section aims to answer is: **which of these two quantities does one have to optimize in order to maximize the signal-to-noise ratio of the detector?**

Here, we consider a simple single-wavelength sensor that consists of an LED with intensity $I(\lambda)$, a sensor substrate with reflectance $R(\lambda, p_{H_2})$, and a photodiode connected to electronic readout circuit with gain G, as schematically shown in Figure 8.4. This means that at any given time, the detected voltage U is:

$$U(\lambda, p_{H_2}) = I(\lambda) \cdot R(\lambda, p_{H_2}) \cdot G. \tag{8.4}$$

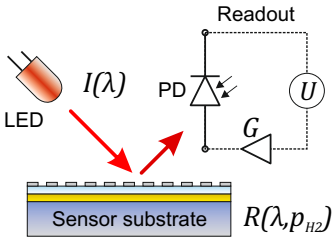

FIGURE 8.4. Schematic representation of an optical plasmonic hydrogen sensor with a single-wavelength readout based on an LED and a photodiode. The measured voltage U is proportional to the LED intensity I, the reflectance R, and the readout circuit gain G.

Each of these three quantities will have some level of noise. In a first-order approximation, this noise is independent of the actual value of each quantity. Inserting these signal noises (and omitting the notation of λ and p_{H_2} for the sake of readability), we obtain the measured voltage plus noise:

$$U + \delta U = (I + \delta I) \cdot (R + \delta R) \cdot (G + \delta G). \tag{8.5}$$

The noise level δU can be estimated as follows:

$$\begin{aligned} \delta U &= \frac{dU}{dI}\delta I + \frac{dU}{dR}\delta R + \frac{dU}{dG}\delta G \\ &= RG \cdot \delta I + IG \cdot \delta R + IR \cdot \delta G, \end{aligned} \tag{8.6}$$

from which we can calculate the *root-mean-square noise*:

$$\begin{aligned} \sqrt{\langle \delta U^2 \rangle} &= \sqrt{(RG\langle \delta I \rangle + IG\langle \delta R \rangle + IR\langle \delta G \rangle)^2} \\ &\approx \sqrt{R^2G^2\langle \delta I^2 \rangle + I^2G^2\langle \delta R^2 \rangle + I^2R^2\langle \delta G^2 \rangle}. \end{aligned} \tag{8.7}$$

In this last simplification, all terms that contain products of different noise levels have been omitted. As long as the three different noise sources are uncorrelated, this can be done since these product terms cancel out and the resulting mean is zero. In the case of the hydrogen sensor considered here, one can safely assume that the light source, sample, and detector noise are uncorrelated.

The *signal* S that is obtained in the end as a function of the hydrogen concentration is the *difference* between the detected voltage and the zero-level voltage:

$$S\left(p_{\mathrm{H}_2}\right) = \Delta U = U\left(p_{\mathrm{H}_2}\right) - U_0. \tag{8.8}$$

In order to achieve a detectable signal at a certain hydrogen concentration, this signal must be bigger than the noise in S; in other words, the SNR must be bigger than one:

$$\mathrm{SNR} = \frac{S}{\sqrt{\langle \delta S^2 \rangle}} > 1. \tag{8.9}$$

The signal noise δS follows from error propagation (leaving out the root-mean-square notation):

$$\delta S = \sqrt{\left(\delta U\left(p_{\mathrm{H}_2}\right)\right)^2 + \left(\delta U_0\right)^2}. \tag{8.10}$$

Assuming that $\delta U\left(p_{H_2}\right)$ is constant, this means that

$$\sqrt{\langle \delta S^2 \rangle} = \sqrt{2\langle \delta U^2 \rangle}. \tag{8.11}$$

It should be mentioned that this is not entirely true: As equation 8.6 shows, the reflectance (and thus p_{H_2}) *does* influence the voltage noise δU. However, as the changes in R close to the detection limit are very small, the assumption that $\delta U\ (R) = \delta U\ (R_0)$ can safely be made for any practical purpose.

Inserting equations 8.4 and 8.6 into equation 8.9, we obtain:

$$\begin{aligned} \mathrm{SNR} &= \frac{IG \cdot \Delta R_{\mathrm{abs}}}{\sqrt{2(R^2G^2\langle \delta I^2 \rangle + I^2G^2\langle \delta R^2 \rangle + I^2R^2\langle \delta G^2 \rangle)}} \\ &= \frac{\Delta R_{\mathrm{abs}}}{R\sqrt{2\left(\frac{\langle \delta I^2 \rangle}{I^2} + \frac{\langle \delta R^2 \rangle}{R^2} + \frac{\langle \delta G^2 \rangle}{G^2}\right)}}. \end{aligned} \tag{8.12}$$

Now we can use equation 8.12 to judge what we have to do in order to *maximize the SNR*, which is how we optimize the sensitivity of our detector. In fact, there are two distinct cases:

1. The noise in the *detector*, meaning the LED, the photodiode and the readout circuit, is prevalent, so that δI and δG (or even only one of these quantities) is larger than the noise in the substrate reflectance δR:

$$\mathrm{SNR} \approx \frac{\Delta R_{\mathrm{abs}}}{R\sqrt{2\left(\frac{\langle \delta I^2 \rangle}{I^2} + \frac{\langle \delta G^2 \rangle}{G^2}\right)}}. \tag{8.13}$$

   Maximizing the SNR can in this case be done by **maximizing** ΔR_{abs}, but also by **minimizing** R. It could thus be beneficial to choose a sensor design which gives the lowest possible reflectance, even if this comes at the expense of a lower ΔR_{abs}.

2. The detector noise be effectively eliminated. In this case, fluctuations of the substrate reflectance (due to any environmental factors such as the temperature, the gas flow rate, or aging of the substrate) play the most important role:

$$\mathrm{SNR} \approx \frac{\Delta R_{\mathrm{abs}}}{R\sqrt{2\frac{\langle \delta R^2 \rangle}{R^2}}} = \frac{\Delta R_{\mathrm{abs}}}{\sqrt{2 \cdot \langle \delta R^2 \rangle}}, \tag{8.14}$$

where R drops out of the equation. We thus only want to maximize the **absolute** reflectance change ΔR_{abs}, while the value of R_0 does not make any difference.

One can safely assume that the *second* case is the more realistic one. A virtually noiseless signal is achievable through careful engineering of the detector hardware and electronics, using e.g. balanced detection [193] or lock-in detection techniques. We consequently learn from this analysis that the primary aim should be to maximize ΔR_{abs}. Of course, if one has to choose between two sensor designs that provide the same ΔR_{abs} at different reflectances R_0, one might argue that the lower R_0 is the better option, but this should *not* be the primary target.

We will thus focus on the question of how ΔR_{abs} can be maximized through tuning of the relevant design parameters. Specifically, we use ensembles of Pd nanodisks on a magnesium fluoride (MgF_2) spacer and a gold mirror as a model system to study the influence of various design parameters. In a first step, we perform numerical calculations on this system to gain a better understanding of the optical response and the underlying physical principles, and to predict an optimum sensor design. We then compare these calculations to microspectroscopic reflectance measurements. As a further step, we extend the measurement setup for Fourier-plane spectroscopy, which enables us to record angle-resolved reflectance spectra and thus to investigate the influence of the readout angle θ on the sensing performance.

In the remainder of this chapter we will use ΔR to indicate ΔR_{abs}.

8.3 NUMERICAL CALCULATIONS

To gain better insight into the optical response of the 'perfect absorber' palladium nanostructures, we carry out numerical calculations using a MATLAB-based in-house implementation of the scattering matrix approach, also known as the Fourier modal method or rigorous coupled-wave analysis [194].

Figure 8.5 shows a pseudocolor plot of the reflectance as a function of the wavelength λ and the thickness of the spacer layer t_{spacer} at normal incidence. The disk diameter d_{disk} has been fixed at 195 nm. The disk height h_{disk} considered in all calculations is 20 nm, and the structures are periodically arranged with a periodicity P of 300 nm.

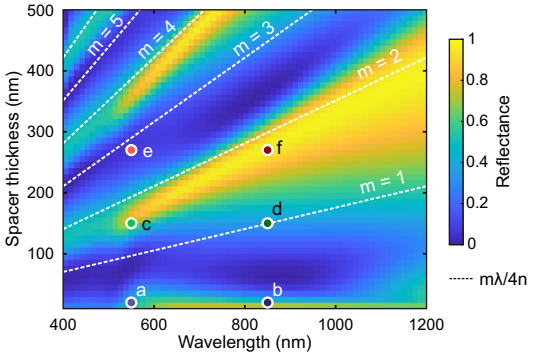

FIGURE 8.5. Calculated reflectance spectra for varying spacer thicknesses, for a disk diameter of 195 nm, a disk thickness of 20 nm, and a periodicity of 300 nm. The dashed white lines indicate the spacer thicknesses necessary to fit $m/4$ wavelengths into the cavity formed by the mirror and the disk array.

The shape of the reflectance plot highlights the importance of the spacer thickness, i.e., the *coupling distance* between the plasmonic nanostructures and the mirror. The dashed white lines show the function $t_{\text{spacer}} = m\lambda/4n$ for different integer values of m, with n being the refractive index of MgF_2 [195]. These lines demonstrate that the reflectance as a function of t_{spacer} exhibits a periodic behavior with a period of $\lambda/2n$, within which one reflectance minimum (perfect absorption) and one reflectance maximum occur. This behavior has been described before in similar coupled antenna-film systems and can be explained by different coupling models, depending on the spacer thickness [86, 196–200]. At small distances between the disks and the mirror, the plasmon resonance in the nanoantennas induces a mirror plasmon in the metal film, leading to near-field coupling between the plasmon and the mirror plasmon and thus to a spectral shift [196].

8.3.1 *Electric field distribution*

To visualize the electric field distribution in the structures, we performed finite-element simulations using CST MICROWAVE STUDIO. Figure 8.6 depicts the electric field enhancement in a cross-section through one unit cell of the structure for two different wavelengths, at three different spacer thicknesses. The incident light is polarized along the x axis in all cases. A radius of 3 nm is used at the edges of the nanodisks to avoid artifacts due to the sharp corners.

When the spacer is relatively thin (Figures 8.6(a,b)), the extent of the electric field enhancement reaching from the plasmonic hotspots at the disk to the mirror charges in the Au layer is clearly visible in this case. At increasing spacer thicknesses, however, a transition to the far-field coupling regime occurs. Here, the structure can be described as a Fabry-Perot cavity with resonating mirrors. The distribution of the electric field enhancement in a thicker spacer (Figures 8.6(d-g)) illustrates the mechanism behind the far-field reflectance, as a standing wave occurs within the cavity formed by the plasmonic layer and the mirror. If an electric field *minimum* exists at the z position of the disks, this means that the incident and reflected waves interfere destructively at this position. This renders the nanoantennas practically invisible for the incident light, so that the reflectance is effectively determined by the mirror. In the case of a Au mirror, this means that the reflectance approaches unity at $\lambda > 600$ nm, and the reflectance at lower wavelengths is dominated by the d-band transition of Au (see Section 4.1.1). If the disks are located in an electric field *maximum*, the resonance condition for the cavity is met, leading to 'perfect absorption' and thus to a reflectance minimum.

A detailed description of this multilayer system can be found in the works of Weiss [201], Ameling and Giessen [198], Bhattarai [202], and, more recently, Berkhout and Koenderink [200]. Essentially, the cavity can be described in terms of the *phase shift* of the electromagnetic wave while passing through the cavity, which is composed of the phase shifts due to propagation through the spacer ($\Delta\phi_{\text{prop}}$), reflection at the mirror-spacer interface ($\Delta\phi_{\text{refl}}$), and reflection at the plasmonic layer due to plasmon excitation ($\Delta\phi_{\text{exc}}$). This leads to the following expression for the resonance wavelength of the cavity [198]:

$$\Delta\phi_{\text{total}} = 2\Delta\phi_{\text{prop}} + \Delta\phi_{\text{refl}} + \Delta\phi_{\text{exc}} \stackrel{!}{=} (m+1)\cdot 2\pi, \tag{8.15}$$

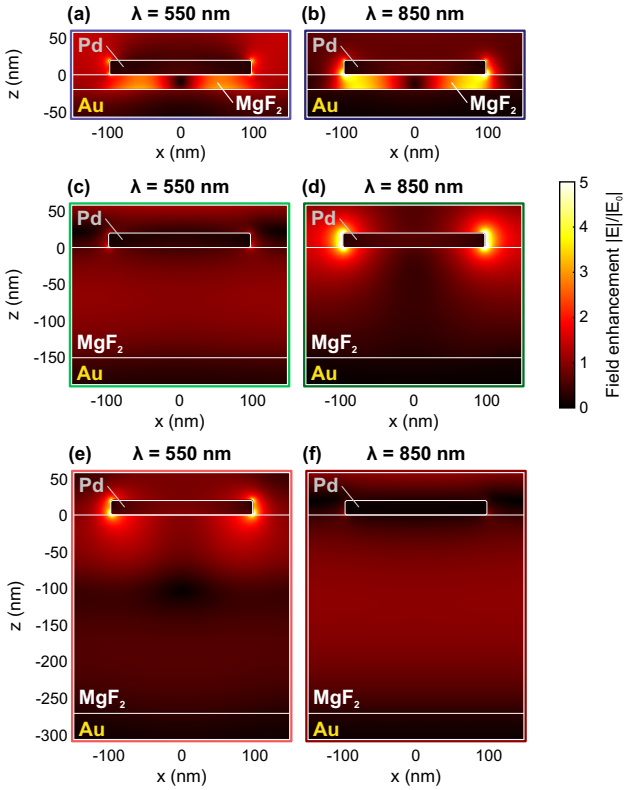

Figure 8.6. Electric field enhancement distributions for selected wavelengths and spacer thicknesses, indicated by the colored and labeled dots in Figure 8.5. At a spacer thickness of 20 nm, one can observe coupling between the Pd disk and the Au mirror (a,b). Structures with thicker spacers, such as 150 nm (c,d) and 270 nm (e,f), act as cavity resonators. If the disk array is positioned in a minimum of the electric field, the disk array is effectively transparent and the far-field response is dominated by the mirror (c,f). If the disk array is in a maximum of the electric field, coupling of the LSPR to the cavity resonance leads to an absorption maximum (d,e).

where $\Delta\phi_{\text{prop}} = 2\pi n_{\text{spacer}} t_{\text{spacer}}/\lambda$, and $\Delta\phi_{\text{refl}}$ can be computed via the Fresnel equations [3]. This means that the plasmon resonance in the Pd disks only influences the phase shift upon reflectance at the plasmonic layer, $\Delta\phi_{\text{exc}}$. This shift is a more complex function involving the plasmon resonance wavelength and damping, as well as the filling fraction of plasmonic

nanoantennas, through an effective medium model. This model provides an explanation for the shape of the $R(\lambda, t_{\text{spacer}})$ 'landscape', and the deviation from the exact course of the $t_{\text{spacer}} = m\lambda/4n$ lines since an additional, wavelength-dependent phase shift is introduced by the plasmon resonance. This resonance, in turn, is influenced by the size, shape, and arrangement of the nanoparticles, as well as their dielectric function.

8.3.2 *Sensor signal*

The next step is to investigate the behavior of the *reflectance difference* ΔR due to hydrogen absorption. To this end, we perform scattering matrix calculations on the same system as in Figure 8.4, but with the dielectric function of the Pd disks replaced by β phase PdH [172]. Furthermore, we take into account the increased lattice constant of PdH compared to Pd, approximated as an isotropic volume expansion of 10%. Since the transition from α phase to β phase PdH_x typically occurs in particles at H_2 concentrations (in N_2 at room temperature) of around 2% (see Section 8.1.1), the system thus represents a Pd perfect absorber structure in the presence of a relatively high concentration of H_2. Figure 8.7 shows the resulting $R(\lambda, t_{\text{spacer}})$ plot for Pd (a) and PdH (b) disks, in this case with a diameter of 160 nm. The optical response of an array of Pd/PdH disks on an infinitely thick MgF_2 layer *without* a mirror, thus without coupling to any cavity, is shown in the one-dimentional pseudocolor plots below the main plots.

Equivalent calculation results of ΔR for other disk diameters are shown in Figure 8.8. These data show that the maximum signal decreases as the disks get very small, but between the larger disk sizes there is no significant difference anymore. Furthermore, an increasing disk diameter, via the redshift of the plasmon resonance of the Pd disks, shifts the ΔR 'landscape' towards higher wavelengths. Tuning the disk size thus offers another method of influencing the sensor signal.

A comparison of the bare disks to the disk-spacer-mirror system (Figure 8.7) reveals how the plasmon resonance influences the behavior of the perfect absorber: Only at wavelengths where the nanoantennas are plasmonically active (thus inducing a significant transmittance modulation in the absence of a mirror), strong modulation of the reflectance as a function of the spacer thickness is reached. If the plasmon resonance undergoes a shift due to the absorption of hydrogen, the resonance condition (equation 8.15) is changed, leading to a shifted 'landscape' of $R(\lambda, t_{\text{spacer}})$, as shown

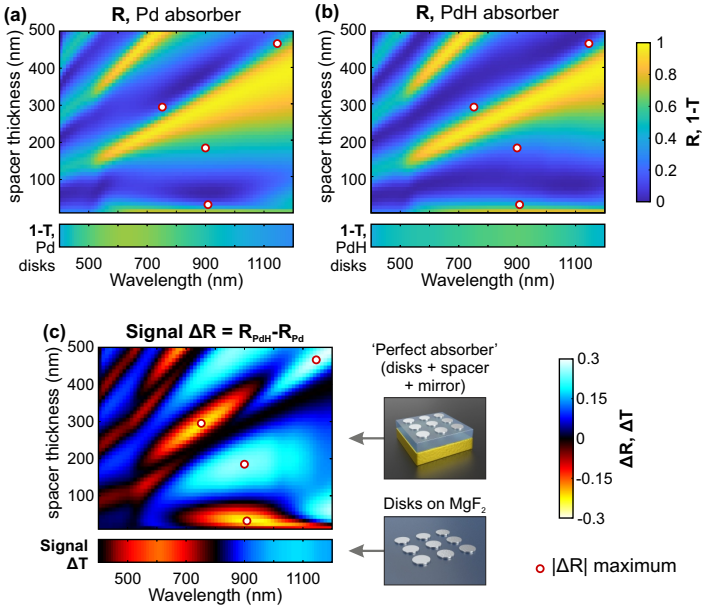

FIGURE 8.7. (a) Calculated reflectance spectra for varying spacer thicknesses for Pd disks with a diameter of 160 nm, at a periodicity of 300 nm. (b) Calculated reflectance spectra for the same structures as in (a), with β phase PdH instead of Pd disks and taking into account a volume expansion of 10%. (c) Plot of the resulting reflectance difference vs. spacer thickness and wavelength. The positions of some exemplary local maxima of $|\Delta R|$ are indicated in all three plots. 1D pseudocolor below the 2D plots show the transmittance of Pd and PdH disks on a substrate and the corresponding signal ΔT. A comparison with the absorber signal (c) shows how the disk-mirror structure can approximately double the maximum optical response.

in Figure 8.7(b). The resulting reflectance difference ΔR is displayed in Figure 8.7(c), along with the equivalent ΔT for bare disks. The positions of four exemplary $|\Delta R|$ maxima are indicated in Figure 8.7(a-c). These positions reveal a key feature of the system: *The highest reflectance differences are obtained at points in between the reflectance minima and maxima.* This implies that the shifting plasmon resonance has the strongest influence on the far-field reflectance neither at the strongest nor at the weakest interaction between the incoming light and the plasmonic antennas. In other words, when the aim is to maximize $|\Delta R|$ (see Equation 8.14), trying to obtain perfect absorption at the readout wavelength is in fact counterproductive.

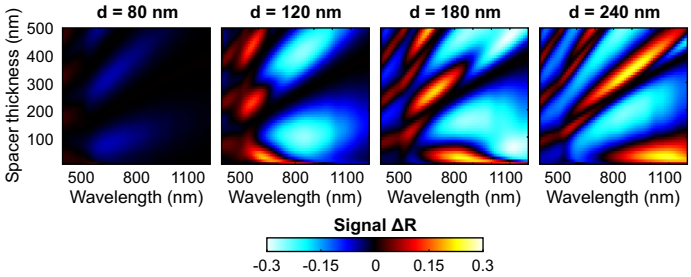

Figure 8.8. Calculated sensor signal ΔR vs. wavelength and spacer thickness for four different disk diameters, at a periodicity P of 300 nm.

Furthermore, a comparison of ΔR with ΔT reveals how the disk-cavity geometry can bring major improvement over a simple transmissive disk array: The maximum $|\Delta R|$ values exceed the maximum $|\Delta T|$ values by almost a factor of two. An intuitive explanation is that the photonic cavity can strongly enhance the interaction of the light with the nanoantennas, leading to a stronger influence on the amount of light that is reflected. However, the interaction can be decreased as well, meaning that the spacer thickness needs to be chosen carefully, taking into account the envisioned readout wavelength of the sensor. The data shown in Figures 8.7(c) and 8.8 thus provide an important guide to choosing the correct parameters.

8.4 Experimental Section

8.4.1 *Sample fabrication*

To verify the numerical results and study the behavior of perfect absorber hydrogen sensors at different H_2 concentrations, we fabricate Pd nanodisk arrays on substrates with an Au mirror and MgF_2 spacers of different thicknesses (60, 110, 160, 210, and 290 nm). Thicker spacer layers were fabricated as well, but these proved unusable due to cracking of the MgF_2 layer. The samples are fabricated by evaporating 120 nm of Au followed by the appropriate thickness of MgF_2 onto plasma-cleaned glass substrates with a Pfeiffer Vacuum PLS 500 electron-beam-assisted evaporation system. These substrates are then annealed for 4 hours at 400° C, as annealing has been shown to increase the MgF_2 film quality [203]. Afterwards, substrates are spin-coated with photoresist (PMMA) for patterning in a RAITH ELINE

PLUS electron-beam lithography system (see Section 4.3.2). After resist development, a 20 nm thick layer of Pd is evaporated onto all substrates simultaneously, followed by resist lift-off in NEP. The fabricated samples contain nanodisk arrays of $100 \times 100\ \mu m^2$ with different disk diameters and periodicities. Figure 8.9 shows several examples of microscope photographs of the finished samples. In a last step, a part of each sample is covered and an 80 nm thick Au layer is deposited on the uncovered part, which is used for spectral referencing (see Section 3.3.1).

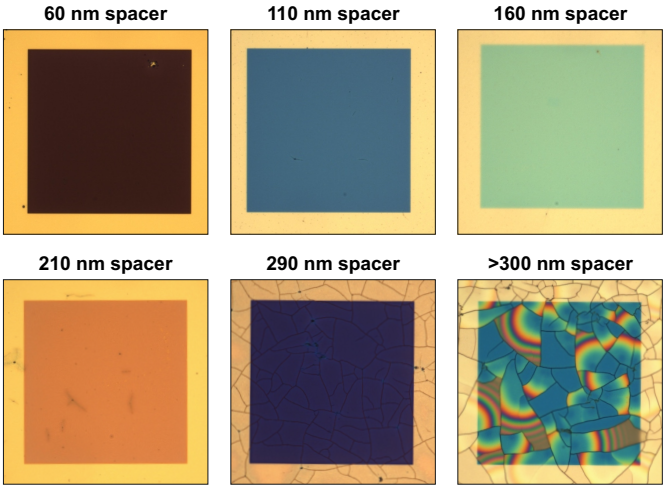

FIGURE 8.9. Microscope images (taken in air) of the fabricated sensor structures with $P = 300$ nm, $d_{disk} = 202 \pm 7$ nm. Each field is $100 \times 100\ \mu m^2$ in size. The changing reflectance spectrum manifests itself in the visible color. As the spacer thickness increases, cracking of the MgF_2 can be observed. At spacer thicknesses exceeding 300 nm, this cracking causes the formation of bending and detaching MgF_2 flakes. The resulting variation in cavity length leads to strongly varying brilliant colors (but also renders the sample unusable for reliable H_2 sensing).

Figure 8.10 shows several examples of SEM images of the fabricated sensor structures. For the experiments shown in this chapter, nanodisk arrays with two different periodicities (300 nm and 500 nm) and with different disk diameters in the range from 60 to 220 nm. The exact disk diameter, which can deviate from the target size, is determined by analysis of SEM images.

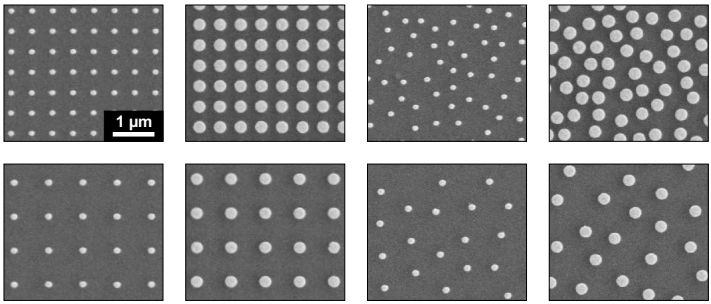

FIGURE 8.10. SEM images of fabricated sensor structures. Arrays of different periodicities P and different disk sizes were fabricated, as well as randomized ensembles with different minimum distances s_{min}. The scale bar is valid for all images.

Apart from these periodic arrays, randomized ensembles were fabricated as well. To this end, a set of randomized positions was generated using a simplified version of the so-called random sequential adsorption (RSA) model, which can be used to simulate the effect of colloidal fabrication processes [204]. In our implementation of the model, particles are placed at randomized (x, y) coordinates, under the condition that a predefined minimum spacing $s_{\min}$ between adjacent particles is maintained. The value of $s_{\min}$ is chosen such that the number of particles per unit area is the same as in the ordered case (corresponding to 250 nm and 420 nm for $P = 300$ nm and 500 nm, respectively).

8.4.2 *Reflectance measurements*

Reflectance measurements in a wavelength range from 400 to 1000 nm are performed in a microspectroscopy setup that consists of a Nikon ECLIPSE TE2000-U inverted microscope combined with a Princeton Instruments SP2500 grating spectrometer and a PIXIS-256E detector (see Figure 8.11). An ultra-stable laser-driven white light source (Energetiq EQ-99XFC) is used to illuminate the sample via a 60× microscope objective (NA = 0.7). The light is tightly focused onto the center of the back focal plane (BFP) of this objective to ensure near-normal incidence, which is necessary for a good comparability to the numerical calculations. A field stop in the illumination path is used to limit the illuminated area to a single 100×100 µm^2 array, so that no

stray light from outside the array can influence the measurement. The collected image is then projected onto the entrance slit of the spectrometer, as described in Section 3.3.1. At a later stage, the setup is extended for angle-resolved reflectance measurements.

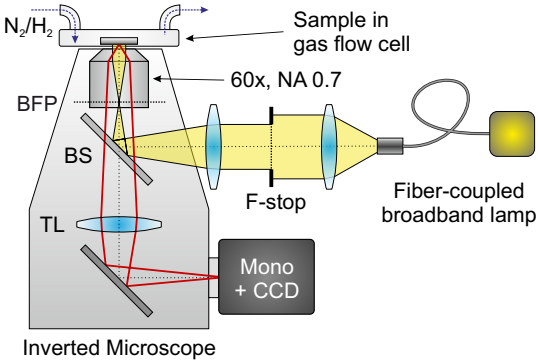

FIGURE 8.11. Schematic of the microspectroscopy setup, consisting of an inverted microscope and a grating spectrometer (monochromator + CCD camera). Light from a broadband light source is focused onto the back focal plane (BFP) of the objective to ensure normal incidence for good comparability with numerical calculations. The sample plane is directly imaged onto the entrance slit of the monochromator (red lines). (BS: beam splitter, TL: tube lens, F-stop: field stop)

During these optical measurements, the sample is situated in a home-made gas flow cell with thin microscopy windows, which is initially flooded with pure nitrogen at a flow rate of 1 nL/min (liter normal per minute) at room temperature. Using Bronkhorst mass flow controllers, different concentrations of hydrogen gas can be added to this gas flow, while keeping the total flow rate constant at atmospheric pressure.

Figure 8.12 shows the measured reflectance spectra for Pd disk arrays with $d_{\mathrm{disk}} = 202 \pm 7$ nm, at a periodicity of 300 nm, for the five different spacer thicknesses. Reflectance measurements were carried out once in pure nitrogen (blue curves) and once at a hydrogen concentration of 5% in N_2 (red curves) at atmospheric pressure. The corresponding calculated spectra are displayed as dashed lines, showing excellent overall agreement. In each plot, the wavelength at which the highest reflectance difference is

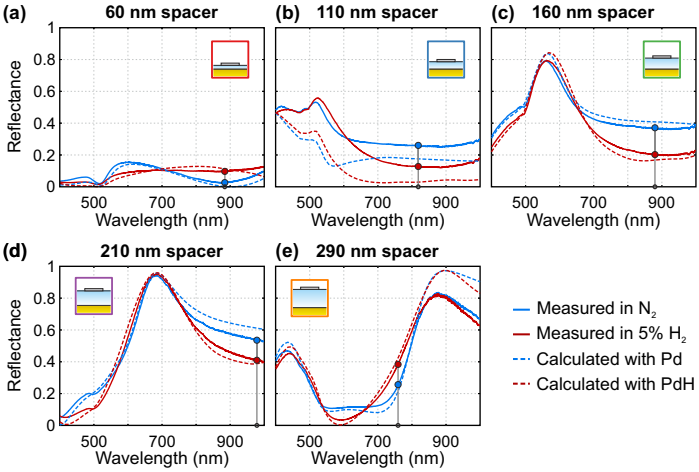

Figure 8.12. Measured (solid lines) and calculated (dashed lines) reflectance spectra for spacer thicknesses between 60 and 290 nm, at $P = 300$ nm, in pure N_2 and in an atmosphere of 5% H_2 gas in N_2. The Pd disk diameter is 202 ± 7 nm. The largest measured reflectance difference is indicated in each plot. Color photographs of each field can be found in Figure 8.9.

obtained is highlighted. One interesting feature is that the spectral position of $\max(|\Delta R|)$ is always achieved in the higher wavelength range, above approximately 700 nm. This effect, which can also be observed in Figure 8.7, can be explained by looking at the dielectric functions of Pd and PdH, as shown in Figure 8.2 [172]. These data reveal that the difference between the dielectric function of Pd and PdH is also highest in this wavelength range, especially in the imaginary part ε_2. This suggests that to maximize $|\Delta R|$, the readout wavelength should be chosen in a range where the modulation of the dielectric function due to hydrogen absorption is as high as possible.

Figure 8.13 depicts the influence of the disk diameter on the maximum reflectance difference for each spacer thickness. Apart from the fact that the highest signal (approx. 17% reflectance difference) is obtained with a spacer thickness of 160 nm, these curves indicate that the disk diameter significantly influences the maximum signal up to around 150 nm, after which increasing the disk diameter further does not yield great improvements anymore. This can be understood by the information presented in Section 8.3.2: If the disks are too small, the plasmon resonance occurs at small wavelengths and does not lead to a significant modulation of R due to the strongly decreased

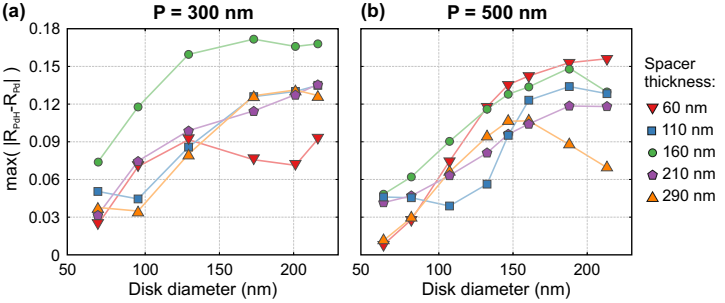

Figure 8.13. Maximum of the measured reflectance difference vs. disk diameter for the five different spacer thicknesses shown in Figure 8.12, for a periodicity of 300 nm (a) and 500 nm (b).

scattering cross-section. Since the plasmon resonance has only an indirect influence on the cavity resonance condition (equation 8.15) and is rather broad anyway, changing the disk diameter does not have a very strong influence on ΔR when the disks are plasmonically active in the wavelength range above approx. 700 nm.

Figure 8.14 displays the spectral shapes of ΔR for spacer thicknesses of 60 and 160 nm, respectively, for a H_2 concentration of 5% as well as 0.5% in N_2. At this lower concentration, the Pd lattice is not saturated with hydrogen; instead, isolated hydrogen atoms are located at interstitial lattice sites (α phase). In addition to a smaller change in ε compared to Pd, the

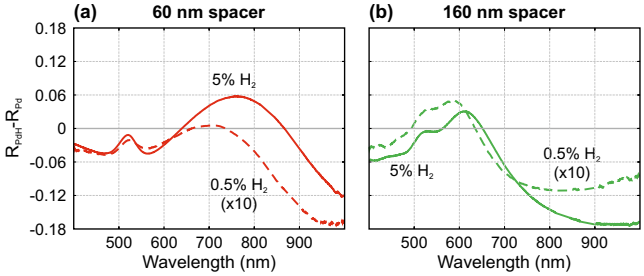

Figure 8.14. Reflectance difference obtained at a high (5%) and a low (0.5%) H_2 concentration for spacer thicknesses 60 nm and 160 nm (disk diameter 174 ± 6 nm). The optimum readout wavelength is not necessarily the same for different concentration ranges of interest.

lattice expansion is much smaller than in the β phase. Interestingly, this does not only lead to a reduced absolute ΔR value, but also to a spectral shift of ΔR. This constitutes another important design principle, namely, that *the hydrogen concentration range of interest must be taken into account for optimizing the sensor*. In a threshold warning sensor that should trigger an alarm when the hydrogen concentration is close to the lower explosion

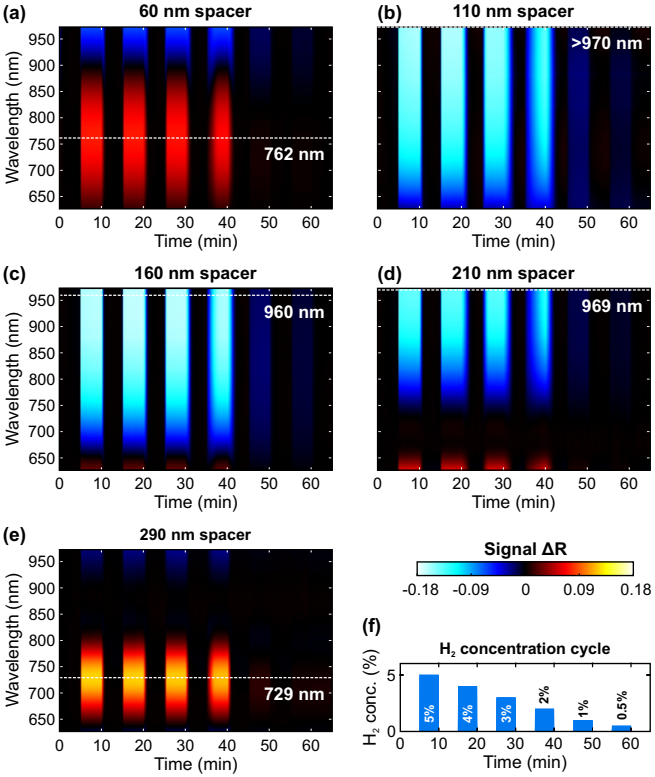

FIGURE 8.15. Measured reflectance differences vs. wavelength and time during hydrogen concentration cycles for all five spacer thicknesses (a-e). Hydrogen concentrations are decreasing from 5% to 0.5% (5000 ppm) in N_2 (f). The Pd disk diameter is 174 ± 6 nm. The wavelength of maximum reflectance difference is indicated in each plot.

threshold, a different sensor design and/or readout wavelength might be required when compared with a sensor meant to reliably detect trace amounts of H_2 in the sub-100 ppm range.

To study the performance of the different sensor geometries at different hydrogen concentrations, we perform time-resolved reflectance measurements during hydrogen concentration cycling. In a typical hydrogen concentration cycle, hydrogen is mixed into the N_2 gas flow at intervals of several minutes, at decreasing concentrations. Hydrogen exposure periods are always separated by several minutes of pure N_2 flow to ensure that the sample goes back to its original state and to avoid hysteresis effects between the absorption and desorption. Figures 8.15(a-e) show pseudocolor plots of the obtained reflectance difference versus wavelength and time for t_{spacer} values of 60 and 160 nm and $d_{disk} = 174 \pm 6$ nm, at H_2 concentrations decreasing from 5% to 0.5%. The reflectance in the absence of H_2 is determined by averaging over all spectra recorded before the first hydrogen exposure, and this spectrum is subtracted from all measured spectra to obtain ΔR. Background correction is performed by fitting a polynomial surface to all data points in the N_2

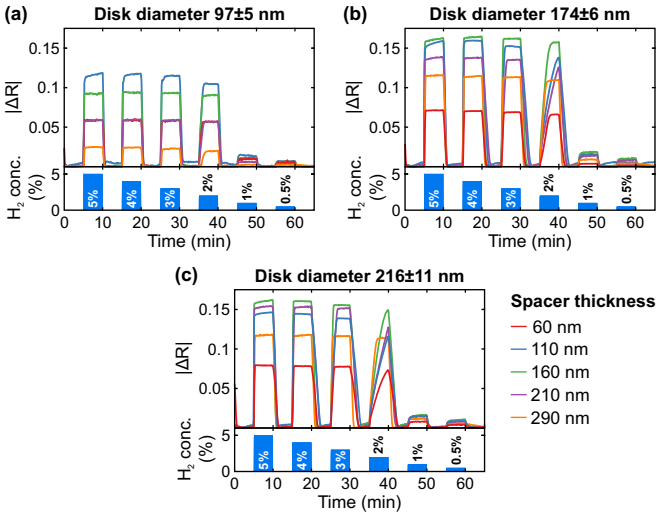

Figure 8.16. Time traces of maximum $|\Delta R|$ during hydrogen concentration cycles (5% to 0.5% in N_2), extracted at the optimum wavelength (see Figure 8.15) for three different disk diameters. For each spacer thickness, the three nanodisk arrays with different disk diameters were measured simultaneously.

exposure periods, excluding times with a strong signal change during hydrogen unloading. From these spectral measurements, the optimum readout wavelength is determined, which is indicated in each plot.

Figure 8.16 shows time traces of the resulting maximum $|\Delta R|$, for all five spacer thicknesses, for three different disk diameters. The $|\Delta R|$ values are determined by convoluting the spectral data (as shown in Figure 8.15) with Lorentzian curve with a linewidth of 10 nm, to mimic the behavior of an actual LED-based sensor. The transition from α to β phase at a hydrogen concentration of 2% (see Section 8.1.1) is clearly visible. At this concentration, the time trace data show a difference in response time for the different disk diameters, with the largest disks exhibiting the slowest hydrogen loading and unloading. This is consistent with the change in hydride formation thermodynamics for different Pd particle sizes that is widely reported in the literature [124, 140, 205]. Furthermore, larger disks show a more thin film-like behavior, in which substrate clamping effects play an increasingly

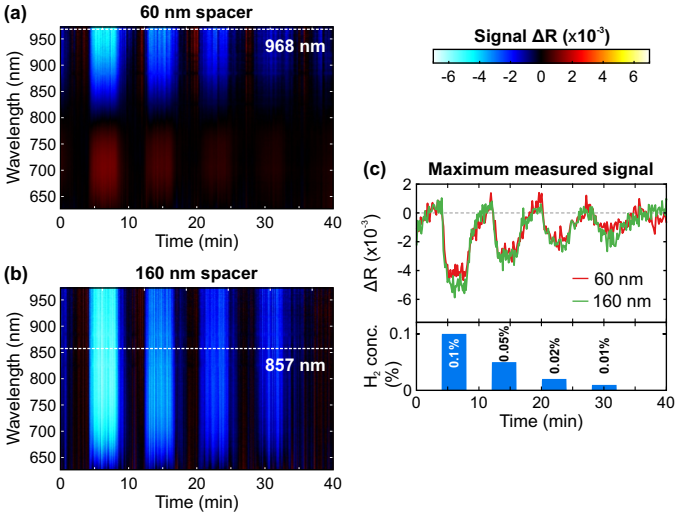

Figure 8.17. (a,b) Measured reflectance differences vs. wavelength and time during hydrogen concentration cycles for spacer thickness 60 nm and 160 nm. Hydrogen concentrations are decreasing from 0.1% to 0.001% (1000 ppm - 100 ppm) in N_2. The Pd disk diameter is 174 ± 6 nm. The wavelength of maximum reflectance difference is indicated in each plot. (c) Time traces of maximum $|\Delta R|$, extracted at the optimum wavelength determined from the measurements in (a,b).

important role, which can influence the nature of the phase transition as well as the absorption-desorption hysteresis [181]. In other words, even though the disk diameter has only a limited influence on the maximum signal above a certain threshold (see Figure 8.13), it *does* influence the sensor response time and should thus not be chosen too large.

Figure 8.17 depicts spectral measurements of ΔR vs. time for the nanodisk arrays that show respectively the lowest and highest response in Figure 8.15, but during a hydrogen cycle at much lower hydrogen concentrations, decreasing from 0.1% (1000 ppm) to 0.01% (100 ppm). Following the insights from Figure 8.14, a separate optimum readout wavelength is determined for this concentration range, and the resulting measured signal is displayed in Figure 8.17(c). Interestingly, the difference between the two spacer thicknesses is much lower than for higher H_2 concentrations in this case. A possible explanation is that the actual maximum of $|\Delta R|$ has shifted out of the accessible wavelength range and is thus not recorded. Nevertheless, these measurements prove that even a low hydrogen concentration of 100 ppm can lead to a detectable optical signal, with a $|\Delta R|$ in the order of 10^{-3}. It is important to note that the signal noise in the data shown here originates purely from the microspectroscopy setup. It has nothing to do with the signal-to-noise ratio in an actual LED-based sensor and thus does not define any lower limit for the detectable hydrogen concentration.

8.4.3 *Angle-resolved measurements*

So far, we have discussed the influence of important structure parameters, namely, the spacer thickness and the disk diameter, and of the hydrogen concentration range of interest. We have, however, not yet taken into account the optical readout angle θ (see Figure 8.3), which is another important parameter in real-world sensor realizations. In particular, when lattice diffraction effects play a role, the angle can significantly influence the detected signal.

To perform angle-resolved reflectance measurements, we adapt the microspectroscopy setup for Fourier-plane imaging spectroscopy (Figure 8.18). A modified 4-f setup projects the Fourier plane, which is conjugated to the objective back focal plane (see Section 2.3) instead of the image plane onto the entrance slit of the spectrometer [1, 13]. The illumination geometry is modified to illuminate the full objective BFP. The CCD camera of the spectrometer records a wavelength-resolved image of the central slice through the Fourier plane. This means that a reflectance spectrum is obtained for

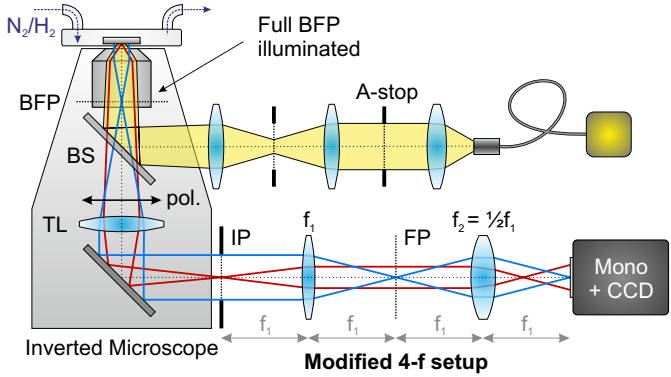

Figure 8.18. Schematic of the k-space microspectroscopy setup used for angle-resolved reflectance measurements, consisting of an inverted microscope and a grating spectrometer (monochromator + CCD camera). Light from a broadband light source is focused onto the substrate, while the full BFP is illuminated; ensuring simultaneous illumination from all available angles. The Fourier plane instead of the image plane is imaged onto the spectrometer entrance slit using a modified 4-f setup, as indicated by the red and blue rays. (BS: beam splitter, TL: tube lens, F-stop: field stop, A-stop: aperture stop, IP: image plane, FP: Fourier plane, pol.: polarizer)

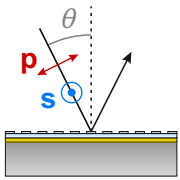

Figure 8.19. Definition of s and p polarization.

each collection angle in one shot, as described in Section 3.3.3. The highest collection angle is defined by the objective NA of 0.7, which corresponds to $\theta_{max} \approx 44°$. Polarization-resolved measurements are recorded by inserting a linear polarizer behind the objective.

The results of angle-dependent reflectance measurements are shown in Figure 8.20(a) for Pd disk arrays with a period P of 300 nm, for s and p polarization (see Figure 8.19). Pseudocolor plots of the reflectance in pure N_2 are displayed for three different spacer thicknesses (60, 160, and 290 nm) in Figure 8.20(a), along with the reflectance difference ΔR obtained at a H_2

concentration of 5%. The reflectance plots at P = 300 nm clearly show how the reflectance spectrum undergoes a blueshift when the angle increases, which is to be expected for Fabry-Perot-like cavity resonators. The effect is most pronounced for the thickest spacer, which can be understood by the far-field coupling that dominates the reflectance behavior, while for thinner spacers, near-field coupling effects play a dominating role. The ΔR plots show two important features. The shape of the ΔR spectrum follows the shape of R, meaning that the highest signal is also obtained at shifted (in general shorter) wavelengths. The *maximum* value of $|\Delta R|$, however, does *not* change significantly. This implies that the readout angle of an optical hydrogen sensor can in principle be chosen arbitrarily for a fixed structure geometry, as long as the readout wavelength is adjusted accordingly.

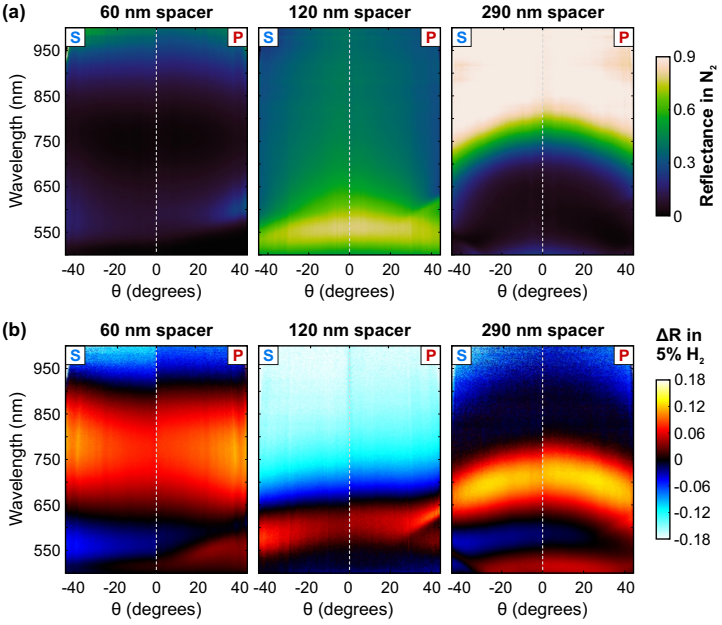

Figure 8.20. Reflectance spectra measured in pure N_2 (a), and the resulting reflectance differences for 5% H_2 in N_2 (b), plotted versus the incidence angle θ for s and p polarization for t_{spacer} = 60 nm, 160 nm, and 290 nm at P = 300 nm. A reflectance blueshift occurs for higher angles. The obtained ΔR values shift along with the reflectance spectrum, while the maximum $|\Delta R|$ value hardly changes or even increases.

A vastly different picture arises when the periodicity of the structures is increased, as Figure 8.21 indicates. At a periodicity of 500 nm, strongly angle- and polarization-dependent features occur in the reflectance spectrum. A detailed analysis of the origin of these features will be given in Section 8.5. These grating effects strongly influence ΔR as well, which is potentially destructive for a robust sensor design, as the sensor response becomes strongly angle-dependent. In particular, at or very close to the grating modes, the obtained signal can be significantly decreased. An intuitive way to understand this decrease is that at the grating modes modes, the far-field response of the structure is not dominated by the localized plasmon resonance of the nanoantennas, but rather by their arrangement, which remains unchanged. At the same time, local maxima in $|\Delta R|$ also seem to occur close to the grating modes.

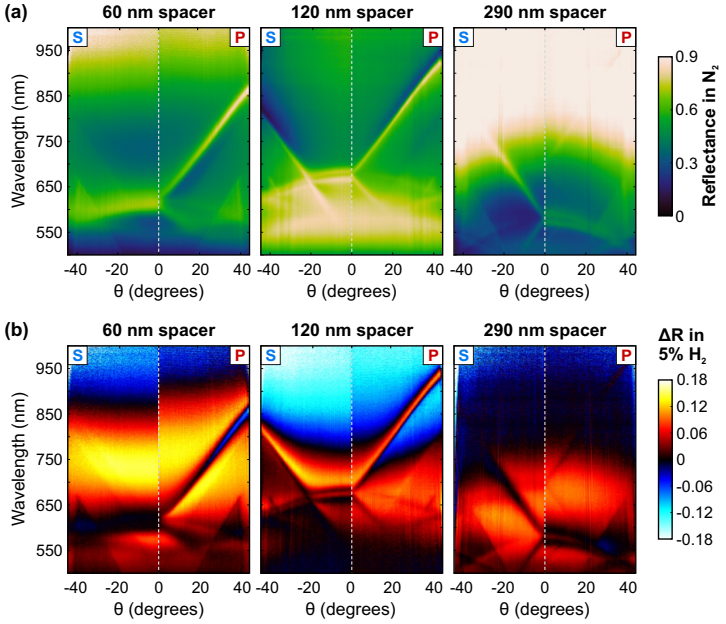

Figure 8.21. Reflectance spectra measured in pure N_2 (a), and the resulting reflectance differences for 5% H_2 in N_2 (b), plotted versus the incidence angle θ for s and p polarization for $t_{\text{spacer}} = 60$ nm, 160 nm, and 290 nm at $P = 300$ nm. A reflectance blueshift occurs for higher angles. The sharp features in the reflectance also show up in the sensor signal.

8.4.4 *Influence of structural disorder*

Lattice effects can be suppressed by using a disordered arrangement of the nanoparticles. In a real-world sensor, the type of arrangement depends on the nanofabrication process. Many large-scale nanopatterning processes, for example laser-interference lithography (see publication P9) or nanosphere lithography [206], produce highly periodic patterns. On the other hand, processes such as colloidal hole-mask lithography [28] and colloidal etching lithography (publication P6) produce disordered structures that exhibit only short-range order, thus suppressing far-field interaction between individual particles (see also Section 4.3.1). To study the effect of a disordered arrangement on the angle-dependent behavior of our Pd-based sensor structures,

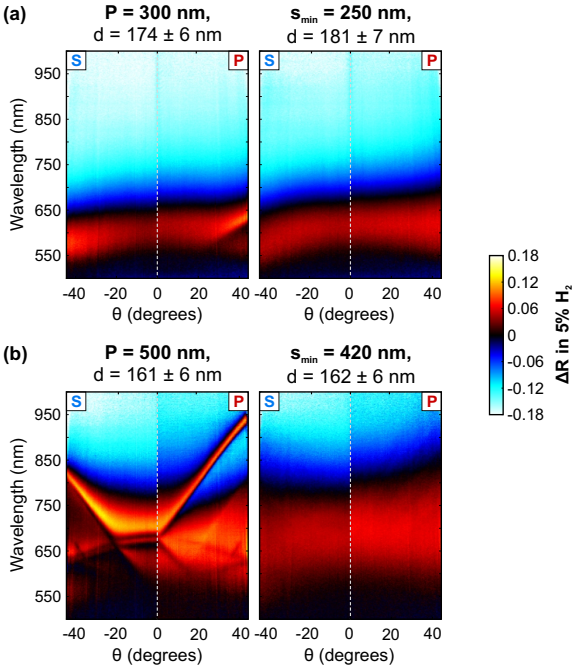

Figure 8.22. Comparison of square nanodisk arrays with disordered ensembles for $P = 300$ nm (a) and $P = 500$ nm (b). Corresponding SEM images can be found in Figure 8.10.

we use the disordered nanodisk ensembles that were fabricated alongside the periodic arrays (see Section 8.4.1).

Figure 8.22(a) shows an example of $\Delta R(\theta, \lambda)$ for $P = 300$ nm at $t_{\text{spacer}} = 160$ nm, alongside the corresponding disordered realization ($s_{\text{min}} = 250$ nm). Almost no difference between the ordered and the disordered case can be identified, especially not in the higher wavelength range, where the highest sensitivity is obtained. At such sub-diffraction nanostructure densities, there is thus no clear advantage in using either lattice-based or disordered fabrication methods. In contrast, a comparison between $P = 500$ nm and the corresponding disordered arrangement with $s_{\text{min}} = 420$ nm clearly reveals how the previously observed lattice diffraction effects are suppressed (Figure 8.22(b). This leads again to a highly angle-independent sensor response. However, the data also reveal another interesting feature of the large-periodicity sensor arrangement: Close to the observed Rayleigh anomalies, the sensor signal $|\Delta R|$ can actually be *higher* than in the corresponding disordered case, by a factor of more than two. This indicates that the interaction between the incoming light and the Pd nanodisks can not only be suppressed, but also enhanced. In other words, a *disordered* nanoparticle arrangement is clearly *advantageous* when a highly angle-independent sensor response is required, but if careful tuning of the readout wavelength and the incidence angle is possible, lattice effects can be *exploited* to enhance the sensor response [207].

8.5 ANALYSIS OF THE ANGLE-DEPENDENT REFLECTANCE

In this section, we provide a detailed analysis of the sharp angle- and polarization-dependent resonance features that occur in the measured reflectance spectra when the periodicity is chosen as large as 500 nm (measurements in Figures 8.20 and 8.21). Corresponding numerically calculated spectra are provided in Figure 8.23(a). The spectra show reflectance vs. wavelength and angle for a Pd absorber structures with $P = 500$ nm, $d_{\text{disk}} = 160$ nm, for the three different spacer thicknesses (60, 160, and 290 nm). These calculations were performed with the scattering matrix approach as described in Section 8.3. The calculated spectra agree very well with the measured ones and exhibit the same resonance features.

Let us now investigate the origin of these features. For an incidence angle of $\theta = 0°$, the occurring resonance peaks are marked with red and blue dots in the calculated spectra. For small spacer thicknesses (60 nm and 110 nm), only one sharp peak is observed (red dots), while for thicknesses of 160 nm

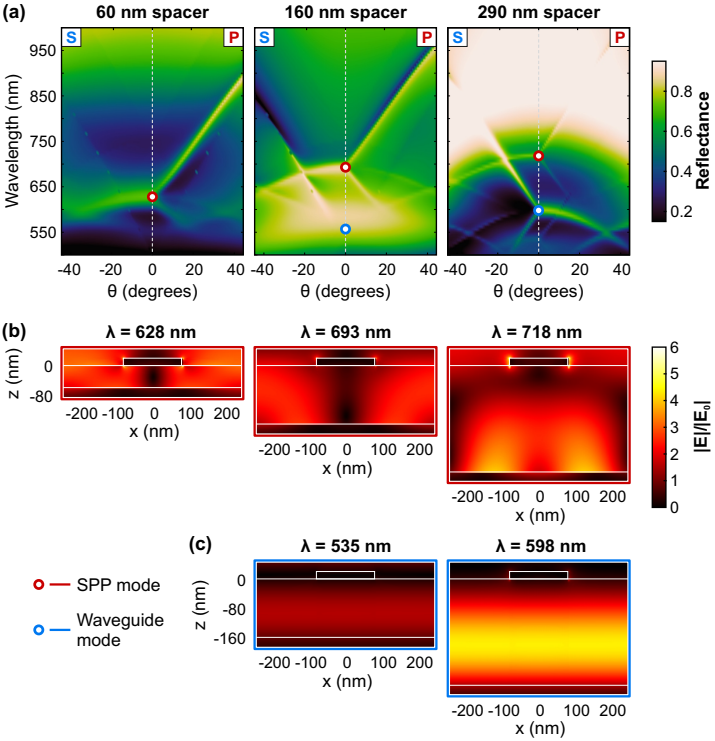

FIGURE 8.23. (a) Calculated reflectance vs. incident wavelength and angle for a Pd absorber structures with $P = 500$ nm, $d_{\text{disk}} = 160$ nm, for three different fabricated spacer thicknesses. (b,c) Calculated field distributions at the spectral positions that are marked with red and blue dots, respectively, in panel (a). The field plots in (b) reveal the excitation of an SPP mode at the interface between the Au mirror and the spacer, while field plots in (c) reveal the excitation of a waveguide mode inside the spacer.

and larger, a second sharp peak arises (blue dots). With increasing spacer thickness, both peaks shift to longer wavelengths.

Figures 8.23(b,c) depict the corresponding electric field distributions (again derived with the scattering matrix approach), corresponding to the spectral positions marked with the red dots (b) and blue dots (c). The fields can be associated with the excitation of a surface plasmon polariton (SPP) mode [208] that propagates along the interface between the gold mirror and the dielectric spacer. Note that for a spacer thickness of 160 nm, only a very

weak waveguide mode feature is visible in the field, since this resonance coincidentally overlaps with a reflection maximum of the perfect absorber, which dominates the optical response in this spectral region. Analyzing the orientations of the fields (not shown here) reveals that the mode exhibits transverse-magnetic (TM) polarization, as it is expected for such SPP modes. The bottom row corresponds to the spectral positions marked with the blue dots. The fields show the excitation of a waveguide mode [209] that propagates inside the spacer layer. Analyzing the field orientation (again not shown), reveals that the waveguide mode exhibits transverse-electric (TE) polarization.

The field distributions imply that the sharp resonances in the spectra can be attributed to SPP and waveguide modes. In order to validate this, let us now switch to a more sophisticated description. The system consists of multiple layers that are stacked in the z direction (from bottom to top: substrate, gold mirror, spacer layer, Pd nanodisks, and air). We note that if we would remove the Pd nanodisks, the system would be completely homogeneous (i.e., translationally symmetric) in the xy plane. Only the presence of the Pd nanodisks breaks this translational symmetry and introduces a periodicity in the x and y direction. In the following, we will refer to the system without the Pd nanodisks as the homogeneous system.

The SPP and the waveguide modes are eigenmodes of the homogeneous system. In general, the dispersion relation of such modes can be written as a function $\omega_\mathrm{m}(k_{||})$ [210], where $k_{||}$ denotes the in-plane momentum (referring to the plane of propagation, i.e., the xy plane) and ω_m with m = {SPP, waveguide} denotes the eigenfrequency of the respective mode. In the above description, $k_{||}$ is a real number, while ω_m is in general complex, with $\mathrm{Re}(\omega_\mathrm{m})$ representing the resonance frequency of the mode and $-2\mathrm{Im}(\omega_\mathrm{m})$ specifying its linewidth [211]. The dispersion relations $\omega_\mathrm{m}(k_{||})$ of the SPP and waveguide modes in the homogeneous system were numerically calculated by following the method provided in Refs. [201, 211]. Note that this method requires that the material parameters of the system can be evaluated at complex frequencies, which has been achieved by modeling the permittivity of the gold according to Ref. [212].

Although the SPP and the waveguide modes are eigenmodes of the homogeneous system, in this system, it would not be possible to excite them from the outside, since their dispersion relation is located outside the light cone of the surrounding medium. However, the situation differs as soon as any periodicity is introduced. In the following, we take into account the periodicity that is caused by the Pd nanodisks, but neglect a possible

direct influence of the Pd nanodisks onto the propagation of the modes. In solid state physics and photonic crystal theory, this approach is known as the empty-lattice approximation [208, 209]. Under this approximation, the dispersion relation of a mode in the periodic system is given by

$$\omega_{\mathrm{m}}\left(k_{||}\right) = \omega_{\mathrm{m}}\left[\sqrt{\left(k_{\mathrm{x}} + \frac{2\pi}{p_{\mathrm{x}}} m_{\mathrm{x}}\right)^2 + \left(k_{\mathrm{y}} + \frac{2\pi}{p_{\mathrm{y}}} m_{\mathrm{y}}\right)^2}\right]. \tag{8.16}$$

Here, k_{x} and k_{y} denote the x and y momentum components, respectively, which are imposed in the periodic system due to the momentum of incoming photons, p_{x} and p_{y} are the periodicities in the respective directions (in our case $p_{\mathrm{x}} = p_{\mathrm{y}} = P$), and $m_{\mathrm{x}}, m_{\mathrm{y}} = 0, \pm 1, \pm 2, \ldots$ represent the possible diffraction orders. Mathematically, Equation 8.16 describes a folding of $\omega_{\mathrm{m}}\left(k_{||}\right)$ into the first Brillouin zone. Due to this folding, formerly non-excitable modes of the homogeneous system that were located outside the light cone are now able to enter the light cone and can become excitable [208, 209].

Let us now take a deeper look at the excitation of the modes. In accordance with the measurements and the calculated spectra, we assume that the system is illuminated by a plane wave that impinges from top onto the structure. Let ω_{inc} be the frequency of the incident wave. The wave can excite a mode if $\omega_{\mathrm{inc}} \approx \mathrm{Re}\left(\omega_{\mathrm{m}}\right)$. In our setup, we have $k_{\mathrm{x}} = \omega_{\mathrm{inc}}/c \sin(\theta)$ and $k_{\mathrm{y}} = 0$. Combining these relations with Equation 8.16, and assuming that the function $\mathrm{Re}\left[\omega_{\mathrm{m}}\left(k_{||}\right)\right]$ is invertible, we can express the angle θ, under which a mode can be excited, as a function of the incident frequency:

$$\sin\theta = \frac{c}{\omega_{\mathrm{inc}}}\left(-\frac{2\pi}{p_{\mathrm{x}}} m_{\mathrm{x}} \pm \sqrt{k_{||}^2(\omega_{\mathrm{inc}}) - \left(\frac{2\pi}{p_{\mathrm{y}}} m_{\mathrm{y}}\right)^2}\right). \tag{8.17}$$

The numerically calculated dispersion relations of the SPP and the waveguide mode enter via the term $k_{||}(\omega_{\mathrm{inc}}) = k_{||}\left[\mathrm{Re}\left(\omega_{\mathrm{m}}\right)\right]$. Besides these two modes, another feature can occur in periodic system, which is the so-called Rayleigh anomaly [213]. It can be described via Equation 8.17 as well, by simply setting $k_{||}(\omega_{\mathrm{inc}}) = n\omega_{\mathrm{inc}}/c$, where n is the refractive index of the surrounding medium ($n = 1$ in our case).

The results of Equation 8.17 with $P = 500$ nm are plotted in Figure 8.24. Red and blue lines correspond to SPP and waveguide modes, respectively, and black dashed lines indicate the Rayleigh anomalies. The different diffraction orders are labeled with their corresponding values of $\left(m_{\mathrm{x}}, m_{\mathrm{y}}\right)$. For an easy

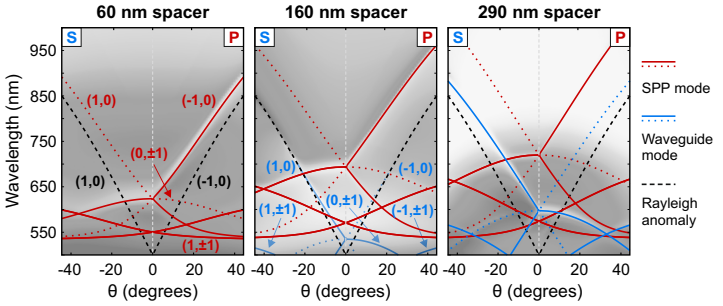

Figure 8.24. Angle-dependent dispersion diagrams, calculated under the empty-lattice approximation (Equation 8.17). Red and blue lines denote SPP and waveguide modes, respectively, and the black dashed lines indicate Rayleigh anomalies. The different diffraction orders are labeled with their corresponding values of (m_x, m_y). For an easy comparison, a grayed-out version of the spectra from panel (a) is plotted in the background. Branches that cannot be excited due to symmetry reasons are displayed by dotted lines.

comparison, a grayed out version of the calculated spectra from Figure 8.23(a) is plotted in the background behind the curves. In consistency with the spectra, the left side of each plot (i.e., negative angles) refers to s polarization, while the right side (i.e. positive angles) refers to p polarization. Simple symmetry considerations that take into account the TM polarization of the SPP mode and the TE polarization of the waveguide mode allow to rule out branches that cannot be excited by the incident s and p polarization, respectively. These branches are plotted with dotted instead of solid lines. As it can be seen, there is an excellent agreement between the numerically calculated spectra and the results of the empty-lattice approximation, which allows to clearly identify all observed spectral features.

8.6 CONCLUSION

In this chapter, we have presented a systematic study of the design parameters for 'perfect absorber'-type plasmonic hydrogen sensors and their influence on the sensor signal. We have shown that the system can be described as a plasmonic cavity generated by the metal mirror and the layer of plasmonic nanoantennas and that reflectance maxima and minima can be obtained by tuning the cavity length, i.e., the spacer thickness.

Based on the numerical calculations as well as the measurements, a set of 'design rules' can be formulated for maximizing the sensitivity of the sensors:

- In a single-wavelength readout scheme, the signal-to-noise ratio of the sensor is maximized by maximizing the *absolute* reflectance change ΔR. This means that it is *not* beneficial to exploit the 'perfect absorption' feature of the plasmonic cavity, contrary to previous claims in the literature.
- The obtained signal at a certain wavelength can be maximized by a careful tuning of the spacer thickness, and is obtained at neither of the reflectance extrema. The Pd disk diameter has only a limited influence, although very small disks lead to a decreased maximum signal and very large disks can lead to an increased sensor response time.
- The readout wavelength should not be chosen entirely at random, but should be in the wavelength range where the change in the dielectric function of the sensor material due to hydrogen incorporation is highest.
- The concentration range of interest must be taken into account when choosing a readout wavelength, as the shape of $\Delta R(\lambda)$ can vary significantly between low and high concentrations. This can be explained by the transition from α- to β-phase PdH_x, and the corresponding volume expansion. A readout at several wavelengths simultaneously can of course be advantageous.
- When lattice effects do not play a role in the reflectance spectrum, a slightly angle-dependent reflectance spectrum is obtained. This is not necessarily a disadvantage, since the maximum sensor signal is hardly affected.
- At increased periodicities, grating effects such as the Rayleigh anomaly and waveguide-plasmon-polariton modes in the spacer layer lead to a highly angle-dependent sensor response. This can be suppressed by employing disordered instead of periodic structures. However, it is also possible to use the lattice effects to enhance the sensor response, at specific combinations of the readout wavelength and the incidence angle.

Using all of these insights, we were able to demonstrate a nanoplasmonic hydrogen sensor with a detectable signal at a H_2 concentration of 100 ppm. This result is entirely based on a single-wavelength reflectance readout.

The use of dedicated, stabilized readout electronics can enable the reliable detection of even lower concentrations.

8.6.1 *Outlook*

At this point, it is important to note that the insights presented in this chapter are not limited to Pd-based plasmonic hydrogen sensors. For any other choice of H_2 sensing material, as well as spacer and/or mirror material, the design principles listed above remain valid. In other words, the 'sensor optimization design principles' can easily be combined with previously reported techniques to improve the hydrogen sensing characteristics, such as alloying or overcoating (see Section 8.1). This enables the further development of reliable, low-cost, and mass-producible all-optical hydrogen sensors. We already demonstrated a possible implementation of such a sensor, to which the found optimization principles can be directly applied, in publication P15.

The 'perfect absorber' geometry can furthermore be applied to any other type of plasmonic sensor as well, as it is designed to enhance the influence of the plasmonic resonance in the sensing structures on the optical far-field. It can thus also be used for sensor schemes based on, e.g., refractive-index sensing [42, 214, 215] or indirect nanoplasmonic sensing (INPS), in which the nanostructures are embedded in a layer that responds to a certain external stimulus [178, 216–218]. We have already successfully used this principle to fabricate highly sensitive plasmonic CO_2 sensors (publication P18). Similarly, a reactive material could be used for the spacer layer as well, in combination with inert or reactive plasmonic structures [31, 189, 219]. We thus believe that our work can be beneficial for a broad range of plasmonic sensor applications.

9

DISORDER IN PLASMONIC SYSTEMS

As we have seen in the previous chapter, the optical properties of plasmonic nanoparticle ensembles are not only determined by the particle shape and size, but also by the nanoantenna arrangement. For example, the angle-dependent transmission/reflection characteristics of a periodic nanoparticle array are strongly influenced by lattice diffraction effects, which are absent in a completely randomized ensemble. In this chapter, we will investigate the influence of the spatial ordering on the far-field optical properties of nanoparticle ensembles in more detail.

We consider different types of spatial disorder. In the case of 'frozen-phonon disorder', each element is displaced from its initial lattice position by a random amount within a variable range. We can thus carry out a continuous transition from a perfect lattice to a fully disordered arrangement. In the case of correlated disorder, the displacement of any element affects the surrounding elements via a certain correlation length and function. We also analyze the two-point correlation function of disordered ensembles generated by these models.

We present experimental as well as computational approaches to gain a better understanding of the impact of disorder on the far-field behavior of complex plasmonic metasurfaces. A designated Fourier microscopy setup, based on a modified 4-f setup, allows us to record the real- and Fourier-space images of plasmonic metasurfaces. The image can either be projected onto a CCD camera to record RGB images, or onto an imaging spectrometer to record the full wavelength- and angle-resolved far-field response. Furthermore, by treating the nanoparticles as dipoles, we calculate the electric field based on dipole-dipole interaction. We can then extract the wavelength-resolved far-field response and convert it to real-space and Fourier-space RGB images.

9.1 INTRODUCTION

The optical appearance of any surface can be characterized via its so-called *bidirectional reflectance distribution function*, or BRDF, which was first defined around 1965 [220]. This quantity can be thought of as a measure of 'shininess'. In general, there are two extreme cases to how 'shiny' a surface is. A surface can act as a perfect mirror, and thus reflect all incoming light into an angle equal to the angle of incidence. Such a surface is called *specular*. On the other hand, incoming light might be isotropically scattered into all directions, so that the angle of incidence cannot be determined from the distribution of reflected light anymore. This is called *Lambertian* scattering.[1] An example of such a surface are the white calibration standards used in dark-field microspectroscopy (see Section 3.3.2). Light absorption and/or transmission by the surface can furthermore decrease the total amount of reflected light. Additionally, these effects can vary with wavelength. The BRDF contains a complete description of the angle- and wavelength-dependent far-field reflectance of a surface. The BRDF can be written as [221]:

$$\mathrm{BRDF}(\theta_{\mathrm{in}}, \phi_{\mathrm{in}}, \theta_{\mathrm{out}}, \phi_{\mathrm{out}}, \lambda) = \frac{dL_{\mathrm{out}}(\theta_{\mathrm{out}}, \phi_{\mathrm{out}}, \lambda)}{dE(\theta_{\mathrm{in}}, \phi_{\mathrm{in}}, \lambda)}, \tag{9.1}$$

where θ_{in} and ϕ_{in} are the polar and azimuthal angles of incidence, and θ_{out} and ϕ_{out} are the angles of reflection/scattering, as illustrated in Figure 9.1. In daily life, most surfaces can be considered rotationally symmetric, in which case the variable ϕ_{in} can be ignored. In a more generalized definition, the polarization of incoming and reflected light can be added as a variable as well.

Furthermore, L_{out} is the spectral radiance leaving the surface, expressed in units of power per unit area per unit solid viewing angle $d\Omega$, while E is the spectral irradiance of the sample, expressed in units of power per unit area. This results in the BRDF being expressed in sr^{-1} (inverse steradian) [222].

The BRDF is widely used in, e.g., computer graphics, to accurately reproduce the appearance of real-world surfaces and materials in photorealistic

1 It is of course a matter of definition whether or not scattered light counts as 'reflection' or not. It is not reflection in the meaning used in the previous chapters, but one can also consider all light leaving the surface in the direction opposite to the incoming light along the vertical axis as reflection R, and all light exiting the surface on the other side as transmission T. In this case, the energy conservation law $R + T + A = 1$ applies, with A being the absorption, and R containing both the 0^{th} order reflection and all light scattered into the upper hemisphere, which is the diffuse reflection.

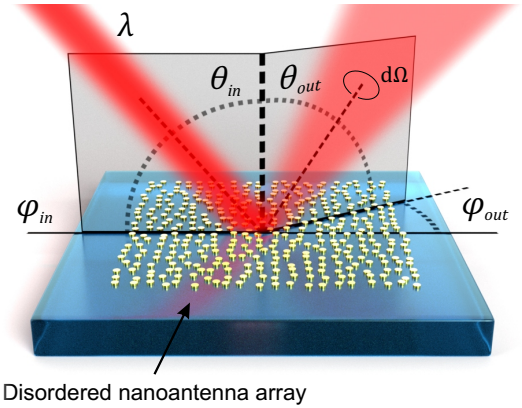

FIGURE 9.1. Schematic of the parameters involved in the definition of the bidirectional reflectance distribution function (BRDF). In this chapter, we will investigate the influence of spatial disorder in plasmonic nanoparticle ensembles on the far-field appearance.

rendering[2], along with inverse problems such as object recognition [223]. Another application is the characterization of surface albedo and vegetation patterns via satellite imaging. At the size scales involved here, BRDF measurements are typically done by goniometer-based setups, in which a light source and a detector are moved through a set of angles relative to a surface [224]. At the sub-100 µm size scale of the work presented here, it is in principle possible to record such measurements using goniometric ellipsometers (actually designed to determine the dielectric function of a material), but these typically suffer from a limited spatial resolution. However, as described in Section 2.3, one can use Fourier microscopy to characterize the angle-dependent optical far-field behavior of a microscale sample. In fact, this concept has already been employed for micro-ellipsometry [225, 226]. In this chapter, we will thus use Fourier microscopy to investigate the influence of structural disorder on the reflectance of plasmonic nanoparticle arrays.

2 See Appendix A for some examples.

9.2 DISORDER THEORY

The concept of structural disorder in physical systems has attracted much attention in recent years, as it has been shown to define the optical properties of many different systems. Functional disorder occurs in nature, for example in flowers or insect scales, determining the optical properties of these surfaces and improving, e.g., temperature control and optical signaling [227, 228]. This has fueled the development of bioinspired disordered materials [229]. Disordered opaque media have been used as programmable optical circuits in combination with wavefront shaping [230, 231], and disorder-engineered metasurfaces have in turn been employed for wavefront shaping and high-resolution microscopy [232]. Disorder due to fabrication errors influences the optical properties of photonic crystals [233], but exploiting effects of structural disorder has also brought forward novel applications such as photon trapping [234] and on-chip spectrometry [235]. Most notably, disordered arrangements of nanostructures have been used to determine the far-field optical properties of metasurfaces, with applications in structural colors [236–238] and enhanced light collection in thin-film solar cells [239–242].

When speaking about disorder, the main question is how one *defines* disorder, and, moreover, how one *quantifies* it. In positional disorder, that is, disorder in the distribution of particles across a surface, one could define the two extreme cases of 'completely ordered' and 'completely randomized', as illustrated in Figure 9.2. In the completely ordered case, each particle occupies a position out of a predefined discrete set, such as a rectangular or hexagonal lattice. In the completely randomized case, any position is accessible and each particle is positioned at random (x, y) coordinates, without being influenced by the other particles at all. This fully randomized distribution inevitably leads to cluster formation. For objects of finite size, it leads to overlapping as well, and is thus not necessarily a realistic model for nanoparticle distribution.

In a more realistic scenario, nanoparticles are randomly distributed while maintaining a certain minimum distance to each other. This is, for example, the case in colloidal fabrication methods (see Section 4.3.1), and was also employed in Chapter 8 (publication P3). Such quasi-randomized distrubitions can be generated by random sequential adsorption (RSA)-based models [204]. Figure 9.2 shows an example of the simplified RSA model, in which the minimum interparticle spacing was set to preserve the number of particles per unit area with respect to the completely ordered case. Other models for

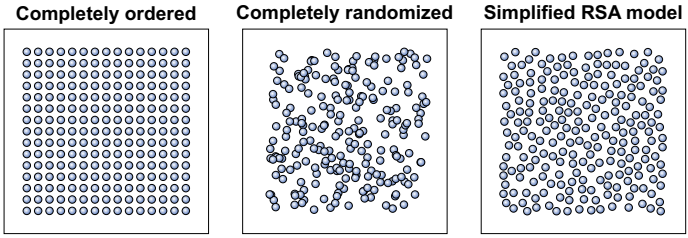

FIGURE 9.2. Example of a fully ordered array of positions (a rectangular 15×15 lattice), a fully randomized set of 225 (15^2) positions distributed over the same area, and a set of 225 positions generated using the simplified random sequential adsorption (RSA) model.

generating quasi-randomized (or, by an equally valid term, quasi-periodic) distributions are Matérn-type distributions [237] and the so-called Penrose tiling, which has also been observed in quasi-crystalline materials [243, 244].

However, in this work, we aim for a *quantification* of the influence of structural disorder on the optical properties of plasmonic metasurfaces. This requires a disorder model that allows for a tunable *degree* of disorder in reproducible disordered arrays.

9.2.1 *Tailored disorder*

To obtain a tunable degree of disorder, we make use of the model employed in nanowire-based photonic crystals by Nau *et al.* [245, 246]. In this model, particles are randomly displaced from their initial lattice positions, with a maximum displacement defined as the *disorder strength*. This configuration is also called 'frozen-phonon'-type disorder or uncorrelated disorder, since the elements do not influence each other. A disorder strength of zero corresponds to the original lattice. In addition to the displacement, a correlation can be introduced. In this case of correlated disorder (also called long-range disorder), the displacement of one element also influences all the other elements. This influence is characterized by a certain *correlation length*. Figure 9.3 displays several examples of disordered arrangements generated by this model, for different values of both parameters.

In the case of frozen-phonon disorder in a perturbed lattice consisting of $n_x \times n_y$ elements, the coordinates of element $i = 1, \cdots, N$ with $N = n_x n_y$ are given by:

$$\begin{bmatrix} x \\ y \end{bmatrix}_i = \begin{bmatrix} x_0 \\ y_0 \end{bmatrix}_i + \begin{bmatrix} \Delta x \\ \Delta y \end{bmatrix}_i, \tag{9.2}$$

with x_0 and y_0 the initial lattice coordinates corresponding to element i, and Δx and Δy the displacement of the element from its lattice position. Several different distributions can be used for the randomly chosen values of Δx and Δy. In Ref. [245], a Gaussian distribution was used, in which case the full width at half maximum (FWHM) of the distribution is a measure for the disorder strength. In this work, we will consider a rectangular distribution, in which the disorder strength s_d is defined as the maximum displacement that any element can have from its lattice position in both directions. This distribution is used to prevent the occurrence of outliers far outside the disordered array. The frozen-phonon disorder can thus be thought of as placing each particle at a random position within a square centered at the lattice position, with s_d defining the size of this square. In the case of a non-isotropic periodicity and/or a non-isotropic disorder strength, the square is replaced by a rectangle.

If a correlation is introduced, each shifted element adds an additional shift to all other elements, which is proportional to its own shift via a correlation function $C(r)$, with r the distance between the two points. Here, we implement this as follows. For each element i, a random shift $\left[\begin{smallmatrix} \Delta x \\ \Delta y \end{smallmatrix}\right]$ is generated as before. Then, all elements $j \neq i$ are assigned an additional shift $\left[\begin{smallmatrix} \Delta x \\ \Delta y \end{smallmatrix}\right]_i \cdot C(r_{ij})$. After N iterations, the coordinates of element i are thus given by:

$$\begin{bmatrix} x \\ y \end{bmatrix}_i = \begin{bmatrix} x_0 \\ y_0 \end{bmatrix}_i + \begin{bmatrix} \Delta x \\ \Delta y \end{bmatrix}_i + \sum_{j \neq i} \begin{bmatrix} \Delta x \\ \Delta y \end{bmatrix}_j C(r_{ij}). \tag{9.3}$$

In our implementation, we use a correlation function with a Gaussian shape:

$$C(r) = \exp\left(-\left[\frac{r}{2L_c P}\right]^2\right), \tag{9.4}$$

with P the period of the initial lattice. The correlation length L_c is directly related to the FWHM of the Gaussian curve (FWHM $= 2\sqrt{2 \ln 2} L_c P$).

The algorithm for generating sets of disordered positions thus uses the periodicity P (which can also be divided into separate periodicities P_x, P_y for the x and y direction), the number of positions n_x, n_y, the disorder strength

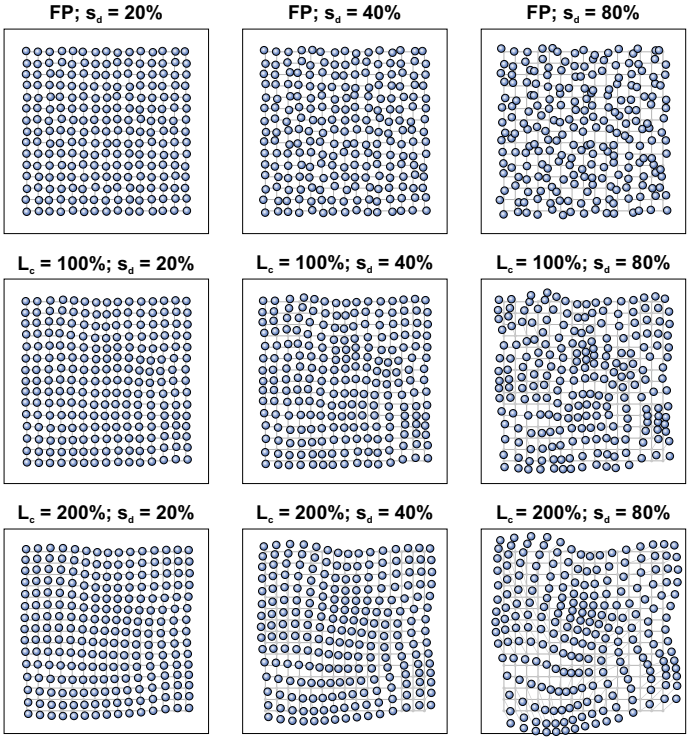

Figure 9.3. Examples of disordered positions using frozen-phonon disorder and correlated disorder, at different disorder strengths s_d and correlation lengths L_c, both expressed in terms of the base lattice constant. The base lattice of 15×15 points is shown in the background in grey. The same seed value is used in each case.

s_d, and the correlation length L_c as input parameters. The parameters s_d and L_c are defined in terms of P. along with a seed value for the random number generator that produces the shift values $\Delta x, \Delta y$. Each combination of s_d and L_c can thus produce an infinite number of different realizations, defined via the seed value. Increasing either disorder parameter while keeping the seed fixed thus results in all particles being shifted further in the same direction. This can also be seen in the examples in Figure 9.3.

In Figure 9.4, SEM images of some examples of disordered aluminum nanodisk arrays are shown. The disk diameter d is 120 nm, and the disk

height h is 60 nm. The structures were fabricated using electron beam lithography (see Section 4.3.2). Panel (a) shows a grid with $P = 500$ nm, and panel (b) shows a completely randomized ensemble (see Fig. 9.2). In this case, clustering of structures occurs, leading to interconnected nanodisks. In panel (c), the correlated disorder model was used, with $s_d = 80\%$ and $L_c = 400\%$.

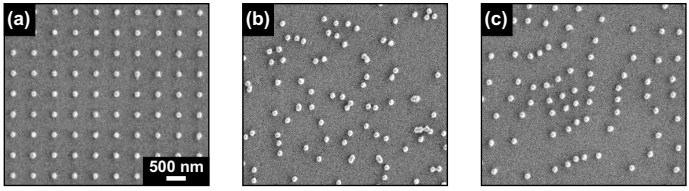

Figure 9.4. SEM images of Al nanodisks ($d = 120$ nm, $h = 60$ nm) within a rectangular lattice with a periodicity $P = 500$ nm (a), in a completely randomized arrangement with the same density (b) and using correlated disorder with $s_d = 80\%$, $L_c = 400\%$ (c). In the completely randomized arrangement, clustering of positions leads to overlapping structures. The scale bare is valid for all images.

9.2.2 *Two-point correlation function*

The disorder model described in the previous section allows us to introduce a tunable degree of disorder in any periodic arrangement of plasmonic nanostructures via two tuning parameters, namely the disorder strength and the correlation length. As a next step, we aim to quantify the effects of both parameters on the structure arrangement. Several different metrics have been established for this, most notably in the fields of astrophysics and crystallography. An overview of such metrics can, for example, be found in the work of Torquato and Stillinger [247]. An often used metric is the *two-point correlation function* (TPCF), which can be regarded as a measure of the probability of finding a particle at a certain distance from any other particle. The more homogeneous this function is at a certain distance, the less correlated and thus the more 'disordered' the ensemble is at this range. The TPCF thus characterizes the ensemble in real space. A reciprocal space (Fourier-space) equivalent is the *structure factor*, which can be calculated from the TPCF via a Fourier transform [248].

In this section, we will investigate the effects of s_d and L_c via the two-point correlation function. In its most basic form, the TPCF can be calculated as follows. For each of the N elements, the distances to all other $N-1$ elements are determined. The TPCF then corresponds to the histogram of all pair distances in this dataset, and thus describes the count of pairs with a distance in the interval from r to $r+\delta r$. For an 'entirely disordered' arrangement, this gives a constant value, while in a periodic array, it gives a set of delta peaks at distances that follow from the lattice constant.

However, this 'direct' method of calculating the TPCF suffers from errors that originate from the finite number and the spatially confined nature of the structures we investigate here. The larger the distance r from a particle, the smaller the number of particles that can be found at this distance. This can be compensated for by normalizing the distance histogram to the number of structures contributing to each bin, but also strongly increases the error. To compensate for these effects, several different TPCF *estimators* have been developed. A comparison of several different estimators has shown that the *Landy-Szalay estimator* performs best in the context of astrophysics for the statistical characterization of clustering in galaxies [249]. This estimator does not only consider the present data (D), but compares it to a reference set of fully randomized positions distributed over the same area (R). The Landy-Szalay estimator $\xi(r)$ is defined as follows [250]:

$$\xi(r) = \frac{\left(\frac{N_R}{N_D}\right)^2 DD(r) - 2\frac{N_R}{N_D} DR(r) + RR(r)}{RR(r)}. \tag{9.5}$$

Here, $DD(r)$ and $RR(r)$ indicate the pair counts in the positions of interest (data-data) and in the fully randomized ensemble (random-random), respectively. $DR(r)$ is the number of cross-correlated data-random pairs, obtained by calculating the distance from every point in D to every point in R. The factors N_R and N_D are the number of elements in the two sets, which are not necessarily the same: The noise in ξ can be reduced by choosing a greater number of positions in R (although this also increases the required computational power).

The resulting values of ξ can be interpreted as a measure of how likely it is to find a particle at distance r from any position, compared to the chance of finding a particle at the same distance if the positions would be fully randomized. A value of $\xi(r) = 0$ indicates no difference, while $\xi(r) = -1$ indicates that no pairs of distance r exist. The results of this calculation are shown for disordered position sets using different disorder parameters in Figure 9.5.

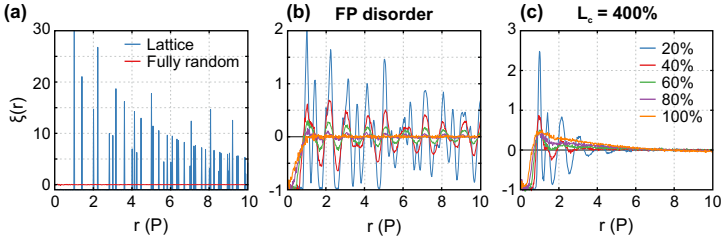

Figure 9.5. Radial two-point correlation functions for a 50×50 rectangular lattice and a fully randomized ensemble (a), for frozen-phonon disorder with different s_d values (b), and for correlated disorder with $L_c = 400\%$ with the same s_d values (c). The TPCF is calculated via the Landy-Szalay estimator. The curves result from averages over 11 different seed values with $N_R = 4N_D$. The pair distance r is expressed in terms of the original lattice period P.

As Figure 9.5(a) shows, a rectangular lattice produces a set of delta peaks. These occur at every whole lattice period P, as well as diagonal lattice parameters $\sqrt{2}P$, etc. In the case of frozen-phonon disorder (panel (b)), these peaks are broadened with increasing s_d. At $s_d = 100\%$, meaning that the square within which each particle is placed is as large as one lattice unit cell and the squares are consequently touching, the set of position strongly resembles a fully randomized one (orange curve). However, at distances smaller than P, the chance of finding another particle is still lower, indicating that there is still a short-range ordering present. In the case of correlated disorder (panel (c)), the peaks are significantly more broadened, so that any long-range ordering disappears at lower s_d values than in frozen-phonon disorder. At $s_d = 100\%$, however, $\xi(r)$ shows slowly decreasing positive values for $r > P$. The range over which these positive values occur is determined by L_c (and the shape with which ξ declines by C; see Eq. 9.4).

In addition to this radial TPCF $\xi(r)$, one can also define a two-dimensional TPCF in Cartesian coordinates, $\xi(x, y)$. In the case of perturbed lattices, this approach can be more insightful than the radial TPCF (especially for non-isotropic lattices). To compute a Cartesian TPCF, the pair distance histograms RR, DD and DR are calculated for distances along the x and y axes separately. Examples of the Cartesian TPCF are shown in Figure 9.6. In this case, one can clearly distinguish how uncorrelated disorder leads to a broadening of the the peaks at multiples of P, with the exception of the area around $x = y = 0$. On the other hand, the introduction of correlated disorder leads to a distance-dependent broadening: peaks further away from

the origin broaden into a uniform 'landscape' of ξ much faster. At the same time, short-range order is present within a larger range from the origin for high s_d values.

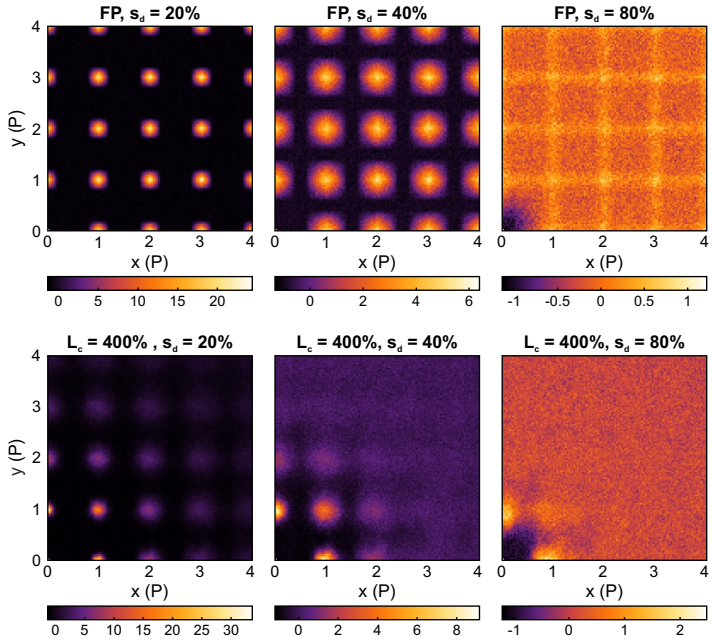

Figure 9.6. Cartesian two-point correlation functions for uncorrelated and correlated disorder with different s_d values ($L_c = 400\%$), calculated via the Landy-Szalay estimator. x and y are expressed in terms of the original lattice period P.

9.3 COLOR VISION

Since the aim of this work is to characterize the optical *appearance* of a disordered plasmonic metasurface, the central question is how the reflected *colors* are influenced by the disorder. To do this, we must first understand what a color actually *is* and how it follows from a surface's reflectivity.

The first important notion about color is that it is in fact only a construct of the brain, arising from the response of the light-sensitive cells in the eye. In the case of the human eye, two different types of such cells exist, called the *rod* cells, which are only sensitive to variations in intensity, and *cone* cells, which provide the ability to distinguish colors. Of this latter type, three different species exist, which feature different wavelength-dependent sensitivities. These cells are called the S-, M-, and L-cells, for short, mid-range, and long wavelengths, respectively. These constitute the three different color channels of the human eye,[3] which can be loosely attributed to the colors 'blue', 'green', and 'red', respectively. The wavelength-dependent sensitivities of these different types have been measured in color matching experiments on human test subjects. Several different data sets exist, which have been measured in different groups of subjects under slightly varying conditions (such as the angle of observation), but there is little variation in the overall shape. Figure 9.7(a) displays the cone cell sensitivity curves as reported by Stockman and Sharpe [252], based on the measurements of Stiles and Burch in 1958 [253].[4]

9.3.1 *Spectrum-to-color conversion*

Because of the overlap of the three different cone spectral sensitivities, it is not possible to directly convert an intensity spectrum into three different colors, as all three channels play a role. For this reason, CIE 1931 XYZ color space was introduced by the International Commission on Illumination [255]. In this color space, an intensity spectrum is converted to the so-called *tristimulus values* XYZ, via the *color matching functions* (CMFs) $\bar{x}$, $\bar{y}$, and $\bar{z}$, which are the experimentally determined numerical description of the chromatic response perceived by the observer. The CIE 1931 standard observer CMFs are shown in Fig. 9.7(b). For a surface with reflectance or

3 Different photoreceptor types have been found in other species. A famous example are mantis shrimp, with up to 16 separate 'color channels' [251].

4 An interesting consequence of the shape of the cone spectral sensitivities is that there exists no such thing as 'pure green', technically speaking. There are wavelengths at which only the S-receptors, or only the L-receptors, are excited, but it is not possible to exclusively excite the M-receptors in a healthy eye.

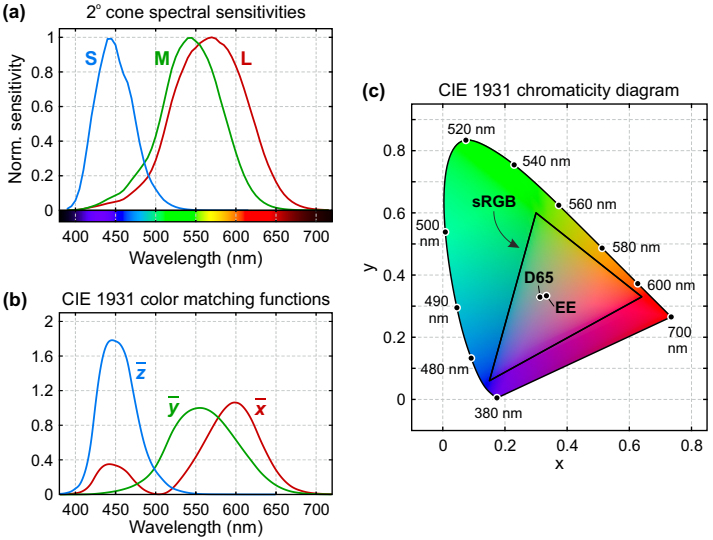

Figure 9.7. (a) Normalized spectral sensitivities of the S-, M-, and L-type human cone cells, from the dataset of 2° fundamentals based on the Stiles & Burch 10° CMFs [252, 253]. (b) Color matching functions as defined in the CIE 1931 standard [254]. (c) CIE 1931 chromaticity diagram. The x, y values of several monochromatic stimuli are indicated, alongside the D65 and EE white points and the gamut of colors representable in the sRGB color space. Colors outside this gamut are thus not accurately displayed.

transmittance $P(\lambda)$, illuminated by a light source with intensity distribution $I(\lambda)$, the conversion to XYZ values is as follows:

$$\begin{aligned} X &= \int \bar{x}(\lambda)P(\lambda)I(\lambda)d\lambda, \\ Y &= \int \bar{y}(\lambda)P(\lambda)I(\lambda)d\lambda, \\ Z &= \int \bar{z}(\lambda)P(\lambda)I(\lambda)d\lambda. \end{aligned} \tag{9.6}$$

These tristimulus values can be converted to the xyY color space, in which the *chromaticity coordinates* x and y hold all the information necessary to define a color, while the tristimulus value Y gives the *luminance*, or perceived

intensity. The chromaticity coordinates follow from a normalization of the XYZ values:

$$\begin{aligned} x &= \frac{X}{X+Y+Z}, \\ y &= \frac{Y}{X+Y+Z}, \\ z &= \frac{Z}{X+Y+Z} = 1-x-y, \end{aligned} \tag{9.7}$$

with z directly following from x and y and thus not containing any additional information. Any spectral intensity distribution can thus be converted to x, y coordinates and plotted in the *chromaticity diagram*, which is shown in Figure 9.7(c). The horseshoe-shaped curve in this diagram follows from the coordinates of strictly monochromatic light and encompasses all observable colors.

The CIE 1931 XYZ color space is *device independent*, as it only specifies the color coordinates of a spectral distribution without taking into account the way in which the color is displayed. Color displays employ three different color channels (typically labeled red, green and blue, or RGB) to mimic the human eye, and thus only produce colors that follow additively from these three channels. In the chromaticity diagram, the complete set of possible colors, or *gamut*, is thus formed by a triangle. Most commonly, colors are represented in the sRGB color space, which is displayed in Fig. 9.7(c). Here, we will also use this color space to represent and compare measured and calculated colors. The three corners of this triangle are the *primaries* of the color space. Together with the *whitepoint*, in other words, the color coordinates that are perceived as pure white, these define the conversion from XYZ to RGB colors.[5] In the sRGB color space, the commonly used whitepoint is the D65 standard, which corresponds to the spectral power distribution of the average midday light in Western/Northern Europe. To simulate a light source with a uniform spectral power density, the *equal-energy* (EE) whitepoint is used.

5 Most color displays use the sRGB color space. However, the exact value of the primaries are different for each display. Technically speaking, color displays thus always produce false colors, but since the 'conversion' of the display is applied to *all* images displayed on it, the comparability between images is not affected. The same goes for printed colors, for example in the printed version of this thesis, which usually use the subtractive CMYK color space.

The conversion from XYZ to RGB values is defined via the transformation matrix $\boldsymbol{M}$:

$$\begin{bmatrix} R \\ G \\ B \end{bmatrix} = \boldsymbol{M}^{-1} \begin{bmatrix} X \\ Y \\ Z \end{bmatrix}, \tag{9.8}$$

with $\boldsymbol{M}$ given by:

$$\boldsymbol{M} = \begin{bmatrix} S_r X_r & S_g X_g & S_b X_b \\ S_r Y_r & S_g Y_g & S_b Y_b \\ S_r Z_r & S_g Z_g & S_b Z_b \end{bmatrix}. \tag{9.9}$$

Here, the indices r, g, and b indicate the values corresponding to the red, green, and blue primaries, respectively. The auxiliary values S_r, S_g, and S_b follow from the XYZ values of the whitepoint and the red, green and blue primaries as follows:

$$\begin{bmatrix} S_r \\ S_g \\ S_b \end{bmatrix} = \begin{bmatrix} X_r & X_g & X_b \\ Y_r & Y_g & Y_b \\ Z_r & Z_g & Z_b \end{bmatrix}^{-1} \begin{bmatrix} X_w \\ Y_w \\ Z_w \end{bmatrix}. \tag{9.10}$$

The highest value in each channel is thus 1, with $(R, G, B) = (1, 1, 1)$ corresponding to white.

The color model is, however, not complete yet. Equations 9.6 - 9.8 provide the *linear* RGB values, in which the response of each channels is linearly connected to the received intensity. The human perception of brightness, in contrast, is strongly nonlinear. To take this nonlinearity into account, a *gamma correction* must be applied. In the sRGB color space, the conversion from linear RGB to gamma-corrected sRGB is defined as:

$$\gamma_u(u) = \begin{cases} 12.92u & u \leq 0.0031308 \\ 1.055u^{1/2.4} - 0.055 & \text{otherwise,} \end{cases} \tag{9.11}$$

where u indicates either the R, G, or B color channel. Low values in each color channel are thus enhanced stronger than high values.

With this color model, we now have a complete holistic approach to convert physical intensities into subjective brightness and color impressions. We will later use this to convert measured as well as calculated reflectance spectra into colors. First, however, we will look at the influence of structural disorder in nanoparticle arrays using spectroscopic measurements and color imaging with an RGB camera.

9.4 OPTICAL MEASUREMENTS

9.4.1 *Bright-field k-space spectroscopy*

In section 8.4.4, we have seen that the introduction of structural disorder into arrays of nanoparticles suppresses the angle-dependent far-field features that arise from the ordering itself, such as the Rayleigh anomalies and quasi-guided modes. Here, we investigate the influence of disorder on the angle-dependent transmittance of nanoparticle arrays on a glass substrate. We make use of arrays of 50×50 gold nanodisks, perturbed using the disorder model described in Section 9.2.1. Arrays with different parameter combinations of s_d, L_c, and random number generator seed values are fabricated on the same substrate using electron-beam lithography (see Section 4.3.2). The disk diameter d is chosen as 120 nm, and the disk height h as 60 nm. A base lattice periodicity of $P = 500$ nm is used, so that diffraction modes of these arrays can be recorded using a sufficiently high microscope objective NA (see Section 2.1.2). The unperturbed array thus measures 25×25 μm^2 in size. The structures are embedded in an approximately 200 nm thick layer of spin-on dielectric coating IC1-200 [256], which serves a dual purpose: It protects the particles, and it nearly matches the refractive index of the glass substrate ($n_{\mathrm{IC1-200}} = 1.41$), thus suppressing the influence of the interface. This is especially important for the comparison to numerical simulations that will follow later.

The Fourier microspectroscopy setup used to record angle-resolved transmittance spectra is illustrated in Figure 9.8. The setup consists of a Nikon ECLIPSE TE2000-U inverted microscope in combination with a Princeton Instruments SP2500 grating spectrometer, which are coupled via a modified 4-f setup [1] (see also Chapter 2). The sample is illuminated by a fiber-coupled halogen lamp using critical illumination under a maximum NA of 0.65, and the transmitted light is collected using a Nikon TU PLAN FLUOR ELWD 60× objective (NA 0.70). The highest accessible angle is approximately 40° (limited by the condenser NA). The Fourier image generated by the Bertrand lens (BL) is projected onto the spectrometer entrance slit via a rotating mirror, which provides the additional option to move the Fourier image across the slit and thus record hyperspectral Fourier images [13].

Figure 9.9 displays a set of k-space transmittance spectra for different disordered Au nanodisk arrays. In panel (a), spectra of the unperturbed array are shown, for unpolarized light as well as for s and p polarization. Similar features are observed as in cavity-coupled nanodisks (Chapter 8),

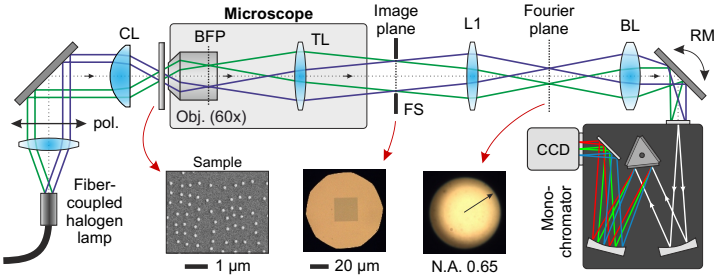

Figure 9.8. (a) Measurement setup used for bright-field k-space transmittance characterization of disordered plasmonic metasurfaces. The sample is illuminated by a fiber-coupled halogen lamp using critical illumination under a maximum NA of 0.65. The transmitted light is collected by a 60× objective (NA 0.70). A modified 4-f setup, consisting of lens L_1 and a second lens that acts as a Bertrand lens (BL), projects the Fourier plane image onto the entrance slit of the grating monochromator. A field stop (FS) is placed in the microscope image plane, which is closed to block all light from outside the nanodisk array. (CL: collector lens, BFP: back focal plane, TL: tube lens, pol.: polarizer, RM: rotating mirror)

which can be attributed to the lattice's Rayleigh anomaly and to waveguide modes in the IC1-200 layer. If uncorrelated disorder is introduced (panel (b)), these features gradually become less sharp as s_d increases. At a disorder strength of 100%, no periodicity-induced modes are distinguishable anymore. If a nonzero correlation length is added to the disorder, as in panel (c), all features disappear at a smaller s_d value. At $L_c = 300\%$, the k-space spectrum for $s_d = 60\%$ can not be distinguished from the spectrum for $s_d = 100\%$, in contrast to the same disorder strength in the uncorrelated case. This indicates that the lattice-induced spectral features in bright-field spectral measurements are influenced by the *long-range* order of the sample. As we know from an analysis of the two-point correlation function (see Figures 9.5 and 9.6), this long-range order diminishes much faster with s_d as L_c increases. However, this does not necessarily apply to the *short-range* order. As the radial as well as the Cartesian TPCF of different disordered arrays show, a pronounced short-range order can still be present, even if no order exists beyond the correlation length. Nevertheless, this can not be distinguished in the bright-field measurements in Fig. 9.9.

Since short-range order appears to be of no influence on the bright-field spectra, different combinations of L_c and s_d can produce the same result. These measurements can thus not be used to *identify* the disorder in the

sample. In a next step, we will introduce a measurement method in which both long- and short-range order can clearly be identified in the optical far-field signal.

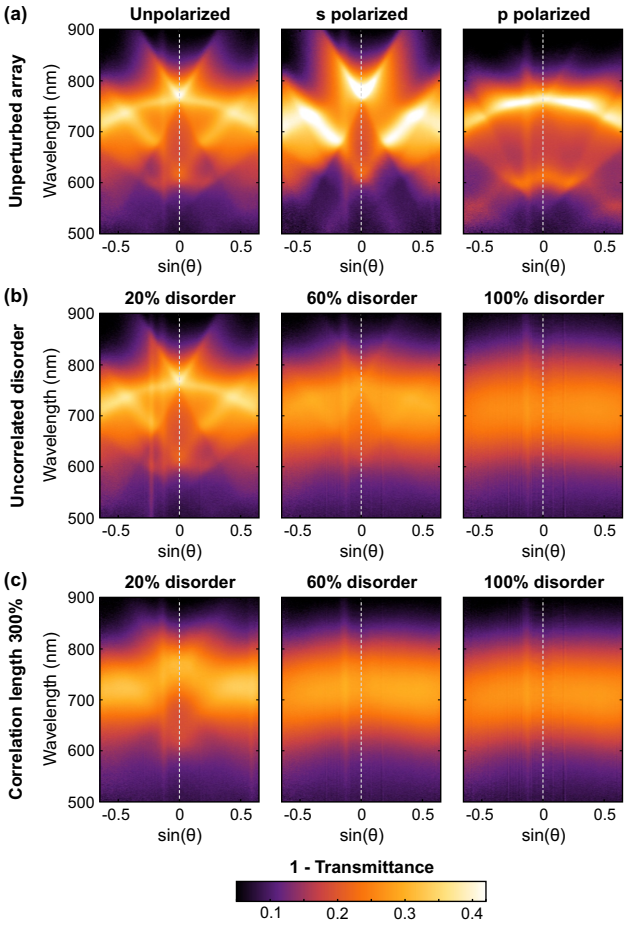

Figure 9.9. Measured k-space transmittance spectra of disordered Au nanodisk arrays (d = 120 nm, d = 120 nm, P = 500 nm). (a) Contributions of s and p polarization, for the unperturbed array. The polarization definitions are according to Figure 8.19. (b) Unpolarized spectra of arrays with frozen-phonon disorder, for increasing disorder strength s_d. (c) Spectra of arrays with correlated disorder (L_c = 300%) for the same s_d values. The seed value is the same everywhere.

9.4.2 *RGB imaging setup*

The far-field optical behavior of a periodic structure is dominated by diffraction effects, as described in Section 2.1.2. To characterize the influence of disorder on the optical response it is thus necessary to image the diffraction. In the previous bright-field transmittance measurements, the diffraction orders are not directly visible. The signal measured at a certain angle (θ, ϕ) consists of the bright 0^{th} order transmittance of light incident at the same angle, overlapped with diffracted light from all other incident angles. To image the diffraction orders, the range of incident angles must be reduced to a minimum. As described in Chapter 2, this can be achieved by illuminating a small spot in the objective back focal plane (BFP). We thus extend the setup in Fig. 9.8 to record RGB images of the reflected Fourier image with near-zero NA illumination, as illustrated in Figure 9.10.

The sample is illuminated via a Köhler illumination path, in which the light from a fiber-coupled white light lamp (Energetiq EQ-99XFC) is focused onto a pinhole (50 µm). An image of this pinhole is then projected onto the objective BFP. The fiber and the pinhole are mounted on a 2D translation stage, so that the illuminated spot can be moved throughout the BFP to change the angle of incidence. To access a range of angles as large as possible, a high-resolution Nikon PLAN APO VC 100× oil-immersion objective with an NA of 1.40 is used, which corresponds to $\theta_{\text{max}} \approx 69°$. The refractive index of the immersion oil is close to that of the glass and the protective polymer layer ($n_{\text{oil}} = 1.518$). The k-space image generated by the modified 4-f setup is projected onto a CCD imaging camera (Allied Vision PROSILICA GC2450C) to record RGB images. Switching between the real-space and k-space images is possible by exchanging the second lens of the 4-f setup by the Bertrand lens (with $f_{\text{BL}} = \frac{1}{2} f_{\text{L1}}$). This is in fact achieved by adding an extra lens in front of L2, so that the resulting lens system acts as the BL (see also Section 3.2). In the intermediate Fourier plane in the 4-f setup, an opaque stop can be inserted to block the 0^{th} order reflection, which is far brighter than the diffracted/scattered light.[6] This configuration is very similar to dark-field microscopy (Section 2.2). Furthermore, we use nanodisks made of aluminum rather than gold, as the plasmonic resonance of Al disks lies at shorter wavelengths and the structures thus show a clear response throughout the entire visible range.

6 The question arises whether or not diffraction is a form of scattering. If one considers all the light that is not reflected/transmitted in the 0^{th} order as scattering, it is.

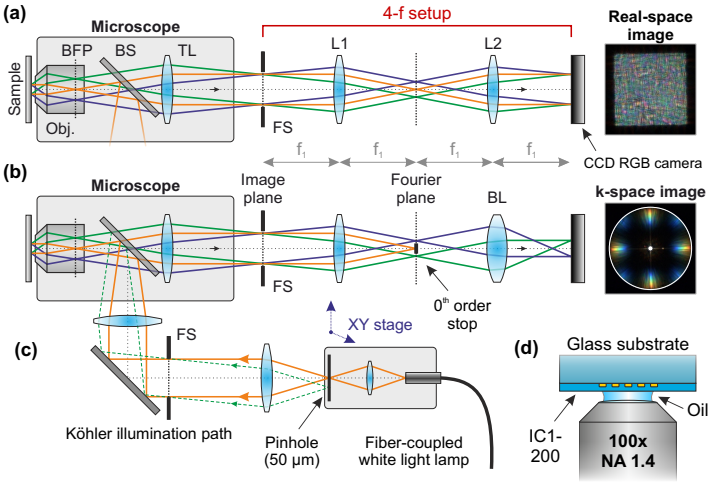

Figure 9.10. Measurement setup used for recording real-space (a) and k-space (b) RGB images of disordered plasmonic metasurfaces. The intermediate Fourier plane can be used to insert an opaque stop, to block the direct (0^{th} order) reflection. The sample is illuminated via a Köhler illumination path, in which the light from a fiber-coupled white light lamp is tightly focused into the objective BFP via a pinhole (c). The illuminated spot can be moved throughout the BFP to change the angle of incidence (dashed green line). The light rays are color-coded by angle in the sample plane. A high-NA oil-immersion objective (100×, NA 1.4) is used to maximize the range of accessible angles and to minimize the effect of changes in refractive index between objective and sample (d). The nanostructures are embedded in IC1-200 for protection. (BS: beam splitter, TL: tube lens, FS: field stop)

Figure 9.11 shows an example of a real-space and a k-space RGB image recorded on a perturbed array of Al nanodisks. As these images show, a background signal is present. This can mainly be attributed to reflection at the interfaces between the oil, the IC1-200 and the substrate (even though the refractive index differences are very small), and to back reflections from optical elements in the setup, such as the beam splitter and the objective itself. The reflections occur close to the optical axis, and could thus in principle be blocked by a 0^{th} order stop. However, in the real-space image, the 0^{th} order reflection also holds information and thus contributes to the optical appearance of the sample. To perform a background correction, we thus record an image of the empty substrate close to the array, which can be subtracted from the recorded image.

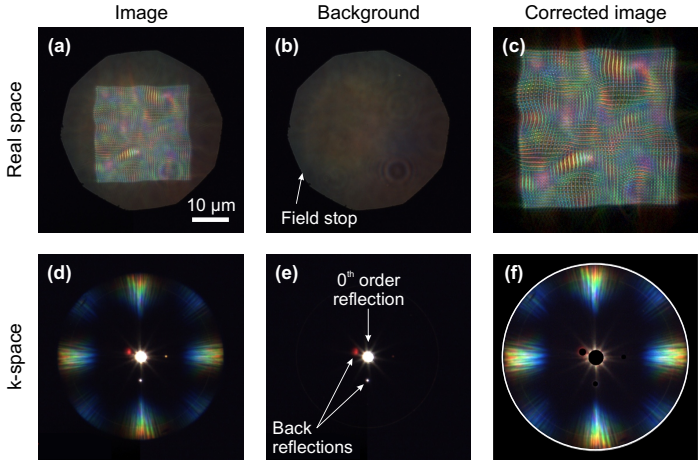

Figure 9.11. Real-space and k-space RGB image of a perturbed Al nanodisk array (s_d = 40%, L_c = 300%, P = 500 nm). To perform a background correction of the recorded real-space image (a), an image is recorded of the empty substrate (b). Both images are converted from sRGB to linear RGB before background subtraction. The resulting image is converted back to sRGB (c). In the k-space image (d), the background contains the 0^{th} order reflection and back reflections from the optical path (e), which are removed from the image (f).

This background correction deserves some extra attention. In principle, the intensity in the R, G, and B channel in each pixel is related to the spectral intensity hitting the pixel convoluted with the spectral sensitivity of the color channel [257]. These spectral sensitivities are determined by color filters, which are engineered to provide a good imitation of the human eye. However, to mimic the eye's sensitivity, the sRGB color space is used. The pixel intensities are thus nonlinearly related to the incident intensity via Equation 9.11. Subtracting two images in the sRGB color space would thus produce false values. Both images must be converted into linear RGB values by inverting Eq. 9.11 before the subtraction can be performed. All pixel intensities in the resulting image are then normalized to the highest value present in the image. After this, the normalized image is converted back to the sRGB color space.

For the k-space image, such a background correction is not necessary, since the substrate reflection and the setup back reflection can clearly be distinguished in the background image and can thus be removed from the

image before normalization. In this case, the 0^{th} order reflection (which produces oversaturated pixels due to its brightness) is removed as well. This is not a problem, as the information about the disorder is contained in the diffraction.

9.4.3 *Real-space RGB imaging*

Figure 9.12 shows a set of real-space RGB images of disordered Al nanoparticle ensembles, generated via completely randomized positions, via the simplified RSA model, and using frozen-phonon (uncorrelated) and correlated disorder as described in Section 9.2.1. Each array is generated using the same seed value. The base lattice periodicity is 500 nm, which is above the diffraction limit of the setup. The individual structures can thus be recognized in the microscope images. In the completely randomized ensemble, overlapping structures exist (see Fig. 9.4). These lead to very strong local scattering peaks, as the overlapping nanoparticles effectively form nanoantennas with a much higher scattering cross-section than the individual Al disks (see Section 4.2.2). In the simplified RSA model, the intensity distribution is again much more uniform, while the color impression is much more diverse than in the unperturbed case.

If frozen-phonon disorder is introduced, a somewhat different picture arises. The overall color impression remains comparable to the base lattice. As s_d increases, more particles at very small distances from each other appear, again leading to stronger intensity peaks in the real-space image. Correlated disorder leads to another clearly recognizable effect. Different colors occur again, but in this case, areas or 'patches' of locally similar colors can be recognized. These areas occur at sizes in the order of the correlation length L_c, as the correlation leads to the formation of locally similar interparticle distances. This indicates that one can think of a lattice perturbed by correlated disorder as a set of different smaller lattices, each with its own periodicity in x and y direction and with its own orientation. As s_d increases, very bright patches occur again. Similar to the uncorrelated case, these can be attributed to particles that are very close together. In this case, the correlation length causes the formation of patches of closely spaced particles, leading to larger areas of high intensity. At the same time, large areas of very large interparticle spacing are formed as well, leading to the formation of 'dark' areas alongside the 'bright' ones. It should be noted that the colors in the very bright patches are not always reproduced

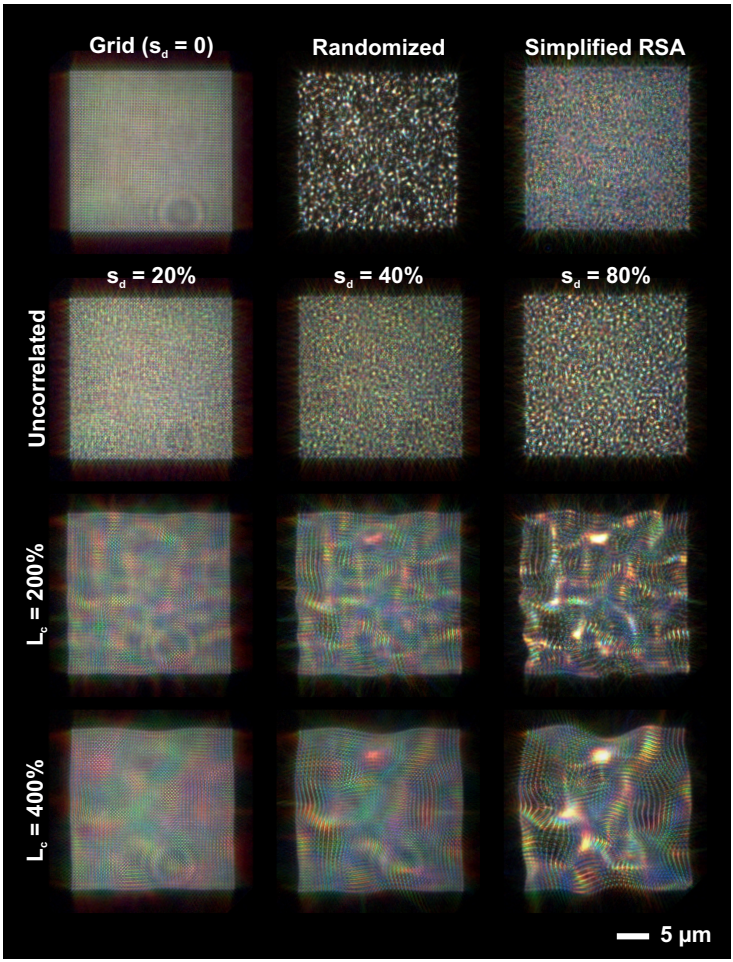

Figure 9.12. Real-space RGB reflected images of different disordered arrays of 50×50 aluminum nanodisks ($d = 120$ nm, $h = 60$ nm, $P = 500$ nm) at normal incidence. The same seed value is used for each array.

accurately, since the high intensity can lead to oversaturation of the CCD camera pixels.

Figure 9.13 shows real-space RGB images of Al nanodisk arrays using the same disorder parameters as in Fig. 9.12, but with a base lattice period of 250 nm instead of 500 nm. This means that the average interparticle

spacing is *below* the diffraction limit, so that the individual particles cannot be resolved anymore. The overall effects are nevertheless similar. A larger s_d value leads to more variation in color, while the introduction correlation leads to the formation of dark and bright patches at typical sizes scaling with L_c.

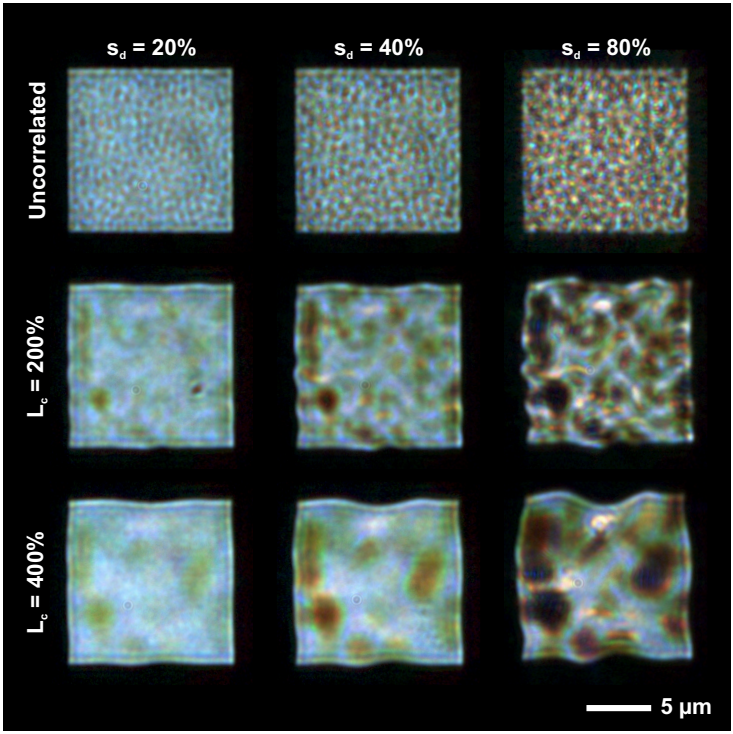

Figure 9.13. Real-space RGB reflected images of nine different disordered arrays of 50×50 aluminum nanodisks ($d = 120$ nm, $h = 60$ nm, $P = 250$ nm) at normal incidence. The same seed value is used for each array.

9.4.4 *k-space RGB imaging*

K-space images corresponding to the real-space images in Fig. 9.12 are displayed in Figure 9.14. In these images, the different disorder types can clearly be distinguished from one another. In the unperturbed grid, the first-order diffraction leads to sharp peaks at scattering angles determined by the lattice period and the wavelength (via Eq. 2.1). In the case of fully randomized positions, no sharp features can be seen anymore, but rather an approximately isotropic scattering into all directions occurs. This can also be interpreted as an overlap of diffraction orders arising from many different lattices with random orientations and periodicities. In the case of simplified RSA disorder, the rotational symmetry of the diffraction pattern is maintained, but the angle-dependence is not. Light is diffracted into large angles, similar to the diffraction of the unperturbed lattice. The diffraction pattern of this disordered array can thus also be interpreted as overlapping diffraction patterns from many arrays with different orientations, but with *similar* periodicities. The range of angles into which the light is diffracted is in this case determined by the minimum distance s_{min} used for generating the set of positions.

In the case of uncorrelated disorder, isotropic scattering can be recognized as well. As s_d increases, the first order diffraction peaks decrease in intensity, while a roughly isotropic background signal occurs which increases in intensity. The introduction of a correlation length has a clearly different effect. In this case, the diffraction orders do not disappear, but show a *broadening* in the polar as well as the azimuthal angle. This confirms the intuitive picture of an array with correlated disorder as a superposition of gratings with different orientations and periodicities. Furthermore, high values of L_c and s_d at the same time lead to a strong enhancement of this broadening, as the variation in 'local' periodicity and angle is increased. Nevertheless, diffraction/scattering into small angles still does not seem to occur.

A comparison of the k-space images in Fig. 9.14 to the shape of the BRDF of perturbed arrays (Fig. 9.6) indicates that the occurence of short-range and long-range order have distinct effects on the diffraction behavior. If only short-range disorder is introduced, but long-range order is still given (in the case of uncorrelated disorder), the diffraction orders of the base lattice can still be recognized. As the disorder strength increases, an isotropic scattering background occurs. The relative intensities of both features depend on s_d. In contrast, if long-range disorder is introduced, while some short-range

order is still maintained (in the case of correlated disorder), a *broadening* rather than a *weakening* of the first-order diffraction is observed. This also means that the diffraction patterns in these 'dark-field' k-space image can

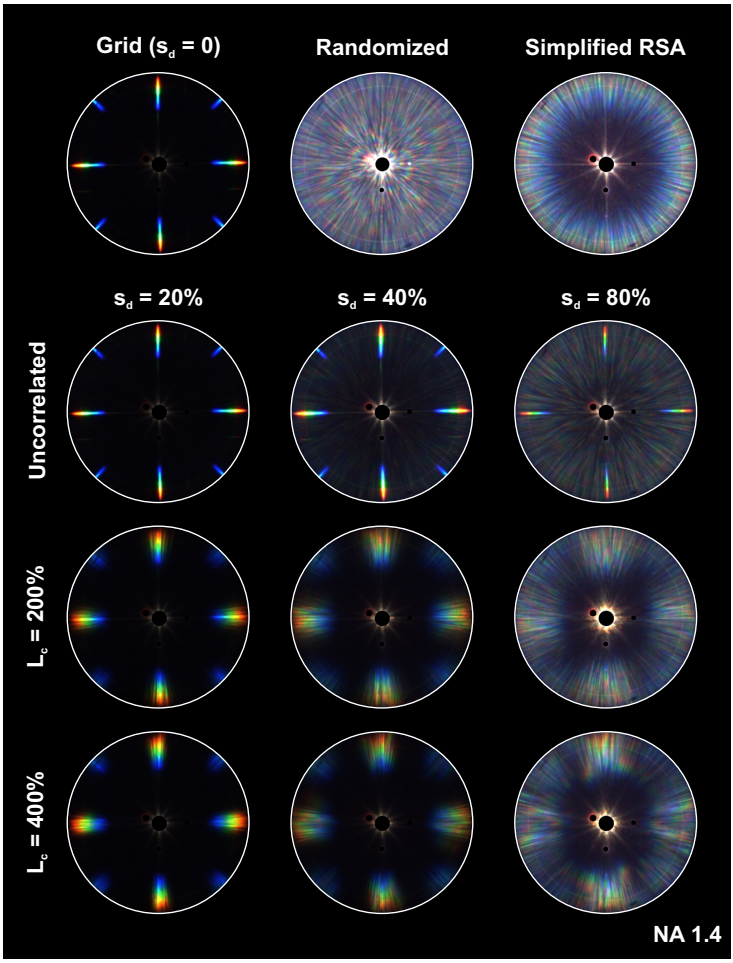

Figure 9.14. K-space RGB reflected images corresponding to the real-space images shown in Figure 9.12. Note that each image is individually contrast-enhanced to improve the visibility of the diffraction patterns, so that the intensities are not comparable between images. This also causes the apparently bright scattering around the 0^{th} order at high L_c and s_d values.

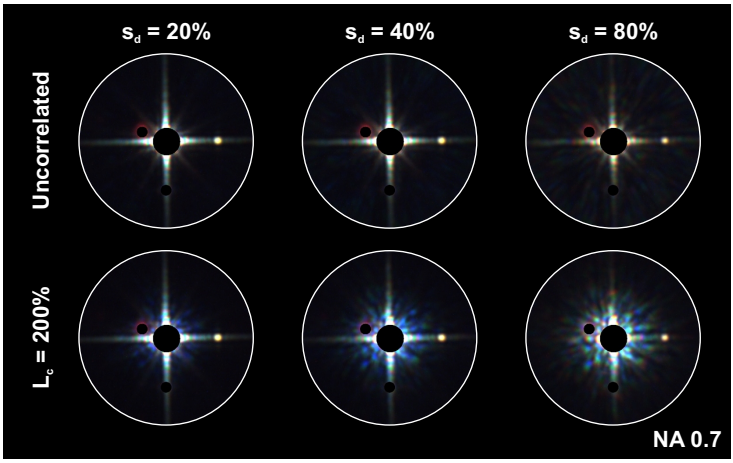

Figure 9.15. Examples of k-space RGB reflected images corresponding to real-space images shown in Figure 9.13. At subdiffraction periodicities, the first order diffraction is not collected anymore. These images show a zoom-in of the inner half of the k-space images, corresponding to an NA of 0.7 or an angle of approx. 27°.

be used to *identify* the type of disorder present in the array, in contrast to bright-field measurements.

Nevertheless, these observations are only valid if the first- or higher-order diffraction from the base lattice is collected by the microscope objective, in other words, for periodicities above the diffraction limit. If P is decreased, this is *not* the case anymore. The loss of spatial resolution in Fig. 9.13 with respect to Fig. 9.12 is directly connected to the loss of first-order diffraction in the collected k-space image (as explained in Section 2.1.2). Nevertheless, the k-space images recorded on these sub-diffraction disordered arrays hold some interesting information as well. As shown in Figure 9.15, a broadening of the 0^{th} order diffraction can be recognized in the case of correlated disorder. For lattices with only very little disorder, only a cross-shaped diffraction pattern is observed. This can be understood diffraction caused by the square-shaped array as a whole, which acts as a single diffracting object. As L_c and s_d are increased, this shape is blurred. Together with the formation of 'bright' and 'dark' patches, this leads to broadening.

9.4.5 *Spectroscopic measurements*

In addition to the RGB imaging measurements, we perform spectroscopic bright-field reflectance measurements on the disordered Al nanodisk arrays, using the same near-normal incidence illumination geometry to quantify the influence of disorder on the spectral far-field behavior. To this end, the real-space image is projected onto the entrance slit of the spectrometer. An aluminum patch on the same substrate is used to record a reference spectrum and calculate the reflectance according to Eq. 3.7. A single measurement can only cover a nearly one-dimensional section of a disordered array. By recording measurements for different sample positions, using the motorized XY stage of the microscope, a hyperspectral image of the whole array can be recorded (see Section 3.3.4). Two examples of such measurements are shown in Figure 9.16. In panels (a) and (c), the reflectance spectrum of each pixel has been converted to colors using the color theory described in Section 9.3.1. The resulting colors are in fact a better representation of the colors observed

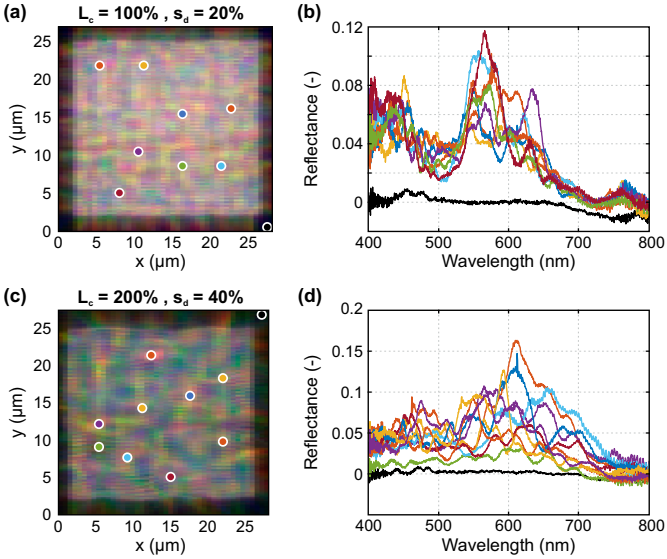

Figure 9.16. Examples of hyperspectral images recorded on disordered Al nanodisk arrays ($P = 500$ nm). The reflectance spectrum in each pixel has been converted to an RGB color in (a) and (c). In (b) and (c), spectra of a randomly determined set of pixels are shown.

by the human eye than the RGB camera images, since the real sensitivity of the human eye is considered, whereas the imaging camera only provides an approximation. Nevertheless, a comparison of the reconstructed color images to the RGB images in Fig. 9.12 reveals a good match.

Panels (b) and (d) show exemplary reflectance spectra of randomly chosen pixels. For an array with higher L_c and s_d values, a larger deviation between individual pixel spectra can be observed, both in spectral shape and in intensity. This is consistent with the emergence of additional colors that was observed in the RGB images. To visualize this broadening of the reflected colors, we convert the reflectance spectra of all pixels to the xyY color space. Scatter plots of the resulting chromaticity coordinates x and y in the CIE 1931 chromaticity diagram are shown in Figure 9.17. The point cloud of

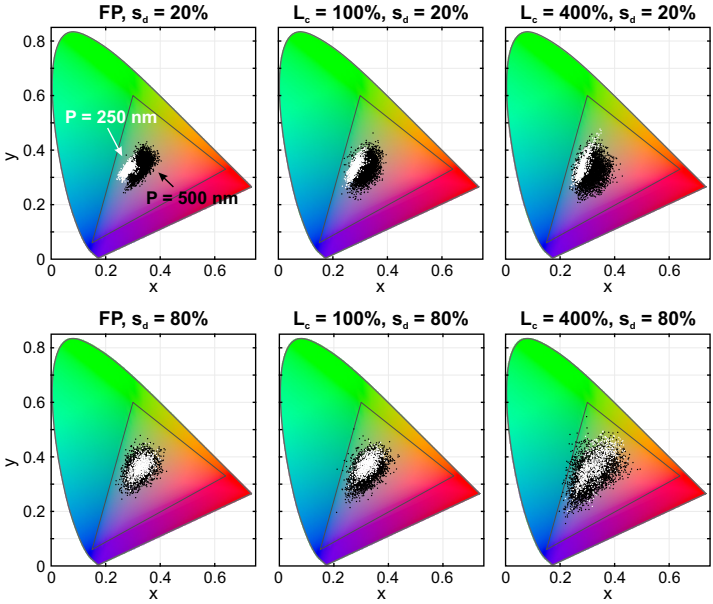

Figure 9.17. CIE 1931 chromaticity diagram with scatter plots of the x, y chromaticity coordinates extracted from hyperspectral bright-field reflectance measurements on disordered Al nanodisk arrays, for frozen-phonon disorder and correlated disorder. The white datapoints were obtained from measurements on subdiffraction arrays with $P = 250$ nm, and the black points from arrays with $P = 500$ nm (see Fig. 9.16). All pixels with a reflectance below a certain threshold (determined individually for each dataset) were omitted.

pixel chromaticity coordinates spreads throughout the color space as more disorder is introduced into the array. This spreading occurs for periodicities above as well as below the diffraction limit, although the initial spread is smaller for sub-diffraction structures. An intuitive explanation is that a sub-diffraction lattice acts as a single object, with a uniform 0^{th} order reflectance. In the larger lattice, the individual particles can be recognized, so that there is a stronger variation between pixels.

9.4.6 *BRDF imaging*

As explained in Section 9.1, the optical appearance of a surface is characterized via its bidirectional reflectance distribution function (BRDF). To obtain the full BRDF, the optical far-field must be characterized not only for different collection angles $(\theta_{\text{out}}, \phi_{\text{out}})$, but also for different angles of incidence $(\theta_{\text{in}}, \phi_{\text{in}})$. While all collection angles are contained in a single k-space image, the angle of incidence can be varied by moving the illuminated spot in the objective BFP (see Fig. 9.10). Figure 9.18 shows a set of k-space images of three different perturbed Au nanoparticle arrays, recorded at different polar angles of incidence θ_{in} for the same azimuthal angle. The corresponding real-space images are shown as well, to demonstrate the effect of a high angle of incidence.

The first observation from these BRDF images is that the shape of the diffraction pattern in the k-space does not change, as the diffraction orders are still centered around the 0^{th} order reflection. As the angle increases, however, the *second* diffraction order enters the observable range of angles. At first, only the lower-wavelength range of the 2^{nd} order is collected. This leads to a change in color in the real-space image, since the lower wavelengths are 'over-represented'. This color change is most pronounced for arrays with small perturbations (Fig. 9.18(a)). As the angle of incidence approaches the objective NA (at 60.8°), the 2^{nd} order is fully visible and the color appearance is restored. The spatial resolution is increased as well, albeit only along one axis. By recording large datasets of hyperspectral bright-field k-space reflectance images for a set of incidence angles spanning the full available objective NA, the entire BRDF of a nanoscale sample could be reconstructed.

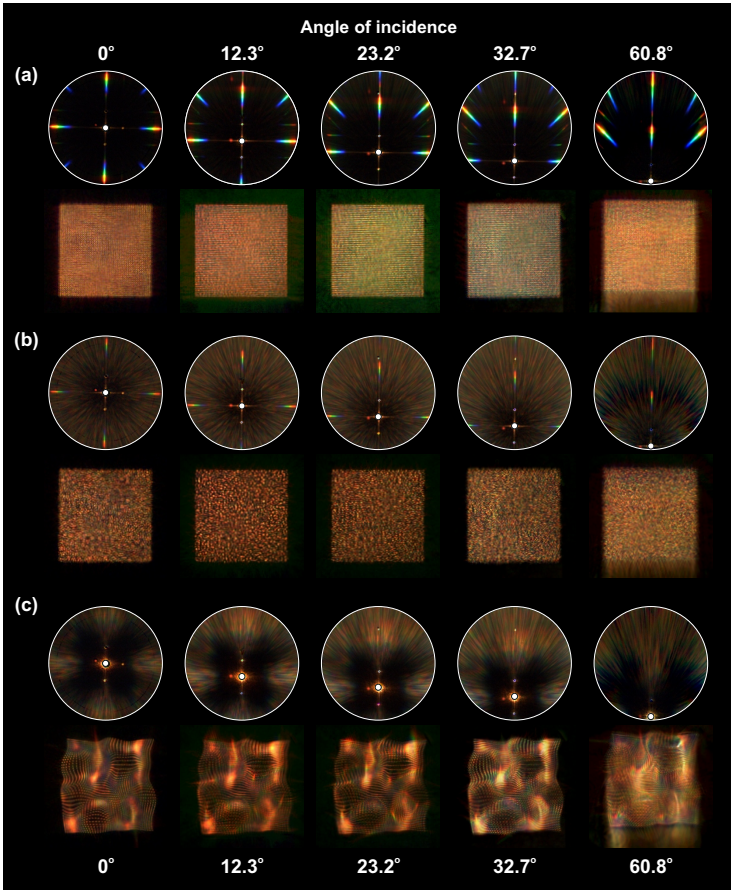

FIGURE 9.18. K-space and corresponding real space RGB images of three different disordered arrays of gold nanodisks (d = 120 nm, h = 60 nm, P = 500 nm) for different polar angles of incidence θ_{in} (calculated from the position of the 0^{th} order). The same seed value is used for the three arrays, which are generated using frozen-phonon disorder at disorder strengths 20% (a) and 80% (b), and correlated disorder at correlation length 400% with disorder strength 80% (c).

9.5 NUMERICAL CALCULATIONS

In addition to the optical measurements presented in the previous sections, we implement a calculation model to predict the far-field appearance of a disordered ensemble of plasmonic nanoparticles. In principle, it would be possible to calculate the optical far-field of such an ensemble using finite-element or FDTD methods. However, due to the large number of particles involved, this is an unpractical approach. We thus use a coupled-dipole model, in which each nanoparticle is approximated as a single dipole. A full description of the underlying theory and the implementation of the model can be found in Ref. [258]. This section will give a short conceptual description of the calculation model and an overview of the obtained results.

9.5.1 *Coupled-dipole model*

As we have seen in Section 4.2.1, a plasmonic nanoparticle can be approximated as a single dipole. This fact can be used to calculated the electric field in and around the particle. In this approximation, the particle is characterized by its polarizability α. In small, spherical particles, the polarizibility is isotropic. For more complex particle shapes, however, this is not the case anymore. In the case of the nanodisks considered here, an electromagnetic wave polarized along the vertical axis will trigger a different response than a wave polarized in the horizontal plane. In this case, the polarizability can thus not be expressed as a scalar anymore, but must be expressed as a *tensor*. The modified expression for the dipole moment (Equation 4.35) then reads:

$$\boldsymbol{p} = \epsilon_0 \epsilon_e \hat{\alpha} \boldsymbol{E}_0, \tag{9.12}$$

in which ϵ_e is the dielectric function of the environment, and $\boldsymbol{E}_0$ the background electric field at the center of the particle. The polarizability tensor $\hat{\alpha}$ is given by:

$$\hat{\alpha} = \left[\boldsymbol{\alpha}_x, \boldsymbol{\alpha}_y, \boldsymbol{\alpha}_z\right] = \begin{bmatrix} \alpha_{xx} & \alpha_{xy} & \alpha_{xz} \\ \alpha_{yx} & \alpha_{yy} & \alpha_{yz} \\ \alpha_{zx} & \alpha_{zy} & \alpha_{zz} \end{bmatrix}, \tag{9.13}$$

with α_{ij} denoting the polarizability along axis i upon excitation by an electric field polarized along axis j.

In the case of a disk-shaped particle of arbitrary size, no direct analytic solution for $\hat{\alpha}$ exists. Nevertheless, $\hat{\alpha}$ can be 'reverse-engineered' if the

electric field is known. This can be done via the following relation, as described by Fradkin *et al.* [259]:

$$\boldsymbol{p} = \epsilon_0 \int_{\text{disk}} \Delta\epsilon \, (\boldsymbol{E}_0 + \boldsymbol{E}_{\text{scatt}}) \, d^3\boldsymbol{r}, \tag{9.14}$$

with $\Delta\epsilon = \epsilon_{\text{metal}} - \epsilon_{\text{e}}$ and $\boldsymbol{E}_{\text{scatt}}$ the scattered electric field. This means that, for a particle embedded in a medium with constant refractive index, the polarizability upon excitation along axis j can be extracted from the electric field as follows:

$$\boldsymbol{\alpha}_j = \frac{\int_{\text{disk}} \Delta\epsilon \left(\boldsymbol{E}_{0,j} + \boldsymbol{E}_{\text{scatt},j}\right) d^3\boldsymbol{r}}{\epsilon_{\text{med}} E_0}, \tag{9.15}$$

with $\boldsymbol{E}_{0,j}$ denoting the incident field (polarized along direction j), E_0 representing its amplitude, and $\boldsymbol{E}_{\text{scatt},j}$ being the resulting scattered field. Assuming that the phase of the electric field does not significantly change while traveling through the particle, the off-diagonal terms of $\hat{\alpha}$ are zero due to the symmetry of the problem. This assumption holds as long as the retardation effect does not play a significant role, which is usually the case for particle sizes of around 100 nm and smaller.

The electric field in and around a *single* nanodisk can easily be extracted from FEM calculations. Here, we model the nanodisk in COMSOL as a cylinder with rounded edges with dielectric function ϵ_{metal} in a constant refractive index of $n_e = 1.5$. A plane wave $\boldsymbol{E}_0(\lambda)$ is launched at the disk along the vertical axis, as illustrated in Figure 9.19(a). By extracting the polarizability from the electric field using Eq. 9.15 and repeating the calculation for different wavelengths, the (complex-valued) z component of $\hat{\alpha}$ can be calculated. This procedure is then repeated for excitation along the x axis to obtain the other two components of $\hat{\alpha}$, which are identical due to the rotational symmetry of the problem. By including a third excitation step along the y axis, this approach can also be applied to rod-shaped particles.

After we have established a method of calculating the effective polarizability of a single particle, the next step is to introduce coupling between particles in an ensemble of arbitrary size. If each dipole i at a location $\boldsymbol{r}_i$ is assumed to interact with all other dipoles $j \neq i$, the local electric field at $\boldsymbol{r}_i$ is equal to the sum of the incident electric field $\boldsymbol{E}_0$ and the electric field radiated by all other dipoles:

$$\boldsymbol{E}_i(\boldsymbol{r}_i) = \boldsymbol{E}_0 + \sum_{j \neq i} \boldsymbol{E}_j(\boldsymbol{r}_i). \tag{9.16}$$

Via Equation 9.12, this leads to a large set of coupled equations, which must be solved to obtain the electric field at each position in the ensemble of dipoles.

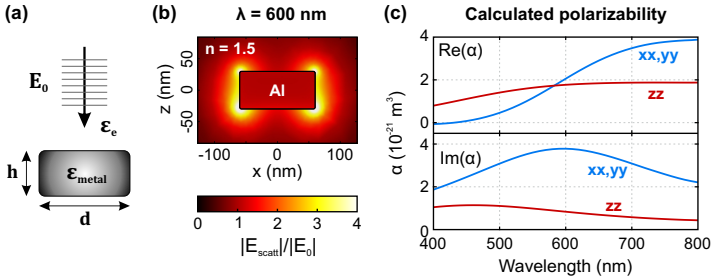

Figure 9.19. The polarizability of a single nanoparticle is obtained from FEM calculations using Comsol, in which a plane wave $\boldsymbol{E}_0$ is launched at a disk-shaped particle with dielectric function ϵ_{metal} in a uniform medium with ϵ_e (a). From the resulting scattered field $\boldsymbol{E}_{\text{scatt}}$ (b), one component of the polarizability tensor $\hat{\alpha}$ can be extracted. By launching the wave once from the z direction and once from the x direction, all three diagonal tensor components can be calculated, as the disk is rotationally symmetric (c). The data shown here are for a bare aluminum nanodisk of diameter $d = 120$ nm and height $h = 60$ nm.

By applying the near-to-far field conversion proposed by Yang *et al.* [260], in which an incoming test plane wave $\boldsymbol{E}_0$ is projected on the scatterers in order to derive the electric field in a surrounding surface (in our case a plane at a typical distance of 1 nm above the dipole ensemble), the k-vector-resolved intensity radiated by the full dipole ensemble can be calculated. The result, truncated at $\sqrt{k_x^2+k_y^2}/|k| \leq 1$, gives the total intensity radiated into the far field. This corresponds to the Fourier plane image or back focal plane that would be visible in a Fourier microscopy setup. To simulate the effect of a microscope objective with a limited NA, the truncation can also be performed at $\sqrt{k_x^2+k_y^2}/|k| \leq \text{NA}/n$. Furthermore, applying an inverse Fourier transform to the obtained k-vector-resolved intensity gives the corresponding real-space intensity distribution. This transform is analogous to the effect of adding a lens behind the Fourier plane to retrieve the real-space image (lens L2 Figure 9.10).

By repeating this procedure for different wavelengths, the spectrally resolved reflected k-space and real-space images of a predefined ensemble of plasmonic nanoantennas, illuminated from a certain angle, can thus be extracted. By varying the angle of incidence of the incoming electric field $\boldsymbol{E}_0$ as well, it is in principle possible to obtain a full dataset in which the reflected intensity as a function of wavelength and observation angle is related to the angle of incidence. This dataset would, in other words, provide the full

BRDF of the nanoparticle ensemble (see Section 9.1) and thus contain all the necessary information for a full characterization of the far-field behavior of the metasurface, similar to hyperspectral measurements. On the other hand, as long as the wavelength range of interest covers the visible range, the three-dimensional datacube of reflectance vs. position or k-vector can also be converted to color images, as described in Section 9.3. This provides a good method to visualize the calculation results, which can be directly compared to optical measurements.

It is also possible to include particles of different sizes, shapes, orientations, or even materials in the calculation. As long as the polarizability tensor $\hat{\alpha}$ is known for each particle, the electric field can be calculated via the coupled equations given by Eq. 9.16. By establishing a database of $\hat{\alpha}$ for many different particles, the dipole coupling model thus becomes a widely applicable tool for predicting far-field behavior of disordered plasmonic metasurfaces.

9.5.2 *Single-particle spectra*

Before using the dipole model described above to verify optical measurements on dipole ensembles, a first step is to compare the calculated and measured far-field signal of a single particle. Figure 9.20 displays a comparison of calculated and measured far-field scattering spectra of single nanodisks made of gold and aluminum. The measured nanodisks are fabricated similarly to the disordered nanodisk arrays described in Section 9.2, situated on a SiO_2 substrate and embedded in IC1-200. The measurements are performed in dark-field transmission mode as described in Section 3.3.2 with unpolarized light, using a Nikon TU PLAN FLUOR ELWD 60× objective with NA 0.70. The incident angle used in the calculations is set to match the average incident angle of the dark-field condenser. The dielectric data are taken from Refs. [17] and [12] for Au and Al, respectively.

For gold nanodisks, a very good agreement of the dipole model with the dark-field spectroscopic measurements is observed. This validates the calculation approach. For aluminum nanodisks, however, the model does not perfectly reproduce the measured spectra. Compared to the expected shape, a redshift of around 80 nm is observed. In the Al particle simulations, a 3 nm thick shell of aluminum oxide (Al_2O_3) was added, as aluminum has been reported to form a self-terminating native oxide layer of typically this thickness [66]. The remaining discrepancy can most likely be attributed to oxidation of the aluminum during evaporation. In contrast to Au, Al is

susceptible to oxidation due very small levels of oxygen still present in the deposition chamber.

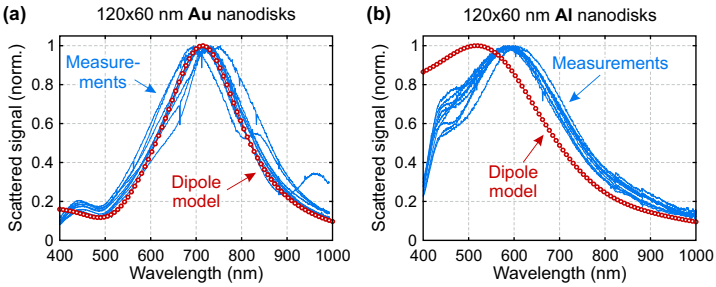

Figure 9.20. Measured and calculated scattering spectra of single nanodisks made of gold (a) and aluminum (b) on SiO_2, embedded in IC1-200. The measurements were carried out on nine particles simultaneously using dark-field microspectroscopy in transmission mode (see Section 3.3.2). The nine resulting scattering curves are shown in blue. In the case of the Al nanodisks, the discrepancy between measurements and calculations can most likely be attributed to oxidation.

9.5.3 *Color images*

Figure 9.21 shows calculated real-space RGB images of disordered Al nanoparticle arrays, using the same disorder parameters as the measured images shown in Figs. 9.12 and 9.14. The corresponding k-space images are shown in Figure 9.22. A comparison between the calculated and measured images reveals an astonishing agreement. Not only the typical features of diffraction broadening and isotropic background scattering are reproduced with a very high accuracy, but also the general color impression is very similar. Individual patches of color in the real-space images can one to one be identified in the measurements. The remaining difference can be attributed to the oxidation of the Al particles (Fig. 9.20) in combination with the different methods through which the color is generated. In the calculations, the conversion from spectral intensity to color is performed via a color model designed to mimic the human eye. In the measurements, the color follows from the spectral sensitivity of the CCD camera. Furthermore, the non-uniform light

source spectrum has an influence as well. In the measurements, this influence is compensated by white calibration of the camera, but can not be fully omitted nonetheless.

The very good agreement between our measurements and numerical calculations demonstrates that our dipole interaction based calculation model is a very useful tool to predict the optical far-field behavior of disordered plasmonic arrays. This can not only be used to verify optical measurements, but also to calculate the fully wavelength-resolved BRDF of nanoparticle ensembles. This can, in turn, be used to determine the necessary combination of disorder parameters to realize a certain desired optical appearance.

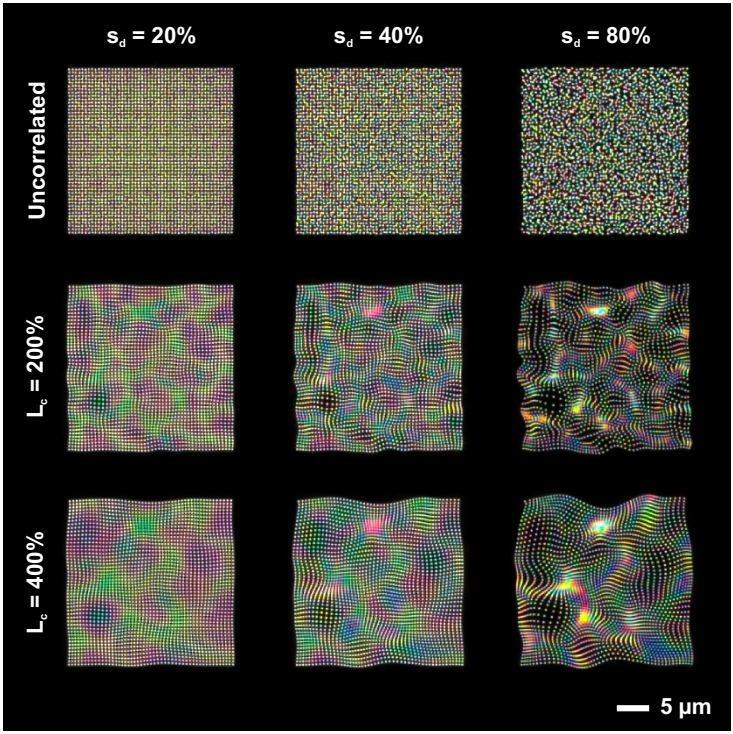

Figure 9.21. Calculated real-space RGB images of nine different disordered arrays of 50×50 aluminum nanodisks ($d = 120$ nm, $h = 60$ nm) at normal incidence, using the same sets of positions as in the measurements shown in Figure 9.12.

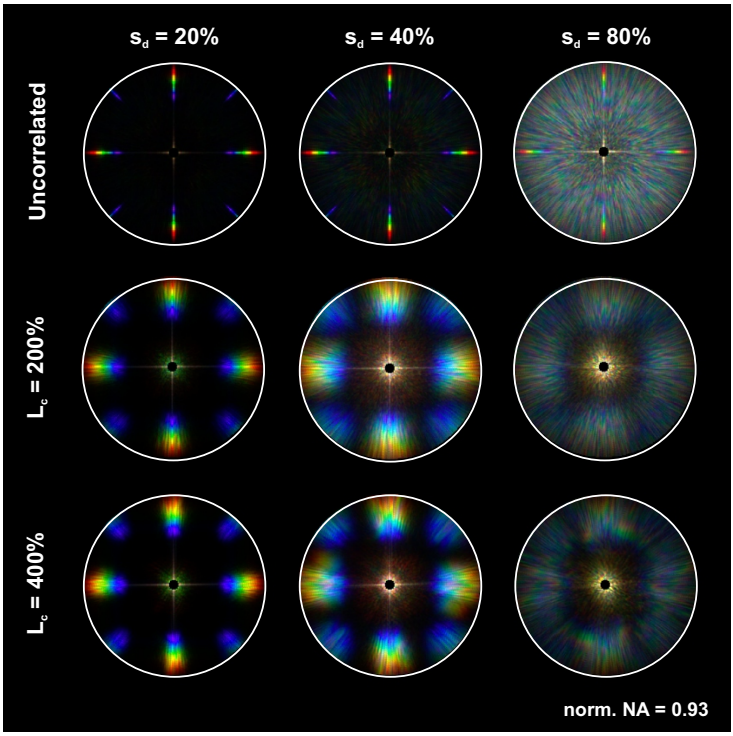

Figure 9.22. Calculated real-space RGB images corresponding to the real-space images in Figure 9.21.

9.6 Conclusion and Outlook

In this chapter, we have investigated the influence of structural disorder on the optical far-field response of plasmonic nanoantenna arrays. We have introduced a disorder model which uses two disorder parameters, namely the disorder strength and the correlation length. To quantify the influence of both parameters, we have performed bright-field k-space microspectroscopic measurements as well as real-space and k-space resolved imaging measurements with near-normal incidence and high collection NA. The measurement results reveal that an increase of both disorder parameters inevitably leads to a broadening of the lattice-based features in the bright-field measurements. This can be attributed to a loss of long-range order, as seen in the radial and Cartesian two-point correlation function of the disordered

arrays. However, a conclusion about the short-range order can not be drawn exclusively from these bright-field measurements. In the measurements recorded at near-zero incidence, in contrast, both disorder parameters reveal a clearly distinguishable influence, manifesting in a weakening of the diffraction orders and the emergence of isotropic scattering as well as a significant broadening of the diffraction orders.

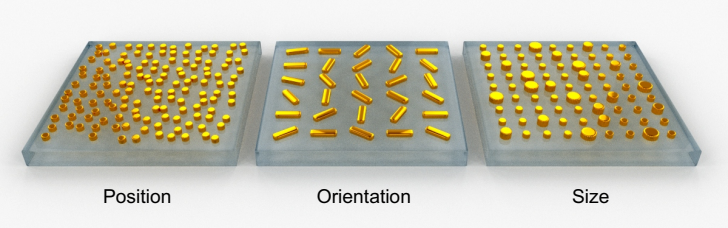

FIGURE 9.23. Examples of different disorder types in plasmonic metasurfaces: Positional disorder, orientational disorder, and size disorder.

We have furthermore verified these observations using a calculation approach based on dipole-dipole interaction, which shows a very good agreement with the measurement results. This calculation approach can thus be widely applied in future investigations of disordered nanoplasmonic systems with other types of disorder, or combinations thereof. Examples of other disorder types are orientational disorder or size disorder, as illustrated in Fig. 9.23.

Another highly interesting prospect for the application of disordered plasmonic systems is the use of tailored disorder to engineer a desired far-field response. This holds potential use in the design and fabrication of nanoparticle coatings to generate desired appearances of surfaces, but also for the design of beam-steering devices and flat metalenses [261, 262]. The dipole model described in Ref. [258] thus also provides a highly useful tool for the design of such nanoplasmonic devices.

10

CONCLUSIONS AND OUTLOOK

In this thesis, we have explored in detail the experimental method of microspectroscopy, specifically the combination of optical microscopes with grating spectrometers. In Chapters 2 and 3, we have reviewed the fundamental principles of optical microscopy and spectroscopy and studied the parameters that influence the spatial as well as the spectral resolution of a microspectroscopy system. In addition to this, we have looked at the different configurations that can be used for illumination, light collection, and imaging, and have established an overview of which configuration can best be used for which type of measurement. As we have seen, bright-field illumination is the method of choice for many applications in which the transmittance and/or reflectance of a sample needs to be characterized, while dark-field illumination enables the recording of only scattered light and is thus suitable to study individual, isolated nanoparticles. Both of these methods provide spectrally as well as spatially resolved information, as the spectrometer effectively replaces one of two spatial dimensions by a spectral dimension. Furthermore, we have seen that Fourier microscopy enables the recording of angle-resolved instead of spatially resolved measurements, thus significantly increasing the amount of information that one can gain of a nanoscale sample with the same setup. We have also addressed the topic of data processing, focusing on the different optical quantities that can be extracted from a typical microspectroscopic measurement.

Following this background information on the experimental methods, we have discussed the theoretical background of plasmonics in Chapter 4. We have seen how an external electric field can excite plasmon resonances, and how these can be detected by far-field optical measurements of the transmittance, reflectance, or scattering. The spectral shape and position of plasmon resonance features in the far-field depend sensitively on parameters such as the particle size, shape, material, and local environment. For this reason,

microspectroscopic measurements can be employed to study the behavior of nanoplasmonic systems, and control of the nanostructure parameters enables tuning of the far-field. Similarly, plasmonic nanostructures can be used for sensing applications, for example by reporting changes in the local environment into the optical far-field.

In the remaining chapters, we have shown several different applications of these principles. In Chapter 5, we have studied the behavior of magnesium plasmonic nanostructures, a material that had not been extensively investigated for plasmonic applications before. We have not only shown that Mg can provide plasmonic resonances throughout the visible wavelength range (and thus poses a suitable and cheap alternative to other plasmonic materials such as Au and Ag), but we have also demonstrated the use of Mg nanoantennas for active plasmonics. We have employed the ability of magnesium to absorb hydrogen, which leads to a transition from metallic Mg to dielectric MgH_2. Switching of Mg nanostructures between these two states at room temperature was achieved via the combination of Mg nanoparticles with a catalytic layer of palladium, which leads to the splitting of H_2 molecules into single H atoms and the subsequent diffusion of these atoms into the Mg crystal lattice. We have shown that this leads to plasmonic nanostructures that can be switched between a plasmonic 'on' and 'off' state via the exposure to hydrogen and oxygen gas. Mg nanoparticles thus provide a truly active plasmonic system, as the plasmon resonance is not only switched off in the presence of H_2, but must be actively brought back by exposure to O_2. This means that it is also possible to keep the structures in the hydrogenated state for a prolonged time.

The use of Mg in active plasmonic systems has applications in different types of optical devices. Mg has been applied in switchable optical devices, most notably for nanoplasmonic color displays, by combining the principles of nanoplasmonic printing with active plasmonics. Using this approach, optical image displays with an unprecedented resolution can be realized. In the future, active plasmonic displays can be further optimized via the development of technologies that enable the switching of individual pixels instead of the full plasmonic ensemble at once. A promising approach for this can be found in electrochemical switching, which, via careful engineering of nanoscale electrical contacts and proton donor materials in combination with tailored nanoantenna geometries, can provide individually addressable pixels comparable to currently established display technologies. Furthermore, we have seen that a certain degradation takes place over the course of several hydrogen absorption-desorption cycles. Tackling this problem requires

a modification of the metal-hydrogen system on the nanoscale. A highly promising approach, which has also been extensively reported in the context of Mg thin films, is the use of Mg-based alloys instead of pure Mg. Using, for example, Mg-Ti or Mg-Pd alloys is consequently a highly interesting future step for the further development of Mg-based active nanoplasmonic systems.

The hydrogen absorption in Mg furthermore holds a second, highly interesting application. The solid-state storage of H_2 in metal hydrides offers a promising approach to the use of hydrogen as an energy carrier, for example in transportation applications. Mg-based H_2 storage materials have been reported as very promising candidates, due to their very high H_2 storage capacity, which can in fact significantly outperform that of gas-phase hydrogen storage. Since H_2 fuel is widely considered one of the most promising technologies for the transition from fossil fuels to sustainable energy sources, it is very important to understand the physical processes behind the absorption of H_2 in metals. Plasmonic Mg nanoparticles can be used to understand the dynamics of H_2 diffusion on the nanoscale. In Chapters 6 and 7, we have studied the effects of repeated absorption-desorption on Mg nanopatches, for which we used optical as well as SEM and AFM measurements. We were able to quantify the change in shape and volume that the particles undergo. In a further step, we have, for the first time, used optical near-field microscopy to observe and track the diffusion of H_2 *within* single Mg nanodisks. This approach, which we have termed *nanoscale hydrogenography*, has enabled us to observe the hydrogenation of individual Mg crystallites.

By further developing the measurement technique to perform in-situ measurements on extended Mg thin films, we have confirmed that the hydrogenation of the entire film is in fact limited by the rate at which individual crystallites turn into MgH_2 one after another. This provides new insights for the optimization of Mg-based H_2 storage systems. A highly interesting future step is the application of our nanoscale hydrogenography technique to other metal-hydride systems, such as Mg-based alloys, in order to investigate the fundamental differences and similarities between these systems on a size scale down to a few tens of nanometers. For example, a detailed study of the effects of crystallinity in different metals promises further insights into the factors that limit the efficiency of H_2 uptake and release. In the future, these insights could be employed for the development of novel hydrogen storage devices via careful engineering of the nanoscale material properties, with a wide range of possible uses in an emerging hydrogen economy.

Shifting our focus to another technology that is of great importance for the use of H_2 fuel (amongst other applications), we have investigated palladium-based plasmonic H_2 sensing structures in Chapter 8. In contrast to Mg, the plasmonic resonance of Pd is not switched off in the presence of H_2, but rather exhibits a concentration-dependent shift. Since this process is reversible, Pd is a good candidate for optical H_2 sensors, enabling a read-out of the local H_2 concentration in the optical far-field. Purely optical sensor read-out is an important technology from a safety point of view, as H_2 is an explosive gas at concentrations exceeding 4%. Specifically, we have performed a systematic investigation of so-called 'perfect absorber'-type sensor structures. These structures are composed of a layer of plasmonic Pd nanodisks suspended above a metal mirror by a dielectric spacer layer. By careful tuning of the structure parameters, most importantly the spacer layer thickness, a near-unity absorption of all incoming light can be achieved at certain wavelengths, giving the structure its name.

In the literature, the 'perfect absorption' feature has been widely claimed to provide a very high change in reflectance in response to H_2 exposure. However, as we have discussed, this is only the case for the *relative* reflectance change. By a careful analysis of the sensor characteristics, we have shown that the *absolute* change in reflectance ΔR should be maximized, especially if a monochromatic read-out is to be employed (as opposed to more complex and costly spectral analysis). Aided by numerical calculations as well as microspectroscopic measurements, we have shown that the system can be regarded as a layer of plasmonic antennas coupled to an optical resonator. We have performed a systematic study of the structure parameters of Pd-based perfect absorpers. From the obtained results, we were able to establish a set of design rules for the optimization of plasmonic H_2 sensors. We have shown that a careful selection of the spacer thickness in combination with the read-out wavelength are the main tuning parameters for maximizing ΔR, and that a maximization of the light absorption is in fact *counterproductive*. Consequently, the 'perfect absorber' structures should in fact be used in a wavelength range *away* from the absorption maximum. We have also investigated the influence of structural disorder on the angle-dependent sensor response. By employing the newly gained insights, we were able to demonstrate a plasmonic H_2 sensor with a sensitivity down to 100 ppm. The design guidelines we have formulated do not only apply to Pd-based sensors. A wide variety of plasmonic sensors for different application, based on different sensor materials and detection methods, can benefit from the results shown in Chapter 8 as well.

Finally, in Chapter 9, we have presented a more detailed investigation of the influence of structural disorder on ensembles of plasmonic nanoantennas. To this end, we have introduced a disorder model which is based on two parameters, namely the *disorder strength* and the *correlation length*. We have characterized the influence of these disorder parameters by means of the two-point correlation function of perturbed arrays of nanodisks. By using a dedicated microspectroscopy setup, based on the concept of k-space imaging, we were furthermore able to study the effects of disorder in the optical far-field, and have shown that different disorder types and parameters lead to clearly distinguishable features. In addition to our measurements, we have implemented a calculation model based on dipole-dipole interaction to predict the far-field response of disordered plasmonic systems. The calculation results exhibit a very good agreement with the microspectroscopic measurements, and thus provide a highly useful tool for predicting the optical response of a certain arrangement of nanostructures. In the future, the insights presented here hold great promise for the development of surfaces with a desired optical response. For example, the use of *tailored* disorder can bring forward nanostructure designs that produce a desired surface appearance to the human eye.

All in all, this thesis has thus presented a detailed description of microspectroscopic measurement techniques and their application to the investigation of different nanoplasmonic systems. The systems considered here are only a small set of examples, as many other applications of plasmonics exist. In all of these applications, the optical far-field is linked to the nanoscale environment of plasmonic nanostructures, which can thus be accessed by means of microspectroscopy.

BIBLIOGRAPHY

[1] J. A. Kurvits, M. Jiang, and R. Zia: *Comparative analysis of imaging configurations and objectives for Fourier microscopy*. Journal of the Optical Society of America A **32**, 2082–2092 (2015).
DOI 10.1364/JOSAA.32.002082, cit. on pp. 6, 7, 23, 32, 159, 186.

[2] Y. Petrov: *Optometrika*, https://de.mathworks.com/matlabcentral/fileexchange/45355-optometrika (visited on Nov. 11, 2017).
Cit. on pp. 6, 7.

[3] E. Hecht and A. R. Ganesan: *Optics*, Fourth edition, Dorling Kindersley India Pvt. Ltd. (Pearson) (Delhi), 2008.
ISBN 978-81-317-1807-0, cit. on pp. 8, 10, 147.

[4] M. W. Davidson: *Resolution*, https://www.microscopyu.com/microscopy-basics/resolution (visited on Feb. 11, 2020).
Cit. on p. 13.

[5] M. Wilson: *Microscope Resolution: Concepts, Factors and Calculation*, https://www.leica-microsystems.com/science-lab/microscope-resolution-concepts-factors-and-calculation/ (visited on Feb. 11, 2020).
Cit. on p. 13.

[6] M. W. Knight, J. Fan, F. Capasso, and N. J. Halas: *Influence of excitation and collection geometry on the dark field spectra of individual plasmonic nanostructures*. Optics Express **18**, 2579–2587 (2010).
DOI 10.1364/oe.18.002579, cit. on p. 18.

[7] L. Jiang, T. Yin, Z. Dong, M. Liao, S. J. Tan, X. M. Goh, D. Allioux, H. Hu, X. Li, J. K. W. Yang, and Z. Shen: *Accurate Modeling of Dark-Field Scattering Spectra of Plasmonic Nanostructures*. ACS Nano **9**, 10039–10046 (2015).
DOI 10.1021/acsnano.5b03622, cit. on p. 18.

[8] R. Attota and R. Silver: *Optical microscope angular illumination analysis*. Optics Express **20**, 6693 (2012).
DOI 10.1364/OE.20.006693, cit. on p. 21.

[9] D. Dominguez, N. Alharbi, M. Alhusain, A. A. Bernussi, and L. G. D. Peralta: *Fourier plane imaging microscopy*. Journal of Applied Physics **116**, 103102 (2014).
DOI 10.1063/1.4895157, cit. on p. 23.

[10] J. F. Bryche, G. Barbillon, B. Bartenlian, G. Dujardin, E. Boer-Duchemin, and E. Le Moal: *K-space optical microscopy of nanoparticle arrays: Opportunities and artifacts.* Journal of Applied Physics **124**, 043102 (2018). DOI 10.1063/1.5029976, cit. on p. 23.

[11] N. V. Tkachenko: *Optics and Optical Devices.* In: Optical Spectroscopy Methods and Instrumentations, Elsevier Science Publisher B.V. (Amsterdam), 2006. ISBN 978-04-445-2126-2, cit. on p. 28.

[12] A. D. Rakić: *Algorithm for the determination of intrinsic optical constants of metal films: application to aluminum.* Applied Optics **34**, 4755 (1995). DOI 10.1364/ao.34.004755, cit. on pp. 36, 205.

[13] R. Wagner, L. Heerklotz, N. Kortenbruck, and F. Cichos: *Back focal plane imaging spectroscopy of photonic crystals.* Applied Physics Letters **101**, 081904 (2012). DOI 10.1063/1.4746251, cit. on pp. 43, 159, 186.

[14] D. J. Griffiths: *Introduction to Electrodynamics*, Third edition, Prentice Hall of India Pvt. Ltd. (New Delhi), 1998. ISBN 978-81-203-1601-0, cit. on pp. 45, 56.

[15] L. Novotny and B. Hecht: *Principles of Nano-Optics*, Cambridge University Press (New Delhi), 2008. ISBN 978-0-521-14903-7, cit. on pp. 45, 49, 51.

[16] A. Derkachova, K. Kolwas, and I. Demchenko: *Dielectric Function for Gold in Plasmonics Applications: Size Dependence of Plasmon Resonance Frequencies and Damping Rates for Nanospheres.* Plasmonics **11**, 941–951 (2016). DOI 10.1007/s11468-015-0128-7, cit. on p. 49.

[17] P. B. Johnson and R. W. Christy: *Optical Constant of the Noble Metals.* Physical Review B **6**, 4370–4379 (1972). DOI 10.1103/PhysRevB.6.4370, cit. on pp. 49, 205.

[18] E. Palik: *Handbook of Optical Constants of Solids III*, Academic Press Inc. (New York), 1997. ISBN 978-0-12-544415-6, cit. on pp. 51, 66, 70.

[19] S. A. Maier: *Plasmonics: Fundamentals and Applications*, First edition, Springer (New York), 2007. ISBN 978-0-387-37825-1, cit. on p. 51.

[20] A. Lalisse, G. Tessier, J. Plain, G. Baffou, and J. Plain: *Quantifying the Efficiency of Plasmonic Materials for Near-Field Enhancement and Photothermal Conversion.* The Journal of Physical Chemistry C **119**, 25518–25528 (2015). DOI 10.1021/acs.jpcc.5b09294, cit. on p. 55.

[21] A. G. Curto, T. H. Taminiau, G. Volpe, M. P. Kreuzer, R. Quidant, and N. F. Van Hulst: *Multipolar radiation of quantum emitters with nanowire optical antennas*. Nature Communications **4**, 1750 (2013). DOI 10.1038/ncomms2769, cit. on p. 55.

[22] I. M. Hancu, A. G. Curto, M. Castro-López, M. Kuttge, and N. F. Van Hulst: *Multipolar interference for directed light emission*. Nano Letters **14**, 166–171 (2014). DOI 10.1021/nl403681g, cit. on p. 55.

[23] B. Metzger, M. Hentschel, T. Schumacher, M. Lippitz, X. Ye, C. B. Murray, B. Knabe, K. Buse, and H. Giessen: *Doubling the Efficiency of Third Harmonic Generation by Positioning ITO Nanocrystals into the Hot-Spot of Plasmonic Gap-Antennas*. Nano letters **14**, 2867–2872 (2014). Cit. on p. 55.

[24] N. Liu, M. L. Tang, M. Hentschel, H. Giessen, P. Alivisatos, and A. P. Alivisatos: *Nanoantenna-enhanced gas sensing in a single tailored nanofocus*. Nature materials **10**, 631–636 (2011). DOI 10.1038/nmat3029, cit. on pp. 56, 65, 106, 139.

[25] T. Shegai and C. Langhammer: *Hydride formation in single palladium and magnesium nanoparticles studied by nanoplasmonic dark-field scattering spectroscopy*. Advanced Materials **23**, 4409–4414 (2011). DOI 10.1002/adma.201101976, cit. on pp. 56, 67, 76, 106, 139.

[26] L. Novotny and N. Van Hulst: *Antennas for light*. Nature Photonics **5**, 83–90 (2011). DOI 10.1038/nphoton.2010.237, cit. on p. 56.

[27] F. Sterl: *Towards efficient photocatalytic water splitting: Increasing the absorption rate of ruthenium-based chromophores by coupling to plasmonic silver nanostructures*. MA thesis, University of Twente, 2013. Cit. on p. 58.

[28] H. Fredriksson, Y. Alaverdyan, A. Dmitriev, C. Langhammer, D. S. Sutherland, M. Zäch, and B. Kasemo: *Hole-mask colloidal lithography*. Advanced Materials **19**, 4297–4302 (2007). DOI 10.1002/adma.200700680, cit. on pp. 59, 163.

[29] S. Syrenova, C. Wadell, and C. Langhammer: *Shrinking-hole colloidal lithography: self-aligned nanofabrication of complex plasmonic nanoantennas*. Nano letters **14**, 2655–63 (2014). DOI 10.1021/nl500514y, cit. on p. 61.

[30] S. Cataldo, J. Zhao, F. Neubrech, B. Frank, C. Zhang, P. V. Braun, and H. Giessen: *Hole-mask colloidal nanolithography for large-area low-cost metamaterials and antenna-assisted surface-enhanced infrared absorption substrates*. ACS nano **6**, 979–85 (2012). DOI 10.1021/nn2047982, cit. on p. 61.

[31] A. Tittl, X. Yin, H. Giessen, X.-D. Tian, Z.-Q. Tian, C. Kremers, D. N. Chigrin, and N. Liu: *Plasmonic smart dust for probing local chemical reactions.* Nano letters **13**, 1816–1821 (2013).
DOI 10.1021/nl4005089, cit. on pp. 65, 170.

[32] K. F. MacDonald and N. I. Zheludev: *Active plasmonics: Current status.* Laser and Photonics Reviews **4**, 562–567 (2010).
DOI 10.1002/lpor.200900035, cit. on p. 65.

[33] K. Appavoo, D. Y. Lei, Y. Sonnefraud, B. Wang, S. T. Pantelides, S. A. Maier, and R. F. Haglund: *Role of defects in the phase transition of VO_2 nanoparticles probed by plasmon resonance spectroscopy.* Nano letters **12**, 780–786 (2012).
DOI 10.1021/nl203782y, cit. on p. 65.

[34] I. M. Pryce, K. Aydin, Y. A. Kelaita, R. M. Briggs, and H. A. Atwater: *Highly strained compliant optical metamaterials with large frequency tunability.* Nano Letters **10**, 4222–4227 (2010).
DOI 10.1021/nl102684x, cit. on p. 65.

[35] M. Abb, P. Albella, J. Aizpurua, and O. L. Muskens: *All-optical control of a single plasmonic nanoantenna-ITO hybrid.* Nano letters **11**, 2457–2463 (2011).
DOI 10.1021/nl200901w, cit. on p. 65.

[36] N. K. Emani, T.-F. Chung, X. Ni, A. Kildishev, Y. P. Chen, and A. Boltasseva: *Electrically Tunable Plasmonic Resonances with Graphene.* Nano letters **12**, 5202–5206 (2012).
DOI 10.1364/CLEO_AT.2012.JTu1M.2, cit. on p. 65.

[37] Y. R. Leroux, J. C. Lacroix, K. I. Chane-Ching, C. Fave, N. Félidj, G. Lévi, J. Aubard, J. R. Krenn, and A. Hohenau: *Conducting polymer electrochemical switching as an easy means for designing active plasmonic devices.* Journal of the American Chemical Society **127**, 16022–16023 (2005).
DOI 10.1021/ja054915v, cit. on p. 65.

[38] X. Fang, M. L. Tseng, J. Y. Ou, K. F. Macdonald, D. P. Tsai, and N. I. Zheludev: *Ultrafast all-optical switching via coherent modulation of metamaterial absorption.* Applied Physics Letters **104**, 141102 (2014).
DOI 10.1063/1.4870635, cit. on p. 66.

[39] D. M. Borsa, A. Baldi, M. Pasturel, H. Schreuders, B. Dam, R. Griessen, P. Vermeulen, and P. H. L. Notten: *Mg–Ti–H thin films for smart solar collectors.* Applied Physics Letters **88**, 241910 (2006).
DOI 10.1063/1.2212287, cit. on pp. 66, 74.

[40] N. Strohfeldt, A. Tittl, M. Schäferling, F. Neubrech, U. Kreibig, R. Griessen, and H. Giessen: *Yttrium hydride nanoantennas for active plasmonics.* Nano Letters **14**, 1140–1147 (2014).
DOI 10.1021/nl403643v, cit. on pp. 66, 77, 103.

[41] A. Tittl, P. Mai, R. Taubert, D. Dregely, N. Liu, and H. Giessen: *Palladium-based plasmonic perfect absorber in the visible wavelength range and its application to hydrogen sensing*. Nano letters **11**, 4366–4369 (2011). DOI 10.1021/nl202489g, cit. on pp. 66, 73, 140, 141.

[42] A. Tittl, H. Giessen, and N. Liu: *Plasmonic gas and chemical sensing*. Nanophotonics **3**, 157–180 (2014). DOI 10.1515/nanoph-2014-0002, cit. on pp. 66, 77, 170.

[43] J. M. Sanz, D. Ortiz, J. M. Saiz, A. S. Brown, M. Losurdo, H. O. Everitt, and F. Moreno: *UV Plasmonic Behavior of Various Metal Nanoparticles in the Near- and Far-Field Regimes: Geometry and Substrate Effects*. The Journal of Physical Chemistry C **117**, 19606-19615 (2013). DOI 10.1021/jp405773p, cit. on p. 66.

[44] M. W. Knight, L. Liu, Y. Wang, L. Brown, S. Mukherjee, N. S. King, H. O. Everitt, P. Nordlander, and N. J. Halas: *Aluminum plasmonic nanoantennas*. Nano letters **12**, 6000–6004 (2012). DOI 10.1021/nl303517v, cit. on p. 66.

[45] K. Appusamy, S. Blair, A. Nahata, and S. Guruswamy: *Low-loss magnesium films for plasmonics*. Materials Science and Engineering: B **181**, 77–85 (2014). DOI 10.1016/j.mseb.2013.11.009, cit. on pp. 66, 69, 106, 118.

[46] K. J. Palm, J. B. Murray, T. C. Narayan, and J. N. Munday: *Dynamic Optical Properties of Metal Hydrides*. ACS Photonics **5**, 4677–4686 (2018). DOI 10.1021/acsphotonics.8b01243, cit. on p. 66.

[47] J. Isidorsson, I. A. M. E. Giebels, H. Arwin, and R. Griessen: *Optical properties of MgH_2 measured in situ in a novel gas cell for ellipsometry/spectrophotometry*. Physical Review B - Condensed Matter and Materials Physics **68**, 115112 (2003). DOI 10.1103/PhysRevB.68.115112, cit. on pp. 66, 67, 72.

[48] A. Zaluska, L. Zaluski, and J. Ström–Olsen: *Nanocrystalline magnesium for hydrogen storage*. Journal of Alloys and Compounds **288**, 217–225 (1999). DOI 10.1016/S0925-8388(99)00073-0, cit. on pp. 67, 72, 88, 104.

[49] B. Sakintuna, F. Lamari-Darkrim, and M. Hirscher: *Metal hydride materials for solid hydrogen storage: A review*. International Journal of Hydrogen Energy **32**, 1121–1140 (2007). DOI 10.1016/j.ijhydene.2006.11.022, cit. on pp. 67, 72.

[50] I. P. Jain, C. Lal, and A. Jain: *Hydrogen storage in Mg: A most promising material*. International Journal of Hydrogen Energy **35**, 5133–5144 (2010). DOI 10.1016/j.ijhydene.2009.08.088, cit. on p. 67.

[51] C. Suryanarayana and F. H. Froes: *Nanocrystalline titanium-magnesium alloys through mechanical alloying*. Journal of Materials Research **5**, 1880–1886 (1990). DOI https://doi.org/10.1557/JMR.1990.1880, cit. on pp. 67, 87.

[52] T. Manivasagam, K. Kiraz, and P. Notten: *Electrochemical and Optical Properties of Magnesium-Alloy Hydrides Reviewed.* Crystals **2**, 1410–1433 (2012).
DOI 10.3390/cryst2041410, cit. on pp. 67, 87.

[53] J.-R. Ares-Fernández and K.-F. Aguey-Zinsou: *Superior MgH_2 Kinetics with MgO Addition: A Tribological Effect.* Catalysts **2**, 330–343 (2012).
DOI 10.3390/catal2030330, cit. on p. 67.

[54] Y. Liu, J. Zou, X. Zeng, X. Wu, D. Li, and W. Ding: *Hydrogen Storage Properties of a Mg - Ni Nanocomposite Coprecipitated from Solution.* Journal of Physical Chemistry C **118**, 18401–18411 (2014).
DOI 10.1021/jp504918x, cit. on p. 67.

[55] L. Zhang, X. Xiao, C. Xu, J. Zheng, X. Fan, J. Shao, S. Li, H. Ge, Q. Wang, and L. Chen: *Remarkably Improved Hydrogen Storage Performance of MgH_2 Catalyzed by Multivalence NbH_x Nanoparticles.* The Journal of Physical Chemistry C **119**, 8554–8562 (2015).
DOI 10.1021/acs.jpcc.5b01532, cit. on p. 67.

[56] B. Yang, Y.-P. He, and Y.-P. Zhao: *Hydrogenation of magnesium nanoblades: The effect of concentration dependent hydrogen diffusion.* Applied Physics Letters **98**, 081905 (2011).
DOI 10.1063/1.3557056, cit. on pp. 67, 72.

[57] K. Higuchi, K. Yamamoto, H. Kajioka, K. Toiyama, M. Honda, S. Orimo, and H. Fujii: *Remarkable hydrogen storage properties in three-layered Pd/Mg/Pd thin films.* Journal of Alloys and Compounds **330-332**, 526–530 (2002).
DOI 10.1016/S0925-8388(01)01542-0, cit. on p. 67.

[58] A. Baldi, V. Palmisano, M. Gonzalez-Silveira, Y. Pivak, M. Slaman, H. Schreuders, B. Dam, and R. Griessen: *Quasifree Mg-H thin films.* Applied Physics Letters **95**, 71903 (2009).
DOI 10.1063/1.3210791, cit. on pp. 67, 72, 73, 106.

[59] A. Baldi, G. K. Pálsson, M. Gonzalez-Silveira, H. Schreuders, M. Slaman, J. H. Rector, G. Krishnan, B. J. Kooi, G. S. Walker, M. W. Fay, B. Hjörvarsson, R. J. Wijngaarden, B. Dam, and R. Griessen: *Mg/Ti multilayers: Structural and hydrogen absorption properties.* Physical Review B - Condensed Matter and Materials Physics **81**, 224203 (2010).
DOI 10.1103/PhysRevB.81.224203, cit. on pp. 67, 72, 79.

[60] J. Ares, F. Leardini, P. Díaz-Chao, I. Ferrer, J. Fernández, and C. Sánchez: *Non-isothermal desorption process of hydrogenated nanocrystalline Pd-capped Mg films investigated by Ion Beam Techniques.* International Journal of Hydrogen Energy **39**, 2587–2596 (2014).
DOI 10.1016/j.ijhydene.2013.11.130, cit. on pp. 67, 104, 106.

[61] A. Tittl, M. G. Harats, R. Walter, X. Yin, M. Schäferling, N. Liu, R. Rapaport, and H. Giessen: *Quantitative Angle-Resolved Small-Spot Reflectance Measurements on Plasmonic Perfect Absorbers: Impedance Matching and Disorder Effects.* ACS nano **8**, 10885–10892 (2014).
DOI 10.1021/nn504708t, cit. on pp. 69, 140.

[62] M. Kurth, P. Graat, and E. Mittemeijer: *The oxidation kinetics of magnesium at low temperatures and low oxygen partial pressures.* Thin Solid Films **500**, 61–69 (2006).
DOI 10.1016/j.tsf.2005.11.044, cit. on p. 70.

[63] K. Asami and S. Ono: *Quantitative X-Ray Photoelectron Spectroscopy Characterization of Magnesium Oxidized in Air.* Journal of The Electrochemical Society **147**, 1408 (2000).
DOI 10.1149/1.1393369, cit. on p. 71.

[64] M. Kurth, P. Graat, H. Carstanjen, and E. Mittemeijer: *The initial oxidation of magnesium: an in situ study with XPS, HERDA and ellipsometry.* Surface and Interface Analysis **38**, 931–940 (2006).
DOI 10.1002/sia, cit. on p. 71.

[65] Y. Song, D. Shan, R. Chen, and E.-H. Han: *Investigation of surface oxide film on magnesium lithium alloy.* Journal of Alloys and Compounds **484**, 585–590 (2009).
DOI 10.1016/j.jallcom.2009.04.137, cit. on p. 71.

[66] M. Knight, N. King, L. Liu, H. Everitt, P. Nordlander, and N. Halas: *Aluminum for plasmonics.* ACS Nano **8**, 834–840 (2014).
DOI 10.1021/nn405495q, cit. on pp. 71, 205.

[67] J. Nordlien, S. Ono, N. Masuko, and K. Nis: *Morphology and structure of oxide films formed on magnesium by exposure to air and water.* Journal of the Electrochemical Society **142**, 3320–3322 (1995).
DOI 10.1149/1.2049981, cit. on p. 71.

[68] R. Lindström, L.-G. Johansson, G. E. Thompson, P. Skeldon, and J.-E. Svensson: *Corrosion of magnesium in humid air.* Corrosion Science **46**, 1141–1158 (2004).
DOI 10.1016/j.corsci.2003.09.010, cit. on p. 71.

[69] A. B. Dahlin, J. O. Tegenfeldt, and F. Höök: *Improving the Instrumental Resolution of Sensors Based on Localized Surface Plasmon Resonance.* Anal. Chem. **78**, 4416–4423 (2006).
DOI 10.1021/ac0601967, cit. on pp. 72, 139.

[70] M. Tanniru, H. Y. Tien, and F. Ebrahimi: *Study of the dehydrogenation behavior of magnesium hydride.* Scripta Materialia **63**, 58–60 (2010).
DOI 10.1016/j.scriptamat.2010.03.019, cit. on p. 72.

[71] P. Walker and W. H. Tarn: *Handbook of Metal Etchants*, CRC Press (Boca Raton), 1991.
ISBN 0-8493-3623-6, cit. on p. 72.

[72] I. A. M. E. Giebels, J. Isidorsson, and R. Griessen: *Highly absorbing black Mg and rare-earth-Mg switchable mirrors*. Physical Review B - Condensed Matter and Materials Physics **69**, 205111 (2004).
DOI 10.1103/PhysRevB.69.205111, cit. on p. 72.

[73] K. Yoshimura: *Anomalous Structure of Palladium-Capped Magnesium Thin Films*. Metals **2**, 253–257 (2012).
DOI 10.3390/met2030253, cit. on pp. 72, 74.

[74] C. Langhammer, I. Zorić, B. Kasemo, and B. Clemens: *Hydrogen storage in Pd nanodisks characterized with a novel nanoplasmonic sensing scheme*. Nano letters **7**, 3122–3127 (2007).
DOI 10.1021/nl071664a, cit. on pp. 73, 106, 139.

[75] T. G. Habteyes, S. Dhuey, E. Wood, D. Gargas, S. Cabrini, P. J. Schuck, A. P. Alivisatos, and S. R. Leone: *Metallic adhesion layer induced plasmon damping and molecular linker as a nondamping alternative*. ACS Nano **6**, 5702–5709 (2012).
DOI 10.1021/nn301885u, cit. on p. 73.

[76] M. Pasturel, R. J. Wijngaarden, W. Lohstroh, H. Schreuders, M. Slaman, B. Dam, and R. Griessen: *Influence of the Chemical Potential on the Hydrogen Sorption Kinetics of Mg_2Ni/TM/Pd (TM = transition metal) Trilayers*. Chemistry of Materials **19**, 624–633 (2007).
DOI 10.1021/cm062157h, cit. on p. 79.

[77] T. Miyoshi, S. Naito, M. Yamamoto, M. Doi, and M. Kimura: *Diffusion of hydrogen in titanium, $Ti_{88}Al_{12}$ and Ti_3Al*. Journal of the Chemical Society, Faraday Transactions **92**, 483 (1996).
DOI 10.1039/ft9969200483, cit. on p. 80.

[78] H. G. Schimmel, G. J. Kearley, J. Huot, and F. M. Mulder: *Hydrogen diffusion in magnesium metal (α phase) studied by ab initio computer simulations*. Journal of Alloys and Compounds **404-406**, 235–237 (2005).
DOI 10.1016/j.jallcom.2004.11.100, cit. on p. 80.

[79] J. Čermák and L. Král: *Hydrogen diffusion in Mg-H and Mg-Ni-H alloys*. Acta Materialia **56**, 2677–2686 (2008).
DOI 10.1016/j.actamat.2008.02.003, cit. on p. 80.

[80] M. Pasturel, M. Slaman, H. Schreuders, J. H. Rector, D. M. Borsa, B. Dam, and R. Griessen: *Hydrogen absorption kinetics and optical properties of Pd-doped Mg thin films*. Journal of Applied Physics **100**, 023515 (2006).
DOI 10.1063/1.2214208, cit. on pp. 80, 87.

[81] R. Gremaud, A. Baldi, M. Gonzalez-Silveira, B. Dam, and R. Griessen: *Chemical short-range order and lattice deformations in $Mg_yTi_{1-y}H_x$ thin films probed by hydrogenography*. Physical Review B - Condensed Matter and Materials Physics **77**, 144204 (2008).
DOI 10.1103/PhysRevB.77.144204, cit. on p. 80.

[82] D. Wang and T. B. Flanagan: *H_2 isotherms and diffusion parameters of H in fcc Pd-Mg alloys*. Journal of Physical Chemistry C **117**, 1071–1080 (2013). DOI 10.1021/jp310978y, cit. on p. 80.

[83] K. Kumar, H. Duan, R. S. Hegde, S. C. W. Koh, J. N. Wei, and J. K. W. Yang: *Printing colour at the optical diffraction limit*. Nature nanotechnology **7**, 557–561 (2012). DOI 10.1038/nnano.2012.128, cit. on p. 82.

[84] A. S. Roberts, A. Pors, O. Albrektsen, and S. I. Bozhevolnyi: *Subwavelength plasmonic color printing protected for ambient use*. Nano letters **14**, 783–7 (2014). DOI 10.1021/nl404129n, cit. on p. 82.

[85] S. J. Tan, L. Zhang, D. Zhu, X. M. Goh, Y. M. Wang, K. Kumar, C.-W. W. Qiu, and J. K. W. Yang: *Plasmonic color palettes for photorealistic printing with aluminum nanostructures*. Nano Letters **14**, 4023–4029 (2014). DOI 10.1021/nl501460x, cit. on p. 82.

[86] T. D. James, P. Mulvaney, and A. Roberts: *The Plasmonic Pixel: Large Area, Wide Gamut Color Reproduction Using Aluminum Nanostructures*. Nano Letters **16**, 3817–3823 (2016). DOI 10.1021/acs.nanolett.6b01250, cit. on pp. 82, 145.

[87] J. Olson, A. Manjavacas, T. Basu, D. Huang, A. E. Schlather, B. Zheng, N. J. Halas, P. Nordlander, and S. Link: *High Chromaticity Aluminum Plasmonic Pixels for Active Liquid Crystal Displays*. ACS Nano **10**, 1108–1117 (2016). DOI 10.1021/acsnano.5b06415, cit. on p. 82.

[88] Z. Li, A. W. Clark, and J. M. Cooper: *Dual Color Plasmonic Pixels Create a Polarization Controlled Nano Color Palette*. ACS Nano **10**, 492–498 (2016). DOI 10.1021/acsnano.5b05411, cit. on p. 82.

[89] M. L. Tseng, J. Yang, M. Semmlinger, C. Zhang, P. Nordlander, and N. J. Halas: *Two-dimensional Active Tuning of an Aluminum Plasmonic Array for Full-Spectrum Response*. Nano Letters **17**, 6034–6039 (2017). DOI 10.1021/acs.nanolett.7b02350, cit. on p. 82.

[90] G. Wang, X. Chen, S. Liu, C.-P. Wong, and S. Chu: *Mechanical Chameleon through Dynamic Real-Time Plasmonic Tuning*. ACS Nano, acsnano.5b07472 (2016). DOI 10.1021/acsnano.5b07472, cit. on p. 82.

[91] T. Ding, C. Rüttiger, X. Zheng, F. Benz, H. Ohadi, G. A. E. Vandenbosch, V. V. Moshchalkov, M. Gallei, and J. J. Baumberg: *Fast Dynamic Color Switching in Temperature-Responsive Plasmonic Films*. Advanced Optical Materials **4**, 877–882 (2016). DOI 10.1002/adom.201600094, cit. on p. 82.

[92] H.-H. Jeong, A. G. Mark, and P. Fischer: *Magnesium plasmonics for UV applications and chiral sensing*. Chem. Commun. **52**, 12179–12182 (2016). DOI 10.1039/C6CC06800F, cit. on p. 84.

[93] Y. Wang, E. M. Peterson, J. M. Harris, K. Appusamy, S. Guruswamy, and S. Blair: *Magnesium as a Novel UV Plasmonic Material for Fluorescence Decay Rate Engineering in Free Solution*. The Journal of Physical Chemistry C **121**, 11650–11657 (2017). DOI 10.1021/acs.jpcc.7b01934, cit. on p. 84.

[94] X. Duan, S. Kamin, and N. Liu: *Dynamic plasmonic colour display*. Nature Communications **8**, 14606 (2017). DOI 10.1038/ncomms14606, cit. on pp. 84, 104.

[95] Y. Chen, X. Duan, M. Matuschek, Y. Zhou, F. Neubrech, H. Duan, and N. Liu: *Dynamic Color Displays Using Stepwise Cavity Resonators*. Nano Letters, acs.nanolett.7b02336 (2017). DOI 10.1021/acs.nanolett.7b02336, cit. on pp. 84, 104.

[96] X. Duan and N. Liu: *Magnesium for Dynamic Nanoplasmonics*. Accounts of Chemical Research **52**, 1979–1989 (2019). DOI 10.1021/acs.accounts.9b00157, cit. on p. 84.

[97] J. Li, S. Kamin, G. Zheng, F. Neubrech, S. Zhang, and N. Liu: *Addressable metasurfaces for dynamic holography and optical information encryption*. Science Advances **4**, eaar6768 (2018). DOI 10.1126/sciadv.aar6768, cit. on p. 84.

[98] P. Yu, J. Li, S. Zhang, Z. Jin, G. Schütz, C. W. Qiu, M. Hirscher, and N. Liu: *Dynamic Janus Metasurfaces in the Visible Spectral Region*. Nano Letters **18**, 4584–4589 (2018). DOI 10.1021/acs.nanolett.8b01848, cit. on p. 84.

[99] M. F. Sterl, P. Delandmeter, and E. van Sebille: *Influence of barotropic tidal currents on transport and accumulation of floating microplastics in the global open ocean*. Journal of Geophysical Research: Oceans **125** (2020). DOI 10.1029/2019JC015583, cit. on p. 85.

[100] A. Sterl, H. Van Den Brink, H. De Vries, R. Haarsma, and E. Van Meijgaard: *An ensemble study of extreme storm surge related water levels in the North Sea in a changing climate*. Ocean Science **5**, 369–378 (2009). DOI 10.5194/os-5-369-2009, cit. on p. 85.

[101] A. Sterl, R. Bintanja, L. Brodeau, E. Gleeson, T. Koenigk, T. Schmith, T. Semmler, C. Severijns, K. Wyser, and S. Yang: *A look at the ocean in the EC-Earth climate model*. Climate Dynamics **39**, 2631–2657 (2012). DOI 10.1007/s00382-011-1239-2, cit. on p. 85.

[102] L. Schlapbach: *Hydrogen-fuelled vehicles*. Nature **460**, 809–811 (2009). DOI 10.1038/460809a, cit. on p. 86.

[103] (editorial): *Hydrogen to the rescue*. Nature Materials **17**, 565 (2018).
DOI 10.1038/s41563-018-0129-y, cit. on p. 86.

[104] S. Sterl, S. Liersch, H. Koch, N. P. Lipzig, and W. Thiery: *A new approach for assessing synergies of solar and wind power: Implications for West Africa*. Environmental Research Letters **13**, 094009 (2018).
DOI 10.1088/1748-9326/aad8f6, cit. on p. 86.

[105] S. Sterl: *Krachten bundelen: de energievoorziening van de toekomst*. In: Het kleine klimaatboek, ed. by G. Cornelis, Gompel & Svacina bvba (Oud-Turnhout), 2019.
ISBN 978-94-6371-141-8, cit. on p. 86.

[106] L. Schlapbach and A. Züttel: *Hydrogen-storage materials for Mobile Applications*. Nature **414**, 353–358 (2001).
DOI 10.1038/35104634, cit. on pp. 86, 104.

[107] A. Züttel: *Materials for hydrogen storage*. Materials Today **6**, 24–33 (2003).
DOI 10.1016/S1369-7021(03)00922-2, cit. on pp. 86, 87.

[108] D. M. Borsa, R. Gremaud, A. Baldi, H. Schreuders, J. H. Rector, B. Kooi, P. Vermeulen, P. H. L. Notten, B. Dam, and R. Griessen: *Structural, optical, and electrical properties of $Mg_yTi_{1-y}H_x$ thin films*. Physical Review B - Condensed Matter and Materials Physics **75**, 205408 (2007).
DOI 10.1103/PhysRevB.75.205408, cit. on p. 87.

[109] I. Darmadi, F. A. A. Nugroho, S. Kadkhodazadeh, J. B. Wagner, and C. Langhammer: *Rationally Designed PdAuCu Ternary Alloy Nanoparticles for Intrinsically Deactivation-Resistant Ultrafast Plasmonic Hydrogen Sensing*. ACS Sensors **4**, 1424–1432 (2019).
DOI 10.1021/acssensors.9b00610, cit. on pp. 87, 139.

[110] K. F. Aguey-Zinsou and J. R. Ares-Fernández: *Hydrogen in magnesium: New perspectives toward functional stores*. Energy and Environmental Science **3**, 526–543 (2010).
DOI 10.1039/b921645f, cit. on p. 88.

[111] Q. Yu, L. Qi, R. K. Mishra, X. Zeng, and A. M. Minor: *Size-dependent mechanical properties of Mg nanoparticles used for hydrogen storage*. Applied Physics Letters **106**, 8–13 (2015).
DOI 10.1063/1.4921003, cit. on p. 88.

[112] L. Mooij and B. Dam: *Nucleation and growth mechanisms of nano magnesium hydride from the hydrogen sorption kinetics*. Physical chemistry chemical physics: PCCP **15**, 11501–11510 (2013).
DOI 10.1039/c3cp51735g, cit. on pp. 88, 106.

[113] L. J. Bannenberg, H. Schreuders, L. van Eijck, J. R. Heringa, N.-J. Steinke, R. Dalgliesh, B. Dam, F. M. Mulder, and A. A. van Well: *Impact of Nanostructuring on the Phase Behavior of Insertion Materials: The Hydrogenation Kinetics of a Magnesium Thin Film.* The Journal of Physical Chemistry C **120**, 10185-10191 (2016).
DOI 10.1021/acs.jpcc.6b02302, cit. on pp. 88, 106.

[114] R. W. Wagemans, J. H. Van Lenthe, P. E. De Jongh, A. J. Van Dillen, and K. P. De Jong: *Hydrogen storage in magnesium clusters: Quantum chemical study.* Journal of the American Chemical Society **127**, 16675–16680 (2005).
DOI 10.1021/ja054569h, cit. on p. 88.

[115] J. C. Crivello, B. Dam, R. V. Denys, M. Dornheim, D. M. Grant, J. Huot, T. R. Jensen, P. de Jongh, M. Latroche, C. Milanese, D. Milčius, G. S. Walker, C. J. Webb, C. Zlotea, and V. A. Yartys: *Review of magnesium hydride-based materials: development and optimisation.* Applied Physics A: Materials Science and Processing **122**, 97 (2016).
DOI 10.1007/s00339-016-9602-0, cit. on p. 88.

[116] X. Duan, R. Griessen, R. J. Wijngaarden, S. Kamin, and N. Liu: *Self-recording and manipulation of fast long-range hydrogen diffusion in quasifree magnesium.* Physical Review Materials **2**, 085802 (2018).
DOI 10.1103/PhysRevMaterials.2.085802, cit. on p. 89.

[117] Q. Yu, M.-M. Mao, Q.-J. Li, X.-Q. Fu, H. Tian, J.-X. Li, S. X. Mao, and Z. Zhang: *In Situ Observation on Dislocation-Controlled Sublimation of Mg Nanoparticles.* Nano Letters **16**, 1156–1160 (2016).
DOI 10.1021/acs.nanolett.5b04439, cit. on p. 93.

[118] R. Griessen: *Heating effect of Mg nanopatches produced by hydrogen absorption.* Private communication (2016).
Cit. on p. 100.

[119] A. Pundt: *Hydrogen in Nano-sized Metals.* Advanced Engineering Materials **6**, 11–21 (2004).
DOI 10.1002/adem.200300557, cit. on p. 104.

[120] V. Berube, G. Chen, and M. S. Dresselhaus: *Impact of nanostructuring on the enthalpy of formation of metal hydrides.* International Journal of Hydrogen Energy **33**, 4122–4131 (2008).
DOI 10.1016/j.ijhydene.2008.05.083, cit. on p. 104.

[121] K.-J. Jeon, H. R. Moon, A. M. Ruminski, B. Jiang, C. Kisielowski, R. Bardhan, and J. J. Urban: *Air-stable magnesium nanocomposites provide rapid and high-capacity hydrogen storage without using heavy-metal catalysts.* Nature materials **10**, 286–90 (2011).
DOI 10.1038/nmat2978, cit. on p. 104.

[122] P. P. Edwards, V. L. Kuznetsov, W. I. F. David, and N. P. Brandon: *Hydrogen and fuel cells: Towards a sustainable energy future.* Energy Policy **36**, 4356–4362 (2008).
DOI 10.1016/j.enpol.2008.09.036, cit. on p. 104.

[123] R. Bardhan, L. O. Hedges, C. L. Pint, A. Javey, S. Whitelam, and J. J. Urban: *Uncovering the intrinsic size dependence of hydriding phase transformations in nanocrystals.* Nature materials **12**, 905–912 (2013).
DOI 10.1038/nmat3716, cit. on p. 104.

[124] R. Griessen, N. Strohfeldt, and H. Giessen: *Thermodynamics of the hybrid interaction of hydrogen with palladium nanoparticles.* Nature Materials **15**, 311–317 (2015).
DOI 10.1038/nmat4480, cit. on pp. 104, 138, 139, 158.

[125] S. Alekseeva, A. B. D. S. Fanta, B. Iandolo, T. J. Antosiewicz, F. A. A. Nugroho, J. B. Wagner, A. Burrows, V. P. Zhdanov, and C. Langhammer: *Grain boundary mediated hydriding phase transformations in individual polycrystalline metal nanoparticles.* Nature Communications **8**, 1084 (2017).
DOI 10.1038/s41467-017-00879-9, cit. on pp. 104, 139.

[126] A. Baldi, T. C. Narayan, A. L. Koh, and J. A. Dionne: *In situ detection of hydrogen-induced phase transitions in individual palladium nanocrystals.* Nature materials **13**, 1143–1148 (2014).
DOI 10.1038/nmat4086, cit. on p. 104.

[127] T. C. Narayan, A. Baldi, A. L. Koh, R. Sinclair, and J. A. Dionne: *Reconstructing solute-induced phase transformations within individual nanocrystals.* Nature Materials **15**, 768–774 (2016).
DOI 10.1038/nmat4620, cit. on pp. 104, 125.

[128] T. C. Narayan, F. Hayee, A. Baldi, A. Leen Koh, R. Sinclair, and J. A. Dionne: *Direct visualization of hydrogen absorption dynamics in individual palladium nanoparticles.* Nature Communications **8**, 14020 (2017).
DOI 10.1038/ncomms14020, cit. on p. 104.

[129] V. Burlaka, V. Roddatis, M. D. Bongers, and A. Pundt: *Defect generation in Pd layers by 'smart' films with high H-affinity.* Scientific Reports **7**, 9564 (2017).
DOI 10.1038/s41598-017-09900-z, cit. on p. 104.

[130] K. Higuchi, H. Kajioka, K. Toiyama, H. Fujii, S. Orimo, and Y. Kikuchi: *In situ study of hydriding-dehydriding properties in some Pd/Mg thin films with different degree of Mg crystallization.* Journal of Alloys and Compounds **293**, 484–489 (1999).
DOI 10.1016/S0925-8388(99)00470-3, cit. on pp. 104, 106.

[131] B. Ham, A. Junkaew, R. Arróyave, J. Park, H. C. Zhou, D. Foley, S. Rios, H. Wang, and X. Zhang: *Size and stress dependent hydrogen desorption in metastable Mg hydride films.* International Journal of Hydrogen Energy **39**, 2597–2607 (2014).
DOI 10.1016/j.ijhydene.2013.12.017, cit. on pp. 104, 106.

[132] A. Yau, R. J. Harder, M. W. Kanan, and A. Ulvestad: *Imaging of the Hydrogen Absorption Dynamics of Individual Grains in Polycrystalline Palladium Thin Films in 3D*. ACS Nano **11**, 10945–10954 (2017).
DOI 10.1021/acsnano.7b04735, cit. on p. 104.

[133] A. Ulvestad and A. Yau: *The self-healing of defects induced by the hydriding phase transformation in palladium nanoparticles*. Nature Communications **8**, 1376 (2017).
DOI 10.1038/s41467-017-01548-7, cit. on p. 104.

[134] R. Gremaud, C. P. Broedersz, D. M. Borsa, A. Borgschulte, P. Mauron, H. Schreuders, J. H. Rector, B. Dam, and R. Griessen: *Hydrogenography: An optical combinatorial method to find new light-weight hydrogen-storage materials*. Advanced Materials **19**, 2813–2817 (2007).
DOI 10.1002/adma.200602560, cit. on p. 104.

[135] R. Gremaud: *Hydrogenography - A thin film optical combinatorial study of hydrogen storage materials*. PhD thesis, Vrije Universiteit, 2008.
Cit. on p. 104.

[136] L. Mooij and B. Dam: *Hysteresis and the role of nucleation and growth in the hydrogenation of Mg nanolayers*. Physical chemistry chemical physics: PCCP **15**, 2782–2792 (2013).
DOI 10.1039/c3cp44441d, cit. on p. 106.

[137] S. Barcelo and S. S. Mao: *High throughput optical characterization of alloy hydrogenation*. International Journal of Hydrogen Energy **35**, 7228–7231 (2010).
DOI 10.1016/j.ijhydene.2010.01.152, cit. on p. 106.

[138] A. Baldi, M. Gonzalez-Silveira, V. Palmisano, B. Dam, and R. Griessen: *Destabilization of the Mg-H system through elastic constraints*. Physical Review Letters **102**, 1–4 (2009).
DOI 10.1103/PhysRevLett.102.226102, cit. on p. 106.

[139] N. Strohfeldt, J. Zhao, A. Tittl, and H. Giessen: *Sensitivity engineering in direct contact palladium-gold nano-sandwich hydrogen sensors*. Optical Materials Express **5**, 2525–2535 (2015).
DOI 10.1364/OME.5.002525, cit. on pp. 106, 139.

[140] S. Syrenova, C. Wadell, F. A. A. Nugroho, T. A. Gschneidtner, Y. A. Diaz Fernandez, G. Nalin, D. Świtlik, F. Westerlund, T. J. Antosiewicz, V. P. Zhdanov, K. Moth-Poulsen, and C. Langhammer: *Hydride formation thermodynamics and hysteresis in individual Pd nanocrystals with different size and shape*. Nature Materials **14**, 1236–1244 (2015).
DOI 10.1038/nmat4409, cit. on pp. 106, 139, 158.

[141] F. Keilmann and R. Hillenbrand: *Near-field microscopy by elastic light scattering from a tip*. Philosophical transactions. Series A, Mathematical, physical, and engineering sciences **362**, 787–805 (2004).
DOI 10.1098/rsta.2003.1347, cit. on pp. 106, 109.

[142] A. J. Huber, F Keilmann, J Wittborn, J Aizpurua, and R Hillenbrand: *Terahertz Near-Field Nanoscopy of Mobile Carriers in Single Semiconductor Nanodevices*. Nano Letters **8**, 3766–3770 (2008).
DOI 10.1021/nl802086x, cit. on p. 106.

[143] I. T. Lucas, A. S. McLeod, J. S. Syzdek, D. S. Middlemiss, C. P. Grey, D. N. Basov, and R. Kostecki: *IR near-field spectroscopy and imaging of single Li_xFePO_4 microcrystals*. Nano Letters **15**, 1–7 (2015).
DOI 10.1021/nl5010898, cit. on p. 107.

[144] P. Li, X. Yang, T. W. W. Maß, J. Hanss, M. Lewin, A.-K. U. Michel, M. Wuttig, and T. Taubner: *Reversible optical switching of highly confined phonon–polaritons with an ultrathin phase-change material*. Nature Materials **15**, 870–875 (2016).
DOI 10.1038/nmat4649, cit. on p. 107.

[145] J. M. Stiegler, R. Tena-Zaera, O. Idigoras, A. Chuvilin, and R. Hillenbrand: *Correlative infrared-electron nanoscopy reveals the local structure-conductivity relationship in zinc oxide nanowires*. Nature Communications **3**, 1131–1137 (2012).
DOI 10.1038/ncomms2118, cit. on p. 107.

[146] L. Jung, B. Hauer, P. Li, M. Bornhöfft, J. Mayer, and T. Taubner: *Exploring the detection limits of infrared near-field microscopy regarding small buried structures and pushing them by exploiting superlens-related effects*. Optics Express **24**, 4431–4441 (2016).
DOI 10.1364/OE.24.004431, cit. on p. 107.

[147] M. Lewin, B. Hauer, M. Bornhöfft, L. Jung, J. Benke, A. K. Michel, J. Mayer, M. Wuttig, and T. Taubner: *Imaging of phase change materials below a capping layer using correlative infrared near-field microscopy and electron microscopy*. Applied Physics Letters **107**, 151902 (2015).
DOI 10.1063/1.4933102, cit. on p. 107.

[148] T. Steinle, F. Mörz, A. Steinmann, and H. Giessen: *Ultra-stable high average power femtosecond laser system tunable from 1.33 to 20 µm*. Optics letters **41**, 4863–4866 (2016).
DOI 10.1364/OL.41.004863, cit. on p. 109.

[149] R. Hillenbrand, B. Knoll, and F. Keilmann: *Pure optical contrast in scattering-type scanning near-field microscopy*. Journal of Microscopy **202**, 77–83 (2001).
DOI 10.1046/j.1365-2818.2001.00794.x, cit. on p. 109.

[150] F. Keilmann, A. J. Huber, and R. Hillenbrand: *Nanoscale conductivity contrast by scattering-type near-field optical microscopy in the visible, infrared and THz domains*. Journal of Infrared, Millimeter, and Terahertz Waves **30**, 1255–1268 (2009).
DOI 10.1007/s10762-009-9525-3, cit. on p. 109.

[151] A. P. Engelhardt, B. Hauer, and T. Taubner: *Visibility of weak contrasts in subsurface scattering near-field microscopy*. Ultramicroscopy **126**, 40–43 (2013).
DOI 10.1016/j.ultramic.2012.12.010, cit. on p. 109.

[152] F. Huth, M. Schnell, J. Wittborn, N. Ocelic, and R. Hillenbrand: *Infrared-spectroscopic nanoimaging with a thermal source*. Nature Materials **10**, 352–356 (2011).
DOI 10.1038/nmat3006, cit. on p. 109.

[153] F. Huth, A. Govyadinov, S. Amarie, W. Nuansing, F. Keilmann, and R. Hillenbrand: *Nano-FTIR Absorption Spectroscopy of Molecular Fingerprints at 20 nm Spatial Resolution*. Nano letters **12**, 3973–3978 (2012).
DOI 10.1021/nl301159v, cit. on p. 109.

[154] T. Taubner, R. Hillenbrand, and F. Keilmann: *Performance of visible and mid-infrared scattering-type near-field optical microscopes*. Journal of Microscopy **210**, 311–314 (2003).
DOI 10.1046/j.1365-2818.2003.01164.x, cit. on p. 110.

[155] A. Cvitkovic, N. Ocelic, and R. Hillenbrand: *Analytical model for quantitative prediction of material contrasts in scattering-type near-field optical microscopy*. Opt. Express **15**, 8550–8565 (2007).
DOI 10.1364/OE.15.008550, cit. on p. 110.

[156] X. Wang and L. Andrews: *Infrared spectra of magnesium hydride molecules, complexes, and solid magnesium dihydride*. Journal of Physical Chemistry A **108**, 11511–11520 (2004).
DOI 10.1021/jp046410h, cit. on p. 132.

[157] P. Patnaik: *A comprehensive guide to the hazardous properties of chemical substances*, 3^{rd} edition, John Wiley & Sons, Inc. (Hoboken (New Jersey)), 2007.
ISBN 978-0-471-71458-3, cit. on p. 136.

[158] M. Aleixandre, P. Corredera, M. L. Hernanz, and J. Gutierrez-Monreal: *Development of fiber optic hydrogen sensors for testing nuclear waste repositories*. Sensors and Actuators, B: Chemical **107**, 113–120 (2005).
DOI 10.1016/j.snb.2004.11.100, cit. on p. 136.

[159] T. Xu, R. Senger, and S. Finsterle: *Corrosion-induced gas generation in a nuclear waste repository: Reactive geochemistry and multiphase flow effects*. Applied Geochemistry **23**, 3423–3433 (2008).
DOI 10.1016/j.apgeochem.2008.07.012, cit. on p. 136.

[160] J. Bodzenta, B. Burak, Z. Gacek, W. P. Jakubik, S. Kochowski, and M. Urbańczyk: *Thin palladium film as a sensor of hydrogen gas dissolved in transformer oil*. Sensors and Actuators, B: Chemical **87**, 82–87 (2002).
DOI 10.1016/S0925-4005(02)00221-6, cit. on p. 136.

[161] F. Yang, D. Jung, and R. M. Penner: *Trace detection of dissolved hydrogen gas in oil using a palladium nanowire array.* Analytical Chemistry **83**, 9472–9477 (2011).
DOI 10.1021/ac2021745, cit. on p. 136.

[162] T. Hübert, L. Boon-Brett, G. Black, and U. Banach: *Hydrogen sensors - A review.* Sensors and Actuators, B: Chemical **157**, 329–352 (2011).
DOI 10.1016/j.snb.2011.04.070, cit. on p. 136.

[163] M. Slaman, R. Westerwaal, H. Schreuders, and B. Dam: *Optical hydrogen sensors based on metal-hydrides.* Proc. SPIE **8368**, 836805 (2012).
DOI 10.1117/12.921404, cit. on pp. 136, 139.

[164] P. Ngene, T. Radeva, M. Slaman, R. J. Westerwaal, H. Schreuders, and B. Dam: *Seeing hydrogen in colors: Low-cost and highly sensitive eye readable hydrogen detectors.* Advanced Functional Materials **24**, 2374–2382 (2014).
DOI 10.1002/adfm.201303065, cit. on p. 136.

[165] M. E. Nasir, W. Dickson, G. A. Wurtz, W. P. Wardley, and A. V. Zayats: *Hydrogen detected by the naked eye: Optical hydrogen gas sensors based on core/shell plasmonic nanorod metamaterials.* Advanced Materials **26**, 3532–3537 (2014).
DOI 10.1002/adma.201305958, cit. on p. 136.

[166] C. C. Ndaya, N. Javahiraly, and A. Brioude: *Recent advances in palladium nanoparticles-based hydrogen sensors for leak detection.* Sensors (Switzerland) **19**, 4478 (2019).
DOI 10.3390/s19204478, cit. on p. 136.

[167] M. A. Butler: *Fiber Optic Sensor for Hydrogen Concentrations near the Explosive Limit.* Journal of the Electrochemical Society **138**, L46–L47 (1991).
DOI 10.1149/1.2086073, cit. on p. 136.

[168] R. J. Westerwaal, J. S. Rooijmans, L. Leclercq, D. G. Gheorghe, T. Radeva, L. Mooij, T. Mak, L. Polak, M. Slaman, B. Dam, and T. Rasing: *Nanostructured Pd-Au based fiber optic sensors for probing hydrogen concentrations in gas mixtures.* International Journal of Hydrogen Energy **38**, 4201–4212 (2013).
DOI 10.1016/j.ijhydene.2012.12.146, cit. on pp. 136, 139.

[169] E. Miliutina, O. Guselnikova, S. Chufistova, Z. Kolska, V. Burtsev, P. S. Postnikov, V. Švor, and O. Lyutakov: *Fast and All-Optical Hydrogen Sensor Based on Gold-Coated Optical Fiber Functionalized with Metal-Organic Framework Layer.* ACS Sensors **4**, 3133–3140 (2019).
DOI 10.1021/acssensors.9b01074, cit. on p. 136.

[170] F. D. Manchester, A. San-Martin, and J. M Pitre: *The H-Pd (hydrogen-palladium) System.* Journal of Phase Equilibria **15**, 62–83 (1994).
DOI 10.1007/BF02667685, cit. on pp. 136, 137.

[171] F. A. Lewis: *The palladium-hydrogen system: Structures near phase transition and critical points.* International Journal of Hydrogen Energy **20**, 587–592 (1995).
DOI 10.1016/0360-3199(94)00113-E, cit. on p. 137.

[172] K. Von Rottkay, M. Rubin, and P. A. Duine: *Refractive index changes of Pd-coated magnesium lanthanide switchable mirrors upon hydrogen insertion.* Journal of Applied Physics **85**, 408–413 (1999).
DOI 10.1063/1.369399, cit. on pp. 138, 148, 154.

[173] T. Flanagan and W. Oates: *The Palladium-Hydrogen System.* Annual Review of Materials Science **21**, 269–304 (1991).
DOI 10.1146/annurev.ms.21.080191.001413, cit. on p. 139.

[174] M. Khanuja, B. R. Mehta, P. Agar, P. K. Kulriya, and D. K. Avasthi: *Hydrogen induced lattice expansion and crystallinity degradation in palladium nanoparticles: Effect of hydrogen concentration, pressure, and temperature.* Journal of Applied Physics **106**, 093515 (2009).
DOI 10.1063/1.3253733, cit. on p. 139.

[175] J. I. Avila, R. J. Matelon, R. Trabol, M. Favre, D. Lederman, U. G. Volkmann, and A. L. Cabrera: *Optical properties of Pd thin films exposed to hydrogen studied by transmittance and reflectance spectroscopy.* Journal of Applied Physics **107**, 023504 (2010).
DOI 10.1063/1.3272047, cit. on p. 139.

[176] N. Strohfeldt, A. Tittl, and H. Giessen: *Long-term stability of capped and buffered palladium-nickel thin films and nanostructures for plasmonic hydrogen sensing applications.* Optical Materials Express **3**, 194–204 (2013).
DOI 10.1364/OME.3.000194, cit. on p. 139.

[177] X. She, Y. Shen, J. Wang, and C. Jin: *Pd films on soft substrates: a visual, high-contrast and low-cost optical hydrogen sensor.* Light: Science and Applications **8**, 2–10 (2019).
DOI 10.1038/s41377-018-0114-x, cit. on p. 139.

[178] C. Wadell, S. Syrenova, and C. Langhammer: *Plasmonic Hydrogen Sensing With Nanostructured Metal Hydrides.* ACS nano **8**, 11925–11940 (2014).
DOI 10.1021/nn505804f, cit. on pp. 139, 170.

[179] Y. Pivak, R. Gremaud, K. Gross, M. Gonzalez-Silveira, A. Walton, D. Book, H. Schreuders, B. Dam, and R. Griessen: *Effect of the substrate on the thermodynamic properties of PdH_x films studied by hydrogenography.* Scripta Materialia **60**, 348–351 (2009).
DOI 10.1016/j.scriptamat.2008.11.012, cit. on p. 139.

[180] S. Wagner and A. Pundt: *Quasi-thermodynamic model on hydride formation in palladium-hydrogen thin films: Impact of elastic and microstructural constraints.* International Journal of Hydrogen Energy **41**, 2727–2738 (2016).
DOI 10.1016/j.ijhydene.2015.11.063, cit. on p. 139.

[181] L. J. Bannenberg, F. A. A. Nugroho, H. Schreuders, B. Norder, T. T. Trinh, N. J. Steinke, A. A. Van Well, C. Langhammer, and B. Dam: *Direct Comparison of PdAu Alloy Thin Films and Nanoparticles upon Hydrogen Exposure.* ACS Applied Materials and Interfaces **11**, 15489–15497 (2019). DOI 10.1021/acsami.8b22455, cit. on pp. 139, 159.

[182] P. Ngene, R. J. Westerwaal, S. Sachdeva, W. Haije, L. C. P. M. de Smet, and B. Dam: *Polymer-Induced Surface Modifications of Pd-based Thin Films Leading to Improved Kinetics in Hydrogen Sensing and Energy Storage Applications.* Angewandte Chemie International Edition **53**, 12081–12085 (2014). DOI 10.1002/anie.201406911, cit. on p. 139.

[183] F. A. A. Nugroho, I. Darmadi, L. Cusinato, A. Susarrey-Arce, H. Schreuders, L. J. Bannenberg, A. B. Da Silva Fanta, S. Kadkhodazadeh, J. B. Wagner, T. J. Antosiewicz, A. Hellman, V. P. Zhdanov, B. Dam, and C. Langhammer: *Metal–polymer hybrid nanomaterials for plasmonic ultrafast hydrogen detection.* Nature Materials **18**, 489–495 (2019). DOI 10.1038/s41563-019-0325-4, cit. on p. 139.

[184] C. Wadell, F. A. A. Nugroho, E. Lidström, B. Iandolo, J. B. Wagner, and C. Langhammer: *Hysteresis-Free Nanoplasmonic Pd–Au Alloy Hydrogen Sensors.* Nano Letters **15**, 3563–3570 (2015). DOI 10.1021/acs.nanolett.5b01053, cit. on p. 139.

[185] F. A. A. Nugroho, B. Iandolo, J. B. Wagner, and C. Langhammer: *Bottom-Up Nanofabrication of Supported Noble Metal Alloy Nanoparticle Arrays for Plasmonics.* ACS Nano **10**, 2871–2879 (2016). DOI 10.1021/acsnano.5b08057, cit. on p. 139.

[186] F. A. A. Nugroho, I. Darmadi, V. P. Zhdanov, and C. Langhammer: *Universal Scaling and Design Rules of Hydrogen-Induced Optical Properties in Pd and Pd-Alloy Nanoparticles.* ACS Nano **12**, 9903–9912 (2018). DOI 10.1021/acsnano.8b02835, cit. on p. 139.

[187] M. ElKabbash, K. V. Sreekanth, Y. Alapan, M. Kim, J. Cole, A. Fraiwan, T. Letsou, Y. Li, C. Guo, R. M. Sankaran, U. A. Gurkan, M. Hinczewski, and G. Strangi: *Hydrogen Sensing Using Thin-Film Perfect Light Absorber.* ACS Photonics **6**, 1889–1894 (2019). DOI 10.1021/acsphotonics.9b00764, cit. on p. 139.

[188] C. Wadell, T. J. Antosiewicz, and C. Langhammer: *Optical absorption engineering in stacked plasmonic Au-SiO_2-Pd nanoantennas.* Nano Letters **12**, 4784–4790 (2012). DOI 10.1021/nl3022187, cit. on p. 139.

[189] T. Beni, N. Yamasaku, T. Kurotsu, N. To, S. Okazaki, T. Arakawa, A. Balčytis, G. Seniutinas, S. Juodkazis, and Y. Nishijima: *Metamaterial for Hydrogen Sensing.* ACS Sensors **4**, 2389–2394 (2019). DOI 10.1021/acssensors.9b00980, cit. on pp. 140, 170.

[190] L. J. Bannenberg, C. Boelsma, H. Schreuders, S. Francke, N. J. Steinke, A. A. van Well, and B. Dam: *Optical hydrogen sensing beyond palladium: Hafnium and tantalum as effective sensing materials.* Sensors and Actuators, B: Chemical **283**, 538–548 (2019).
DOI 10.1016/j.snb.2018.12.029, cit. on p. 140.

[191] C. Boelsma, L. J. Bannenberg, M. J. Van Setten, N. J. Steinke, A. A. Van Well, and B. Dam: *Hafnium - An optical hydrogen sensor spanning six orders in pressure.* Nature Communications **8**, 15718 (2017).
DOI 10.1038/ncomms15718, cit. on p. 140.

[192] N. Liu, M. Mesch, T. Weiss, M. Hentschel, and H. Giessen: *Infrared perfect absorber and its application as plasmonic sensor.* Nano Letters **10**, 2342–2348 (2010).
DOI 10.1021/nl19041033, cit. on p. 140.

[193] G. D. Houser and E. Garmire: *Balanced detection technique to measure small changes in transmission.* Applied Optics **33**, 1059–1062 (1994).
DOI 10.1364/ao.33.001059, cit. on p. 144.

[194] T. Weiss, G. Granet, N. A. Gippius, S. G. Tikhodeev, and H. Giessen: *Derivation of plasmonic resonances in the Fourier modal method with adaptive spatial resolution and matched coordinates.* Optics Express **17**, 238–244 (2009).
DOI 10.1364/oe.17.008051, cit. on p. 144.

[195] M. J. Dodge: *Refractive properties of magnesium fluoride.* Applied Optics **23**, 1980–1985 (1984).
DOI 10.1364/ao.23.001980, cit. on p. 145.

[196] R. Taubert, R. Ameling, T. Weiss, A. Christ, and H. Giessen: *From near-field to far-field coupling in the third dimension: Retarded interaction of particle plasmons.* Nano Letters **11**, 4421–4424 (2011).
DOI 10.1021/nl202606g, cit. on p. 145.

[197] M. A. Schmidt, D. Y. Lei, L. Wondraczek, V. Nazabal, and S. A. Maier: *Hybrid nanoparticle-microcavity-based plasmonic nanosensors with improved detection resolution and extended remote-sensing ability.* Nature Communications **3**, 1–8 (2012).
DOI 10.1038/ncomms2109, cit. on p. 145.

[198] R. Ameling and H. Giessen: *Microcavity plasmonics: Strong coupling of photonic cavities and plasmons.* Laser and Photonics Reviews **7**, 141–169 (2013).
DOI 10.1002/lpor.201100041, cit. on pp. 145, 146.

[199] A. Kwadrin, C. I. Osorio, and A. F. Koenderink: *Backaction in metasurface etalons.* Physical Review B **93**, 104301 (2016).
DOI 10.1103/PhysRevB.93.104301, cit. on p. 145.

[200] A. Berkhout and A. F. Koenderink: *Perfect Absorption and Phase Singularities in Plasmon Antenna Array Etalons.* ACS Photonics **6**, 2917–2925 (2019).
DOI 10.1021/acsphotonics.9b01019, cit. on pp. 145, 146.

[201] T. Weiss, N. A. Gippius, G. Granet, S. G. Tikhodeev, R. Taubert, L. Fu, H. Schweizer, and H. Giessen: *Strong resonant mode coupling of Fabry-Perot and grating resonances in stacked two-layer systems.* Photonics and Nanostructures - Fundamentals and Applications **9**, 390–397 (2011).
DOI 10.1016/j.photonics.2011.03.007, cit. on pp. 146, 166.

[202] K. Bhattarai, S. Silva, K. Song, A. Urbas, S. J. Lee, Z. Ku, and J. Zhou: *Metamaterial Perfect Absorber Analyzed by a Meta-cavity Model Consisting of Multilayer Metasurfaces.* Scientific Reports **7**, 1–9 (2017).
DOI 10.1038/s41598-017-10520-w, cit. on p. 146.

[203] J. Reuna, V. Polojärvi, P. Pääkkönen, K. Lahtonen, M. Raappana, T. Aho, R. Isoaho, A. Aho, M. Valden, and M. Guina: *Influence of ex-situ annealing on the properties of MgF_2 thin films deposited by electron beam evaporation.* Optical Materials **96**, 109326 (2019).
DOI 10.1016/j.optmat.2019.109326, cit. on p. 150.

[204] P. M. Piechulla, L. Muehlenbein, R. B. Wehrspohn, S. Nanz, A. Abass, C. Rockstuhl, and A. Sprafke: *Fabrication of Nearly-Hyperuniform Substrates by Tailored Disorder for Photonic Applications.* Advanced Optical Materials **6**, 1701272 (2018).
DOI 10.1002/adom.201701272, cit. on pp. 152, 174.

[205] M. L. Tang, N. Liu, J. A. Dionne, and A. P. Alivisatos: *Observations of shape-dependent hydrogen uptake trajectories from single nanocrystals.* Journal of the American Chemical Society **133**, 13220–13223 (2011).
DOI 10.1021/ja203215b, cit. on p. 158.

[206] C. L. Haynes and R. P. Van Duyne: *Nanosphere Lithography: A Versatile Nanofabrication Tool for Studies of Size-Dependent Nanoparticle Optics.* Journal of Physical Chemistry B **105**, 5599–5611 (2001).
DOI 10.1080/14427591.2008.9686601, cit. on p. 163.

[207] J. M. McMahon, J. Henzie, T. W. Odom, G. C. Schatz, and S. K. Gray: *Tailoring the sensing capabilities of nanohole arrays in gold films with Rayleigh anomaly-surface plasmon polaritons.* Optics Express **15**, 18119–18129 (2007).
DOI 10.1364/oe.15.018119, cit. on p. 164.

[208] A. Christ, T. Zentgraf, S. G. Tikhodeev, N. A. Gippius, J. Kuhl, and H. Giessen: *Controlling the interaction between localized and delocalized surface plasmon modes: Experiment and numerical calculations.* Physical Review B - Condensed Matter and Materials Physics **74**, 155435 (2006).
DOI 10.1103/PhysRevB.74.155435, cit. on pp. 165, 167.

[209] A. Christ, T. Zentgraf, J. Kuhl, S. G. Tikhodeev, N. A. Gippius, and H. Giessen: *Optical properties of planar metallic photonic crystal structures: Experiment and theory*. Physical Review B - Condensed Matter and Materials Physics **70**, 125113 (2004).
DOI 10.1103/PhysRevB.70.125113, cit. on pp. 166, 167.

[210] G. Kichin, T. Weiss, H. Gao, J. Henzie, T. W. Odom, S. G. Tikhodeev, and H. Giessen: *Metal-dielectric photonic crystal superlattice: 1D and 2D models and empty lattice approximation*. Physica B: Condensed Matter **407**, 4037–4042 (2012).
DOI 10.1016/j.physb.2012.01.128, cit. on p. 166.

[211] T. Weiss, M. Mesch, M. Schäferling, H. Giessen, W. Langbein, and E. A. Muljarov: *From Dark to Bright: First-Order Perturbation Theory with Analytical Mode Normalization for Plasmonic Nanoantenna Arrays Applied to Refractive Index Sensing*. Physical Review Letters **116**, 237401 (2016).
DOI 10.1103/PhysRevLett.116.237401, cit. on p. 166.

[212] P. G. Etchegoin, E. C. Le Ru, and M. Meyer: *An analytic model for the optical properties of gold*. Journal of Chemical Physics **125**, 164705 (2006).
DOI 10.1063/1.2360270, cit. on p. 166.

[213] T. Weiss, M. Schäferling, H. Giessen, N. A. Gippius, S. G. Tikhodeev, W. Langbein, and E. A. Muljarov: *Analytical normalization of resonant states in photonic crystal slabs and periodic arrays of nanoantennas at oblique incidence*. Physical Review B **96**, 045129 (2017).
DOI 10.1103/PhysRevB.96.045129, cit. on p. 167.

[214] K. Sugawa, H. Tahara, A. Yamashita, J. Otsuki, T. Sagara, T. Harumoto, and S. Yanagida: *Refractive index susceptibility of the plasmonic palladium nanoparticle: Potential as the third plasmonic sensing material*. ACS Nano **9**, 1895–1904 (2015).
DOI 10.1021/nn506800a, cit. on p. 170.

[215] M. Mesch, C. Zhang, P. V. Braun, and H. Giessen: *Functionalized hydrogel on plasmonic nanoantennas for noninvasive glucose sensing*. ACS Photonics **2**, 475–480 (2015).
DOI 10.1021/acsphotonics.5b00004, cit. on p. 170.

[216] E. M. Larsson, C. Langhammer, I. Zorić, and B. Kasemo: *Nanoplasmonic probes of catalytic reactions*. Science **326**, 1091–1094 (2009).
DOI 10.1126/science.1176593, cit. on p. 170.

[217] C. Langhammer, E. M. Larsson, B. Kasemo, and I. Zorić: *Indirect nanoplasmonic sensing: ultrasensitive experimental platform for nanomaterials science and optical nanocalorimetry*. Nano letters **10**, 3529–38 (2010).
DOI 10.1021/nl101727b, cit. on p. 170.

[218] F. A. A. Nugroho, C. Xu, N. Hedin, and C. Langhammer: *UV–Visible and Plasmonic Nanospectroscopy of the CO_2 Adsorption Energetics in a Microporous Polymer*. Analytical Chemistry **87**, 10161–10165 (2015). DOI 10.1021/acs.analchem.5b03108, cit. on p. 170.

[219] J. Qin, Y.-H. Chen, B. Ding, R. J. Blaikie, and M. Qiu: *Plasmonic Gas Sensing based on Cavity-Coupled Metallic Nanoparticles*. Journal of Physical Chemistry C **121**, 24740–24744 (2017). DOI 10.1021/acs.jpcc.7b06502, cit. on p. 170.

[220] F. E. Nicodemus: *Directional Reflectance and Emissivity of an Opaque Surface*. Applied Optics **4**, 767–773 (1965). DOI 10.1364/ao.5.000715, cit. on p. 172.

[221] F. E. Nicodemus: *Reflectance Nomenclature and Directional Reflectance and Emissivity*. Applied Optics **9**, 1474 (1970). DOI 10.1364/ao.9.001474, cit. on p. 172.

[222] J. R. Shell:
Bidirectional Reflectance: An Overview with Remote Sensing Applications & Measurement Recommendations,
Tech. rep.,
Rochester, NY: Center for Imaging Science, Rochester Institute of Technology, 2004.
Cit. on p. 172.

[223] K. J. Dana, B. V. Ginneken, S. K. Nayar, and J. J. Koenderink: *Reflectance and Texture of Real-World Surfaces*. ACM Transactions on Graphics **18**, 1–34 (1999). DOI 10.1145/300776.300778, cit. on p. 173.

[224] J. D. Harms, C. M. Bachmann, J. W. Faulring, and A. J. Ruiz Torres: *A next generation field-portable goniometer system*. Proceedings of SPIE **9840**, 98400J (2016). DOI 10.1117/12.2223180, cit. on p. 173.

[225] K. R. Neumaier, G. Elender, E. Sackmann, and R. Merkel: *Ellipsometric microscopy*. Europhysics Letters **49**, 14–19 (2000). DOI 10.1209/epl/i2000-00113-x, cit. on p. 173.

[226] F. Linke: *Development of Ellipsometric Microscopy as a Quantitative High-Resolution Technique for the Investigation of Thin Films at Glass-Water and Silicon-Air Interfaces*, Forschungszentrum Jülich GmbH (Jülich), 2004. ISBN 3-89336-373-4, cit. on p. 173.

[227] E. Moyroud, T. Wenzel, R. Middleton, P. J. Rudall, H. Banks, A. Reed, G. Mellers, P. Killoran, M. M. Westwood, U. Steiner, S. Vignolini, and B. J. Glover: *Disorder in convergent floral nanostructures enhances signalling to bees*. Nature **550**, 469–474 (2017). DOI 10.1038/nature24285, cit. on p. 174.

[228] D. T. Meiers, M. C. Heep, and G. Von Freymann: *Invited Article: Bragg stacks with tailored disorder create brilliant whiteness.* APL Photonics **3**, 100802 (2018).
DOI 10.1063/1.5048194, cit. on p. 174.

[229] R. H. Siddique, Y. J. Donie, G. Gomard, S. Yalamanchili, T. Merdzhanova, U. Lemmer, and H. Hölscher: *Bioinspired phase-separated disordered nanostructures for thin photovoltaic absorbers.* Science Advances **3**, e1700232 (2017).
DOI 10.1126/sciadv.1700232, cit. on p. 174.

[230] S. R. Huisman, T. J. Huisman, S. A. Goorden, A. P. Mosk, and P. W. H. Pinkse: *Programming balanced optical beam splitters in white paint.* Optics Express **22**, 8320 (2014).
DOI 10.1364/oe.22.008320, cit. on p. 174.

[231] S. R. Huisman, T. J. Huisman, T. A. W. Wolterink, A. P. Mosk, and P. W. H. Pinkse: *Programmable multiport optical circuits in opaque scattering materials.* Optics Express **23**, 3102 (2015).
DOI 10.1364/oe.23.003102, cit. on p. 174.

[232] M. Jang, Y. Horie, A. Shibukawa, J. Brake, Y. Liu, S. M. Kamali, A. Arbabi, H. Ruan, A. Faraon, and C. Yang: *Wavefront shaping with disorder-engineered metasurfaces.* Nature Photonics **12**, 84–90 (2018).
DOI 10.1038/s41566-017-0078-z, cit. on p. 174.

[233] A. F. Koenderink, A. Lagendijk, and W. L. Vos: *Optical extinction due to intrinsic structural variations of photonic crystals.* Physical Review B - Condensed Matter and Materials Physics **72**, 153102 (2005).
DOI 10.1103/PhysRevB.72.153102, cit. on p. 174.

[234] E. R. Martins, J. Li, Y. Liu, V. Depauw, Z. Chen, J. Zhou, and T. F. Krauss: *Deterministic quasi-random nanostructures for photon control.* Nature Communications **4**, 2665 (2013).
DOI 10.1038/ncomms3665, cit. on p. 174.

[235] P. Varytis, D.-N. Huynh, W. Hartmann, W. Pernice, and K. Busch: *Design study of random spectrometers for applications at optical frequencies.* Optics Letters **43**, 3180–3183 (2018).
DOI 10.1364/ol.43.003180, cit. on p. 174.

[236] L. Maiwald, S. Lang, D. Jalas, H. Renner, A. Y. Petrov, and M. Eich: *Ewald sphere construction for structural colors.* Optics Express **26**, 11352 (2018).
DOI 10.1364/oe.26.011352, cit. on p. 174.

[237] A. Rahimzadegan, D. Arslan, R. N. Suryadharma, S. Fasold, M. Falkner, T. Pertsch, I. Staude, and C. Rockstuhl: *Disorder-Induced Phase Transitions in the Transmission of Dielectric Metasurfaces.* Physical Review Letters **122**, 15702 (2019).
DOI 10.1103/PhysRevLett.122.015702, cit. on pp. 174, 175.

[238] V. Neder, Y. Ra'Di, A. Alù, and A. Polman: *Combined Metagratings for Efficient Broad-Angle Scattering Metasurface.* ACS Photonics **6**, 1010–1017 (2019).
DOI 10.1021/acsphotonics.8b01795, cit. on p. 174.

[239] V. E. Ferry, M. A. Verschuuren, M. C. V. Lare, R. E. Schropp, H. A. Atwater, and A. Polman: *Optimized spatial correlations for broadband light trapping nanopatterns in high efficiency ultrathin film a-Si:H solar cells.* Nano Letters **11**, 4239–4245 (2011).
DOI 10.1021/nl202226r, cit. on p. 174.

[240] S. Nanz, A. Abass, P. M. Piechulla, A. Sprafke, R. B. Wehrspohn, and C. Rockstuhl: *Strategy for tailoring the size distribution of nanospheres to optimize rough backreflectors of solar cells.* Optics Express **26**, A111 (2018).
DOI 10.1364/oe.26.00a111, cit. on p. 174.

[241] C. Carlson and S. Hughes: *Disordered nanophotonic surfaces for enhanced light collection in semiconductor solar cells.* Journal of the Optical Society of America B **35**, 1093–1104 (2018).
DOI 10.1364/josab.35.001093, cit. on p. 174.

[242] N. Tavakoli and E. Alarcon-Llado: *Combining 1D and 2D waveguiding in an ultrathin GaAs NW/Si tandem solar cell.* Optics Express **27**, A909–A923 (2019).
DOI 10.1364/OE.27.00A909, cit. on p. 174.

[243] C. Bauer, G. Kobiela, and H. Giessen: *2D quasiperiodic plasmonic crystals.* Scientific Reports **2**, 1–6 (2012).
DOI 10.1038/srep00681, cit. on p. 175.

[244] C. Bauer and H. Giessen: *Optical properties of aperiodic metallic photonic crystal structures: Quasicrystals and disorder.* Journal of Optics (United Kingdom) **16**, 114001 (2014).
DOI 10.1088/2040-8978/16/11/114001, cit. on p. 175.

[245] D. Nau, A. Schönhardt, C. Bauer, A. Christ, T. Zentgraf, J. Kuhl, and H. Giessen: *Disorder issues in metallic photonic crystals.* Physica Status Solidi (B) Basic Research **243**, 2331–2343 (2006).
DOI 10.1002/pssb.200668054, cit. on pp. 175, 176.

[246] D. Nau, A. Schönhardt, C. Bauer, A. Christ, T. Zentgraf, J. Kuhl, M. W. Klein, and H. Giessen: *Correlation Effects in Disordered Metallic Photonic Crystal Slabs.* Physical Review Letters **98**, 133902 (2007).
DOI 10.1103/PhysRevLett.98.133902, cit. on p. 175.

[247] S. Torquato and F. H. Stillinger: *Local density fluctuations, hyperuniformity, and order metrics.* Physical Review E - Statistical Physics, Plasmas, Fluids, and Related Interdisciplinary Topics **68**, 041113 (2003).
DOI 10.1103/PhysRevE.68.041113, cit. on p. 178.

[248] H. Liu and S. J. Paddison: *Direct calculation of the X-ray structure factor of ionic liquids*. Physical Chemistry Chemical Physics **18**, 11000–11007 (2016). DOI 10.1039/c5cp06199g, cit. on p. 178.

[249] M. Kerscher, I. Szapudi, and A. S. Szalay: *A Comparison of Estimators for the Two-Point Correlation Function*. The Astrophysical Journal **535**, L13–L16 (2000). DOI 10.1086/312702, cit. on p. 179.

[250] S. D. Landy and A. S. Szalay: *Bias and Variance of Angular Correlation Functions*. The Astrophysics Journal **412**, 64–71 (1993). DOI 10.1086/172900, cit. on p. 179.

[251] T. W. Cronin, M. J. Bok, N. Justin Marshall, and R. L. Caldwell: *Filtering and polychromatic vision in mantis shrimps: Themes in visible and ultraviolet vision*. Philosophical Transactions of the Royal Society B: Biological Sciences **369**, 20130032 (2014). DOI 10.1098/rstb.2013.0032, cit. on p. 182.

[252] A. Stockman and L. T. Sharpe: *The spectral sensitivities of the middle- and long-wavelength-sensitive cones derived from measurements in observers of known genotype*. Vision Research **40**, 1711–1737 (2000). DOI 10.1016/S0042-6989(00)00021-3, cit. on pp. 182, 183.

[253] W. S. Stiles and J. M. Burch: *N.P.L. Colour-matching investigation: Final report (1958)*. Optica Acta: International Journal of Optics **6**, 1–26 (1959). DOI 10.1080/713826267, cit. on pp. 182, 183.

[254] Color and Vision Research Labs: *Colour & Vision Research laboratory and database*, http://cvrl.ioo.ucl.ac.uk/ (visited on Jan. 21, 2020). Cit. on p. 183.

[255] T. Smith and J. Guild: *The C.I.E. colorimetric standards and their use*. Transactions of the Optical Society **33**, 73–134 (1931). DOI 10.1088/1475-4878/33/3/301, cit. on p. 182.

[256] Futurrex Inc.: *Intermediate Coating IC1-200*, https://futurrex.com/en/products/spin-on-glass-coatings.html (visited on Mar. 8, 2019). Cit. on p. 186.

[257] Allied Vision Technologies GmbH: *Prosilica GC 2450*, https://www.alliedvision.com/en/products/cameras/detail/ProsilicaGC/2450.html (visited on Aug. 6, 2018). Cit. on p. 191.

[258] E. Herkert: *Computing the Influence of Structural Disorder op Plasmonic Metasurfaces*. MA thesis, University of Stuttgart, 2019. Cit. on pp. 202, 209.

[259] I. M. Fradkin, S. A. Dyakov, and N. A. Gippius: *Fourier modal method for the description of nanoparticle lattices in the dipole approximation*. Physical Review B **99**, 075310 (2019).
DOI 10.1103/PhysRevB.99.075310, cit. on p. 203.

[260] J. Yang, J. P. Hugonin, and P. Lalanne: *Near-to-Far Field Transformations for Radiative and Guided Waves*. ACS Photonics **3**, 395–402 (2016).
DOI 10.1021/acsphotonics.5b00559, cit. on p. 204.

[261] M. Khorasaninejad, W. T. Chen, R. C. Devlin, J. Oh, A. Y. Zhu, and F. Capasso: *Metalenses at visible wavelengths: Diffraction-limited focusing and subwavelength resolution imaging*. Science **352**, 1190–1194 (2016).
DOI 10.1126/science.aaf6644, cit. on p. 209.

[262] X. Yin, T. Steinle, L. Huang, T. Taubner, M. Wuttig, T. Zentgraf, and H. Giessen: *Beam switching and bifocal zoom lensing using active plasmonic metasurfaces*. Light: Science & Applications **6**, e17016 (2017).
DOI 10.1038/lsa.2017.16, cit. on p. 209.

[263] M. van Garderen: *Pictures of the Past: Visualization and visual analysis in archaeological context*. PhD Thesis, Universität Konstanz, 2018.
Cit. on p. 245.

A

SCIENTIFIC ARTWORK

An often quoted proverb is that a picture can say more than a thousand words. This definitely holds true for the presentation of scientific work, where visualization is one of the most important elements [263]. Besides an accurate description of scientific concepts, a logical storyline, and a correct and easily understandable display of data, the aesthetic appeal of an illustration is also an essential ingredient for effective scientific visualizations. For this reason, artwork is a highly important aspect in the presentation and communication of scientific research.

During my time as a PhD student, I have several times had the honor of developing such artwork for a the visualization of a variety of concepts. A selection of my work is presented below.

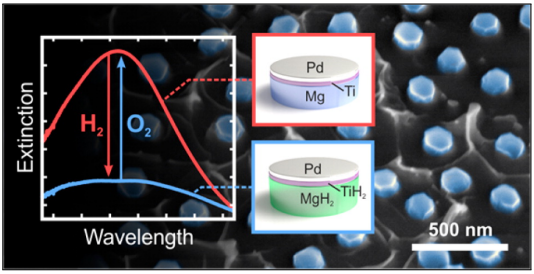

Figure A.1. Table of Contents figure of P1.

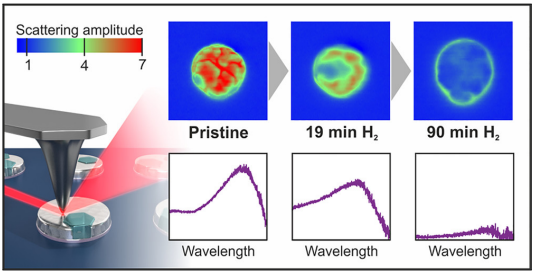

Figure A.2. Table of Contents figure of P2.

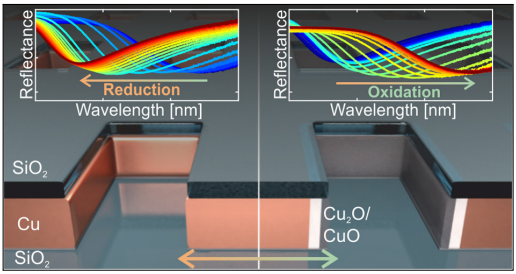

Figure A.3. Table of Contents figure of P12.

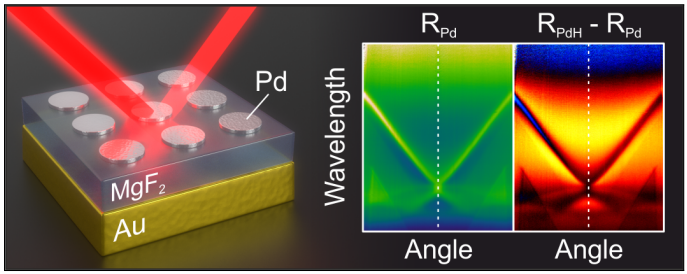

Figure A.4. Table of Contents figure of P3.

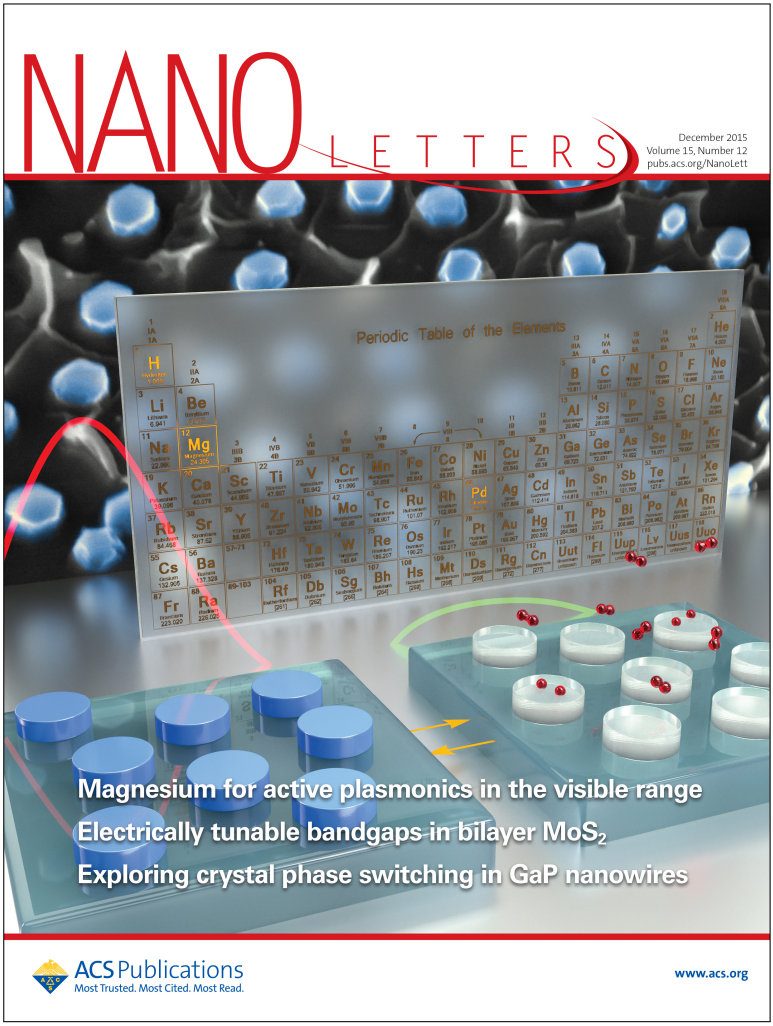

Figure A.5. Cover of the December 2015 issue of Nano Letters, highlighting publication P1.

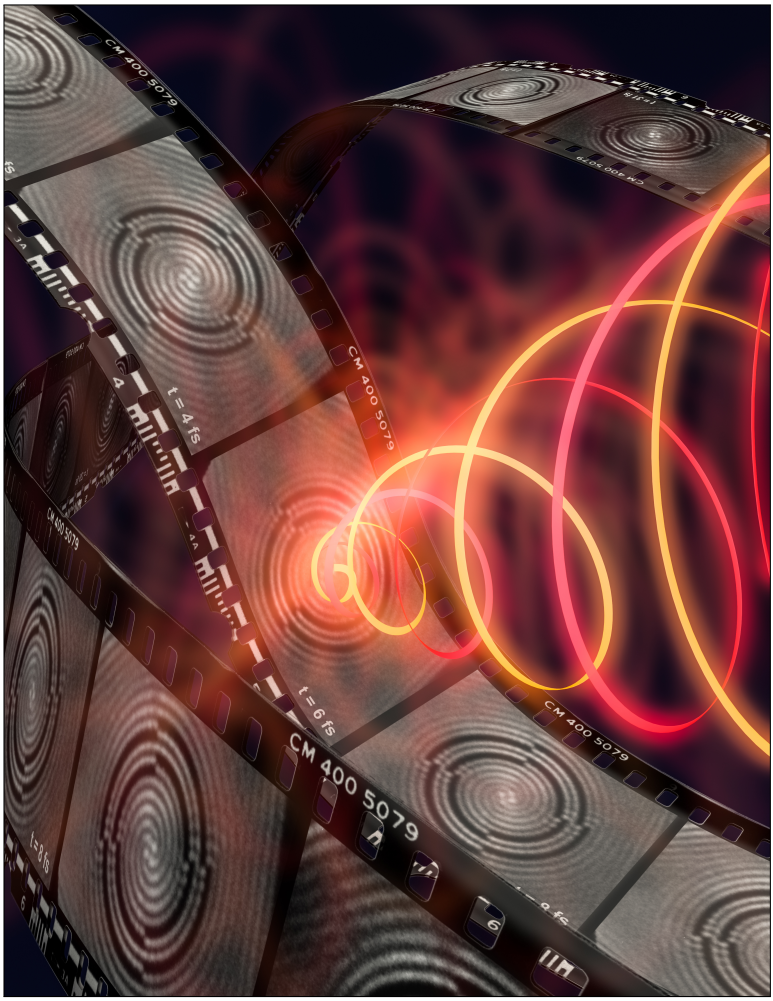

Figure A.6. Cover image proposal (not published) for the March 2017 issue of Science, intended to highlight: G. Spektor, D. Kilbane, A. K. Mahro, B. Frank, S. Ristok, L. Gal, P. Kahl, D. Podbiel, S. Mathias, H. Giessen, F.-J. Meyer zu Heringdorf, M. Orenstein, and M. Aeschlimann, "**Revealing the subfemtosecond dynamics of orbital angular momentum in nanoplasmonic vortices**", *Science* **355**, 1187-1191 (2017), DOI 10.1126/science.aaj1699.

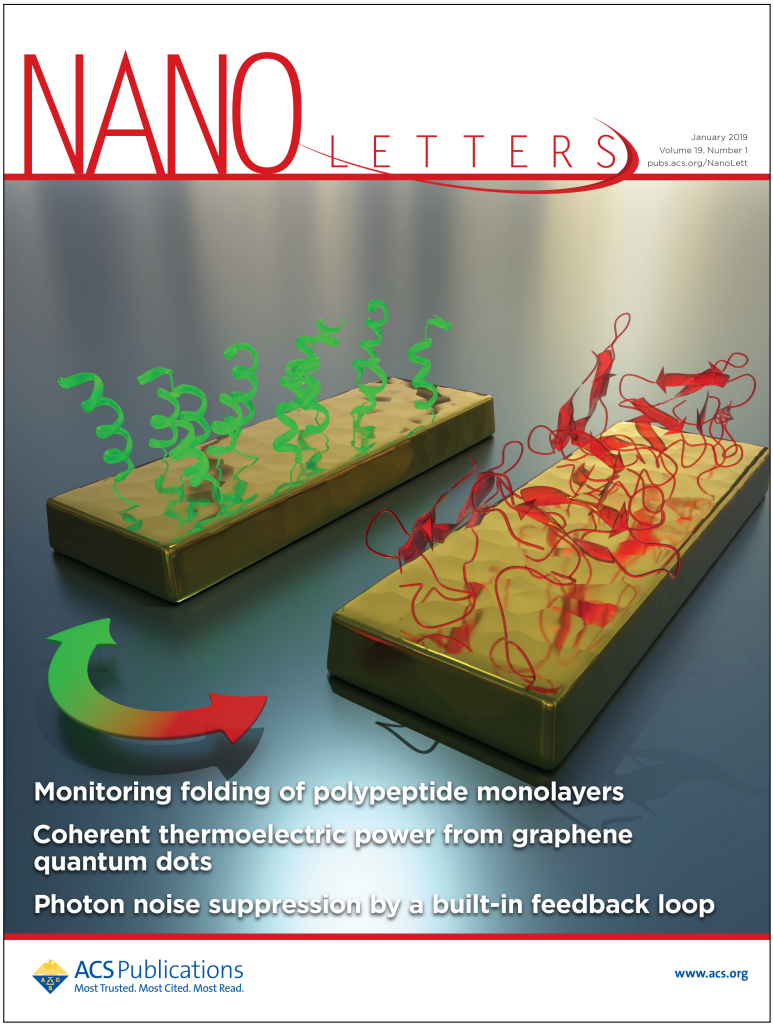

Figure A.7. Cover of the January 2019 issue of Nano Letters, highlighting: R. Semenyshyn, M. Hentschel, C. Stanglmair, T. Teutsch, C. Tarin, C. Pacholski, H. Giessen, and F. Neubrech, "**In-vitro monitoring conformational changes of polypeptide monolayers using infrared plasmonic nanoantennas**", *Nano Letters* **19**(1), 1-7 (2019), DOI 10.1021/acs.nanolett.8b02372.

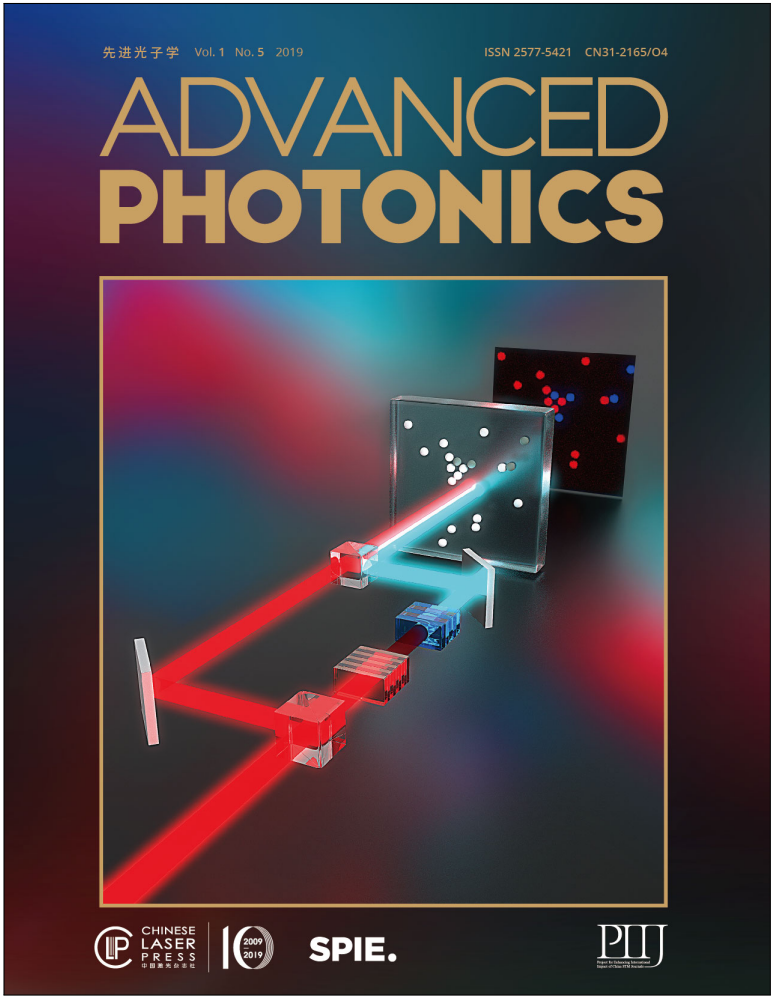

Figure A.8. Cover of the September 2019 issue of Advanced Photonics, highlighting: H. Linnenbank, T. Steinle, F. Mörz, M. Flöss, H. Cui, A. Glidle, and H. Giessen, "**Robust and rapidly tunable light source for SRS/CARS microscopy with low-intensity noise**", *Advanced Photonics* **1**(5), 055001 (2019), DOI 10.1117/1.AP.1.5.055001.

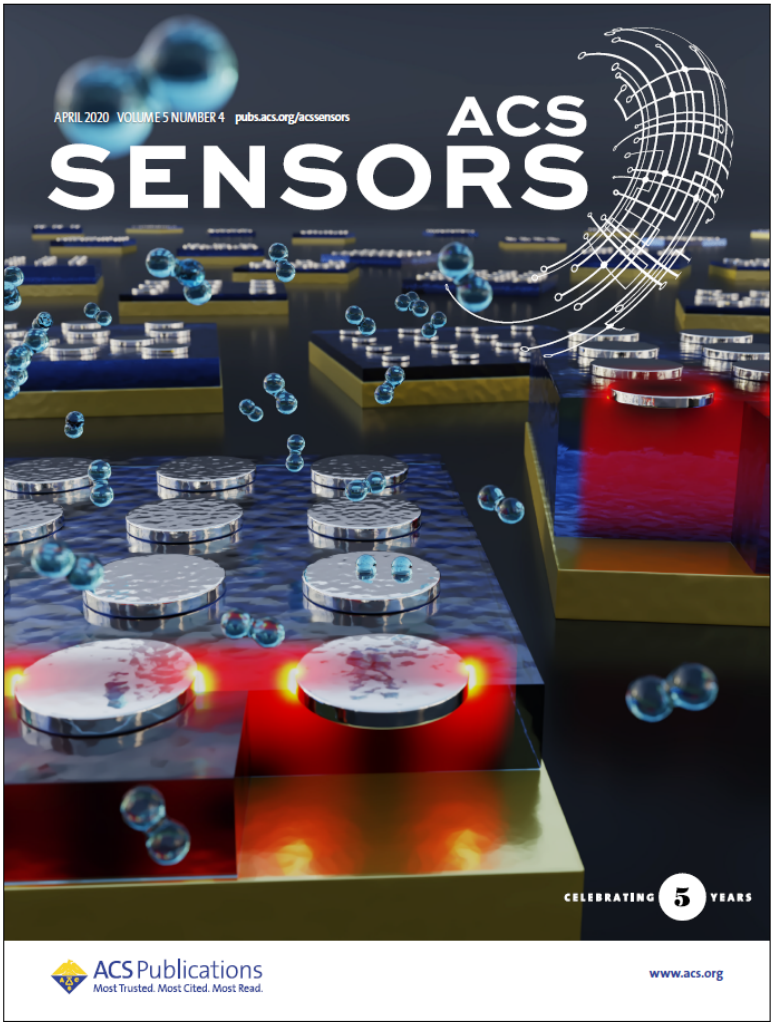

Figure A.9. Cover of the April 2020 issue of ACS Sensors, highlighting publications P3 and P15.

ACKNOWLEDGMENTS

I am right now looking back at six years of doing my PhD at the 4th Physics Institute at the University of Stuttgart, plus some Coronavirus-induced extra months (it is the year 2020, after all). Six years is a long time, but it has been an amazing ride. Obviously, a lot of people have contributed to the success of my work, scientifically and otherwise, for which I am incredibly grateful.

First and foremost, of course, I want to thank Prof. Dr. Harald Giessen, who gave me the opportunity to work in his group in the first place. Besides infecting me with his enthusiasm and supporting me throughout my work - and sending me to several great conferences - he introduced me to the world of scientific commercialization, in which I hope to continue on at least a small scale.

I am of course very grateful as well to Prof. Dr. Stefanie Barz and Prof. Dr. Siegfried Dietrich, for agreeing to be my second examiner and the head of my examination committee, and for taking the time and effort to read and examine my work and for arranging a PhD examination despite the interesting times we live in right now.

I would have been completely lost without Dr. Christine von Rekowski, who was always a great help with all administrative matters and helped me navigate the mazes of bureaucracy (which is really not one of my talents). A lot of my work would not have been possible either without Ralf Kamella and his team in the university workshop, specifically Jessie Linnenbank, who would always take the time to discuss and improve the drawings I had come up with. The technical support of Michael Kube - and our many random chats about bikes, the weather, and the Netherlands - should also not be missing from this list.

Since a significant part of my work took place in the cleanroom, I am very grateful to the team that manages all the facilities. Ramon Walter, Moni Ubl (who will, by the way, never forgive you if you buy the wrong type of beer for the Christmas party), Dr. Mario Hentschel, and Philipp Flad: thanks a lot for teaching me all kinds of different processes in the MSL, for being great supervisors and problem-solvers, and of course for giving me the freedom

to work with a lot of machines myself, which I don't think should be taken for granted.

A lot of people have also contributed directly to the work shown in this thesis. I am very grateful to my colleague Dr. Nik Strohfeldt, who not only introduced me to the whole concept of microspectroscopy, but who is also a good friend outside of work and has been involved in some commercial activities together with me. The same goes for Dr. Heiko Linnenbank, together with whom I carried out the s-SNOM measurements. I am of course also grateful to Prof. Dr. Ronald Griessen, our go-to expert for all things concerning hydrogen in metals, and to Prof. Dr. Tim Davis and Prof. Dr. Thomas Weiss for taking the time to discuss my work with me.

Many, many others have of course contributed by simply making life at the institute more enjoyable. I am grateful to Dr. Dominik Floess, for the good years we had together in room 4.507. To Dr. Martin Schäferling, Dr. Tobi Steinle, Dr. Xinghui Yin, Dr. Gelon Albrecht, Dr. Shahin Bagheri, Dr. Rostyslav Semenyshyn, Simon Ristok, Ksenia Weber, and all the rest, for being great friends, not only at work but also outside of it. The same applies to 'the Theorists' Steffen Both, Sascha Böhrkircher, Swaathi Upendar (except for having me slapped in the face by a scary barkeeper over a candlestick), and Izzatjon Allayarov; to Qi Ai, who taught me the importance of always eating enough fruit; to Josselin Defrance, Flo Mörz, and Philipp Geser, with whom I share my enthusiasm for cycling, mountain biking, and riding the Critical Mass in Stuttgart; and to my office buddy Dr. Asa Asadollahbaik. And, of course, to Moritz Floess, Dr. Bettina Frank, Parmida Shabestary, Ramon Walter, sir McBoth, and señor Steinle, for taking the time to read parts of my thesis and help me improve it.

A very special thanks goes out to all the students that I had the honor of supervising. To Caroline Grenet, who ran the first systematic study of different hydrogen sensor designs. To Elinor Kath, for joining me on the CM rides, for the 3D printer talk, and for all of her many questions. To Tobi Pohl, for his great work and all his technical assistance. To Annette Böhme, for teaching me words like 'Nübsel' and 'hurgeln', and for being an awesome ski instructor. To Julian Karst, for all our discussions and for his impressive work on several different subjects. To Ediz "Oh by the way, I quickly built a graphical user interface and also rewrote everything in Python" Herkert, for his crazy programming skills. To all of you guys, for the publications your work has led to. And, most importantly, thank you all for the great time - my involvement in your projects probably cost me about a year of my work, but that was, without a doubt, the best year.

Last but definitely not least, I am incredibly grateful to my parents, Andreas (the first Dr. Sterl!) and Caroline, and to my bro Sebastian (Dr.-to-be) and my sisters Miriam and Xenia, for having inspired me to pursue a career in scientific research in the first place and for always having supported me - I hope I'm doing a proper job at returning the favor.

And, of course, to Mereke. For being with me since almost twelve years, for being the reason that I came to Germany in the first place, for patiently supporting me through six years of PhD-ing, and simply for everything.

CURRICULUM VITÆ

NAME	Florian Frederik Sterl
BORN	April 16, 1990 in Pinneberg, Germany
CITIZENSHIPS	German, Dutch
ADDRESS	Rübezahlweg 62, 70567 Stuttgart, Germany
PHONE	+49 172 7364231
E-MAIL	floriansterl@gmail.com

SINCE 2017	Own company *Sterltech Optics* (Meyenhagen 37, 3721XA Bilthoven, The Netherlands). Specializing in scientific artwork, software development and design and implementation of optical laboratory setups.
2014 - 2020	Ph.D. thesis: *"Imaging microspectroscopy of functional nanoplasmonic systems"*, 4th Physics Institute and Research Center SCoPE, University of Stuttgart, Stuttgart, Germany.
2011 - 2013	MSc. Applied Physics (Optics and Biophysics track), University of Twente, Enschede, The Netherlands. MSc. thesis: *"Towards efficient photocatalytic water splitting: Increasing the absorption rate of ruthenium-based chromophores by coupling to plasmonic silver nanostructures"* at research group Optical Sciences (OS).
2012	Research Internship, ICFO - The Institute of Photonic Sciences, Castelldefels (Barcelona), Spain, at research group Molecular Nanophotonics.
2010 - 2011	Minor Werktuigbouwkunde (Mechanical Engineering), University of Twente, Enschede, The Netherlands.
2008 - 2011	BSc. Technische Natuurkunde (Applied Physics), University of Twente, Enschede, The Netherlands.
2006 - 2008	Junior College Utrecht (JCU), Utrecht, The Netherlands.
2002 - 2008	Voortgezet Wetenschappelijk Onderwijs, Het Nieuwe Lyceum, Bilthoven, The Netherlands.

COLOPHON

This thesis was typeset with LaTeX 2_ε using Robert Slimbach's Minion Pro font. The style was inspired by Robert Bringhurst's "*The Elements of Typographic Style*". It is available for LaTeX via CTAN as CLASSICTHESIS.